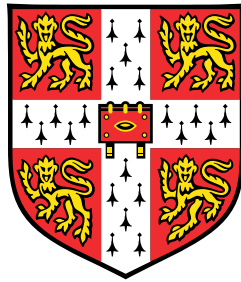


# Spin transport through nanopillar superconducting spin valves



**Ben Stoddart-Stones**

Department of Materials Science and Metallurgy  
University of Cambridge

This thesis is submitted for the degree of  
*Doctor of Philosophy*



## Declaration

This thesis is my own work and contains nothing which is the outcome of work done in collaboration with others, except as specified in the text and Acknowledgements. This work has been carried out in the Department of Materials Science and Metallurgy, University of Cambridge, U.K. since October 2017. No part of this dissertation has been submitted previously at Cambridge or any other University or similar institution for a degree, diploma or other qualification. This dissertation does not exceed 60,000 words.

Ben Stoddart-Stones  
November 2021



# Spin transport through nanopillar superconducting spin valves: Summary

This thesis details an investigation into the interaction of non-equilibrium spin currents with superconductivity using spin valves, where the difference in resistance between the antiparallel (AP) and parallel (P) alignments of the magnetic layers within the device [magnetoresistance,  $\Delta R = R^{AP} - R^P$ ] has been used to quantify the spin decay occurring as the current passes through the central spacer layer. Py (15 nm)/Cu (10 nm)/Nb ( $x$  nm)/Cu (10 nm)/Py (15 nm)/FeMn (10 nm) spin valves with 200 nm Cu contact layers were deposited using dc magnetron sputtering, and fabricated into current-perpendicular-to-plane (CPP) nanopillars using optical lithography and Ar ion milling followed by focused ion beam milling. Magnetic and electrical characterisation of these devices at temperatures between 0.3-10 K demonstrate a decrease of magnetoresistance (increasing spin decay), with increasing  $x$ , the thickness of the central Nb. This trend occurs in the normal state, and also for devices in the superconducting state, which demonstrate a shorter spin decay length. This is supported by measurement of  $\Delta T_c = T_c^{AP} - T_c^P$ , where  $T_c$  is the superconducting transition temperature of the device, and  $\Delta T_c$  is negative for these CPP devices demonstrating positive  $\Delta R$ . However, devices in the superconducting state with  $x < 26$  nm demonstrate negative magnetoresistance and positive  $\Delta T_c$ , behaviour that is typically seen for superconducting spin valves in the current-in-plane regime, where this behaviour is a result of the dominant effect of the exchange fields of the ferromagnets on the superconducting order parameter of the central layer. A crossover between these two parameters ( $\Delta R$  and  $\Delta T_c$ ) is observed with increasing thickness of the central Nb. A toy model is developed and fit to these data which suggests this crossover occurs when the thickness of the central Nb exceeds two coherence lengths.

Ben Stoddart-Stones



## Acknowledgements

Dr Xavier Montiel reviewed the phenomenological model presented in Section 7.3.3 and provided input to ensure it was physical. This is also noted as a footnote to the text when the model is presented.

This thesis is the result of four years of experimental research and analysis, and many people have helped and supported me along the way. Firstly, I owe my supervisor, Professor Jason Robison, an enormous debt of gratitude for helping me through this process, from initial experimental struggles, through to the later stages of analysis and writing, and in particular for his support through my most stressful moments. I am also grateful to other members of the Device Materials Group, especially Dr Nadia Stelmashenko, for her friendship and tireless assistance with equipment maintenance, and Professor Mark Blamire, Dr Guang Yang, Dr Xavier Montiel, Dr Sachio Komori, and Dr Mario Amado-Montero for the advice and discussions they all provided throughout my PhD. I would also like to thank the other student members of the Device Materials Group for putting up with my complaints and raging about experimental failures, and for the bonding we shared over such struggles. In particular, I must mention Graham Kimbell, who has endured thousands of my complaints, stupid questions, and worries over the years, and most importantly is the joint founder of the hotly contested and eternally debated Biscuit League of 2018.

I acknowledge the Engineering and Physical Sciences Research Council, U.K. for funding me for four years.

Outside of the lab, I am extraordinarily grateful to my parents and family, who have given everything to enable me to succeed, and whom I can never fully repay. Thank you also to all of my friends for supporting me, particularly Laura Taylor and Casey Shephard for putting up with me as a housemate for this final, difficult year in a pandemic hit world. Beyond that, thank you to everyone who has been there for me and helped me grow through these four years.

Following my viva examination, I must thank Professor Malte Grosche and Professor Carmine Attanasio, for their interest in my work, and their identification of errors in this thesis, including missing information, and unclear or flat out wrong statements. This version of the thesis contains corrections made according to their suggestions.



# Contents

<b>Symbols</b>	<b>xiii</b>
<b>Abbreviations</b>	<b>xv</b>
<b>List of Figures</b>	<b>xvi</b>
<b>List of Tables</b>	<b>xix</b>
<b>1 Introduction</b>	<b>1</b>
<b>2 Theoretical Background</b>	<b>3</b>
2.1 Magnetism . . . . .	3
2.1.1 Atomic origins . . . . .	3
2.1.1.1 Spin-orbit coupling . . . . .	4
2.1.2 Magnetic Materials . . . . .	4
2.1.2.1 Diamagnetism and Paramagnetism . . . . .	4
2.1.2.2 Ferromagnetism . . . . .	6
2.1.2.3 Antiferromagnetism . . . . .	9
2.1.3 Anisotropy, domains and hysteresis . . . . .	9
2.1.3.1 Hysteresis loops . . . . .	11
2.2 Electron Transport . . . . .	14
2.2.1 Density of States . . . . .	15
2.2.2 Electron Bands . . . . .	16
2.2.3 Conductivity . . . . .	17
2.2.4 Magnetoresistance . . . . .	20
2.3 Superconductivity . . . . .	22
2.3.1 Phenomenological theories . . . . .	23
2.3.1.1 Ginzburg-Landau theory . . . . .	24
2.3.2 Magnetic fields . . . . .	26
2.3.3 Cooper pairs . . . . .	27
2.3.4 Proximity effect . . . . .	29
2.3.4.1 S/N interfaces . . . . .	29

2.3.4.2	S/F interfaces . . . . .	30
2.3.4.3	Triplet pairs . . . . .	31
2.3.5	Quasiparticles and non-equilibrium . . . . .	32
2.3.6	Superconducting spin valves . . . . .	34
2.4	Thin films . . . . .	36
2.4.1	Microstructure and growth . . . . .	36
2.4.2	Thin film properties . . . . .	38
2.4.2.1	Electric properties . . . . .	38
2.4.2.2	Magnetic Properties . . . . .	39
2.4.2.3	Superconductivity . . . . .	39
<b>3</b>	<b>Experimental Methods</b>	<b>41</b>
3.1	Magnetron Sputter Deposition . . . . .	42
3.1.1	Experimental Process . . . . .	44
3.2	Optical Lithography and Ion Milling . . . . .	45
3.3	Focused ion beam milling . . . . .	48
3.4	Low Temperature Measurements . . . . .	49
3.5	Vibrating Sample Magnetometry . . . . .	52
3.6	X-ray Diffraction . . . . .	53
3.7	Atomic Force Microscopy . . . . .	54
<b>4</b>	<b>Spin valve construction</b>	<b>55</b>
4.1	Background . . . . .	55
4.1.1	Exchange bias . . . . .	55
4.1.2	Magnetic properties of thin films and devices . . . . .	57
4.1.2.1	Permalloy in devices . . . . .	57
4.1.2.2	Roughness . . . . .	59
4.1.2.3	FIB and ion milling . . . . .	60
4.2	Experimental Results . . . . .	61
4.2.1	FeMn pinning . . . . .	61
4.2.2	Contact layers . . . . .	67
4.2.3	Cu buffer layers and Py . . . . .	69
4.2.4	Roughness . . . . .	70
4.2.5	Effect of FIB on $R(H)$ . . . . .	71
4.3	Conclusions . . . . .	72
<b>5</b>	<b>Magnetoresistance in normal state spin valves</b>	<b>75</b>
5.1	Background . . . . .	75
5.1.1	CIP vs CPP . . . . .	75
5.1.2	Modelling CPP magnetoresistance . . . . .	76

5.1.3	Experimental background on factors affecting CPP GMR . . . . .	79
5.1.3.1	Spacer Layers . . . . .	79
5.1.3.2	Ferromagnetic Layers . . . . .	80
5.1.3.3	Asymmetric scattering . . . . .	81
5.1.3.4	Construction . . . . .	82
5.2	Experimental Results . . . . .	84
5.2.1	GMR . . . . .	84
5.2.2	Spacer layer spin diffusion length . . . . .	87
5.2.3	Device Dimensions . . . . .	89
5.2.4	Negative Magnetoresistance . . . . .	90
5.2.5	Single Cuts . . . . .	94
5.2.6	Consistency . . . . .	95
5.3	Conclusions . . . . .	97
<b>6</b>	<b>Superconducting spin valves</b>	<b>99</b>
6.1	Background . . . . .	99
6.1.1	Current-perpendicular-to-plane spin valves . . . . .	99
6.1.2	Current-in-plane spin valves . . . . .	101
6.1.3	Superconducting transport . . . . .	104
6.2	Experimental Results . . . . .	106
6.2.1	Superconducting transition . . . . .	106
6.2.1.1	$\Delta T_c$ . . . . .	110
6.2.2	$R(H)$ response . . . . .	111
6.2.3	Complicating factors . . . . .	113
6.2.3.1	Double transition . . . . .	113
6.2.3.2	Wires . . . . .	116
6.2.3.3	Single Cuts . . . . .	119
6.2.4	Layer dependence . . . . .	120
6.2.4.1	Cu and Py . . . . .	120
6.2.5	Coherence length . . . . .	122
6.2.6	CIP devices . . . . .	122
6.3	Conclusions . . . . .	125
<b>7</b>	<b>Transport regimes in superconducting spin valves</b>	<b>127</b>
7.1	Background . . . . .	127
7.2	Experimental Results . . . . .	129
7.2.1	Quasiparticle giant magnetoresistance . . . . .	129
7.2.1.1	Current dependence . . . . .	131
7.2.1.2	Temperature dependence . . . . .	133
7.2.2	Proximity effect . . . . .	135

7.2.2.1	Current dependence . . . . .	137
7.2.2.2	Temperature dependence . . . . .	139
7.3	Crossover between behaviours . . . . .	139
7.3.1	Layer dependence . . . . .	140
7.3.1.1	Nb thickness . . . . .	140
7.3.1.2	Cu and Py . . . . .	141
7.3.2	Dependence on superconducting order . . . . .	142
7.3.3	Modelling . . . . .	145
7.4	Conclusions . . . . .	147
<b>8</b>	<b>Conclusions and future work</b>	<b>149</b>
8.1	Summary of conclusions . . . . .	149
8.2	Future Work . . . . .	150
8.2.1	Device construction . . . . .	150
8.2.2	Spin-orbit coupling . . . . .	151
8.2.3	Superconducting spin valve effect . . . . .	152
	<b>References</b>	<b>153</b>

# Symbols

$A$	Device area	$H_{\text{ex}}$	Exchange bias field
$\mathbf{A}$	Magnetic vector potential	$H_{\text{c}}$	Critical field of superconductor
$A, B$	Toy model fitting parameters	$H_{\text{c}}$	Coercive field of ferromagnet
$AR_{i,j}$	Areal interfacial resistance	$I$	Current
$B, \mathbf{B}$	Magnetic flux density	$I_{\text{c}}$	Critical current of superconductor
$d$	Film thickness	$I_{\text{S}}$	Stoner exchange parameter
$d_0$	Crossover thickness	$j, \mathbf{j}$	Current density
$d_{h,k,l}$	Plane spacing	$J$	Exchange energy
$D$	Electron diffusivity	$k, \mathbf{k}$	Momentum
$\mathcal{D}(E)$	Density of states	$k_{\text{B}}$	Boltzmann constant
$e$	Electronic charge	$\mathbf{l}$	Orbital angular momentum
$E$	Energy	$l_{sf}$	Spin flip length
$E_{\text{ex}}$	Exchange interaction energy	$l_{\text{S}}$	QP GMR model parameter
$E_{\text{a}}$	Magnetocrystalline anisotropy energy	$m$	Mass
$E_{\text{d}}$	Demagnetisation energy	$m_{\text{e}}$	Mass of an electron
$E_{\text{F}}$	Fermi energy	$M$	Magnetisation
$\mathbf{E}_{\text{field}}$	Electric field	$M_{\text{R}}$	Remanent magnetisation
$E_{\text{Z}}$	Zeeman energy	$M_{\text{S}}$	Saturation magnetisation
$\mathcal{E}$	Single particle energy difference from $E_{\text{F}}$	$n$	Integer per unit volume
$f(E)$	Fermi-Dirac distribution function	$n_{\text{N}}$	Normal electron density
$F$	Force	$n_{\text{S}}$	Superconducting electron density
$\mathcal{F}$	Free energy	$N$	Integer
$\mathcal{F}_0$	Free energy in normal state	$P$	Pressure
$h$	Planck's constant	$PD$	Pressure-distance product
$\hbar$	Planck's constant / $2\pi$	$q$	Charge
$h, k, l$	Miller indices	$Q^*$	Effective charge
$H, \mathbf{H}$	Magnetic field strength	$\mathbf{r}$	Position
		$r$	Small resistance
		$r_{\text{N}}$	Resistance of spacer layer
		$R$	Resistance

$\mathbf{S}, \mathbf{s}$	Spin angular momentum	$\lambda$	Wavelength
$t$	Time	$\lambda$	Mean free path of electron
$T$	Temperature	$\lambda_{\mathbf{GL}}$	Ginzburg-Landau penetration depth
$T^*$	Effective temperature	$\Lambda_{\mathbf{S}}$	Proximity effect model parameter
$T_{\mathbf{C}}$	Curie temperature	$\mu$	Chemical potential
$T_{\mathbf{c}}$	Critical temperature of superconductor	$\Delta\mu$	Spin accumulation
$T_{\mathbf{device}}$	Start of superconducting transition	$\mu_0$	Permittivity of free space
$\mathbf{v}$	Velocity	$\mu_B$	Bohr magneton
$v_F$	Fermi velocity	$\xi_0$	Pippard coherence length
$Z$	Atomic number	$\xi_F$	Coherence length in ferromagnet
$Z(E)$	Occupied density of states	$\xi_{\mathbf{GL}}$	Ginzburg-Landau coherence length
$\alpha, \beta$	Ginzburg-Landau parameters	$\xi_N$	Coherence length in normal metal
$\beta$	Bulk spin anisotropy parameter	$\xi_S$	Coherence length in superconductor
$\gamma$	Interface spin anisotropy parameter	$\rho$	Resistivity
$\delta$	Interfacial spin flip parameter	$\sigma$	Conductivity
$\Delta(T)$	Superconducting gap	$\tau$	Scattering time
$\theta$	Angle	$\phi$	Magnetic flux
$\theta$	Phase	$\Phi_0$	Magnetic flux quantum
$\Theta$	Difference between two phases	$\chi$	Magnetic susceptibility
$\kappa$	Ginzburg-Landau ratio	$\psi(\mathbf{r})$	Wavefunction

# Abbreviations

AF	Antiferromagnet
AFM	Atomic force microscopy
AP	Antiparallel
AMR	Anisotropic magnetoresistance
bcc	Body-centred cubic
CIP	Current in-plane
CPP	Current perpendicular-to-plane
dc	Direct current
F	Ferromagnet
fcc	Face-centred cubic
FIB	Focused ion-beam
GL	Ginzburg-Landau
GMR	Giant magnetoresistance
N	Normal metal
OMR	Ordinary magnetoresistance
P	Parallel
Py	Permalloy, Ni <sub>80</sub> Fe <sub>20</sub>
QP	Quasiparticle
RRR	Residual resistivity ratio
S	Superconductor
SEM	Scanning electron microscope
SQUID	Superconducting quantum interference device
UV	Ultra-violet
VF	Valet-Fert
VSM	Vibrating sample magnetometry

# List of Figures

2.1	Simplified picture of Pauli paramagnetism . . . . .	5
2.2	Density of states for Fe, Co, Ni and Cu . . . . .	8
2.3	3Q spin structure of FeMn . . . . .	10
2.4	Domain formation within a ferromagnet . . . . .	11
2.5	A typical $M(H)$ hysteresis loop for a ferrromagnet . . . . .	12
2.6	Exchange bias . . . . .	13
2.7	$M(H)$ loops for spin valves . . . . .	14
2.8	Occupied density of states for free electron model . . . . .	16
2.9	Electron bands from Bragg reflection . . . . .	17
2.10	Fermi sphere picture of electronic conduction . . . . .	19
2.11	Anisotropic magnetoresistance . . . . .	21
2.12	Superconducting transition and Meissner effect in a superconductor . . . . .	23
2.13	Type I and Type II superconductors from Ginzburg-Landau theory . . . . .	26
2.14	$T-H-I$ phase diagram of the superconducting and normal states . . . . .	27
2.15	Electronic state pairing in BCS theory . . . . .	28
2.16	Proximity effect and Andreev reflection . . . . .	30
2.17	Triplet pair formation at a superconductor/ferromagnet interface . . . . .	31
2.18	Semiconductor model of quasiparticle states . . . . .	33
2.19	Non-equilibrium modes in a superconductor . . . . .	35
2.20	Island and layer growth of thin films . . . . .	37
2.21	Thornton's zone model for sputter deposited thin films . . . . .	38
3.1	Thin film multilayer structure of the main device . . . . .	42
3.2	Sputter deposition . . . . .	43
3.3	Lift off calibration AFM scan and flange schematic . . . . .	44
3.4	Lithography . . . . .	47
3.5	Focused ion beam milling of nanopillars . . . . .	48
3.6	Current setups . . . . .	50
3.7	Major and minor $R(H)$ loops . . . . .	51
3.8	Vibrating sample magnetometer . . . . .	53

4.1	Compensated and uncompensated antiferromagnets . . . . .	56
4.2	Exchange bias dependence on layer thickness . . . . .	57
4.3	Shape effects on magnetic domains . . . . .	58
4.4	Interlayer coupling dependence on spacer layer . . . . .	60
4.5	Coercivity dependence on nanowire width . . . . .	61
4.6	$M(H)$ loops from Py/FeMn bilayers . . . . .	62
4.7	Exchange bias dependence on Nb and Cu underlayers . . . . .	63
4.8	Exchange bias vs. coercive field . . . . .	63
4.9	X-ray diffraction scans on Py/FeMn bilayers . . . . .	64
4.10	Roughness of Py/FeMn bilayers . . . . .	65
4.11	$M(H)$ loops of a full spin valve at varying temperature . . . . .	66
4.12	Complications in early devices with Nb contacts . . . . .	67
4.13	Current flow and current bunching in devices . . . . .	69
4.14	Normal state magnetoresistance dependence on $d_{\text{Cu}}$ and $d_{\text{Py}}$ . . . . .	70
4.15	Roughness through increasing layers of the structure . . . . .	71
4.16	Variation in magnetic switching from FIB milling . . . . .	72
5.1	CIP vs CPP magnetoresistance . . . . .	76
5.2	Two current series resistor model for magnetoresistance . . . . .	77
5.3	Heterostructure basis for Valet-Fert equations . . . . .	78
5.4	Spin flip lengths for normal metals and permalloy . . . . .	79
5.5	Inverse relationship of spin flip length and resistivity . . . . .	80
5.6	Area and width dependence of magnetoresistance . . . . .	83
5.7	Minor $R(H)$ loops measured in the normal state . . . . .	85
5.8	Comparison of major $M(H)$ and $R(H)$ loops . . . . .	86
5.9	Magnetoresistance vs. Nb thickness in the normal state . . . . .	88
5.10	Effect of nanopillar area and aspect ratio on magnetoresistance . . . . .	90
5.11	Effect of nanopillar length and width on magnetoresistance . . . . .	91
5.12	Negative magnetoresistance in a major $R(H)$ loop . . . . .	92
5.13	Negative magnetoresistance dependence on layer thickness . . . . .	93
5.14	Negative magnetoresistance dependence on nanopillar length . . . . .	93
5.15	Magnetoresistance from normal state ‘single cut’ devices . . . . .	94
5.16	Superconducting transition temperature vs. residual resistivity ratio of reference Nb films . . . . .	96
6.1	Spin decay in superconducting spin valves . . . . .	100
6.2	Prediction of $\Delta T_c$ for different interfacial transparencies, from Tagirov . . . . .	101
6.3	Large values of $\Delta T_c$ from the superconducting spin valve effect . . . . .	103
6.4	The inverse spin valve effect . . . . .	104
6.5	Spin transport measurement devices . . . . .	105

6.6	Change of spin transport in the superconducting state . . . . .	105
6.7	Transition temperature dependence on Nb thickness . . . . .	107
6.8	Effect of pillar size on superconductor current dependence . . . . .	108
6.9	Resistance increase below superconducting transition . . . . .	109
6.10	Three different $\Delta T_c$ behaviours . . . . .	110
6.11	Link between $\Delta R$ and $\Delta T_c$ . . . . .	112
6.12	Two different $R(H)$ behaviours . . . . .	113
6.13	Device and wire transition temperature comparison . . . . .	114
6.14	Magnetoresistance response of the wires in the superconducting state . . . . .	117
6.15	Magnetoresistance from superconducting state ‘single cut’ devices . . . . .	119
6.16	$T_c$ and superconducting state magnetoresistance dependence on $d_{Cu}$ . . . . .	121
6.17	$T_c$ and superconducting state magnetoresistance dependence on $d_{Py}$ . . . . .	121
6.18	Measurement of coherence length in an isolated Nb film . . . . .	122
6.19	Normal state $R(H)$ loops on current-in-plane structures . . . . .	123
6.20	Current-in-plane structure with a thin spacer layer . . . . .	124
6.21	Current-in-plane structure in the superconducting state . . . . .	125
7.1	Changes of sign of $\Delta T_c$ . . . . .	128
7.2	Two different superconducting transport regimes . . . . .	129
7.3	Spin decay in devices demonstrating quasiparticle magnetoresistance . . . . .	130
7.4	Current bias dependence of quasiparticle giant magnetoresistance . . . . .	132
7.5	Superconducting transitions and $\Delta R(T)$ . . . . .	134
7.6	Temperature dependence of quasiparticle giant magnetoresistance . . . . .	135
7.7	Cartoon of the effect of interface transparency . . . . .	136
7.8	Current dependence of proximity effect dominated behaviour . . . . .	137
7.9	The transition between proximity effect dominated behaviour and quasi- particle giant magnetoresistance . . . . .	138
7.10	Temperature dependence of proximity effect dominated behaviour . . . . .	139
7.11	Systematic dependence of transport behaviour on Nb thickness . . . . .	141
7.12	Systematic dependence of transport behaviour on nanopillar transition temperature . . . . .	142
7.13	Systematic dependence of transport behaviour on nanopillar transition temperature suppression . . . . .	143
7.14	Crossover of behaviour linked to superconducting coherence length . . . . .	144
8.1	Spin valves with Pt layers to investigate spin-orbit coupling . . . . .	151

# List of Tables

3.1	Sputter deposition parameters . . . . .	45
3.2	Measured resistivities of bare films . . . . .	52
5.1	Literature values of relevant spin flip lengths . . . . .	81
6.1	Upper and lower transition temperatures across three substrates . . . . .	115



# Chapter 1

## Introduction

Computers have become a vital part of the modern world, and as Moore's law comes to an end, research into alternative computing technologies is expected to accelerate [1]. However, the rapid growth of computing in all walks of life is associated with a dramatic increase in energy demand, from large scale supercomputers and data centres to consumer electronics. In a worst case scenario, communication technology has been estimated to contribute up to 23% of globally released greenhouse gas emissions by 2030 [2]. This suggests the need for computing technologies that are extremely energy efficient as well as powerful, using energy efficient superconducting architectures [3]. Superconducting spintronics is one such potential technology [4, 5].

While semiconductor-based computing uses charge to control current flow in transistors, spintronics ('spin electronics') allows for more efficient computing circuits [6] by utilising the spin degree of freedom in devices. These devices often use ferromagnetic materials, which feature long range ordering of parallel spins within the material, leading to a spin polarised density of states in which one spin direction is favoured. Superconducting spintronics aims to introduce superconducting materials into these devices and circuits. Superconducting materials can transport charge with no energy loss below critical values of temperature, current and applied magnetic field. However, the charge carriers in superconductors are pairs of electrons with antiparallel spin, known as Cooper pairs. Superconductors and ferromagnets are fundamentally antagonistic, favouring different alignments of electron spins. Spin transport in a superconductor also cannot be performed by Cooper pairs, which have a net spin of zero, below the superconducting gap and instead requires single particle excitations within the superconductor known as quasiparticles.

Beyond energy savings, introducing superconductors to spintronics has a number of advantages, such as the potential for infinite magnetoresistance in a superconducting spin valve [7], extended spin lifetimes of quasiparticles compared to electrons in the normal state [8] and the introduction of superconducting phase coherence [9, 10] as another property to be used in logic and memory devices [3]. Furthermore, it has been demonstrated

that with inhomogeneous magnetic fields, Cooper pairs can be converted into a triplet state [11–13], featuring electrons of parallel spin, allowing the possibility of lossless spin currents.

These exciting developments highlight the importance of understanding spin transport within superconductors. One method for investigating spin transport is to use a spin valve, which has magnetoresistance that depends on the spin decay within the central spacer layer, including superconducting layers, as demonstrated in [14]. This thesis shows that focused ion beam milled nanopillar superconducting spin valves in the current-perpendicular-to-plane regime may also be used to investigate quasiparticle spin decay within superconductors and furthermore that these devices demonstrate unexpected behaviour for superconductor thicknesses below a critical value of two coherence lengths.

The structure of this thesis is as follows. The next chapter covers relevant theoretical background, including magnetism, electron transport and superconductivity. The third chapter then covers the experimental methods used for deposition, fabrication, characterisation and measurement of the superconducting spin valves. Chapters four to seven present experimental results, preceded by a review of literature relevant to the results of that chapter. Chapter four covers the fabrication and characterisation of the nanopillar spin valves, and chapter five presents the spin decay results from the devices in their normal state. Chapter six focuses on the superconducting properties of the devices, before chapter seven details investigation into their systematic change of transport behaviour. Conclusions and future work that could build from these results are presented in the final chapter.

# Chapter 2

## Theoretical Background

### 2.1 Magnetism

#### 2.1.1 Atomic origins

Magnetism is a macroscopic phenomenon resulting from a number of different quantum mechanical effects. Fundamentally, magnetic effects in materials are all the result of properties and movement of electrons.

Magnetism results from the angular momentum of electrons. Particles such as electrons have two forms of angular momentum; so called ‘orbital angular momentum’, ‘ $\mathbf{l}$ ’, which is linked to their motion, and an intrinsic angular momentum known as ‘spin’, ‘ $\mathbf{s}$ ’. Both of these give rise to a magnetic moment, quantised in units of the Bohr magneton,  $\mu_B = \frac{e\hbar}{2m_e} = 9.3 \times 10^{-24} \text{ J T}^{-1}$  (for charge of an electron  $e = 1.6 \times 10^{-19} \text{ C}$ , mass of electron  $m_e = 9.1 \times 10^{-31} \text{ kg}$  and reduced Plank’s constant  $\hbar = h/2\pi$ ). The magnetic properties of a material result from the way electrons fill energy levels in the atoms of that material, and the resulting interaction of the spin and orbital moments; for example, filled electron shells result in both the spin and orbital moments cancelling, such that magnetic materials result from atoms with incompletely filled orbitals [15].

Different magnetic materials can have different electronic origins; an example of this is the magnetic rare-earth elements and the magnetic transition metal elements, which, because of their different electronic structures, have slightly different interactions between electrons fundamental to their magnetism. In this study, transition metal magnets are exclusively used, and therefore this background section will focus on effects and models relevant to these materials. In the transition metal magnets, the orbital angular momentum of electrons does not contribute to the overall magnetic moment of the complete atom. This is known as ‘quenching’ of the orbital moment and occurs as a result of the shape of the electron orbitals. Due to the electrostatic potential from the ions in the surrounding crystal lattice (the ‘crystal field’), the electron orbitals take particular shapes to minimise their energy, which removes the degeneracy between different orbitals, pre-

venting a change in orbital momentum of electrons such that the time averaged orbital angular momentum is zero: i.e. no magnetic moment results [16].

### 2.1.1.1 Spin-orbit coupling

Consider the reference frame of a single electron in an orbital: it is stationary, with a positively charged nucleus orbiting it. This orbiting electric charge will form an associated magnetic moment, which can then interact with the spin magnetic moment of the electron. This is the origin of spin-orbit coupling in a material, which links the spin and orbital properties of an electron, with resulting effects including magnetocrystalline anisotropy and anisotropic magnetoresistance. It also affects the way electrons tend to fill energy levels within an atom, and therefore affects whether certain atoms are magnetic or not. As the charge on the nucleus is fundamental to the origin of this effect, the strength of spin-orbit coupling is dependent on the atomic number,  $Z$ , of an atom, tending to be more significant for elements with higher  $Z$ .

## 2.1.2 Magnetic Materials

A material whose atoms have magnetic moments will not necessarily be magnetic. There is a range of magnetic responses of materials to an applied field, resulting from the interactions between atoms in the structure of the material. When considering an entire magnetic material rather than individual atoms, the magnetic moment per unit volume or magnetisation,  $M$ , is a convenient parameter. Different material responses can be compared using a parameter called the magnetic susceptibility,  $\chi$ , which is the constant of proportionality between the applied field  $H$  and the resultant magnetisation  $M = \chi H$ .

### 2.1.2.1 Diamagnetism and Paramagnetism

All materials demonstrate a diamagnetic response to an applied magnetic field. If a material has atoms without a magnetic moment, this will be the only response, but in other materials it is typically overwhelmed by other effects. Diamagnetism results from the response of electron orbits to an applied field; the orbital tends to precess around the applied field, which results in a magnetic moment. Lenz's law dictates that this moment is in opposition to the field that caused it, and so diamagnetism is a weak negative effect, with  $\chi$  typically around  $-10^{-5}$ .

Paramagnetism is a weak positive effect observable in materials whose atoms have magnetic moments with a weak interaction between them, such that they do not tend to align except in an applied magnetic field, which results in a small positive susceptibility. This susceptibility can be modelled by the so called Curie law, which considers a number of localised electron spins in an applied flux density  $B$ . The resulting moment resolved in a

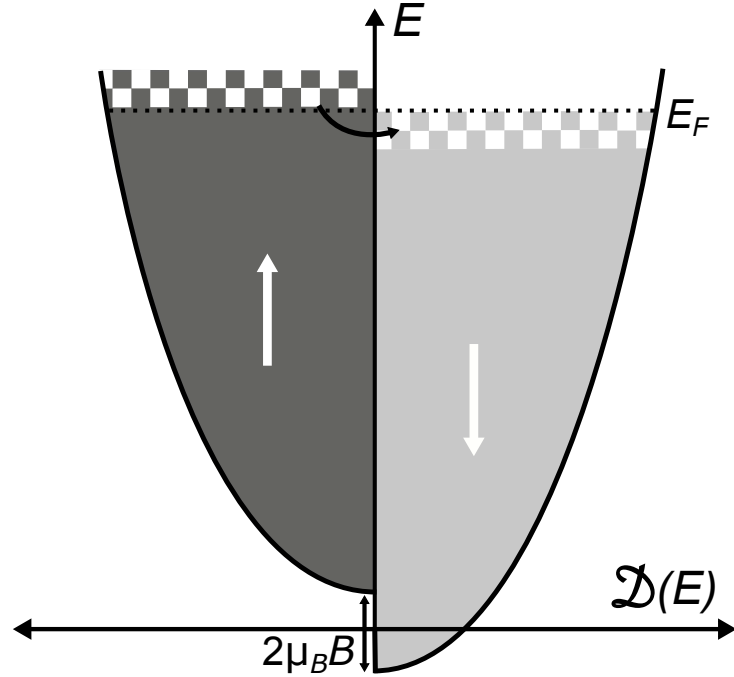


**Figure 2.1:** Simplified picture of the band model for Pauli paramagnetism, using a free electron theory density of states. The applied flux density  $B$  causes a shift in the relative energies of the spin subbands. The change in electron density (designated by the cross-hatched areas) is associated with a paramagnetic susceptibility. A similar picture is used in the Stoner model for ferromagnetism, where the band shift is caused by the internal exchange energy rather than an externally applied field.

particular direction is based on the relative Boltzmann populations of each spin direction given the energy shift of  $\pm\mu_B B$  caused by the applied field, such that

$$M = n\mu_B \tanh(x) \quad (2.1)$$

where  $n$  is the number of electrons per unit volume,  $x = \mu_B B/k_B T$ ,  $k_B$  is the Boltzmann constant and  $T$  is temperature. At most temperatures, we can say  $\mu_B B \ll k_B T$  such that  $\tanh x \approx x$ . In this case the Curie susceptibility

$$\chi = \frac{\mu_0 M}{B} = \frac{n\mu_0\mu_B^2}{k_B T} = \frac{C}{T} \quad (2.2)$$

where  $C$  is the Curie constant. For similar collections of magnetic moments, such as atoms within a material,  $n\mu_B^2$  may be replaced by  $nm^2$  where  $m$  is the strength of the individual moments and  $n$  is now the number of these moments per unit volume.

An additional form of paramagnetism may be found in transition metals, which tend to form bands of delocalised electrons across an entire structure, rather than remaining localised in atomic orbitals [15]. In this case, the bands may be considered in terms of two subbands corresponding to the two spin directions (Fig. 2.1). An applied flux density  $B$  will shift these bands by  $\pm\mu_B B$  respectively, which is small compared to the Fermi level.

This shift leads to a change in population of electrons in each band as they equilibrate, which results in a magnetisation

$$M = \Delta n \mu_B = 2\mathfrak{D}(E_F) \mu_B^2 B \quad (2.3)$$

so the Pauli paramagnetic susceptibility

$$\chi = \frac{\mu_0 M}{B} = 2\mu_0 \mu_B^2 \mathfrak{D}(E_F) = \frac{3n\mu_0 \mu_B^2}{2k_B T} \quad (2.4)$$

for  $\mathfrak{D}(E_F)$ , the density of states at the Fermi energy  $E_F$ , and where the final expression is based on the free electron model (see Section 2.2). The susceptibility of paramagnets is positive and tends to be around  $10^{-5}$ , although it can be as large as  $10^{-2}$ .

### 2.1.2.2 Ferromagnetism

A material demonstrating ferromagnetism is capable of developing a spontaneous magnetisation, i.e. a magnetisation that can be maintained in the absence of an external field. This magnetisation arises as the interactions between atomic moments within the material are strong enough to encourage alignment of these moments, leading to an overall magnetisation in a particular direction.

The origin of the internal alignment of the atomic moments within a ferromagnet was uncertain for some time. An early theory was that of Weiss' intermolecular field, in which an internal field, proportional to the magnetisation of the entire sample encourages the alignment. Weiss' theory also predicted a temperature,  $T_C$ , above which the intermolecular field was overcome and the moments did not align, behaving independently, as in a paramagnet. This temperature can be included in an adaptation of the Curie law for paramagnets, the Curie-Weiss law

$$\chi = \frac{C}{T - T_C} \quad (2.5)$$

where the value  $T_C$  is now known as the Curie temperature.

However, the Weiss model did not describe ferromagnetism completely accurately; for instance, it predicted that temperature dependent parameters such as the specific heat dropped immediately at  $T_C$ , whereas in fact the change is slightly gradual, suggesting clustering of spins that the model could not account for. Instead of an intermolecular field resulting from the entire lattice of spins, Heisenberg suggested the origin of alignment was based upon interaction of neighbouring moments. The energy of a pair of atoms due to their spin alignments may be given as:

$$E_{ex} = -2J \mathbf{S}_i \cdot \mathbf{S}_j \quad (2.6)$$

where  $\mathbf{S}_{i,j}$  are the spins of the two atoms, and  $J$  is the exchange energy. This exchange energy is a result of the overlapping wavefunctions of the electron orbitals surrounding the atoms under consideration. In a ferromagnet, it is positive, and as a result it is favourable for adjacent atoms to align spins parallel with each other. This exchange interaction is a very short range effect and is only truly significant for nearest neighbour interactions. However, this spreads across the material and provides long range order. This model for magnetism is known as the Weiss-Heisenberg model, and may be used to accurately predict a Curie temperature for a material, using the semiclassical equation:

$$T_C = \frac{2S(S+1)J_0}{3k_B} \quad (2.7)$$

where  $S$  is the magnitude of atomic spin,  $k_B$  is the Boltzmann constant and in this nearest neighbour model,  $J_0 = Jz$  where  $J$  is the exchange constant from equation 2.6 and  $z$  is the lattice coordination number. Being based only upon nearest-neighbour interactions explains the clustering of spins above  $T_C$ , as above this temperature the atoms have too much thermal energy for this interaction to persist across the entire lattice, but as a reasonably strong effect it can still be responsible for some local alignments.

In a transition metal, such as those used as part of this investigation, the valence electrons of the elements involve occupying the  $3d$  orbital. These orbitals tend to combine across the lattice to create an overall crystalline band structure. For a magnetic material, these may be used as part of Stoner's model to illustrate magnetism in an alternate way that can better describe bulk behaviours, such as fractional values of Bohr magnetons per atom. An exchange field within the material, which can be compared with Weiss' intermolecular field, causes a shift in the relative energies of energy bands for electrons of each spin direction. As a result, a redistribution of electrons in terms of spin occurs to minimise energy, resulting in an overall spin polarisation of a ferromagnetic material (Figure 2.2) [17]. The exchange field here is far stronger than an externally applied field, leading to a much greater effect than Pauli paramagnetism.

Stoner's model leads to Stoner's criterion for ferromagnetism, based upon electron band populations. Considering initially an unpolarised material with equal numbers  $N_{\uparrow,\downarrow}$  in each spin band, the energy cost for adjusting the spin population,  $\Delta E_1$ :

$$\Delta E_1 = \frac{(N_{\uparrow} - N_{\downarrow})^2}{2\mathfrak{D}(E_F)} \quad (2.8)$$

where  $\mathfrak{D}(E_F)$  is the density of states at the Fermi energy  $E_F$ . This energy is balanced by the energy gain from the electrons being involved in the exchange interaction,

$$\Delta E_2 = -\frac{I_S}{2\mathfrak{D}(E_F)}(N_{\uparrow} - N_{\downarrow})^2 \quad (2.9)$$

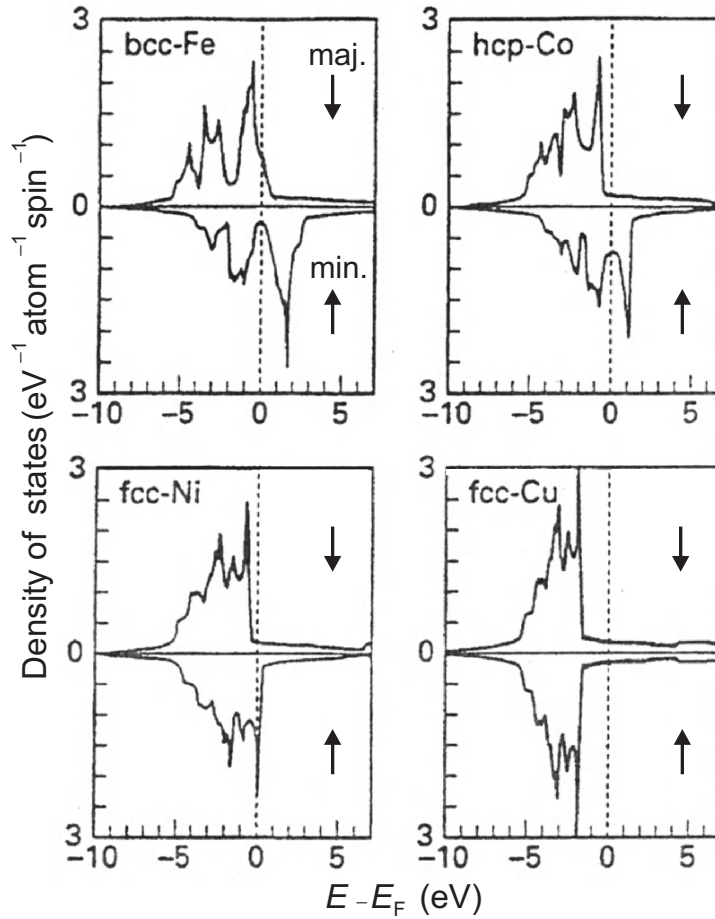


**Figure 2.2:** Density of states diagrams for some transition metals. The uneven density of states at the Fermi level for the ferromagnets Fe, Co and Ni can be seen, compared to the even density of states in Cu. Note how in bcc-Fe, there is a greater density of states for the major spin direction at the Fermi level, whereas in Co or Ni the minority spin direction has a greater density of states at the Fermi level. This influences the electron transport and scattering of different spin directions passing through these ferromagnets. From [17].

where  $I_S$  is an exchange energy known as the Stoner exchange parameter. The ‘Stoner criterion’ is then

$$\Delta E_1 + \Delta E_2 < 0 \quad (2.10)$$

$$I_S \mathfrak{D}(E_F) > 1 \quad (2.11)$$

which indicates whether a band structure ferromagnet will be stable.

The ferromagnet used in this investigation is permalloy, an alloy of Ni and Fe in the ratio 80:20. Permalloy is a soft ferromagnet, which tends to have an easy axis along  $\langle 111 \rangle$  directions, and a Curie temperature around 590°C. For this permalloy composition, the values of magnetocrystalline anisotropy and magnetostriction constants are extremely small, and these effects therefore are expected to have minimal impact in permalloy films [16]. The different moments of Ni and Fe atoms mean that permalloy is quite susceptible to induced anisotropy.

### 2.1.2.3 Antiferromagnetism

Ferromagnetism is a result of a positive exchange energy  $J$  that encourages adjacent spins to align parallel. If  $J$  is instead negative, then spins are encouraged to align in an antiparallel state. In a material where these antiparallel spins have the same magnetic moment, this leads to antiferromagnetism. An antiferromagnet (AF) has a magnetisation of zero and if a field is applied parallel to the spin axis magnetisation remains at zero up to some (large) value of the magnetic field. Antiferromagnetic behaviours are also temperature dependent, similar to ferromagnetism: the temperature below which they are demonstrated is known as the Néel temperature.

Antiferromagnets are characterised by antiparallel spins, but the exact spin structure varies between different materials and interfaces within those materials. In this study, face centred cubic  $\gamma$ -FeMn is used as an antiferromagnet, which has been shown to have a spin state in which the spin of each atom in the structure aligns along a  $\langle 111 \rangle$  direction [18, 19] as shown in Fig. 2.3.

### 2.1.3 Anisotropy, domains and hysteresis

A ferromagnetic material does not necessarily have a measurable external field. The field emitted depends on its domain structure, where domains are regions of different magnetisation direction, separated by so called ‘domain walls’. Domains are a direct result of a magnetic material trying to minimise its internal energy per unit volume,  $E_{\text{tot}}$ :

$$E_{\text{tot}} = E_{\text{ex}} + E_Z + E_a + E_d \quad (2.12)$$

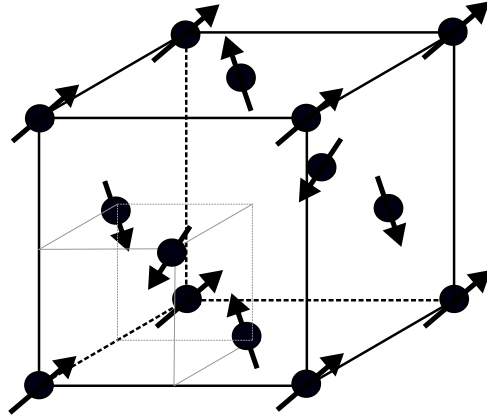


**Figure 2.3:** A face centred cubic unit cell of  $\gamma$ -FeMn, with arrows indicating the ‘3Q’ spin structure, in which spin moment of each atom aligning along a  $\langle 111 \rangle$  direction. After [20].

where  $E_{ex}$  is the energy resulting from the exchange interaction of adjacent spins, and  $E_Z$  is the Zeeman energy, which encourages spins to align with an applied field. The remaining competing energies are forms of magnetic anisotropy, which causes energy differences depending on the direction of magnetisation, hence leading to different magnetic properties in different directions. The first,  $E_a$ , is the magnetocrystalline anisotropy, which favours the spin directions lying along particular crystallographic directions. This is a result of the crystal field (the potential generated by the lattice surrounding an atom) and spin-orbit interaction, which respectively cause particular orbitals and therefore certain spin directions to be lower energy. This competes with ‘induced anisotropy’, which is a favoured magnetisation direction caused by depositing or annealing a magnet in an applied field. The moments within the material arrange to minimise the Zeeman energy during the process, which can be fixed as the sample cools and the atoms are no longer free to move. In permalloy for example, the Fe atoms have a larger moment than the Ni atoms, and so the Fe atoms tend to order such that their spins are arranged head-to-tail, contrasting with the standard random arrangement of Ni and Fe atoms within the crystal structure [16]. The second energy,  $E_d$ , is the demagnetisation energy, which results from the self-field of the magnet (the field generated by the magnetisation itself), known as the ‘demagnetisation field’ within the magnet and the ‘stray field’ outside it. It is minimised by reducing stray fields outside the magnet, which means avoiding magnetisation directions with components normal to the surface of the magnet. This energy is therefore heavily shape dependent and leads to a form of anisotropy known as shape anisotropy, in which the magnetisation favours lying along the long axis of a shape, such as a wire, with the aspect ratio of the shape affecting the strength of the effect. This is a particularly important anisotropy in thin films, as it strongly encourages the magnetisation to lie in-plane rather than perpendicular to the plane, which would lead to a large energy cost. The ideal minimisation of  $E_d$  features the magnetisation lying along the major axis of an ellipsoid; for all other shapes of a single magnetisation, stray fields will be produced. To

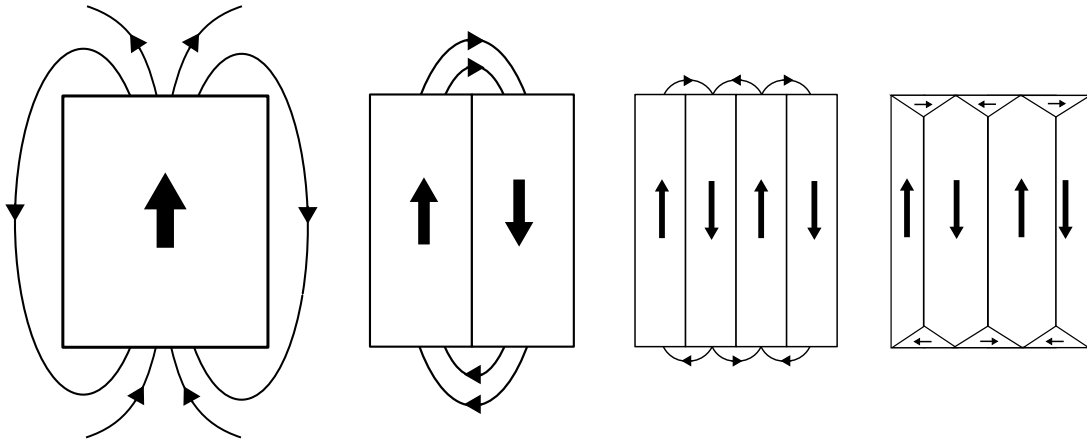


**Figure 2.4:** A ferromagnetic material may break up into domains which reduces the net stray field flux density and therefore the stray field energy. Stray fields are reduced by breaking up into multiple domains, and for the magnetisation aligning with the long axis of the sample. The number and size of domains is a result of balance between stray field, domain wall, and strain energies. Closure domains can form to prevent any stray field escaping the sample.

counter this, ferromagnetic materials tend to break up into domains.

Domains of opposing magnetisation allow a ferromagnet to further minimise stray field flux emission at the edges of the material, as depicted in Fig. 2.4. This flux is further reduced by the formation of the ‘closure domains’ near the edges. Domains are separated by domain walls, which are regions containing spins that do not align with those in adjacent domains, but feature a gradual rotation between one and the other. The width of a domain wall is determined by the balance between the magnetocrystalline anisotropy energy, which is high when moments do not align along the favoured direction, and the exchange energy, which favours adjacent spins aligning. There are two common types of domain wall, ‘Bloch walls’, in which the spins rotate out-of-plane, and ‘Néel walls’ featuring spins rotating in plane (which avoids costly stray fields being emitted out-of-plane in thin ferromagnetic films). ‘Cross-tie’ walls feature a mix of both characters.

### 2.1.3.1 Hysteresis loops

The distinct anisotropy with a ferromagnet results in hysteretic behaviour of the magnetisation in an applied field. Depending on the relative alignment of field and material (including shape and magnetocrystalline ‘easy axes’), the switching of the magnetisation will vary. An annotated magnetisation-field hysteresis loop, or  $M(H)$  loop, describing the switching is shown in Fig. 2.5.

In all but the very smallest ferromagnets, which do not form domains, switching will occur via domain walls sweeping through the material, causing favourably oriented domains (with respect to the applied field) to grow at the expense of unfavourably oriented ones. Eventually, the magnet becomes single domain, and the magnetisation can only align further with the field by rotating away from the easy axis of the material. Once

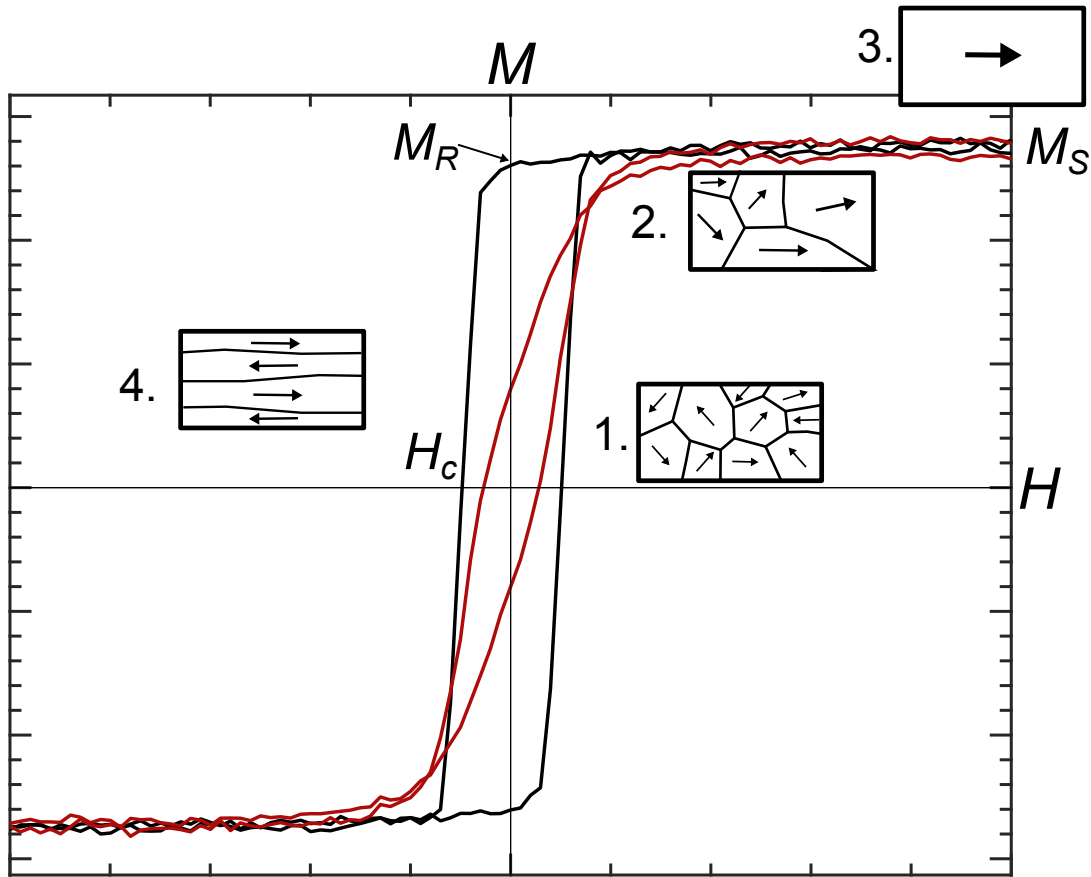


**Figure 2.5:** Experimentally measured  $M(H)$  loops highlighting the values of magnetisation saturation  $M_S$ , remanent magnetisation  $M_R$ , and coercive field  $H_c$ . The black loop is for field parallel to the easy axis, red loop is for field applied at an angle to the easy axis. The ferromagnet has large anisotropy, as  $M_R$  is similar to  $M_S$ . Rectangles are simplified indications of the domain structure in part of a ferromagnet in various states. 1: In a virgin state, domains are mostly randomised, with magnetisation of each domain conforming to one of the crystallographic easy axes. 2: As a field is applied to the sample, domains with a favourable magnetisation orientation will grow at the expense of others, and will rotate towards the applied field (represented by the changing domains from left to right). 3: At saturation, the ferromagnet is single domain and magnetisation aligns with applied field. 4: Applying field in the reverse direction leads to nucleation and growth of oppositely aligned domains, passing through zero net magnetisation at  $H_c$ .

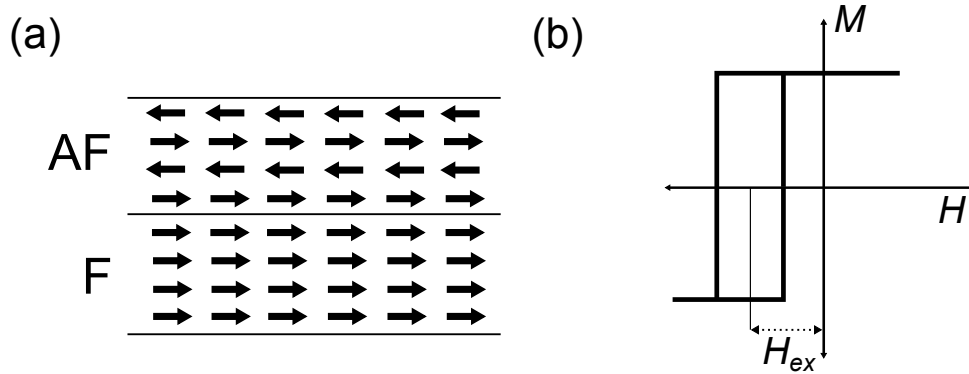


**Figure 2.6:** (a) Idealised picture of exchange bias. The antiferromagnet (top) has a defined spin structure that hardly reacts to a field applied along its spin axis. An adjacent ferromagnet is ‘pinned’ to point in a certain direction by the exchange interaction between the two materials at the interface. (b) This results in a shift of the  $M(H)$  loop along the field axis, as if it is ‘biased’ by an effective field,  $H_{ex}$ . This effect is known as exchange bias.

this has occurred, the magnet has reached its saturation magnetisation,  $M_S$ . As the field is reduced, the magnetisation will return to its easy axis, and the ferromagnet may tend to break into domains, depending on the relative balance of energies as discussed above, until the field is completely removed, at which point the magnetisation has reduced to its remanent magnetisation value,  $M_R$ . As the field grows in the opposite direction, domains in that direction will start to nucleate and grow, reducing net magnetisation to zero at a value known as the coercive field,  $H_c$ . As the applied field increases in this direction, domains move until the magnet has again reached  $M_S$ , now in the opposite direction. Subsequent application of field in the original direction will affect the magnetisation in the same way as before, forming a rotationally symmetric loop.

The exact shape of the loop is a result of the balance of different energies within the ferromagnet. Fields aligned with the easy axis (black curve, Fig. 2.5) will tend to create a more square loop, contrasted with loops when a field is applied at an angle to the easy axis, which will tend to be more ‘S-shaped’ (red curve, Fig. 2.5) as the magnetisation now rotates away from its favoured direction. In a homogeneous sample, domain wall motion requires no energy, and so the critical step in magnetisation reversal is the nucleation of reverse domains. However, defects and impurities in crystal structure, including grain boundaries, may ‘pin’ domain walls, resulting in higher fields required to move them, which increases  $H_c$ .

Another effect that may affect the shape of an  $M(H)$  loop is that of exchange bias. Exchange bias occurs when an antiferromagnet is in contact with a ferromagnet. The exchange coupling between the two materials at their interface ‘pins’ the magnetisation direction of the ferromagnet to lie in a certain direction relative to the spin directions within the antiferromagnet, causing a unidirectional anisotropy to develop within the ferromagnet - the magnetisation is favoured to align along one direction (as opposed to either direction along one axis, known as uniaxial anisotropy). An overly simplified picture

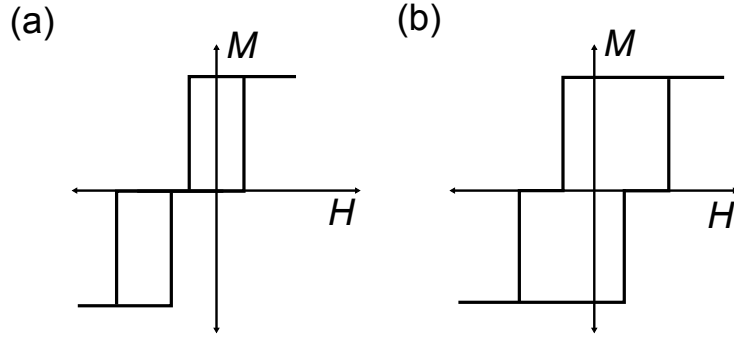


**Figure 2.7:**  $M(H)$  loops for (a) a spin valve, F/N/F/AF and (b) a pseudo-spin valve, F/N/F. For simplicity, the magnetisation of both ferromagnetic layers is assumed to be the same. In each case, the ideal device has a stable ‘antiparallel’ state where the magnetisations of the layers lie antiparallel (here, where  $M = 0$ ).

of exchange bias is shown in Fig. 2.6(a). Exchange bias appears in an  $M(H)$  loop as a ‘shift’ of loop in one direction along the  $H$ -axis, where the magnitude of the shift is known as the exchange field,  $H_{\text{ex}}$  [Fig. 2.6(b)]. One of the main uses of exchange bias is to create spin valves. Spin valves are useful magnetoelectronic devices featuring two ferromagnetic layers separated by a non-magnetic spacer layer. The resistance of the device is changed by the relative orientation of the two ferromagnetic layers. By pinning one ferromagnet with an antiferromagnet, the  $M(H)$  loops of the two layers may be separated, allowing independent switching of the ‘free’ (unpinned) layer and therefore enabling the device to work. An idealised  $M(H)$  loop of a spin valve is shown in Fig. 2.7(a). Instead of using an antiferromagnet and exchange bias, another way of achieving independent switching of the two ferromagnetic layers is to use layers with very different  $H_c$  values, so that small fields only affect the layer with smaller  $H_c$ . This is known as a ‘pseudo-spin valve’ [Fig. 2.7(b)].

## 2.2 Electron Transport

Considering electron transport through materials begins with considering the free electron model, a simplified approximation that nevertheless introduces some key concepts and parameters. In this model, electrons are considered not to interact with each other or the lattice of ions that makes up the crystal structure of a material, but do follow the Pauli exclusion principle. The valence electrons of a material become the conduction electrons.

Solving the time independent Schrödinger equation

$$\frac{-\hbar^2}{2m} \nabla^2 \psi(\mathbf{r}) = E \psi(\mathbf{r}) \quad (2.13)$$

gives the wavefunction  $\psi(\mathbf{r})$  for an electron at position  $\mathbf{r}$  with energy  $E$ , as a plane wave:

$$\psi(\mathbf{r}) = C e^{-i\mathbf{k}\cdot\mathbf{r}} \quad (2.14)$$

for some constant  $C$ . Consider the electron in a cube of side length  $L$ , using periodic boundary conditions so that surfaces are ignored. The wavevector,  $\mathbf{k}$ , is quantised, such that

$$k_{x,y,z} = \frac{2\pi N_{x,y,z}}{L}$$

where  $N_{x,y,z}$  is an integer, leading to energy,  $E$

$$E(k) = \frac{\hbar^2 k^2}{2m}$$

also being quantised. This demonstrates that in a material, there are a limited number of states for electrons to occupy, rather than a continuous distribution of energies. The Pauli exclusion principle requires that only one electron can occupy each quantum state, so there are two electrons in each  $E(k)$  state, one for each spin direction.

### 2.2.1 Density of States

The density of states of a material,  $\mathfrak{D}(E)$ , is the number of electron states available at a certain energy  $E$ . It is a key concept in electron transport, influencing the probability that an electron can change energy, as it defines the number of states available. The number of available electron states,  $N$ , is defined by the states in  $k$ -space enclosed by a sphere of radius  $\mathbf{k}$ , called the ‘Fermi surface’. This leads to the density of states for a 3D material:

$$\mathfrak{D}(E) = \frac{dN}{dE} = \frac{V}{2\pi^2} \left( \frac{2m}{\hbar^2} \right)^{3/2} E^{1/2} \quad (2.15)$$

where  $V$  is the volume per  $k$ -state in the material. In the ground state, at 0 K, electrons fill the density of states. The highest occupied energy level is known as the Fermi energy,  $E_F$ . As temperature,  $T$ , is increased, the occupied density of states,  $Z(E)$ , becomes relevant:

$$Z(E) = \mathfrak{D}(E)f(E) \quad (2.16)$$

where  $f(E)$  is the Fermi-Dirac distribution representing occupation probability. For a temperature of zero, this is a step function, with an occupation probability of 1 below  $E_F$ , and occupation probability of 0 above it. For temperatures greater than zero, this step becomes ‘smeared’ somewhat, rather than sharp, as illustrated in Fig. 2.8.

Electrons around the Fermi energy (within  $k_B T$  of the Fermi surface) are responsible for the observable electron dependent properties of a material, such as conduction. The spherical Fermi surface and square-root density of states are simplifications resulting from the assumptions within the free electron model, including a completely isotropic material with a lattice that does not interact with the electrons. With such simplifications, the model fails to predict semiconductors or insulators; to account for these materials, the concept of electron bands are needed.

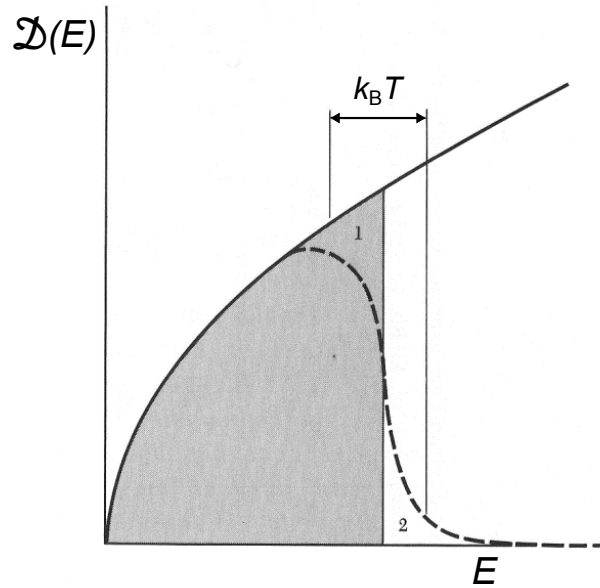


**Figure 2.8:** The occupied density of states. The basic quadratic shape is from equation 2.15, and the dotted line is from the Fermi-Dirac function, showing the ‘smearing’ of the surface at raised temperatures. After [21].

### 2.2.2 Electron Bands

Electron bands result from considering the interaction of electrons with a periodic lattice of ions that make up the crystal structure of a material. In this case, electron wavefunctions are plane waves modulated by the lattice potential, known as Bloch waves. These Bloch waves scatter from the regular lattice, leading to Bragg reflection occurring for certain wavevectors. In this case, standing waves are set up from the two opposing Bloch waves. These standing waves either have maxima (corresponding to a high probability of finding an electron, i.e. a higher electron density) near positive ions (low energy), or in the space between them (high energy). This energy difference leads to the formation of electron bands of different energies, with an energy gap (band gap) between them. The size of this gap is dependent on the magnitude of the crystal potential [21].

Electron bands then lead to the distinguishing of materials as metals and insulators: if the Fermi energy of a material is in the middle of a band, then it is a metal. If instead the highest electron state is at the top of a band, with a large energy gap to the next available state, then the material is an insulator, as an applied electric field cannot adjust the electron states such that there is an overall momentum of electrons, because all states are occupied (over a reasonable energy range).

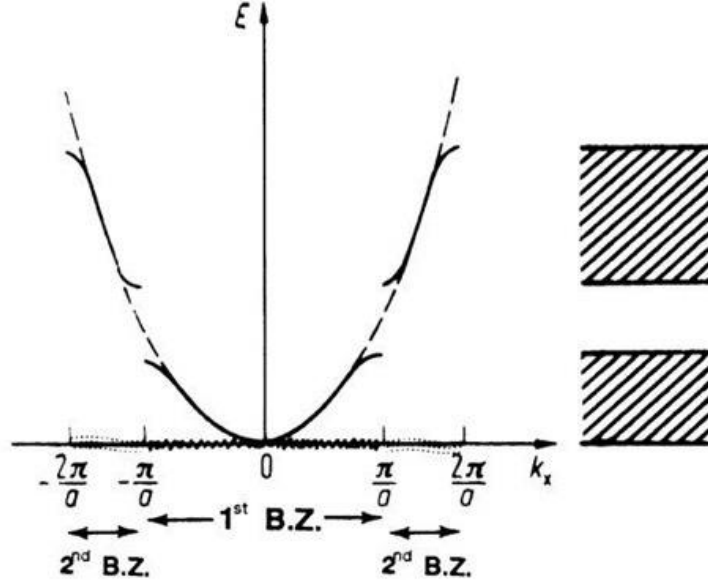


**Figure 2.9:** Bragg reflection of Bloch waves causes development of different energy levels for electron occupation. The dashed line represents the quadratic dispersion relation from the free electron model. These energy levels develop into electron bands across the crystal, given its symmetry, as shown on the right. After [22].

### 2.2.3 Conductivity

In a classical interpretation of conductivity, an electric field,  $\mathbf{E}_{field}$ , acting on a free electron has an accelerating effect:

$$\mathbf{F} = m_e \frac{d\mathbf{v}}{dt} = \hbar \frac{d\mathbf{k}}{dt} = -e\mathbf{E}_{field} \quad (2.17)$$

where  $F$  is the force acting on the electron and  $\mathbf{v}$  is the velocity of the electron. Extending this to the momentum of a group of electrons, which start with average velocity zero, the overall momentum after time  $t$  is

$$m_e \mathbf{v}(t) - m_e \mathbf{v}(0) = -e\mathbf{E}_{field}t \quad (2.18)$$

$$\mathbf{v} = \frac{-e\mathbf{E}_{field}t}{m_e}. \quad (2.19)$$

Assuming a system of  $n$  electrons per unit volume reaches a steady state equilibrium with relaxation time  $\tau$  (specifically the time between collisions of electrons and background ions), the current density will be

$$\mathbf{j} = nq\mathbf{v} = \frac{ne^2\tau\mathbf{E}_{field}}{m_e} \quad (2.20)$$

where  $q$  is electric charge. This equation for current density compares with Ohm's Law,  $\mathbf{j} = \sigma \mathbf{E}_{field}$ , giving an equation for conductivity,  $\sigma$ , in terms of electron density:

$$\sigma = \frac{ne^2\tau}{m_e}. \quad (2.21)$$

where  $\tau$  is the time between collisions. Alternatively, the conductivity can be considered in terms of the occupied density of states, by considering the application of an electric field as a shift in the Fermi surface such that the centre (and therefore average) of the sphere is no longer at zero (Fig. 2.10). In this case,  $n = Z(E_F)\Delta E$ , and using the momentum of the electrons  $\hbar\mathbf{k}$  travelling at the Fermi velocity  $v_F$ ,

$$\mathbf{j} = nq\mathbf{v} = Z(E_F)\Delta Eev_F \quad (2.22)$$

$$\mathbf{j} = Z(E_F)\hbar v_F \frac{e\mathbf{E}_{field}\tau}{\hbar} ev_F \quad (2.23)$$

$$\mathbf{j} = \frac{1}{3}v_F^2e^2\tau Z(E_F)\mathbf{E}_{field} \quad (2.24)$$

so that

$$\sigma = \frac{1}{3}v_F^2e^2\tau Z(E_F). \quad (2.25)$$

In equation 2.24, the factor of 1/3 appears when considering the 3D problem, averaging across all possible directions of electron momenta to give the component in the direction of the Fermi surface shift. This equation for conductivity emphasises the importance of the density of states in electron transport; a different density of states leads to a different susceptibility to scattering and hence a different conductivity [23]. It also introduces the effect of impurities and defects on conductivity, by considering  $\tau$ , which is smaller for a more imperfect crystal. This may also be expressed in terms of the average distance travelled by an electron between collisions, known as the mean free path,  $\lambda = v_F\tau$ . Scattering of electrons from various sources is the cause of decrease of conductivity (or increase in resistivity). At low temperatures, where numbers of particles such as phonons are reduced, scattering from impurities and defects are the main source of resistivity in a material. As impurity scattering is typically elastic, it is the density of states at  $E_F$  that is key. In sputtered samples such as used in this investigation, the level of impurities can be relatively high.

For each energy state there can be two associated electron states, corresponding to each spin direction. Within an electron band, this is represented by two subbands corresponding to each direction. In a material for which the density of states at the Fermi level differs for each subband, then the number of electrons of each participating in conduction will differ, and the scattering for each will also differ, leading to different mobilities for each direction. This is the origin of spin polarised currents and spin accumulation [23].

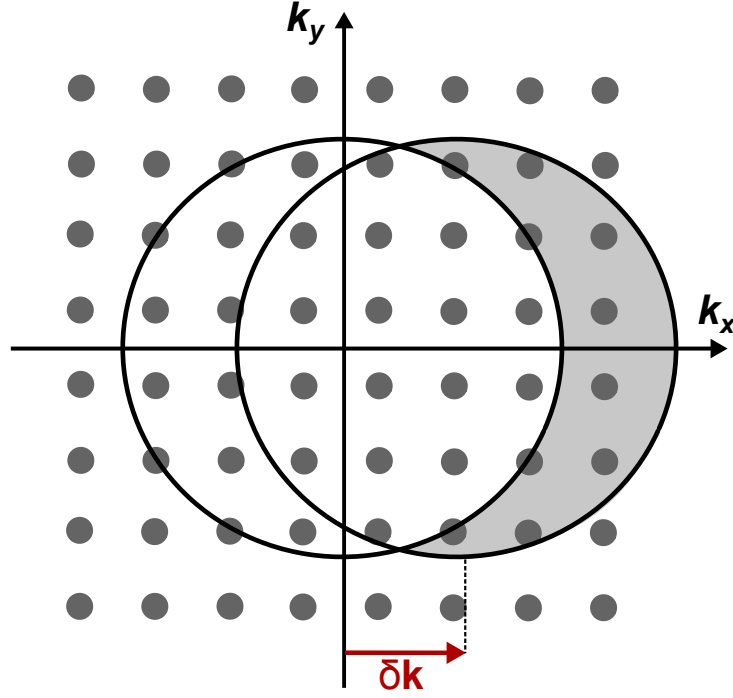


**Figure 2.10:** The Fermi surface in momentum space (in 2D). The points represent the different quantised values of  $\mathbf{k}$ , with occupied states enclosed by the Fermi surface. Upon application of an electric field, the Fermi surface shifts by  $\delta\mathbf{k}$  due to the imparted momentum, leaving some occupied states uncompensated for (grey area). The electrons of the material near the Fermi level therefore have a net momentum, leading to electrical conduction.

In a material such as a ferromagnet, which does have a different density of states for each spin subband at  $E_F$ , current is carried by electrons of one spin more than the other, considered a polarisation,  $P$ :

$$P = \frac{N^\uparrow - N^\downarrow}{N^\uparrow + N^\downarrow} \quad (2.26)$$

where  $N^{\uparrow\downarrow}$  is the number of electrons of each spin direction. If a current then passes from the ferromagnet into an adjacent material, the injected current will also follow this polarisation, as demonstrated by early tunnelling experiments which measured the polarisation of different ferromagnets [24] by showing the tunnelling current was dependent on the number of states available in each spin subband of superconducting Al, which had its states split by an applied magnetic field. Through injection of a spin polarised current, a material may be disrupted away from its equilibrium spin distribution (e.g. a normal material suddenly has more electrons of one spin direction). This is known as spin accumulation, which will gradually decay within a material. This spin accumulation is associated with a (very small) magnetic moment within the normal metal [25], and is represented by the difference in chemical potential,  $\mu$ , between the two different spin directions of electrons; this may be represented as

$$\frac{\delta^2(\mu_\uparrow - \mu_\downarrow)}{\delta x^2} = \frac{(\mu_\uparrow - \mu_\downarrow)}{(l_{sf})^2} \quad (2.27)$$

which has the 1-D solution

$$\Delta\mu = A \exp\left(-\frac{x}{l_{sf}}\right) + B \exp\left(\frac{x}{l_{sf}}\right). \quad (2.28)$$

Here,  $l_{sf}$  is the lengthscale over which the spin accumulation decays in a material, known as the spin diffusion (or spin flip) length, and is related to the mean free path by  $l_{sf} = \sqrt{D\tau_{sf}} = \sqrt{1/3\lambda v_F \tau_{sf}}$  where  $D$  is the diffusivity of electrons in the material and  $\tau_{sf}$  is the spin flip time, the average time between spin flip events for an electron. Considering the equation for conductivity, and with  $\sigma = 1/\rho$  (where  $\rho$  is resistivity of a material) this implies that  $l_{sf} \propto 1/\rho$ . An early demonstration of spin accumulation and the associated potential difference was in [26, 27], which presented what later became known as the ‘non-local’ method for measuring spin accumulation.

Spin flip scattering events occur when electrons collide with particles with a magnetic moment, such as a magnetic lattice or magnetic impurities. In an alloy material, the ‘impurity’ atoms of a known concentration may be present in greater numbers than other defects. As a result, scattering from these will dominate and the resultant  $l_{sf}$  can be considered a more intrinsic value, compared to ‘pure’ materials where the spin flipping is more dependent on random impurities and therefore tends to vary more [28]. Spin flip scattering may also occur from non-magnetic impurities via the spin-orbit interaction, which will tend to be more important in materials or for impurities with a greater atomic number.

## 2.2.4 Magnetoresistance

Magnetoresistance of a material or structure is the variation of resistance with an applied magnetic field. There are a number of types of magnetoresistance, of various sizes. The first, ordinary magnetoresistance (OMR) exists in all conducting materials, and occurs as the Lorentz force acting on a travelling electron deflects the electron from its forwards trajectory, and is always positive (increasing field increases resistance).

Anisotropic magnetoresistance is exclusive to magnetic materials, resulting from a resistance dependence on the angle between current and magnetisation of the magnet, which follows:

$$R_{\text{tot}} = R_{\text{min}} + \Delta R_{\text{AMR}} \cos^2(\theta) \quad (2.29)$$

where  $\Delta R_{\text{AMR}}$  differs in both magnitude and sign for different materials, and  $\theta$  is the angle between current and magnetisation. In devices, magnetic fields are often applied along the axis of magnetisation. In this case, no gradual rotation of magnetisation occurs, rotation only occurring near the coercive field, leading to distinctive peaks (troughs) at those values which change to troughs (peaks) when the current is applied orthogonally, as shown in Fig. 2.11.

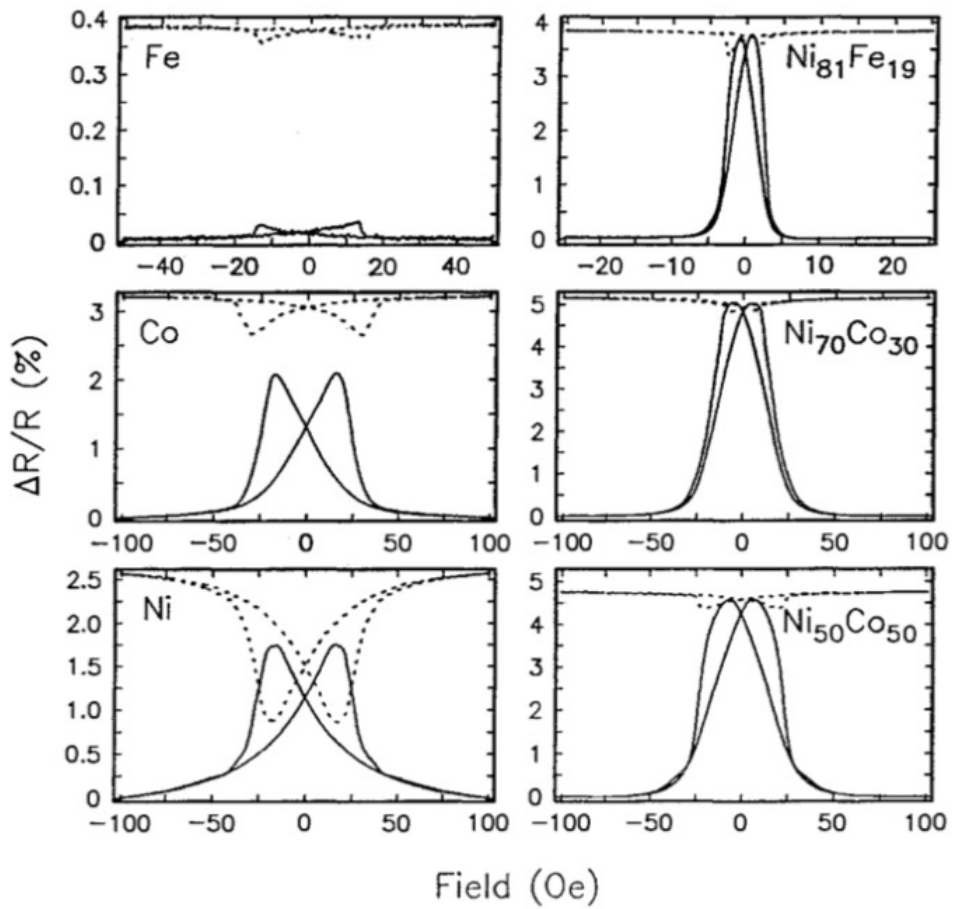


**Figure 2.11:**  $R(H)$  traces demonstrating AMR in different polycrystalline ferromagnetic thin films. Full and dotted lines correspond to current orthogonal and parallel to the applied field respectively. In each case, a rotation of  $90^\circ$  leads to a flip in the sign of the peak. From [29].

In structures featuring multiple layers of different magnetic materials, a form of magnetoresistance known as giant magnetoresistance (GMR) can be measured. The origin of GMR lies in the spin scattering asymmetry at interfaces between materials with different electron bands, which will occur between, for instance, a normal metal (N) and a ferromagnet (F). Although initially demonstrated in metallic multilayer structures with antiferromagnetic exchange coupling [30, 31], GMR may be simply pictured using a spin valve structure, in which two ferromagnetic materials sandwich a normal metal spacer (F/N/F). A current passing through one F layer will be spin polarised. Upon passing through N and reaching the other F, the potential step at the interface is determined by the relative density of states of that F layer. If the majority spin direction of the current matches with the majority spin direction of F, such that there are many states available, the potential step is small, so resistance is low. If the majority spin direction of the current matches the minority direction of F, there are not many states available, and the potential step is large, leading to high resistance; this means that if the magnetisations of F are parallel (P), the device has low resistance, and if they are antiparallel (AP) the device has high resistance. This spin valve picture demonstrates that the degree of spin scattering within the structure affects the magnitude of GMR; the more scattering that occurs to the spin polarised current, the less polarised it is upon reaching the second ferromagnetic layer, and so the less of a difference there is between the P- and AP-states. Giant magnetoresistance can in fact occur in two current regimes, current-in-plane (CIP) and current-perpendicular-to-plane (CPP), which work similarly, although the relevant lengthscales in each case differ, as CIP depends upon the mean free path, whereas CPP depends upon the spin flip length. GMR is a much larger effect than OMR or AMR (hence the name) and has been used in hard drive read heads for a number of years.

## 2.3 Superconductivity

Superconductivity is a state exhibited by certain materials below critical values of temperature, electric current, and magnetic field. In this superconducting state the material conducts electricity with zero resistance [it is a perfect conductor, as in Fig. 2.12(a)] and also expels flux from its interior [Meissner effect, Fig. 2.12(a)]. These are the two main experimental observations associated with superconductivity, which lead to this phenomenon having a multitude of potential applications.

The superconducting state is a result of interactions between pairs of electrons of opposite momentum and spin, leading to condensation of electronic states to a single energy level. These pairs of electrons ('Cooper pairs') act like bosons, as multiple pairs exist at the same energy level (Fermi energy) in a condensate. This condensate does not scatter with the atomic lattice, leading to perfect conductivity. These ideas stem from the microscopic Bardeen-Cooper-Schrieffer (BCS) theory [32] and are explored more in

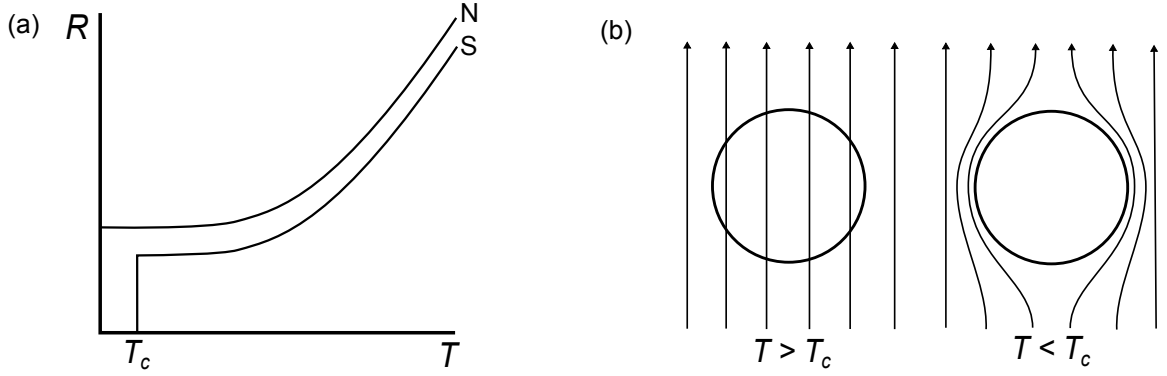


**Figure 2.12:** (a) Example resistance-temperature curves for normal metals, N, (top) and superconductors, S, (bottom). At a critical temperature  $T_c$  the resistance of the superconductor falls to zero. (b) The Meissner effect in superconductors. Above  $T_c$  a superconductor is a normal metal, and may be penetrated by an external field. Below  $T_c$ , flux is expelled by screening currents at the surface of the superconductor, even if the flux was penetrating the material as it was cooled into this state.

### Section 2.3.3.

The Meissner effect is the expulsion of magnetic flux from the interior of a superconductor -  $\mathbf{B} = 0$  T. This effect is distinct from the diamagnetic effect that would be expected from a perfect conductor, as this would only oppose changes in the flux penetrating the material,  $d\mathbf{B}/dt = 0$ ; in the Meissner effect, flux that penetrates the material in the ‘normal’ state (N) is expelled when the material is cooled into the superconducting state (S). Superconductors are therefore also perfect diamagnets, with magnetic susceptibility  $\chi = -1$ .

## 2.3.1 Phenomenological theories

An early phenomenological theory which successfully described the Meissner effect and perfect conduction was the London theory, which consisted of the two London equations:

$$\frac{\partial \mathbf{j}}{\partial t} = \frac{n_S e^2}{m_e} \mathbf{E}_{\text{field}} \quad (2.30)$$

$$\nabla \times \mathbf{j} = -\frac{n_S e^2}{m_e} \mathbf{B} \quad (2.31)$$

where  $\mathbf{j}$  is the superconducting current density,  $\mathbf{E}_{\text{field}}$  is an electric field,  $\mathbf{B}$  is the magnetic flux density, and  $m_e$  and  $e$  respectively represent the mass and charge of an electron.  $n_S$  is the density of superconducting charge carriers; the London theory is based upon a ‘two-fluid’ model, in which the total electron density  $n$  is considered split into ‘superconducting electrons’ with density  $n_S$  and ‘normal electrons’ with density  $n_N$  where  $n = n_S + n_N$ . From the Maxwell equation

$$\nabla \times \mathbf{B} = \mu_0 \mathbf{j} \quad (2.32)$$

and the second London equation, we obtain

$$\nabla^2 \mathbf{B} = \frac{\mathbf{B}}{\lambda_L^2} \quad (2.33)$$

where

$$\lambda_L = \sqrt{\frac{m}{\mu_0 n_S e^2}} \quad (2.34)$$

which is known as the London penetration depth. Equation 2.33 describes the Meissner effect, as there can be no solution for constant  $\mathbf{B}$  except  $\mathbf{B} = 0$  T. Instead, the solution is satisfied by  $B = B_0 \exp(-x/\lambda_L)$ ; an exponential decay of magnetic flux density from the surface into the interior of S.

The London theory is only an approximation and cannot explain every aspect of superconductivity; an example is the mismatch between the London penetration depth and experimentally measured values [21]. It was proposed that these discrepancies resulted from the fact that  $n_S$  could only change over a certain lengthscale rather than at a point - the proposed lengthscale is known as the (Pippard) coherence length,  $\xi_0$ , and an initial approximation using an argument based on the uncertainty principle [33] is

$$\xi_0 = a \frac{\hbar v_F}{k_B T_c} \quad (2.35)$$

where  $a$  is a numerical parameter found to be  $\approx 0.18$ ,  $v_F$  is the Fermi velocity,  $k_B$  is Boltzmann's constant and  $T_c$  is the critical temperature of the superconductor.

### 2.3.1.1 Ginzburg-Landau theory

A second phenomenological theory developed later was the Ginzburg-Landau (GL) theory. This considered the transition to the superconducting state as a second order phase transition, associated with the free energy  $\mathcal{F}$ :

$$\mathcal{F} = \mathcal{F}_0 + \alpha(T) |\psi|^2 + \frac{1}{2} \beta(T) |\psi|^4 + \frac{1}{2m^*} \left| \left( \frac{\hbar}{i} \nabla - q^* \mathbf{A} \right) \psi \right|^2 + \frac{(\mathbf{B} - \mathbf{B}_{\text{ex}})^2}{2\mu_0} \quad (2.36)$$

where  $\mathcal{F}_0$  is the free energy in the normal state,  $m^*$  is the effective mass of the superconducting charge carriers and  $q^*$  is their effective charge, which Gor'kov [34] showed were equal to  $2m$  and  $2e$  respectively, linking GL theory with Cooper pairs of BCS theory (Section 2.3.3).  $\mathbf{B} = \nabla \times \mathbf{A}$  is the magnetic vector potential and  $\mathbf{B}_{\text{ex}}$  is the external magnetic flux density. GL theory introduces the quantity  $\psi = \psi_0 \exp(i\theta)$ , which describes a wavefunction for the superconducting charge carriers such that  $|\psi|^2$  is an order parameter, found to be equal to the density of superconducting charge carriers,  $|\psi_0|^2 = n_S$  and  $\theta$  is the 'phase' of the wavefunction [Fig. 2.13(a)].  $\alpha$  and  $\beta$  are material-dependent phenomenological parameters, where  $\beta$  must be positive,  $\alpha > 0$  in the normal state, and

$\alpha < 0$  in the superconducting state. Minimising this free energy with respect to the order parameter and the vector potential obtains the two GL equations:

$$\alpha(T) + \beta(T) |\psi|^2 \psi + \frac{1}{2m} (-i\hbar\nabla + 2e\mathbf{A})^2 \psi = 0 \quad (2.37)$$

$$\mathbf{j} = \frac{2en_S}{m} (\hbar\nabla\theta + 2e\mathbf{A}) \quad (2.38)$$

which have solutions featuring the penetration depth  $\lambda$  and the coherence length,  $\xi_{\text{GL}}$ :

$$\lambda_{\text{GL}} = \sqrt{\frac{m}{4\mu_0 e^2 n_S}}, \quad (2.39)$$

$$\xi_{\text{GL}} = \sqrt{\frac{\hbar^2}{2m|\alpha|}}. \quad (2.40)$$

The penetration depth again describes the length over which magnetic fields decay when entering the surface of a material in the S state.  $\xi_{\text{GL}}$  describes the length over which the order parameter changes without significant energy costs [21], and is typically different from the coherence length  $\xi_0$ , although it does tend towards that value at low temperatures, according to  $\xi(T) = 0.74\xi_0[1 - T/T_c]^{-1/2}$ . Strictly, GL theory is only valid near the transition temperature  $T_c$ , but it handles situations that the London model cannot, such as fields strong enough to cause spatial variation of  $\psi$ .

$\lambda_{\text{GL}}$  and  $\xi_{\text{GL}}$  are the key lengthscales of a superconductor, and their relative magnitudes have a large impact on the behaviour of the material [Fig. 2.13(b)]. Their ratio  $\kappa = \lambda_{\text{GL}}/\xi_{\text{GL}}$  signifies the response of the superconductor to a magnetic field, and as both order parameter and penetration depth have associated energies, total surface energy is defined by which one dominates. For small  $\kappa$  the positive magnetic field energy has a larger effect, so surface energy is positive. As a result, the interface between superconducting and normal regions is minimised. In contrast, if  $\kappa$  is large, the ordering energy dominates, so the surface energy is negative, leading to a maximisation of surface area between normal and superconducting regions. These two different regimes describe Type I (such as Sn and Pb) and Type II (for example, Nb and V) superconductors.  $\kappa < \frac{1}{\sqrt{2}}$  is taken to be the criterion for a Type I superconductor, whereas  $\kappa > \frac{1}{\sqrt{2}}$  leads to Type II.

Flux in a superconductor is quantised. Consider a superconducting ring, threaded by flux  $\phi$ : by equation 2.38, far from the surface where there is no screening current ( $\mathbf{j} = 0$ ) then

$$\mathbf{A} = -\frac{\hbar\nabla\theta}{2e}. \quad (2.41)$$

Relating this to the flux through the ring by considering a loop enclosing the flux and all the currents

$$\phi = \int B \cdot d^2r = \oint A \cdot dS = -\frac{\hbar}{2e} \oint \nabla\theta \cdot dS = -\frac{\hbar}{2e} \Delta\theta. \quad (2.42)$$

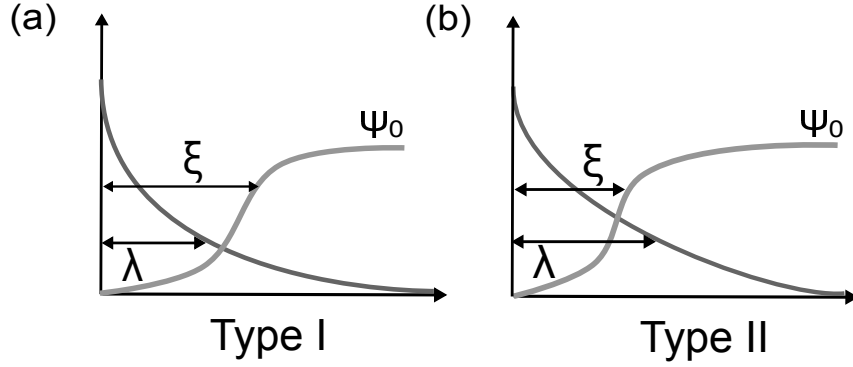


**Figure 2.13:** The relative magnitudes of the penetration depth and coherence length of a superconductor determine how the material reacts to an applied magnetic field, by changing the surface energy associated with an S/N interface. (a) Type I: The magnetic penetration depth is shorter than the coherence length, so the positive magnetic energy grows more quickly, leading to a positive surface energy. (b) Type II: The coherence length is shorter, so the negative ordering energy dominates, leading to a negative surface energy.

Now  $\Delta\theta$  must be an integer multiple of  $2\pi$ , as the wavefunction  $\psi$  of the superconductor must be constant around the ring, so the flux within the loop must be quantised in terms of  $\Phi_0$ :

$$\Phi_0 = -\frac{h}{2e} \approx 2.068 \times 10^{-15} \text{Wb}. \quad (2.43)$$

### 2.3.2 Magnetic fields

The superconducting state exists below critical values of temperature, magnetic field, and electric current ( $T_c$ ,  $H_c$ ,  $I_c$ , Fig. 2.14). Exceeding these values provides the electrons with energy that overcomes the attractive potential between electrons in their pairs, returning the material to the normal state. These values are linked; for instance, the maximum critical current is that which is associated with a magnetic field that will exceed  $H_c$  (although the actual critical current may well be less than this) [33]. Similarly, the critical field is dependent on temperature:

$$H_c(T) = H_c(0) \left[ 1 - \left( \frac{T}{T_c} \right)^2 \right]. \quad (2.44)$$

This is valid for Type I superconductors, which use the value  $H_c$  and return to the normal state in fields that exceed this value. Type II superconductors instead have two critical field values of interest,  $H_{c1}$  and  $H_{c2}$ . Below  $H_{c1}$ , a Type II material exhibits the Meissner effect, but between  $H_{c1}$  and  $H_{c2}$  magnetic flux penetrates the superconductor, forming ‘vortices’ consisting of a single flux quantum in a normal ‘core’, surrounded by a circulating vortex current in the superconductor. As the field increases, the density of these vortices increases until the field exceeds  $H_{c2}$ , at which point the material returns to the normal state. At  $H_{c2}$ , vortices are as tightly packed as possible, separated by the coherence

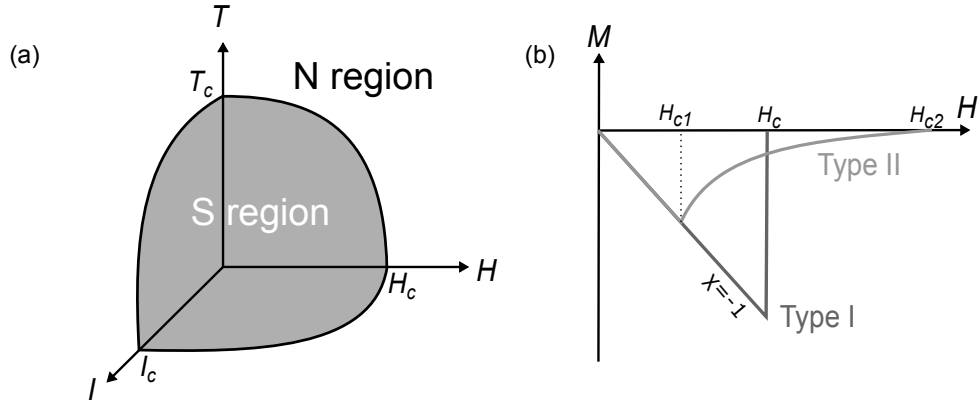


**Figure 2.14:** (a) Critical values of temperature, current and magnetic field ( $T_c$ ,  $H_c$ ,  $I_c$ ) must not be exceeded for a material to remain in the superconducting state. (b) Ideal virgin magnetisation-field curves for Type I and Type II superconductors as labelled. Type I materials demonstrate the Meissner effect and perfect diamagnetism up to  $H_c$ . Type II materials do up to the (lower) value  $H_{c1}$  at which point flux penetrates the material in the vortex state, the amount penetrating gradually increasing with field until  $H_{c2}$ , at which point the superconductor returns to the normal state.

length in the superconductor,  $\xi_S$ , the limiting distance over which superconducting order can change, i.e.:

$$H_{c2} = \frac{\Phi_0}{2\pi\xi_S^2} \quad (2.45)$$

where  $\Phi_0$  is the flux quantum. In a type II superconductor, the critical current is that which causes the vortices to move via the Lorentz force, which is associated with Ohmic losses in the normal core. However, vortices will typically be ‘pinned’ by defects in the superconductor, which allows engineering of these materials to have large values of critical current.

### 2.3.3 Cooper pairs

A microscopic theory of superconductivity arose based on two notable experimental observations: a dependence of  $T_c$  on the isotope mass observed in superconductors, and a Boltzmann-like dependence of the specific heat capacity from the superconducting state. The first, by analogy with the Debye temperature, suggests phonons may play a role. The second suggests the presence of an energy gap around the Fermi level, due to the dependence on thermal excitations. The theory that links these observations with the experimental properties of superconductors already discussed is known as BCS theory.

BCS theory suggests that the current in a superconductor is carried by pairs of electrons with opposing momentum  $|k \uparrow\rangle$  and  $|-k \downarrow\rangle$ . These pairs form when an attractive interaction exists between electrons, which is often considered to be an electron-phonon interaction. A simplified explanation is that as an electron passes through the lattice of positive ions, there is interaction between the electron and the ions. This interaction is

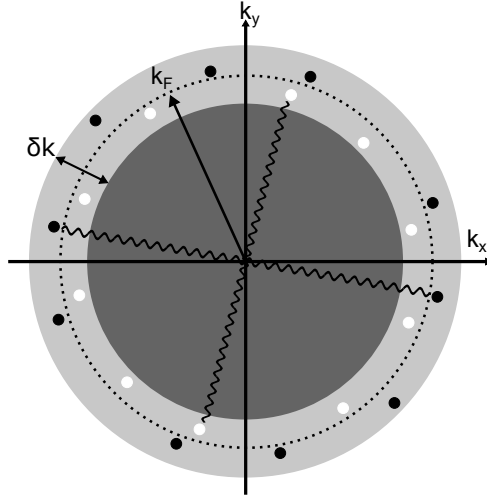


**Figure 2.15:** Electrons (black) or holes (white) in opposite momentum states may interact via phonon exchange and condense to form Cooper pairs. Here  $k_F$  is the Fermi velocity, representing the Fermi surface, and  $\delta k$  is the range of states (shown by the light ring) around the Fermi surface (dotted circle) which can undergo such pairing (where  $\delta k \ll k_F$ ). After [35].

screened by localised electrons. However, this screening is not perfect, due to the larger mass and inertia of ions compared to electrons; as the electron passes, there are regions of net positive and negative charge left in its wake. Another electron following the first may come across these effects, and its behaviour would be affected by them; in such a case, the electrons have indirectly interacted via the coupled vibrations of the lattice, or, viewed in another way, these electrons have interacted via phonon exchange (Fig. 2.15). This interaction overcomes the negative Coulomb interaction between the electrons, resulting in a net positive interaction. The Fermi sea is unstable compared to these interactions [33], leading to condensation of opposite momentum states into Cooper pairs at the ground state energy level. This condensation continues pairing opposite momentum states until the net energy lowering, the condensation energy,  $E_c = \frac{1}{2}\mathcal{D}(E_F)\Delta^2$  [where  $\mathcal{D}(E_F)$  is the density of states at the Fermi energy] is insufficient to compensate for the pairing of higher states. The creation of this condensate is associated with the formation of an energy gap,  $\Delta$ , which equals the range of  $\mathbf{k}$ -states either side of the Fermi level associated with electrons that paired. This energy gap leads to the characteristic zero resistance of a superconductor, as normal scattering events are insufficient to overcome the energy gap. Depairing effects are ones that act to break the symmetry of the Cooper pair, such as by changing the relative momentum of the electrons. To break apart pairs energy equivalent to  $2\Delta$  must be provided to a pair, to raise both electrons into the single electron states - however, as all pairs exist at the same energy as a condensate, the condensate as a whole is robust, as all pairs must behave in the same way, leading to

$$2\Delta(0) \approx 3.54k_B T_c. \quad (2.46)$$

where  $\Delta(0)$  is the gap at zero temperature. As in GL theory, changes in the condensate can only occur over the lengthscale of the coherence length,  $\xi_S$ , which here represents the average distance between electrons of a pair.

## 2.3.4 Proximity effect

### 2.3.4.1 S/N interfaces

The order parameter of a superconductor is not constant throughout the entire material, but instead it changes near an interface with another material. The degree of this change is proportional to the transparency of the interface; for a completely opaque interface (for example, with an electrically insulating material in a tunnel junction)  $\Delta$  will not change, but for a normal conducting metal, N, it will. The effects associated with superconductors at interfaces are known as proximity effects. The basic proximity effect is the penetration of superconducting character - the leaking of Cooper pairs - into the normal material [Fig. 2.16(a)]. The inverse proximity effect is the reverse: the decrease of superconducting character (leading to the decrease in order parameter as the Cooper pairs leak into N) nearing the interface. These effects occur via the mechanism of Andreev reflection.

Consider a conduction electron in N approaching the N/S interface, with energy  $E < \Delta$ . In S, there are no single electron states the electron can enter due to the energy gap. To enter, the electron takes with it another electron from N (of opposite momentum and spin) and forms a pair, transferring  $2e$  charge to the superconductor and continuing the transport of current. The additional electron taken leaves a hole behind in N. This is often considered as the incoming electron being Andreev reflected as a hole with directly opposite momentum, which therefore travels back along the path of the incoming electron [Fig. 2.16(b)]. The reverse process of a Cooper pair approaching the interface from S and filling a hole and leaving an unpaired electron can also occur. This electron-hole pair is correlated however, causing a small development of superconducting character in N within a short distance  $\xi_N$  (referred to as the coherence length in N) of the interface, the distance over which this correlation fades:

$$\xi_N = \sqrt{\frac{\hbar D_N}{k_B T_c}} \quad (2.47)$$

where  $D_N$  is the electron diffusivity in N. Similarly, the decay of electrons into the pair state as they enter S from N occurs over a coherence length as well, which can be written in a similar form:

$$\xi_{S,d} = \sqrt{\frac{\hbar D_S}{k_B T_c}} \quad (2.48)$$

where  $D_S$  is the electron diffusivity in S and the notation ‘ $d$ ’ refers to the fact that this is the ‘dirty limit’ coherence length, in which the mean free path of an electron is much

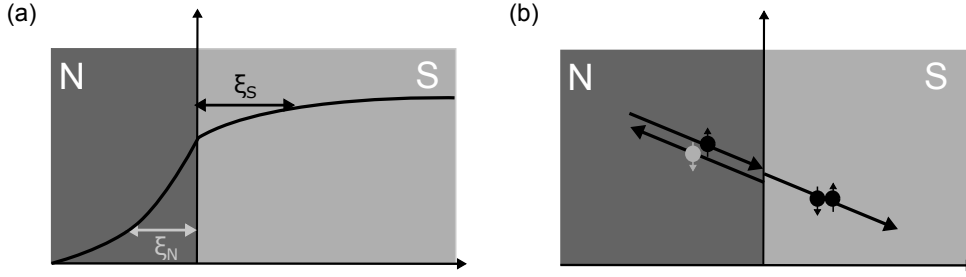


**Figure 2.16:** (a) The proximity and inverse proximity effects at an S/N interface, showing the superconducting wavefunction penetrating N from S and similarly reduced in S near the interface. In this example, the interface is assumed to be perfectly transparent and so the wavefunction across the interface is continuous. (b) Andreev reflection at an S/N interface: an incoming electron (black) from N is retroreflected as a hole (light grey) of exactly opposite momentum, transferring charge  $2e$  across the interface to inject a Cooper pair into the condensate. In reality, this conversion takes place over a distance, as the electron enters S as a decaying evanescent quasiparticle state, leading to the change in order parameter as in (a). Similarly, correlation between the electron and the hole in N are linked to the penetrating superconducting character of the proximity effect.

less than the coherence length in the superconductor. Many realistic superconductors, especially those grown as thin films, are in the dirty limit. The coherence lengths derived from theory ( $\xi_0$  and  $\xi_{GL}$ ) are for the ‘clean limit’, where the mean free path is much greater than the coherence length, although they can be adapted for the dirty limit.

### 2.3.4.2 S/F interfaces

At an S/F interface, the situation is modified due to the exchange energy in F. Now, when a pair enters F from S, the electrons (being of opposing spin) are at different potential energy levels, which causes them to start to dephase, as the pair develops a net momentum, leading to an oscillation of character as the pair decays [Fig. 2.17(a)]. Considered exclusively in terms of the wavefunctions of the electrons, the difference in energy due to the exchange energy is considered as a change in wavelength of the wavefunctions, leading to an oscillation of the overall pair. Due to this added effect of the exchange energy, which tends to be much larger than  $k_B T_c$ , the coherence length in a ferromagnet,  $\xi_F$ , is much shorter than in N:

$$\xi_F = \sqrt{\frac{\hbar D_F}{J}} \quad (2.49)$$

where  $J$  is the exchange energy and  $D_F$  is the electron diffusivity in F. The inverse proximity effect is also changed: there is a preferred spin direction in F, so that electrons of one spin are more likely to enter. Over a number of Cooper pairs, there will be a dominant spin direction at the surface of S, inducing a small magnetic moment in the opposite direction to that of the ferromagnet [36]. Finally, Andreev reflection is a spin dependent process, as two electrons of opposite spin must enter S to form a pair. In a ferromagnet, electrons are polarised, with the population of one spin direction greater

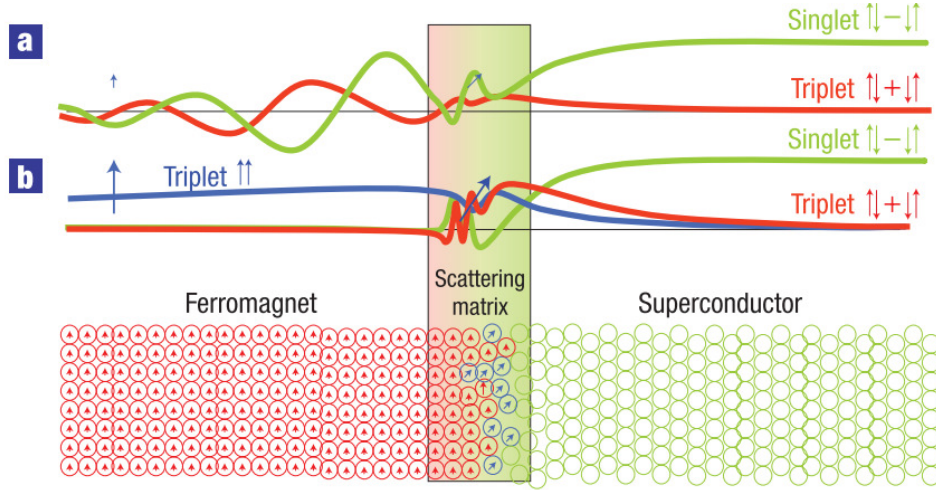


**Figure 2.17:** (a) At an S/F interface, a Cooper pair entering F from S starts to dephase due to the exchange energy, and the difference in energies of the two electrons of the pair leads to an oscillatory decay of the singlet state order parameter. The spin mixing that occurs at the interface means that some spin zero triplet character is generated. (b) An inhomogeneous magnetic field can cause a spin rotation that stabilises either of the spin  $S_z = \pm 1$  triplet states from the  $S_z = 0$  state, which survives over a long distance in the ferromagnet. From [37].

than the other: this affects the probability of Andreev reflection occurring. To picture this, consider the extreme case of a half-metal in place of F, which only has electrons of one spin direction at the Fermi level. In this case, Andreev reflection cannot occur.

### 2.3.4.3 Triplet pairs

The electrons in a Cooper pair follow the Pauli exclusion principle, such that under an exchange of electrons, the overall wavefunction must be antisymmetric. For singlet states in a superconductor with an isotropic gap (which this thesis is limited to) this requires that the spins of the electrons are in opposite directions -  $\frac{1}{\sqrt{2}} |\uparrow\downarrow - \downarrow\uparrow\rangle$  (from this point, the  $\frac{1}{\sqrt{2}}$  normalisation will be omitted for convenience). Upon entering a ferromagnet, the different energy levels for the different spin directions introduce a ‘spin-mixing’ [5] - requiring the wavefunction of the pair to have components of both the spin singlet and the spin zero ( $S_z = 0$ ) triplet state,  $|\uparrow\downarrow + \downarrow\uparrow\rangle$  near the S/F interface:

$$(\uparrow\downarrow - \downarrow\uparrow)\cos(\Theta) + i(\uparrow\downarrow + \downarrow\uparrow)\sin(\Theta) \quad (2.50)$$

where  $\Theta = \theta_1 - \theta_2$  is the difference in phase between the two electrons introduced by the different energy levels of the ferromagnet [Fig. 2.17(a)]. The ferromagnet breaks the time symmetry of the pair, allowing the spin directions of the electrons to be the same: if the pair subsequently travels through an inhomogeneous magnetic field after this spin mixing (such as by entering a ferromagnet with perpendicular magnetisation direction to the first), then ‘spin rotation’ may occur, forming  $S_z = \pm 1$  pairs,  $|\uparrow\uparrow\rangle$  or  $|\downarrow\downarrow\rangle$ , which then decay in the ferromagnet over a longer length scale, as they do not experience pair

breaking effects from the exchange energy, so that  $\xi_{\text{triplet}} = \sqrt{\frac{\hbar D_F}{k_B T}}$ , analogous to the decay of singlets in a normal metal. [Fig. 2.17(b)]

The existence of these so-called ‘long-range’ triplet pairs has been experimentally demonstrated [11–13]. Although spin triplets are excited states and are expected to decay over a coherence length in a superconductor [5], the ability to use superconducting currents to transport spin, using superconducting pairs that survive for long distances in ferromagnets is an exciting prospect for superconducting spintronics [4, 5].

### 2.3.5 Quasiparticles and non-equilibrium

The density of states of a superconductor is changed compared to the normal metal. It is often represented in a simplified ‘semiconductor’ picture (Fig. 2.18), which clearly shows the energy gap of  $\Delta$  either side of  $E_F$ , with a larger density of states occurring just above the gap, as  $\mathbf{k}$ -states associated with electrons that condensed into pairs have their energies raised in the superconducting state. This semiconductor model does not show Cooper pairs, which do not affect the density of states, but instead describes the unpaired states that may be occupied by excited particles, as a result of thermal excitation, pair breaking, or voltage bias and current injection.

At non-zero temperatures, thermal excitation of electrons above the energy gap into these unpaired states may occur. Electrons in these states have excitation energy

$$E_k = \sqrt{\Delta^2 + \mathcal{E}^2} \quad (2.51)$$

where  $\Delta$  is the energy gap between the Fermi energy and the lowest single particle states, and  $\mathcal{E}$  is the energy of a single particle relative to the Fermi energy. A one-to-one correspondence exists between single particle states in the superconducting state of a material and that in the normal state i.e.  $\mathfrak{D}_S(E_k)dE_k = \mathfrak{D}_N(\mathcal{E})d\mathcal{E}$ , where  $\mathfrak{D}_S(E_k)$  is the single particle density of states in the superconducting state, and  $\mathfrak{D}_N(\mathcal{E})$  is the density of states in the normal state. Using the fact that over small energies such as those considered here,  $\mathfrak{D}_N(\mathcal{E}) = \mathfrak{D}_N(E_F)$  and setting the Fermi energy to zero,  $\mathfrak{D}_N(\mathcal{E}) = \mathfrak{D}(0)$ ,

$$\frac{\mathfrak{D}_S(E_k)}{\mathfrak{D}(0)} = \frac{d\mathcal{E}}{dE} = \begin{cases} \frac{E_k}{\sqrt{E_k^2 - \Delta^2}} & E_k > \Delta \\ 0 & E_k < \Delta \end{cases} \quad (2.52)$$

which shows that there are a large number of single particle states around the gap edge, when  $\mathcal{E} \approx \Delta$ , but at higher energies, where  $\mathcal{E} \gg \Delta$ , the density of states is closer to the density of states in the normal state [33].

The excited ‘quasiparticles’ in these single particle states are not superconducting, do not respond to phase differences, and instead only flow (with an associated resistance) in response to an applied voltage (and are therefore essentially stationary in an isolated

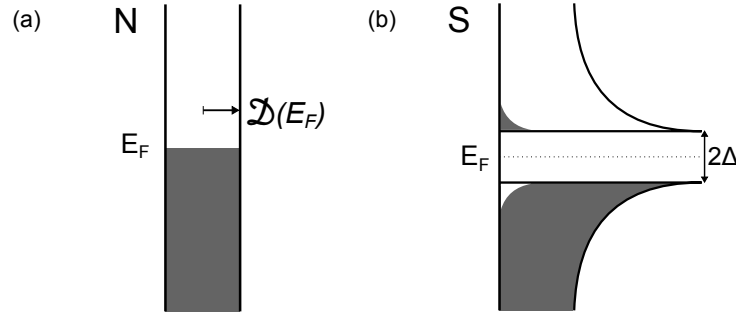


**Figure 2.18:** Semiconductor model pictures of a metal in (a) the normal state and (b) the superconducting state. In the superconducting state, an energy gap of  $2\Delta$  must be overcome to promote electrons into the excited quasiparticle states. This simplified picture has issues as it cannot accurately show the condensate and does not illustrate the energy dependent nature of the quasiparticle states, having both electron-like and hole-like character. However, it demonstrates the energy dependent density of states in the superconductor, whereas the density of states in the normal metal is essentially constant over the same energy range.

superconductor). An analogy can be drawn between these quasiparticles and the normal state electrons of the ‘two-fluid’ models used in early phenomenological theories, although here the occupation of quasiparticle states influences the superconducting gap.

The nature of a quasiparticle is extremely energy dependent. The  $\mathbf{k}$ -states around  $E_F$  are in fact combinations of electron-like and hole-like states, and the ‘nature’ of the state changes continuously from one to the other as energy (or momentum) varies from far from  $E_F$ , through  $E_F$  and then far the other side [Fig. 2.19(a)]. Charge of the particle occupying the state is an example of one property that varies, allowing quasiparticles to be used for pure spin current transport if they are kept at low energies, as near the gap edge, they have an effective charge of zero. The charge transport is performed by the superconducting condensate instead (‘spin-charge separation’). It should be noted that energy, momentum and spin of these quasiparticle states are definite and not mixed.

So far the discussion has focused on equilibrium scenarios. However, it is possible for a superconductor to be driven out of equilibrium, for example by injection of an external current into the superconductor. There are two non-equilibrium modes, known as energy imbalance and charge imbalance [Fig. 2.19(b-c)]. Any departure from equilibrium can be broken down into a sum of these two situations. The first, energy imbalance, is a result of equal excitation of both electron-like and hole-like quasiparticles above the equilibrium state (e.g. via incoming radiation). In this case, the superconductor may be described in terms of an effective temperature  $T^*$ , such that the distribution of excited states appears to conform to  $\Delta(T^*)$  (for clarity,  $T^*$  is simply a descriptor, and not an actual thermodynamic temperature). The second non-equilibrium scenario is that of charge imbalance, which may result from external current injection into a superconductor (usually along with energy imbalance). In this case, quasiparticle states are filled unequally, with either electron-like or hole-like dominating. To maintain overall charge neutrality, the condensate

changes in response to a charge imbalance, leading to a measurable difference in potential between the condensate and quasiparticles in this scenario [38].

These non-equilibrium scenarios will decay over a certain distance within the superconductor. Energy imbalance requires inelastic processes to decay, such as electron-phonon scattering. In general, such processes are limited in the superconducting state, and the energy decay length may be long. As more highly charged quasiparticle states have higher energies, charge imbalance also typically requires inelastic processes to decay, including particle-hole conversion processes. The charge imbalance decay length,  $\Lambda_{Q^*}$ , is given by:

$$\Lambda_{Q^*} = \sqrt{D_S \tau_{Q^*}} = \sqrt{1/3 v_F \lambda \tau_{Q^*}} \quad (2.53)$$

where  $v_F$  is the Fermi velocity,  $\lambda$  is the mean free path, and  $\tau_{Q^*}$  is the time between scattering events that relax charge imbalance.

Another dimension of imbalance exists when the spin of quasiparticle states is considered. As in normal metals, spin imbalance in a superconductor of quasiparticle states can be expressed in terms of a spin accumulation and associated change in potential,  $\Delta\mu$ , and decays via spin flip processes, mainly scattering from magnetic impurities or spin orbit scattering from non-magnetic impurities, given the reduced electron-phonon scattering at low temperatures. Compared to the normal state, the superconducting state has the added complication of an energy dependent density of states, which affects the spin-orbit scattering processes [39]. As a result, the decay of spin imbalance in a superconductor has been the subject of various studies (Section 6.1.3) and is still of interest today.

### 2.3.6 Superconducting spin valves

Spin valves feature two ferromagnetic layers sandwiching a nonmagnetic spacer layer between them. This central spacer layer can be made a superconductor to create a superconducting spin valve, which, analogously to a normal spin valve, controls supercurrent flow based upon the orientation of the two ferromagnetic layers.

A superconducting spin valve was initially proposed using ferromagnetic insulator layers [40]. Due to the antiparallel spins of Cooper pairs, the exchange fields of the ferromagnetic layers tend to break Cooper pairs and hence reduce the  $T_c$  of the central superconducting layer. Within the central superconducting layer, the average exchange field depends upon the orientation of the ferromagnetic layers: in the P-state, the average exchange energy in the superconductor is high, suppressing  $T_c$  further compared to the AP-state, in which the average exchange energy is low. As a result, there is a temperature window,  $\Delta T_c = T_c^{AP} - T_c^P$ , within which a device could sit, and act as a valve for superconducting currents depending on the orientation of the layers, being fully superconducting in the antiparallel state, but resistive in the parallel state. This effect, of a  $\Delta T_c$  resulting from the orientation of ferromagnetic layers adjacent to a superconductor, is known as

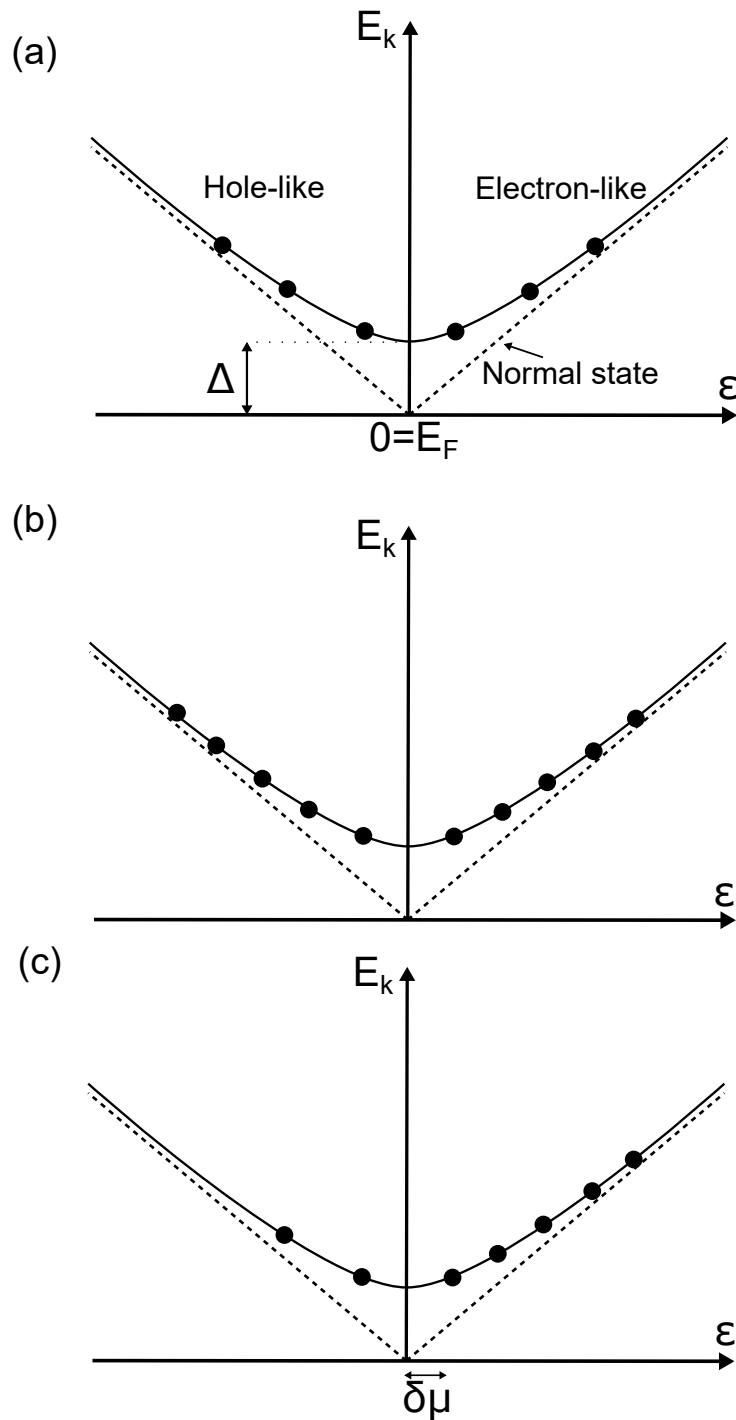


**Figure 2.19:** (a) Energy dependent quasiparticle states in a superconductor at equilibrium at non-zero  $T$ . All states are at least  $\Delta$  above the Fermi energy, and the single particle energy  $\epsilon$  determines the level of hole-like or electron-like character of the state. (b) Energy mode non-equilibrium. Particles have been excited to fill hole-like states and electron-like states equally. (c) Charge mode non-equilibrium. Particles have been excited so that either hole-like or electron-like states are occupied more, leading to a charge imbalance in the material. This is associated with a shift in potential  $\delta\mu$  between the quasiparticle states and the condensate. After [33].

the superconducting spin valve effect. Other theoretical papers [7, 41, 42] later proposed similar devices, using conducting ferromagnetic layers. The predictions of these papers and the parameters relevant to device construction are discussed in Section 6.1.2.

## 2.4 Thin films

Properties of thin films tend to significantly differ from those of the bulk. Microstructurally, this occurs because the vapour to solid transition is far from equilibrium. Many properties can be traced to the distinct microstructures and small lengthscales associated with the films.

### 2.4.1 Microstructure and growth

Polycrystalline thin films grow via nucleation and growth of crystals, as the adatoms from a vapour source condense onto a substrate [43]. Growth tends to occur via island growth, layer growth, or island plus layer growth, depending on the relative surface energies involved (Fig. 2.20). In island growth, the surface energy of the film is high, and adatoms tend to bond better to each other than to the substrate, leading to films growing in distinct islands which then coalesce at later stages. This type of growth is common for metals growing on insulator substrates. Layer growth occurs when adatoms bond to the substrate better than to each other, leading to the immediate formation of planar sheets which then build up. Island plus layer growth occurs when surface energies make layer growth favourable, but strain energies increasing layer by layer (from lattice mismatch for example) force the film to adopt island growth after one or more layers have been deposited. The stability of the crystals that form also affects the structure of the film: a low nucleation rate will lead to a few nuclei which grow larger before coalescing, forming a coarse grained film, whereas a higher nucleation rate leads to a more finely grained film as coalescence occurs when the grains are smaller.

Microstructure of a thin film is dependent on a few primary factors. Firstly, the mobility of adatoms, including their diffusion rates, arrival rates at the surface, and their energy is key. Additionally, it is more energetically favourable for an adatom to join an exposed surface in a consistent manner, so crystallographic orientations tend to propagate through whole films, which is known as granular epitaxy. Geometric shadowing is another important effect, in which existing protuberances in the film surface tend to grow and block incoming adatoms from reaching behind the protuberance, leading to an angle dependent shadowing effect. For a given deposition process, these factors and the degree to which they have an effect are experimentally related to the deposition rate and substrate temperature, leading to the development of structural zone models, detailing the different microstructures that tend to form based upon which atomic movement processes and other

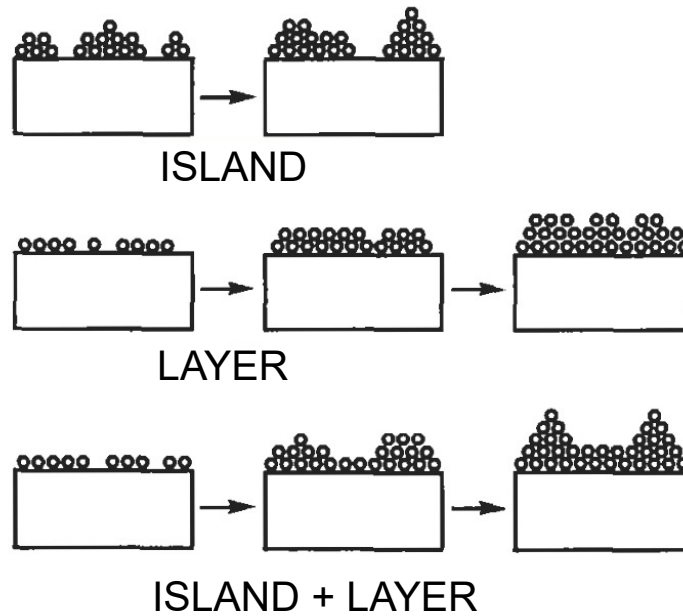


**Figure 2.20:** Growth of thin films. Island mode occurs when adatoms bind more closely to each other than to the substrate, whereas layer growth occurs when atoms bind more closely to the substrate. Island plus layer growth occurs as a result of strain energy building up in the film. From [43].

effects are dominant for changing experimental conditions. For sputter deposition, the model is known as Thornton's zone model, and is shown in Fig. 2.21. Here, the substrate temperature and sputtering pressure are considered, as these effect the adatom energies and mobility when condensed. However, the model does not consider the adatom arrival rate, which also has a significant effect on structure. In zone 1 the microstructure tends to be dominated by shadowing effects, and atom mobility is not enough to overcome this, leading to structures with significant voids at grain boundaries and fibrous grains. At higher substrate temperatures, the transition zone, 'zone T' is reached, which has higher quality, more dense films than zone 1, although grains are still fibrous and microstructure is heavily pressure dependent. By zone 2 atom mobility is enough to overcome most effects, leading to structure being mostly independent of pressure as structures are a result of surface diffusion controlled growth. It is characterised by columnar grains with dense grain boundaries. In all forms of thin films, including polycrystalline ones, columnar structures are a common microstructural feature, leading to very anisotropic properties. Finally, zone 3 has properties which near bulk properties, and features large, equiaxed grains as a result of high levels of bulk diffusion [43].

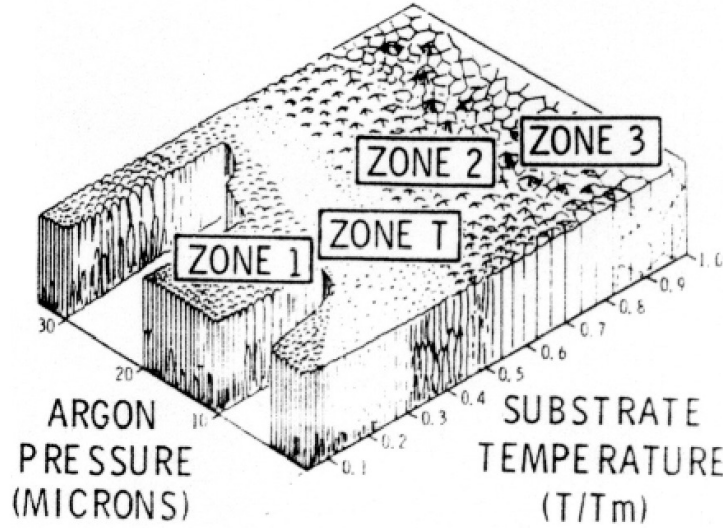


**Figure 2.21:** Thornton's zone model for the microstructure of thin films deposited by sputter deposition, taking into account the atom mobilities from the substrate temperature and the sputter gas pressure. From [44].

## 2.4.2 Thin film properties

### 2.4.2.1 Electric properties

The fibrous grain structures, frequency of defects and voids, and potential for impurities in thin films can often result in higher values of resistivity ( $\rho$ ) than for bulk materials. Like bulk materials, the resistivity of thin films follows Matthiessen's rule, which states that the resistivities from different sources within a material are independent and may be summed to give the total resistivity,  $\rho_{\text{tot}}$ :

$$\rho_{\text{tot}} = \rho_{\text{defects}} + \rho_{\text{impurities}} + \rho_{\text{thermal}} \quad (2.54)$$

where  $\rho_{\text{thermal}}$  is the temperature dependent contribution from electron-phonon scattering,  $\rho_{\text{defects}}$  is the constant contribution from defects and  $\rho_{\text{impurities}}$  is the constant contribution from impurities. This gives rise to one method of comparing the resistivity of different thin films and with that of the bulk: the residual resistivity ratio (RRR):

$$\text{RRR} = \frac{\rho_{\text{tot}}^{298\text{K}}}{\rho_{\text{tot}}^{10\text{K}}} = \frac{R_{\text{tot}}^{298\text{K}}}{R_{\text{tot}}^{10\text{K}}} \quad (2.55)$$

where the low temperature resistivity may be at 10 K, 4.2 K, or some other consistent temperature. This gives the ratio of resistivity due to defects to that due to thermal phonon effects.

Thin films can have an extra source of resistance that is not significant in bulk samples, known as surface scattering. In the case that the thickness of the film,  $d$ , is similar to that of the mean free path of the electron in the sample,  $\lambda$ , the path of the electron

may be interrupted by it reaching the surface of the sample, where it will scatter. If this scattering is diffuse scattering the mean free path is changed, effectively adding another source of resistivity. Similarly, scattering from grain boundaries may be more significant in thin films if the typical grain diameter becomes smaller than  $\lambda$ . These extra sources of resistance also contribute to the deviation from bulk properties.

#### 2.4.2.2 Magnetic Properties

Magnetic properties in thin films are dominated by a few particular energy considerations. In general, it can be expected that there are thickness dependent properties in very thin magnetic films because spins at the surface do not experience exchange energies from one side, and therefore are less tightly bound, an effect that becomes less significant as the film increases in size and the surface spins contribute less to total magnetisation. In terms of energies, the demagnetising factor for out of plane magnetisation is large, so there is usually a strong incentive from the demagnetising energy for the magnetisation to lie in the plane of the film.

It is also worth considering the energies involved in domain walls. Previously it has been noted that two distinct types of domain wall exist: where the spins rotate out of plane (Bloch wall) or where the spins rotate in plane (Néel wall). Néel walls are favoured in the thinnest films as they avoid atomic moments pointing out of plane, whereas Bloch walls are favoured in the bulk (and typically films greater than  $\approx 100$  nm thick) [43]. At intermediate film thicknesses, ‘cross-tie’ walls may form, which are of mixed character, containing sections of both Bloch type and Néel type. For the smallest of magnetic particles, the energy of a domain wall may exceed the energy associated with stray fields leaking from the sample. In this case, the material will remain entirely single domain.

#### 2.4.2.3 Superconductivity

Thin films can often be susceptible to high levels of impurities compared to bulk materials as a result of their fabrication processes. In general, the superconducting state (and the critical temperature of a material,  $T_c$ ) is impervious to non-magnetic impurities in the bulk, but magnetic impurities do tend to lower  $T_c$ . As a result, magnetic impurities, including paramagnetic impurities such as oxygen atoms, tend to have a large effect on the transition temperature of thin films, and it is possible for  $T_c$  to vary widely between different depositions. Deviation from bulk behaviours is typically expected when the thickness of the film is comparable to either the coherence length or the magnetic penetration depth [43]. For these regimes, non-magnetic impurities may also affect  $T_c$ .

An example of deviation from bulk behaviour in thin films is the penetration of a magnetic field parallel to the plane of the film when the film thickness is less than the penetration depth. In this case, the field penetrates the film extremely uniformly, even if

the superconductor is Type I, but the film remains superconducting. The energy of the film is hardly changed by an increase of the field strength, and the critical field  $H_c$  of the film can be much higher than that of the bulk [21, 33].

# Chapter 3

## Experimental Methods

In this study, GMR of a spin valve is used to quantify spin decay across its spacer layer, firstly in the normal state, followed by the superconducting state. A

substrate/Nb(10)/Cu(200)/Py(15)/Cu(10)/Nb( $d_{\text{Nb}}$ )/Cu(10)/Py(15)/FeMn(10)/Cu(200) heterostructure (all layer thicknesses in nm) is the main structure of the investigation (Fig. 3.1). A Nb seed layer (initially of 10 nm, then reduced to 5 nm), is deposited before the first Cu contact layer to improve adhesion to the substrate. The structure is very similar to the one used in [14], although with thinner Py (permalloy;  $\text{Ni}_{80}\text{Fe}_{20}$ ) layers. The thickness of Nb ( $d_{\text{Nb}}$ ) is the main change between different devices, allowing characterisation of the spin decay through different thicknesses of spacer layer. The Cu(10) layers between Nb and Py improve the magnetoresistance of the spin valve, as discussed in Section 4.2.3. The Py layers are the ferromagnetic layers, which are thinner than in [14] to allow improved superconducting properties of the device and improve magnetic switching characteristics. The FeMn is the antiferromagnetic layer, where 10 nm is used to ensure any thickness variation does not affect the degree of exchange bias (see Section 4.1.1). The 200 nm Cu layers above and below the main spin valve are the contact layers, which are required to be thick to allow use of focused ion-beam (FIB) milling to completely isolate the spin valve in a nanopillar current perpendicular-to-plane (CPP) device [45, 46].

The process for fabrication and measurement of devices was as follows:

- dc magnetron sputtering of entire heterostructure in single deposition
- optical lithography and Ar ion milling define device regions and contact wires from the heterostructure
- FIB milling is used to isolate nanopillars, defining up to seven devices per substrate
- individual devices are then measured using various experimental apparatus

In the following sections the various experimental techniques used are described, including parameters and details specific to this investigation.

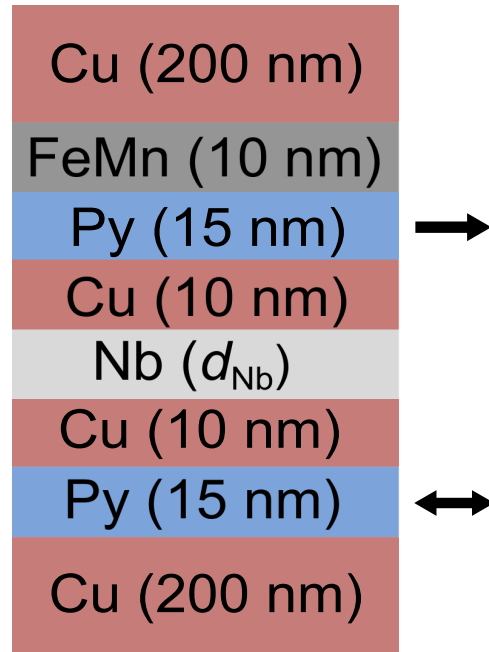


**Figure 3.1:** A schematic diagram of the heterostructure used in this investigation, with typical thicknesses of each layer in nm units. The arrows indicate the pinned and free Py layers.

### 3.1 Magnetron Sputter Deposition

Sputter deposition is a physical vapour deposition process, in which the vapour flux to be deposited is generated using a ‘target’ of material, which is bombarded with high energy species. The vapour flux is ejected from the target and deposits onto the substrate - a schematic of the setup is shown in Fig. 3.2(a). In dc (direct current) sputter deposition, this is achieved by applying a negative high voltage to the target (hence also the ‘cathode’). The target attracts positively charged species and repels negatively charged ones, which allows a self sustaining glow discharge (a plasma) to be established from an inert gas (commonly Ar, which is unreactive but ionises relatively easily). Positive  $\text{Ar}^+$  ions are accelerated towards the cathode; upon colliding, species are ejected from the target [Fig. 3.2(b)] including secondary electrons which are repelled from the cathode and collide with neutral Ar ions, ionising them, continuing the discharge. Also ejected from the target are sputtered atoms, which diffuse through the plasma to deposit onto the substrate, and typically have energies ranging between a few eV to 10s of eV. The large degree of scattering sputtered atoms experience during this diffusion means there is little directionality to the depositing flux, including a large proportion of the flux depositing on surfaces other than the substrate, such as the chamber walls. To improve this, the Ar pressure can be reduced, but this makes the plasma harder to maintain.

To allow sputtering to occur at lower pressures, magnetron sputtering is used. Now, a magnetic field is added at the target surface, such that this field is perpendicular to the electric field. This means that secondary electrons ejected from the target are forced

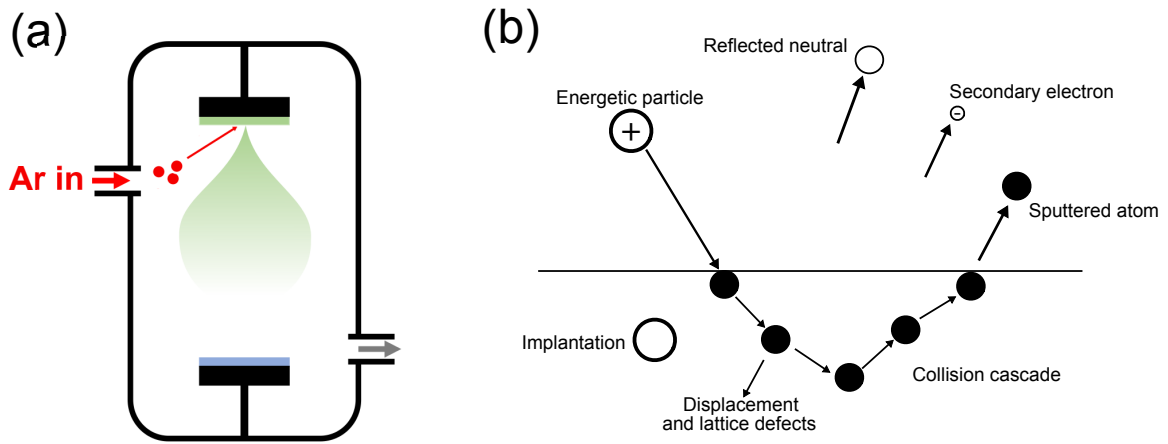


**Figure 3.2:** (a) A schematic diagram of a sputter deposition chamber, featuring the Ar flowing in, Ar ions (red) attracted to the target (green) before the sputtered atoms diffuse through the plasma to deposit on the substrate (blue). (b) Sputtering features energetic particles colliding with a surface, from which there are multiple possibilities. Sputtered atoms, secondary electrons and reflected neutrals (reflected Ar ions after picking up an electron from the surface) can all be detected originating at the target. Within the target, defects and implanted ions may develop. Adapted from [43].

into cycloidal motion, confining them near the target surface, increasing the efficiency of the ionisations they cause, as they tend to last for longer time and the generated ions are already close to the target. A side effect of these crossed fields is that the electrons tend to ‘hop’ along the target around the ‘racetrack’ region specifically defined by the crossed fields. This racetrack tends to experience much more sputtering, and hence is eroded faster than the rest of the target.

The deposition rate for sputter deposition is a balance of factors; the balance of pressure between sustaining the plasma and minimising diffusion time has already been discussed, and the sputter yield from a target for a given bombarding species is also dependent on the relative masses of the inert gas forming the plasma and the target material. Typically, deposition rate at a given pressure is considered to be proportional to the power applied to the target, and the inverse square of the target-substrate distance.

Sputtering involves relatively high energy species, and this has effects on the growing film, which is bombarded by the incoming atoms and also reflected neutrals from the target, leading to defects, compaction, resputtering of material or implantation of the neutrals. These effects can be reduced at increasing pressure as the energy of species is reduced due to increased collisions - the energy loss of these species is proportional to the pressure-distance ( $PD$ ) product, where the distance is the target-substrate distance. The bombardment during growth means sputtered films tend to be under compressive stress, although this is dependent on pressure, and a transition between tensile and compressive stress can be seen for varying  $PD$  product.

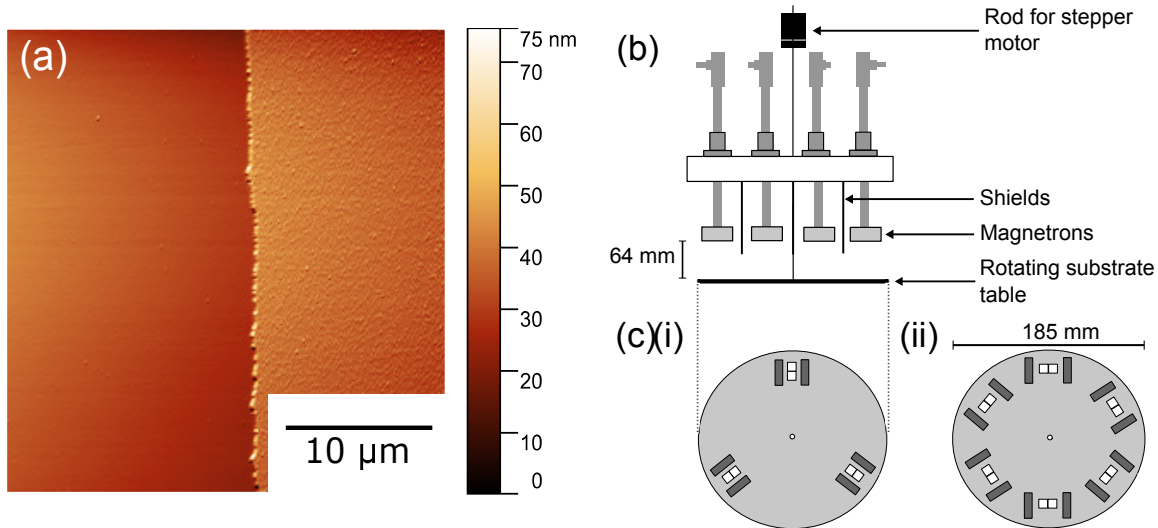


**Figure 3.3:** (a) An AFM scan of a step made by lift-off used for calibration of sputtering rate. All calibration scans were performed over  $30\ \mu\text{m} \times 30\ \mu\text{m}$  areas. (b) The removable flange holding the magnetron targets and rotating substrate table that is inserted into the vacuum chamber. (c) Plan views of the substrate table part of the flange used in sputtering. (i) is the three slot setup used for the majority of the work, (ii) is the six slot setup developed for more systematic investigations. Not to scale. White squares represent substrates, grey rectangles represent magnets.

### 3.1.1 Experimental Process

Thin film metallic layers were deposited onto (001) oriented silicon substrates with a 250 nm thick oxide layer. These  $5 \times 5$  mm substrates were cut from a larger wafer into individual substrates by snapping the wafer along lines scored with a diamond scribe. On the reverse of substrates, an arrow was marked to define an orientation. Before deposition, substrates were bathed in acetone for 5 minutes in an ultrasonic bath, before rinsing with isopropanol and dried with nitrogen. The substrates were then checked for cleanliness using an optical microscope.

Substrates were placed on a rotating substrate table on a removable flange that was then loaded into the vacuum chamber [Fig. 3.3(b)]. The chamber was baked and pumped down at least overnight, if not longer, in order to achieve an ultra-high vacuum that was typically around  $(6.5 \pm 2) \times 10^{-6}$  Pa before liquid nitrogen was added into a ‘jacket’ surrounding the main vacuum chamber, which helped decrease the base pressure further by cooling the chamber walls and encouraging adsorption onto those walls of any impurities not removed by the pumping (of which water vapour was the only species of significance). After confirming the vacuum levels again, at this point typically better than  $9 \times 10^{-7}$  Pa, the Ar flow rate of  $0.1\ \text{Pa s}^{-1}$  into the chamber was set, and sputtering would commence. As the heterostructure was deposited the plasma was ignited for each target in the order required when the pressure was above 8 Pa. The pressure was then reduced to 1.5 Pa, and a ‘presputtering’ process intended to remove any impurities at the surface of the target was run for 10 minutes. A stepper motor was then used to rotate each substrate in

Layer	Power (W)	Pressure (Pa)	Rate (rpm nm W <sup>-1</sup> )
Nb	30.0 ± 0.1	1.50 ± 0.03	0.031 ± 0.002
Cu (contact)	60.1 ± 0.1	1.49 ± 0.03	0.016 ± 0.0012
Cu (Py/Nb interface)	15.0 ± 0.1	1.49 ± 0.03	
Ni <sub>80</sub> Fe <sub>20</sub> (bottom)	60.1 ± 0.2	1.50 ± 0.03	0.0091 ± 0.0007
Ni <sub>80</sub> Fe <sub>20</sub> (top)	30.0 ± 0.1	1.49 ± 0.03	
FeMn	30.0 ± 0.1	1.49 ± 0.03	0.0078 ± 0.0008

**Table 3.1:** Typical deposition parameters for all layers. The rate value is obtained from the calibration step scans, multiplying the measured thickness and rpm used for the calibration film divided by the deposition power.

turn under the active magnetron, where the rate of rotation directly affected the time the substrate spent in the vapour flux and hence the rate of deposition. The target-substrate distance was maintained at 64 mm throughout separate depositions, so the rate of rotation and power producing a given thickness of material were combined into a single rate value that was calibrated for each deposited material using a ‘lift-off’ method to create a step edge [Fig. 3.3(a)] that was measured using atomic force microscopy (Section 3.7). The powers used for each layer of the heterostructure are given in Table 3.1.

All spin valve structures were deposited in a magnetic field stronger than 100 mT, which was aligned with the arrow on the reverse of each substrate, to ensure consistency of the resulting induced unidirectional magnetic anisotropy during later stages of the fabrication process and measurement. This field was applied by SmCo bar magnets added to the rotating substrate table. Initially, only three pairs of magnets were used, such that three different structures (typically two heterostructures and one reference) were deposited at once [Fig. 3.3(c)]. Limited time available using the vacuum chamber meant more structures could not be deposited at once. Later in the investigation, as the equipment was used less by others, modification of the substrate table was undertaken such that five heterostructures and one reference could be deposited in a single deposition [Fig. 3.3(cii)], which allowed increased systematic investigation of different structures. The reference films deposited during the depositions were 30 nm of Nb, which were measured for their superconducting critical temperature,  $T_c$ , to allow some level of comparison between different depositions (Section 5.2.6).

## 3.2 Optical Lithography and Ion Milling

Optical lithography and Ar ion-milling have been used to define the thin film heterostructure into a 2D pattern consisting of seven wires of width 4  $\mu\text{m}$  with contact leads suitable

for four-point measurements emerging from each; the mask used is shown in Fig. 3.4(a). Optical lithography involves use of a photosensitive resist to transfer a pattern from a mask onto the sample; the resist is applied, and exposed to ultraviolet (UV) light in the desired pattern. This UV-light activates the resist, rendering it either soluble (for a ‘positive’ resist) or insoluble (for a ‘negative’ resist) in a developer. The remaining resist is then of the desired shape and acts as a ‘shield’ in a subsequent Ar ion-milling step, resulting in the thin film heterostructure adopting the shape of the pattern as the surrounding material not covered by the resist is milled away. For this investigation, the positive resist AZ 4533B was applied to the sample in a single drop, followed by spinning at 8000 rpm for 30 seconds, which applies the resist in an even layer across the majority of the substrate, excluding a build-up near the edges of the substrate, known as an ‘edge bead’. The sample is then baked at 110°C for one minute, which removes solvent from the resist. In the contact lithography used here, the distance between the mask pattern and the sample is key, as it defines the resolution of the resulting pattern. The edge bead therefore needs to be removed before the true pattern is applied to the resist, which is done by exposing the edge bead area to UV for 1 minute, before at least 45 seconds in the developer solution, which was a 1:2 mixture of AZ 351B developer with distilled water. After edge bead removal, the sample was placed under the mask to apply the pattern, exposed for 10 seconds, and developed for 10 seconds, followed by short dips in developer solution alternating with examination under an optical microscope, the purpose of which was to ensure all resist was removed where desired without ‘overdeveloping’ the remaining resist, which would lead to a poor resulting shape of heterostructure after milling, or possibly even severed contacts. Following optical lithography, the sample was milled with Ar ion milling. The complete process is illustrated in Fig. 3.4(b).

Ion milling is a purely physical milling process that uses a confined plasma to generate ions which are accelerated into the material to be milled using biased grids. The ions mill away material through physical interaction. This process is highly anisotropic, the milling only occurring in the direction of the ion beam, which makes it suitable for patterning as there is clear definition of the remaining structure based upon the resist mask in place. It is also highly unselective, milling all materials the beam comes into contact with, meaning the resist in this process is a physical barrier to protect the heterostructure underneath. Redeposition of milled material can also occur as part of this process, which was observed in this investigation as the formation of ‘walls’ alongside the resist. Redeposition did not cause issues as any significant shorts that may have formed were visible and easily removed in the focused ion-beam milling step. In this investigation, a mixture of Ar-O<sub>2</sub>(2%) gas was used, which slightly increased etching rate and minimised redeposition as milled material would react with oxygen and be removed. The milling was undertaken with a discharge voltage of 40.0 V, a beam voltage of 700 V and an accelerator voltage of 100 V, resulting in currents of  $0.33 \pm 0.07$  A,  $20.0 \pm 0.1$  mA, and  $1.8 \pm 0.2$  mA respectively.

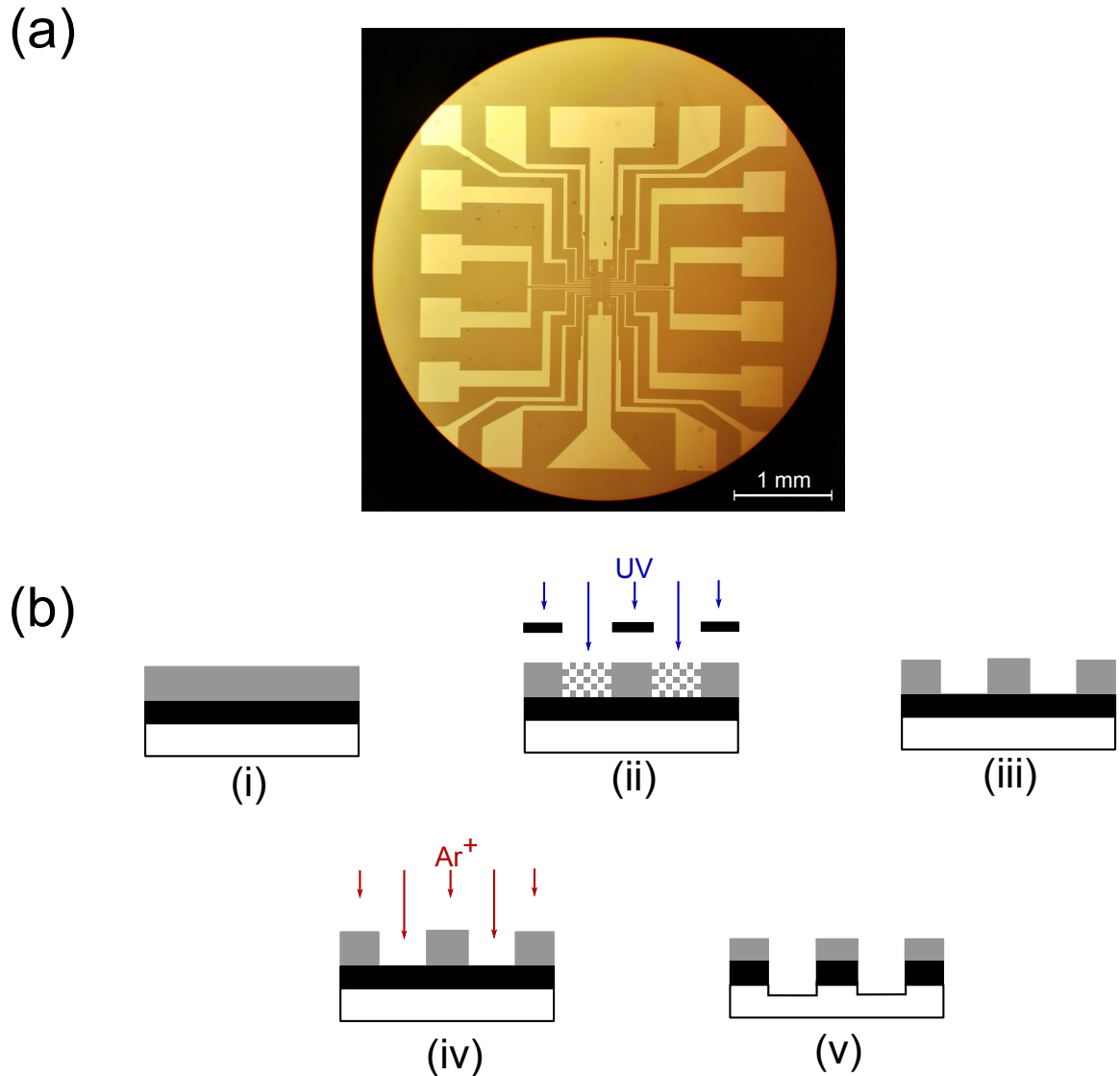


**Figure 3.4:** (a) The mask used in optical lithography, featuring seven ‘device regions’ defined by contact wires. (b) The lithography and milling process, from (i-v). (i) The resist (grey) is spun onto the heterostructure (black) on top of the substrate (white). (ii) After baking, flooding the resist with UV light makes the exposed parts soluble in developer, whereas the parts covered by the mask remain insoluble, as in (iii). Ar ion-milling is then undertaken, which mills the whole sample (iv), removing the metallic layers that are not physically protected by the remaining resist. To ensure no shorts across the pattern, the structure may be slightly overmilled, removing some of the substrate (v). The resist can then be removed in an ultrasonic bath in acetone, and is ready for FIB milling.

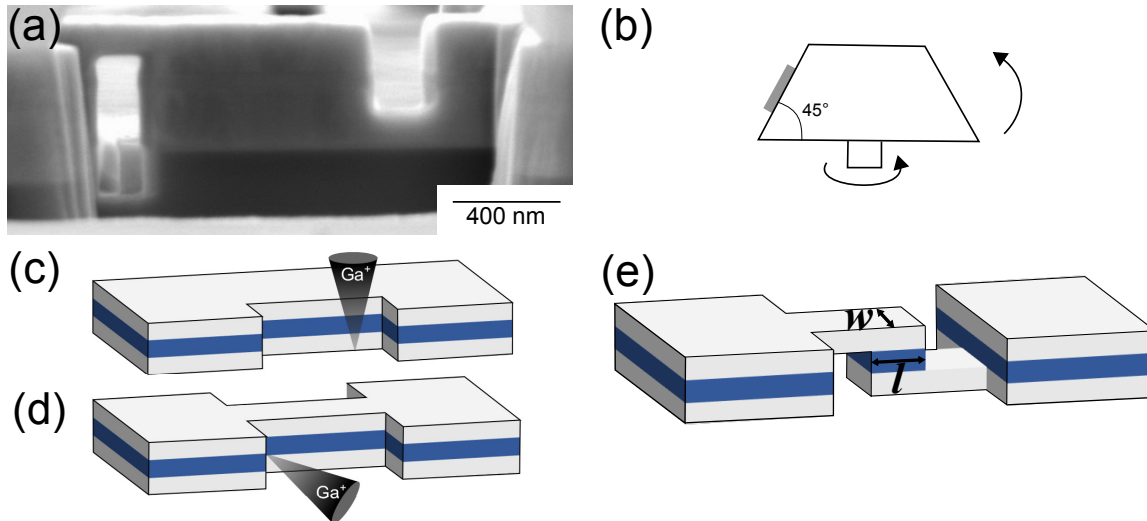


**Figure 3.5:** (a) A scanning electron micrograph of a nanopillar from a side view, showing the ‘side cuts’ that isolate the pillar from the surrounding material, which, not being superconducting, also contributes to the measured resistance. The device within the nanopillar makes the largest contribution to the resistance and  $\Delta R$  due to its low area and CPP regime. (b) The custom stub used during the FIB process to access the necessary beam angles. The grey box represents a substrate mounted on the stub. (c) Two steps of the pillar fabrication process: the initial channel is milled by the beam pointing orthogonal to the sample surface. After an edge cleaning step, the stage is rotated to allow the ‘top’ and ‘bottom’ side cuts (d), with the beam at  $3^\circ$  from the sample surface. (e) A schematic diagram of a completed pillar, with the dimensions referred to as length,  $l$ , and width,  $w$ , of the pillar labelled. The central (blue) layer represents the complete spin valve structure within the Cu contact layers, which must be fully isolated by the FIB cuts. Figures inspired by [47, 48]

### 3.3 Focused ion beam milling

A focused ion-beam (FIB) microscope contains a liquid metal Ga ion source, which emits  $\text{Ga}^+$  from a sharp tip upon application of a strong electric field. These ions are accelerated by an acceleration voltage of 30 keV and directed down a column of electromagnetic lenses, which are used to control aspects of the beam. The probe current is defined by a series of variable apertures and the electrostatic condenser which helps to collimate and focus the beam. The final objective lens is used to focus the beam onto the surface. The diameter of the beam is controlled by the beam voltage and also by the working distance, which here is around 5.2 mm. The FIB column is tilted at  $54^\circ$  from the scanning electron microscope column (SEM) that is also present in the apparatus. During operation, the SEM was used for imaging the sample, as electron microscopy is less damaging than FIB imaging, and the FIB was used primarily for milling.

Nanopillars were milled from the  $4 \mu\text{m}$  wire between 4-point contacts resulting from the optical lithography and ion milling step using FIB milling with a Zeiss Crossbeam 540 microscope. Substrates were placed upon a custom built  $45^\circ$  stub, which, given the normal freedom of tilt in the sample stage, allowed the angle between the beam and the sample

surface to vary between  $0 - 90^\circ$ . The milling order of the different pillars was randomised, to help distinguish between systematic changes across devices based upon beam changes during deposition, or (for example) any thickness gradients which may have been present across the multilayer. First, using a  $90^\circ$  beam angle, a 100 pA beam was used to thin the  $4 \mu\text{m}$  wide wire down to a width of between 500-1200 nm, over a roughly  $2 \mu\text{m}$  length, depending on desired device dimensions. This was then thinned further at a low current of 10 pA, in an ‘edge cleaning’ step that removed any resputtered material from the higher current mill. This step was done with a line scan, the beam rastering line-by-line into the wire to encourage the cleanest surface. The final step involved readjusting the stage by rotating  $180^\circ$  and changing the tilt, so the angle between beam and sample surface was  $3^\circ$ , which was used instead of  $0^\circ$  to allow increased visibility during the process. Again using a 10 pA beam, the ‘side cuts’ were made to isolate the nanopillar, one ‘top cut’ that milled all layers except the bottom Cu contact layer and one ‘bottom cut’ that milled all except the top Cu contact layer, such that the current is forced to flow vertically through the layers of the spin valve device. These ‘side cuts’ were required to overmill significantly into the relevant Cu contact, to ensure the spin valve layers were completely milled through. An SEM image of the final pillar is shown in Fig. 3.5(a), with schematic diagrams in (c-e) detailing the process and indicating the relevant device dimensions. These dimensions were measured using an in-program tool giving the length of a line drawn across an image, using the central spin valve as the point of measurement; the error in these measurements was estimated by comparing the maximum and minimum line lengths that could reasonably be drawn for a given pillar, leading to a relatively high error of  $\pm 40$  nm for each dimension. Device dimensions ranged between  $400 - 1500$  nm in length, and  $300 - 1000$  nm for width. The most common device dimensions used were around 800 nm long and 500 nm wide.

### 3.4 Low Temperature Measurements

Low temperature measurements including the change in resistance with temperature,  $R(T)$ , the change of resistance with magnetic field  $R(H)$  and differential resistance measurements were performed across different apparatus at different stages of the investigation. The first was a electronic dip probe with electromagnet attached, for inserting into a dewar of liquid helium to conduct  $R(H)$  measurements at 4.2K, and the second was a pulse-tube measurement system capable of temperatures down to 1.5 K and fields of up to 1 T with the standard probe, and temperatures down to 0.3 K using a He-3 insert probe. All warming and cooling of devices, both from room temperature, and as part of  $R(T)$  measurements, took place at zero applied field. For both pieces of equipment current control and measurement were done using a Keithley 6220 current source and a 2182A nanovoltmeter. These were run in the reverse polarity ‘delta measurement’ mode,

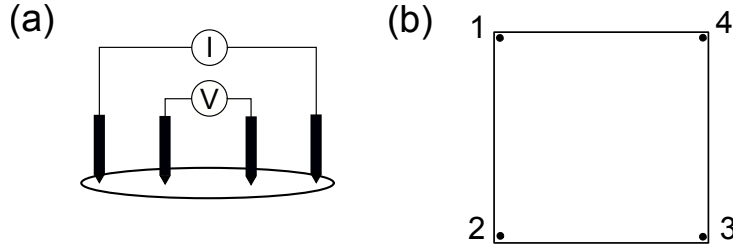


**Figure 3.6:** (a) A four-point current geometry - the separation of current and voltage contacts eliminates contact resistance from the resulting resistance value. (b) The current contact setup for a van der Pauw measurement, with contacts in the corners (for a quadrilateral sample) and as close to the edges as possible.

in which the current source supplies a square wave, and the nanovoltmeter measures at both high and low current levels, with a moving-average between the last three measurements taken to provide a new delta reading every time the current swaps levels. This mode is used to minimise the effects of thermal electromotive forces in the measurement and to reduce noise.

Measurements were performed using a standard 4-point current geometry [Fig. 3.6(a)], using the contact leads defined by the lithography. The 4-point geometry is typically used to eliminate the effects of contact and resistances by separating the current path from the voltage measurement, as only the section of sample between the two voltage leads contribute to the measured voltage. However, given that the contact layers are not superconducting Nb, but instead are Cu, in addition to the CPP spin-valve device, the leads between the voltage contacts that the pillar was milled from (around  $20\ \mu\text{m}$  long,  $4\ \mu\text{m}$  wide) also contribute to the measured resistance (see Section 4.2.2). The setup could therefore be considered a ‘quasi 4-point’ measurement with respect to the spin valve devices. The current used for measurements was  $50\ \mu\text{A}$ , which was chosen as the lowest value of current that gave a reasonable signal:noise ratio. Measurements of  $R(T)$  at different currents suggest this current did not affect  $T_c$  compared to  $10\ \mu\text{A}$ , which did not give a usable signal:noise ratio.

After cooling the devices to low temperatures in zero field, they were saturated in a  $100\ \text{mT}$  field before returning to zero field, ensuring the devices were all in the parallel (P) state before measurement.  $R(H)$  measurements would then be performed; although major loops were often performed to ensure switching of devices were as expected, the majority of measurements used for extracting  $\Delta R$  were minor loops, measured from  $100\ \text{mT}$  to  $-30\ \text{mT}$ , from the P-state to the antiparallel (AP) state in the first sweep, and then back to  $100\ \text{mT}$  in the reverse sweep, only the free layer of the spin valve having switched (as also described in Section 3.5). A major and minor loop of a device are plotted together in Fig. 3.7. The field sweep rate was  $0.03\ \text{T min}^{-1}$ . The  $\Delta R$  value was taken as the resistance difference between  $R^{AP}$  at zero applied field, and the saturated  $R^P$  value at  $100\ \text{mT}$ .  $R(T)$  measurements were performed in both the P- and AP-states, at zero applied field, at a

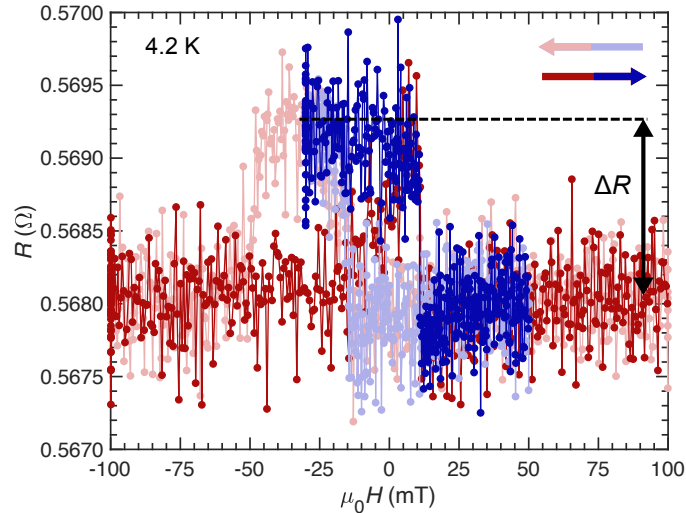


**Figure 3.7:** (a)  $R(H)$  loop of a device in the normal state, showing both a major loop (red) and minor loop (blue). Light colours represent the sweep from positive to negative fields, dark represent the return sweep. Note the agreement between the switching fields corresponding to the free layer switching in each loop. The value of  $\Delta R$  is the difference between the AP-state at -30 mT and the P-state at 100 mT, as shown.

temperature sweep rate of  $0.3 \text{ K min}^{-1}$ . Higher cooling rates gave the same value of  $T_c$ , but this lower rate was used to ensure accuracy.  $\Delta T_c$  values were extracted from these separate  $R(T)$  measurements in P- and AP- state at  $R(T_c) = 0.5R_N^{AP}$ , where  $R_N^{AP}$  is the resistance at  $T_{\text{device}}$ , the onset of the device transition in the AP-state. A single  $0.5R_N$  value is used for both states as this gives a more representative value of the temperature instability allowed for a working superconducting spin valve device. Temperature values are also taken at  $0.45R_N$  and  $0.55R_N$  to provide errors in each  $T_c$  measurement. The errors of each  $T_c$  are added in quadrature to give the error in  $\Delta T_c$ .

Resistivity measurements were also performed on 300 nm thick films of Py, Cu and Nb using a van der Pauw setup. The van der Pauw technique involves using separate voltage and current contacts at four corners of the square substrates, as shown in Fig. 3.6(b) and is valid for thin films, where the thickness is much less than the length and width of the film. Measurements of resistance can be made, for example, when current flows through contacts 1 and 2, and voltage is measured across contacts 3 and 4, such that

$$R_{12,34} = \frac{V_{34}}{I_{12}}. \quad (3.1)$$

Measurements of resistance are then made both forwards and backwards along the edges of the sample (both horizontally and vertically) so that

$$R_{\text{horizontal}} = \frac{R_{14,23} + R_{41,32} + R_{23,14} + R_{32,41}}{4} \quad (3.2)$$

Metal	$\rho$ (n $\Omega$ m)
Nb	$93 \pm 20$
Cu	$6.2 \pm 1.2$
Ni <sub>80</sub> Fe <sub>20</sub>	$182 \pm 15$

**Table 3.2:** Values of resistivity measured for Nb, Cu and Py (Ni<sub>80</sub>Fe<sub>20</sub>) at 4.2 K using the van der Pauw method on deposited 300 nm-thick films.

and

$$R_{vertical} = \frac{R_{12,34} + R_{21,43} + R_{34,12} + R_{43,21}}{4}. \quad (3.3)$$

Given that for these simple films,  $R_{horizontal} = R_{vertical}$ , these can then be used in the van der Pauw formula,

$$\exp(-\pi R_{horizontal}/R_{sheet}) + \exp(-\pi R_{vertical}/R_{sheet}) = 1 \quad (3.4)$$

where the sheet resistance  $R_{sheet} = \rho/d$  can be used with the film thickness  $d$  to calculate the resistivity of the film. The resistivities of Cu, Py and Nb measured with this method are given in Table 3.2.

### 3.5 Vibrating Sample Magnetometry

Vibrating sample magnetometry (VSM) is used to measure the magnetic properties of a material. The sample is mounted or held by a rigid rod, which then oscillates at around 70 Hz. An applied field magnetises the sample, and the oscillating field response induces an electromotive force in adjacent sense coils according to Faraday's law. The electromotive force is only sensitive to the change in magnetic field, allowing the applied field to be discounted, and results from a controlled oscillation so a lock-in amplifier may be used to pick up the signal. Control over the applied magnetic field allows  $M(H)$  loops to be measured. A schematic diagram of a VSM is shown in Figure 3.8.

In addition to room temperature VSM, magnetic characterisation at a range of low temperatures was performed in a high field cryogen free measurement system from Cryogenic Ltd., and also in a Quantum Design Magnetic Property Measurement System (MPMS) 3, which uses a superconducting quantum interference device (SQUID) for detection. The SQUID offers increased sensitivity ( $< 1 \times 10^{-8}$  emu) and a lower background noise. A SQUID is a superconducting circuit containing two Josephson junctions in a loop, where the phase difference between the two Josephson junctions caused by a magnetic flux passing through the loop, controls the critical current of the loop. During operation, a current greater than  $I_c$  is applied to the SQUID. Different levels of flux threading the loop change  $I_c$  by different amounts, which alters the voltage measured across the loop.

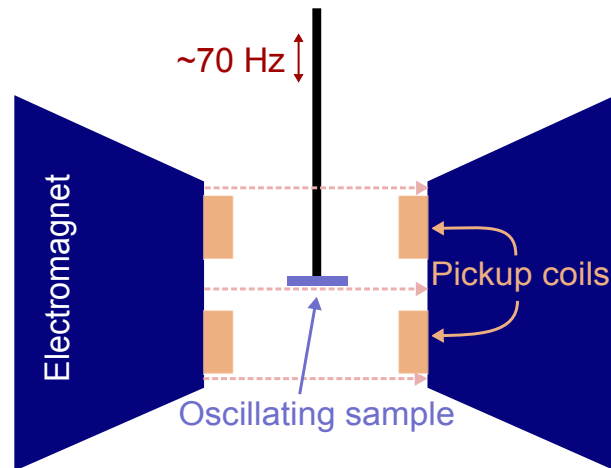


**Figure 3.8:** A schematic diagram of a vibrating sample magnetometer, such as used in this investigation. For clarity in the diagram, the sample is enlarged. In reality, it is much smaller than the rest of the apparatus, such that the fields across the sample are homogeneous.

$M(H)$  loops were measured to ensure complete spin valve switching was observed for the deposited heterostructure, with a stable AP-state, which ensures good giant magnetoresistance between the P- and AP-states. Switching between magnetic states of the devices can be performed either in a major loop or minor loop. In a major loop, the field is taken from one extreme (e.g. high positive fields, where the device is in the P-state), through the switching of both layers (first the free layer at low negative fields, putting the device in the AP-state, then at higher fields the pinned layer switches, as the field becomes strong enough to overcome the exchange bias between the pinned layer and the antiferromagnet) so that the device is again in the P-state, with both layers pointing in the opposite direction to the start. The reverse sweep then occurs, where the pinned layer first switches back while the applied field is still negative, due to the strong coupling from the antiferromagnetic layer, putting the device in the AP-state. At small positive fields, the free layer switches, returning the device to its starting P-state. A minor loop, by contrast, is switching of only the free layer; from the initial P-state, the field is swept until the free layer has completely switched and the device is in the AP-state, and then the return sweep is performed, the free layer switching back to its original orientation. The minor loop is the expected behaviour of a spin valve in use in e.g. hard drives.

## 3.6 X-ray Diffraction

X-ray diffraction is an extremely useful technique for probing the crystal structure of materials. In this investigation it was used only once in a limited manner, and therefore only the fundamentals are covered here.

X-ray radiation has a wavelength similar to the atomic spacing in a crystal lattice. X-ray diffraction uses this to investigate crystallographic spacing and structure by inves-

tigating the diffraction of x-rays through the lattice. X-rays diffract off tightly bound atomic electrons in the regular crystal lattice, leading to constructive interference causing peaks at certain angles, as determined by Bragg's law:

$$n\lambda = 2d_{hkl} \sin(\theta) \quad (3.5)$$

where  $n$  is an integer,  $\lambda$  is the wavelength of the radiation,  $d_{hkl}$  is the spacing of the plane with Miller indices  $(hkl)$ , and  $\theta$  is the angle between the plane and the incoming radiation, or more precisely,  $2\theta$  is the angle between the incoming and diffracted x-ray beams.

The intensity of each diffraction peak in an x-ray spectra is related to crystal structure, the scattering factors of the atoms in the structure, and the amount of sample contributing to that peak, which includes both the thickness of the crystal, and also the crystallinity or texture of the grains in the sample; if a material has grains which tend to be more aligned, a peak will tend to be taller and narrower, due to increased agreement between different grains.

X-ray characterisation was used to investigate the crystal structures of the different layers in the heterostructure; a divergent beam of Cu  $K\alpha$  radiation ( $\lambda = 0.1541$  nm) was used, with an offset angle of  $1.5^\circ$  to limit the size of the substrate peak in comparison to the film peaks, which were much weaker as they were far less thick and less crystalline.

## 3.7 Atomic Force Microscopy

Atomic force microscopy (AFM) is used to measure the low level topography of surfaces, using a sharp 'tip' attached to a cantilever. The deflection of the cantilever as the tip moves across the surface is measured by reflection of a laser from the top of the cantilever. AFM is used in this investigation to measure roughness and the heights of step edges for calibration of sputter deposition rates. In the tapping mode used here, the cantilever is oscillated at or near its resonant frequency; a feedback loop maintains constant oscillation amplitude to keep tip-sample interaction constant as the tip crosses the surface of the material, by adjusting the vertical position of the scanner, which is recorded as the sample height. The resolution of the AFM is determined by the size of the tip; a wide tip may not be able to completely fit into every valley on a surface, and the resulting trace can therefore be 'smoothed out' compared to the actual topography.

Surface roughness of a film is often quantified along line profiles, as these are easier to measure. Two common parameters are  $R_a$ , the average deviation from the average height, or  $R_q$ , the root-mean squared deviation from the average height of the surface. Roughness in general is typically a function of area: a smaller area will have a smaller roughness, and as such an area should always be quoted with a roughness value for the purposes of comparison.

# Chapter 4

## Spin valve construction

To investigate the interaction of non-equilibrium spin and superconductivity, superconducting spin valves were constructed in a current perpendicular-to-plane (CPP) regime. This forces current through the central superconducting layer, driving it into a non-equilibrium state. The magnetoresistance of the spin valve is used to measure the spin behaviour of this current; with increased spin decay of the current, the spin is more randomised upon reaching the second ferromagnetic layer, leading to reduced magnetoresistance.

This chapter reports on the construction of the spin valves and modifications made to the structure throughout the investigation. For reliable results in later stages, the aim was to achieve consistent and clear giant magnetoresistance (GMR) effects whilst ensuring the spin valve went superconducting at measurable temperatures. Reliable and repeatable magnetic switching is essential for spin valves. However, there are many potential complications affecting the switching of these devices, and their general interaction with an external magnetic field.

### 4.1 Background

#### 4.1.1 Exchange bias

One of the most common ways to ensure reliable decoupled switching of the ferromagnetic layers is to use the exchange bias of an antiferromagnetic layer (AF) to ‘pin’ the switching of one adjacent ferromagnetic layer. This exchange bias is manifested as a ‘shift’ in the  $M(H)$  loops of the ferromagnet (F) along the  $H$  axis, away from zero. The magnitude of this shift,  $H_{\text{ex}}$ , changes with the degree of exchange bias. In this study, the antiferromagnet FeMn has been used, as it matches well with the Py ferromagnetic layer. The majority of this background focuses on the Py/FeMn system used in this investigation, as details of exchange bias tend to vary between different systems [49].

The antiferromagnetic phase of FeMn is the metastable face-centred cubic (fcc)  $\gamma$ -

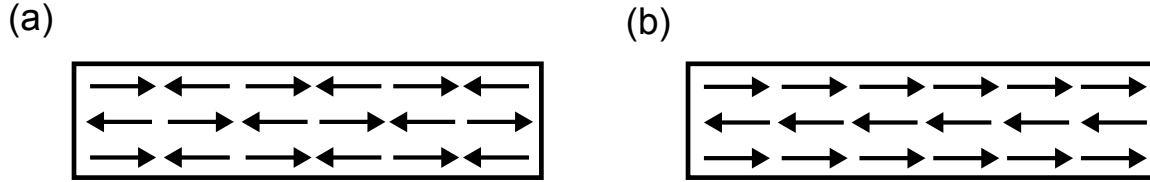


**Figure 4.1:** A simplified picture of (a) compensated and (b) uncompensated antiferromagnetic moments in planes. Interfacial roughness means that even compensated antiferromagnets will have points at an interface that are uncompensated.

phase rather than the equilibrium body centred cubic phase (bcc) [50]. In thin films, setting this phase usually involves using an ‘fcc conforming substrate’ - depositing the FeMn on an fcc material, which can either be the Py layer being pinned [51, 52], or a layer such as Cu if the Py is on top of the FeMn [53, 54]. Beyond this crystal structure requirement, the texture of the FeMn also has an effect on the magnitude of the exchange bias. FeMn has a  $\langle 111 \rangle$  spin structure [18], in which the spin of all atoms orient along a  $\langle 111 \rangle$  direction. This leads to cancellation along certain plain faces, such as (111); making this a compensated interface (Fig. 4.1), whereas other plane faces are not [52]. The (111) plane gives rise to the largest exchange bias for smallest coercive field [18], and hence crystallographic texture promoting that plane is beneficial, as observed in [52]. Note however, that other studies of the same system have found no dependence on texture [55].

Exchange bias is not the only effect expected when antiferromagnets are adjacent to ferromagnets: an increase in coercivity of the ferromagnetic layer ( $H_c$ ) is also observed [18, 56], as a result of coupling between the ferromagnet/antiferromagnet spins, causing the antiferromagnet spins to be irreversibly rotated as the ferromagnet spins change. The magnitude of this effect tends to inversely correlate with the strength of exchange bias, as layers providing greater exchange bias are more aligned due to greater internal exchange energy, reducing the amount they are rotated and therefore the degree to which they affect coercivity.

The thickness of both the ferromagnetic ( $d_{\text{Py}}$ ) and antiferromagnetic ( $d_{\text{FeMn}}$ ) layers is found to influence the magnitude of both  $H_{\text{ex}}$  and  $H_c$ : increasing  $d_{\text{FeMn}}$  past a critical thickness dramatically increases  $H_{\text{ex}}$  [18, 57] until some thickness (which differs study to study) [18, 50, 57] beyond which increasing  $d_{\text{FeMn}}$  either leads to no further effect on  $H_{\text{ex}}$ , or  $H_{\text{ex}}$  decreasing [58].  $H_c$  tends to peak and then decrease, as shown in Fig. 4.2(a), although it depends on orientation [18, 57]. This dependence on  $d_{\text{FeMn}}$  arises as a balance of a number of phenomena, which accounts for the slight differences between different systems, and include the changing grain and domain size, and the variation of interfacial exchange energy with  $d_{\text{FeMn}}$ , due to changing anisotropy energy [49, 59]. Increasing  $d_{\text{Py}}$  decreases both  $H_{\text{ex}}$  and  $H_c$  [50, 57, 60], as in Fig. 4.2(b). This inverse dependence arises as the the coupling is a purely interfacial effect.

Beyond the thickness of the layers, roughness and grain size may also affect  $H_{\text{ex}}$ .

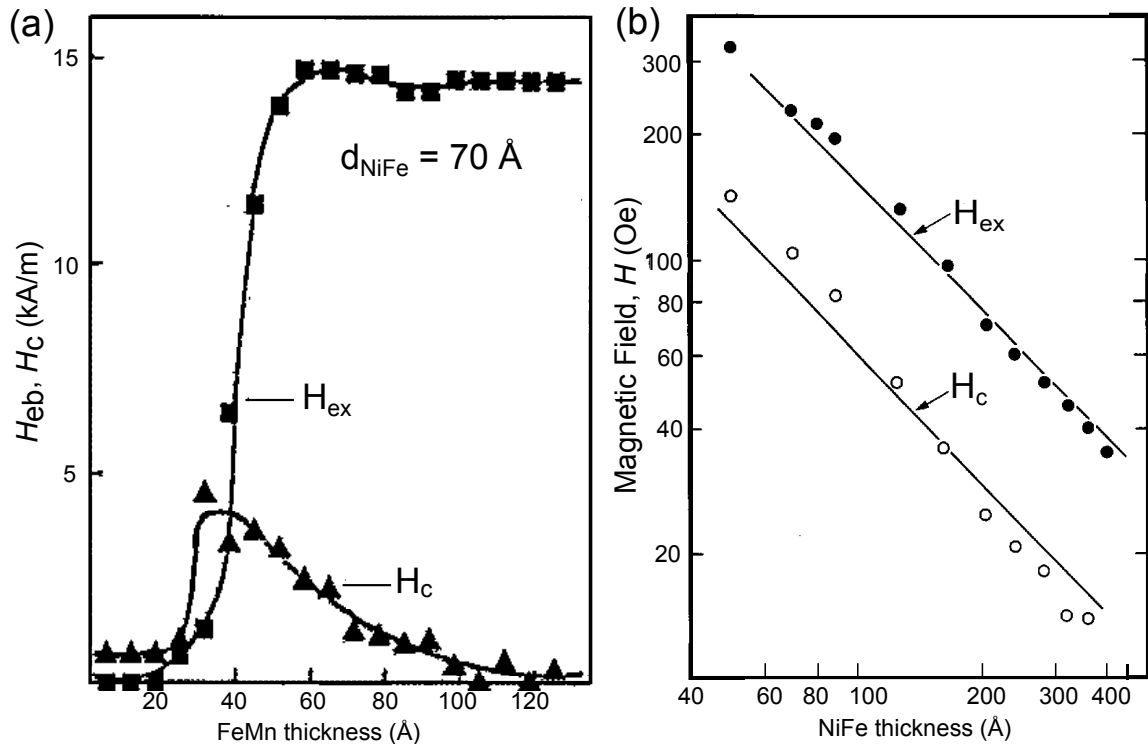


**Figure 4.2:** (a) Dependence of exchange bias  $H_{ex}$  and coercive field on  $d_{FeMn}$ , showing a sharp rise and then plateau at some thickness which also corresponds to a peak in  $H_c$ . For comparison,  $1 \text{ kA/m} \approx 12.5 \text{ Oe}$ . After [18]. (b)  $1/d_{Py}$  dependence of the exchange bias in a FeMn/Py system. After [57].

Experimentally increasing roughness has been shown to reduce  $H_{ex}$  [55, 61], although other works demonstrated no effect from roughness on  $H_{ex}$  [62], or reduced  $H_{ex}$  for smoother interfaces [63, 64]. Compensated interfaces, such as the (111) plane of FeMn may be less sensitive to roughness [49]. Interdiffusion and impurities at the interface also reduce  $H_{ex}$  [50]. The effect of grain size is difficult to determine considering the intrinsic relationship between it and other factors such as roughness and texture in thin films. However, it is suspected grains must be above a certain size for exchange bias effects to develop [49, 61, 65], although in general the dependence varies system to system [59].

## 4.1.2 Magnetic properties of thin films and devices

### 4.1.2.1 Permalloy in devices

Thin film properties, such as magnetic properties, often differ from those in the bulk. For instance, any compositional variation (common in thin films) in the ferromagnets could alter their properties. The ferromagnetic layers used here are permalloy, Py, a  $Ni_{80}Fe_{20}$  alloy, which is notable for having essentially zero magnetocrystalline anisotropy [66] and zero magnetostriction for films above 7 nm in thickness [67]. This small magnetocrystalline anisotropy means the crystallographic texture of Py does not have a large effect on its properties [68]. Furthermore, magnetocrystalline anisotropy tends to be minimal

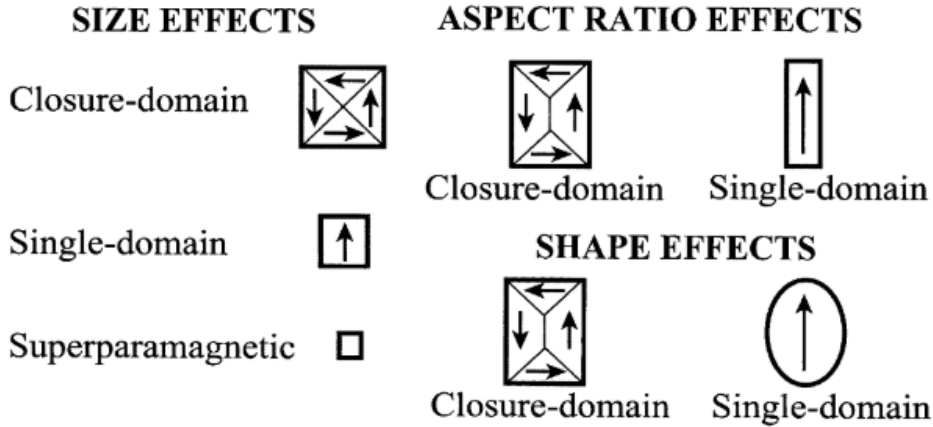


**Figure 4.3:** The effects of changing ferromagnet size and shape on domain structure, although not all experimental results conform to these expectations. From [70].

in polycrystalline films as the effect is averaged out over multiple grains of different orientation. Another composition dependent effect in Py was observed in [69], where the coercivity of  $\text{Ni}_{80}\text{Fe}_{20}$  decreased upon annealing, due to removal of defects, in contrast to other compositions.

The domain structure of a thin film ferromagnetic layer is dependent on the surrounding layers, thickness, and shape of the ferromagnet. In a F/AF bilayer, the antiferromagnet encourages the ferromagnet to be single domain, but as multiple magnetic layers and coupling between layers are considered, these domain structures become more complicated [71]. Domains are also affected by ferromagnet thickness due to the finite size and associated energy of domain walls. In Py, a transition from Néel to Bloch walls occurs as the thickness increases past 60 nm [15], and the domain wall width for each type is of the order of 500 nm [72]. As a result, devices fabricated with lateral dimensions less than a certain value demonstrate a change in domain switching behaviour, such as the 700 nm value observed in [73], or the 200 nm value in [74], below which single domain switching was observed. Ferromagnet shape also has an effect on domain structure; in [75] junctions with areas less than  $0.45 \mu\text{m}^2$  demonstrated sharper switching consistent with a reduced number of domains. Even without size effects, shape anisotropy of devices and nanowires causes effects such as increasing of coercivity as the width of wires decreases [76–78]. Larger aspect ratios and more ellipsoid shapes should encourage single domains (Fig. 4.3) [70], although no aspect ratio dependence of domain behaviour was observed in [75]. These changes in domain number and pattern affect the  $R(H)$  response of devices [73]: narrower, lower aspect ratio shaped devices encouraged the AP-state in [46, 73]. However, an AP-state was considered to be assisted by a large aspect ratio in [79]. Overall, the domain structure can be expected to vary in fabricated spin valve devices, affecting the  $R(H)$  response. Disagreement in the literature suggests this variation may not be entirely predictable.

At an interface between a ferromagnetic layer and another metallic layer, a ‘magnetic dead layer’ can form. While insignificant for bulk ferromagnets, in thin films these dead layers can be an appreciable fraction of the total ferromagnet thickness. The atoms in these dead regions are non-magnetic and do not contribute to the total magnetisation of the ferromagnet [80]. Such dead layers have been observed for various interface combinations, including Ni/Cu [81, 82], Py/Nb [80, 83], Py/Cu [62] and Py/Pt and Py/Ta [84]. Although not fully understood for pure metal ferromagnets, it is suspected the origin of such dead layers for alloy ferromagnets such as Py may be compositional changes or the effects of strain and lattice mismatch at the interfaces. Magnetic dead layers also modify the transport of currents passing perpendicularly to the interface [80], and therefore these layers do not contribute to giant magnetoresistance.

#### 4.1.2.2 Roughness

Texture and roughness of films and in heterostructures can affect the magnetic properties and hence the GMR of magnetic multilayers [85]. This can be difficult to directly relate, especially as interfacial parameters can be hard to directly measure [86]. Thick contact layers deposited for CPP devices can also be significantly rough and affect the structural and magnetic properties of a heterostructure, decreasing magnetoresistance [86]. Smoother contact layers are associated with improved magnetic properties such as reduced coercivities and increased squareness of  $M(H)$  loops [87]. These contact layers are required to be of certain thickness when pillar fabrication is via FIB milling and isolation [46], leading to a rougher layer which may affect GMR [45].

Film roughness may affect magnetoresistance of spin valve devices; however, the exact effect is uncertain as different studies oppose each other, with magnetoresistance decreasing [62, 86], increasing [88] and remaining unaffected [89] in different investigations. It has been suggested roughness could increase GMR by enhancing spin dependent scattering [88], although it has also been proposed that roughness increases scattering between both spin channels equally, increasing overall resistance and therefore decreasing magnetoresistance [86]. It is possible the opposing results observed may occur as a competition between the effect of roughness on spin scattering and on magnetic coupling, as with increased coupling there is less difference between the P- and AP-states [88]. Interlayer coupling of two ferromagnetic layers is heavily dependent on roughness and spacer layer thickness. At low spacer layer thicknesses and for roughnesses less than 0.4 nm, interlayer coupling appears to be dominated by exchange-like behaviour [90]. As roughness increases beyond 0.7 nm, instead magnetostatic, or ‘orange-peel’ coupling is more influential [62, 90]. Increased roughness increases the degree of this type of coupling if it is correlated between the two ferromagnetic layers, otherwise, random roughness reduces it. Spacer layer thicknesses beyond around 4 nm [90] have only minimal coupling between ferromagnetic layers, as shown in Fig. 4.4.

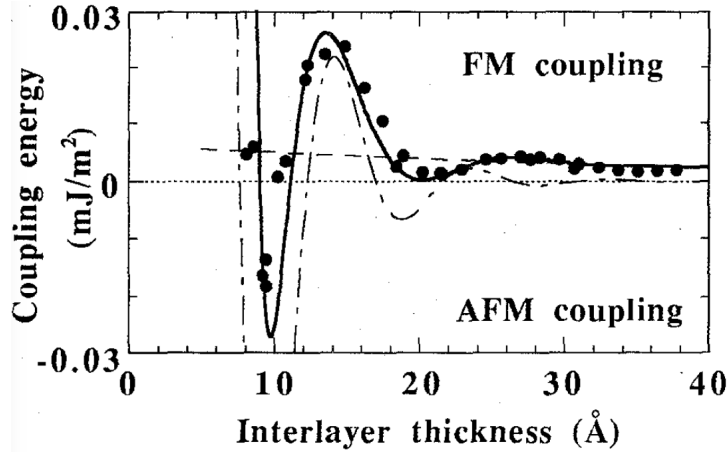


**Figure 4.4:** Dependence of interlayer coupling energy as a function of Cu spacer layer thickness for a Py(7)/Cu/Py(5)/FeMn(8) spin valve. Dashed line is magnetostatic coupling, dot-dashed is unstrained exchange coupling, solid line is magnetostatic plus strained exchange coupling. After [90].

#### 4.1.2.3 FIB and ion milling

Using FIB milling to create nanodevices has the advantage of flexibility [91] and potentially improved interfacial qualities as no breaking of vacuum is required during deposition [45]. However, ion milling is also likely to cause damage and implantation to samples.

A number of studies have attempted to estimate the depth over which damage and implantation of ions should occur as part of milling. For the technique used to fabricate nanopillars in this study, the sequence of cuts made is expected to lead to lateral implantation of less than 10 nm [45] for the high current beam of 100 pA, and minimal damage for the lower current beams, so is considered an effective process [46, 80]. Similarly, the penetration depth of  $\text{Ga}^+$  ions into Cu is also expected to be around 10 nm [91]. However, the damage done to structures may well be greater than these implantation values, up to 200 nm, due to the stress fields resulting from the implantation and etching [91, 92].

The change of magnetic properties of 30 nm of Py with different doses of  $\text{Ga}^+$  ions was investigated in [93], which showed domain wall pinning and movement changed significantly in a sample dosed at  $10^{16}$  ions/ $\text{cm}^2$ , and noticeably at a dose of  $10^{15}$  ions/ $\text{cm}^2$ . The increased lattice parameter resulting from implantation of ions inserting strain into the lattice was proposed as the main reason, although compositional, thickness and grain size changes may also have had an effect. Ion milling and patterning increasing coercivity has been observed elsewhere (Fig. 4.5) [74, 92, 94, 95], although the opposite effect has been recorded [96], in a study which also revealed milling had an effect on magnetic properties - including up to the point of removing ferromagnetism at room temperature - without fully milling through the 9 nm NiCr protective cap on top of the structure. In addition to the effects on Py, the exchange bias is also reduced by  $\text{Ga}^+$  implantation from FIB milling used to thin 10  $\mu\text{m}$  wide wires down to between 0.5-7  $\mu\text{m}$  [97], either due to reducing anti-

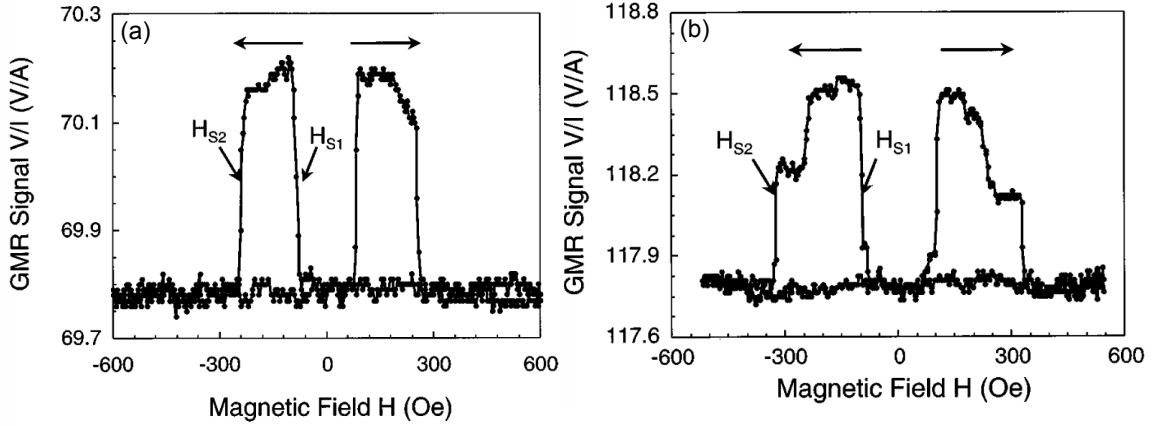


**Figure 4.5:**  $R(H)$  loops on CIP Py(10)/Co(10)/Cu(13)/Co(10)/Py(2) spin valves (all thicknesses in nm units) patterned with lithography and ion milling into bars of different widths showing increased coercivity in a narrower ion milled nanowire. (a)  $300 \text{ nm} \times 3 \mu\text{m}$  bar. (b)  $200 \text{ nm} \times 3 \mu\text{m}$  bar. From [74].

ferromagnetic order in the AF or reducing the coupling at the F/AF interface, preventing full antiparallel states. It is suspected this damage is from implantation through the top cap layer rather than lateral side penetration, although the cap layer in this case is 5 nm Ta rather than hundreds of nm of a contact layer such as Nb or Cu.

Fabrication of samples into multiple nanowires suggest that milling effects tend to be consistent [98], although the variation in grain size and crystallographic orientation within nanodevices may have a greater effect than in bulk films as there is reduced averaging [70].

## 4.2 Experimental Results

### 4.2.1 FeMn pinning

To develop the full spin valve structure, exchange bias between the top Py layer and the antiferromagnetic FeMn was required. In order to ensure this was present,  $M(H)$  loops of Py/FeMn bilayers were investigated. The complete structure was

$$\text{substrate/Nb/Cu/Py/FeMn/Nb.}$$

The base Nb was a 200 nm thick seed layer, for consistency with the required thickness for FIB milling of nanopillars at subsequent stages [46]. The cap Nb (to prevent oxidation of the magnetic layers) was 5 nm, the 10 nm Cu layer was present to minimise dead layers at the Nb/Py interface [62, 80, 83] and  $d_{\text{Py}} = 24 \text{ nm}$  and  $d_{\text{FeMn}} = 10 \text{ nm}$ . Thicknesses were based upon the successful spin valve structure in [14].

Figure 4.6(a) shows that the initial bilayers had relatively large coercive fields and no exchange bias, indicating a more detailed investigation into this structure was required. Subsequent investigation changed deposition conditions and layer thicknesses for the Nb

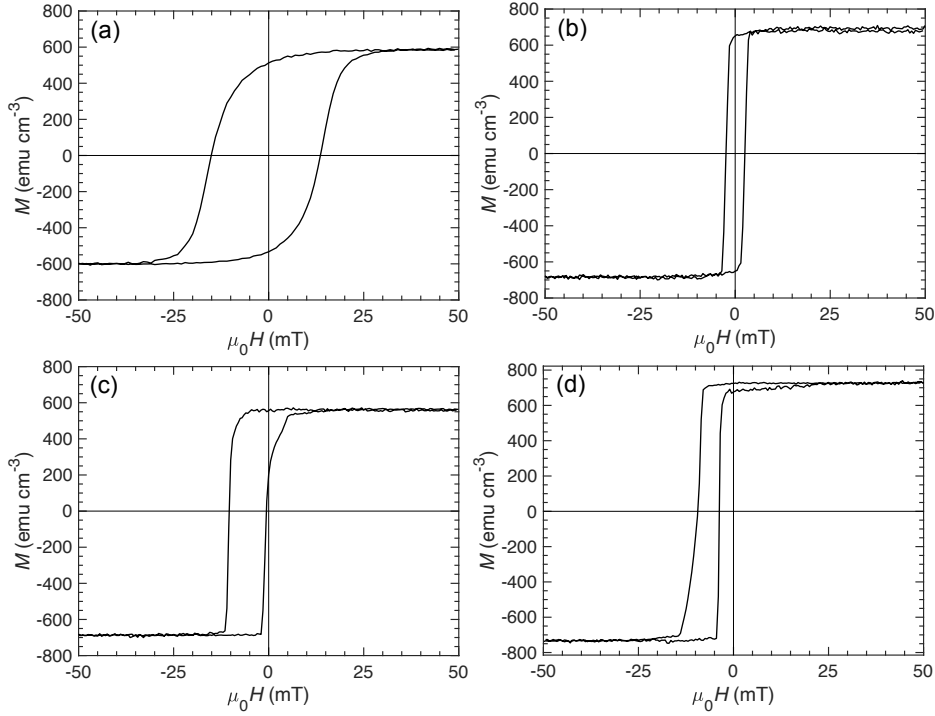


**Figure 4.6:**  $M(H)$  loops from Nb(200)/Cu( $d_{\text{Cu}}$ )/Py(24)/FeMn(10)/Nb(5) bilayers, where layer thicknesses are in nm units, all measured at 293 K. (a)  $d_{\text{Cu}} = 10$  nm; an early  $M(H)$  loop which does not demonstrate exchange bias. (b)  $d_{\text{Cu}} = 10$  nm; introducing magnets to the substrate table during depositions increased induced anisotropy of the Py leading to a more square loop, but did not lead to increased  $H_{\text{ex}}$ . (c)  $d_{\text{Cu}} = 20$  nm; thicker Cu layers were found to encourage exchange bias. (d) Depositing Cu at lower power also encouraged exchange bias, even with the original Cu thickness  $d_{\text{Cu}} = 10$  nm.

and Cu underlayers, as [14] suggested that the chosen values for  $d_{\text{Py}}$  and  $d_{\text{FeMn}}$  could demonstrate exchange bias. The other loops in Fig. 4.6 show the results of key changes made as part of this investigation; introducing magnets to the substrate table, so the substrates were in a strong field of 100 mT during deposition, reduced  $H_c$  and made the  $M(H)$  loops more square [Fig. 4.6(b)], as seen in [69]. Figure 4.6(c,d) show later bilayers, which successfully demonstrate exchange bias. In both cases, the key change was to the Cu layer: in (c) the Cu is thicker at 20 nm, and in (d) the Cu was deposited at reduced power (15 W rather than 30 W).

Figure 4.7 summarises the development of exchange bias across the bilayers deposited. The exchange bias is quantified using  $H_{\text{ex}}/H_c$ , as loops with small  $H_c$  could be shifted so that both critical fields were negative, and yet still have a smaller value of  $H_{\text{ex}}$  than a loop with large  $H_c$  that is minimally pinned. In Fig. 4.7(a), increasing  $d_{\text{Nb}}$  correlates with decreasing  $\mu_0 H_{\text{ex}}$ , with essentially no bias seen for  $d_{\text{Nb}} > 100$  nm, except for bilayers with modified Cu layers. In Fig. 4.7(b), comparing points with the same shape shows that increasing  $d_{\text{Cu}}$  increases exchange bias. Additionally, decreasing the power used to deposit the Cu layer also increases the exchange bias, for 10, 15, and 20 nm of Cu. This is effective enough that  $d_{\text{Cu}} = 10$  nm at 15 W demonstrates a similar level of pinning to

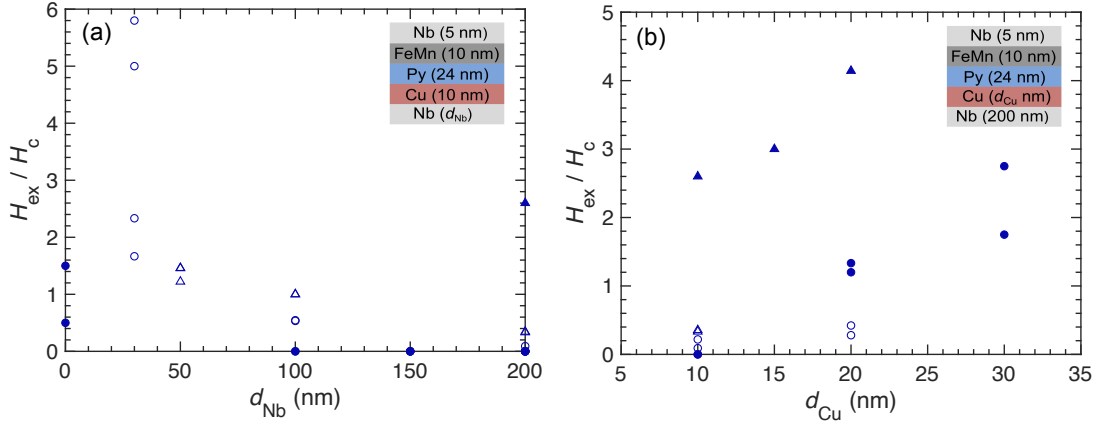


**Figure 4.7:**  $H_{\text{ex}}/H_c$  vs. layer thickness for bilayer structures with varying (a) base layer thickness  $d_{\text{Nb}}$  and (b) Cu underlayer thickness  $d_{\text{Cu}}$ . In both plots, filled shapes correspond to those deposited with magnets on the deposition table, and unfilled without. Circles show devices where Cu was deposited at 30 W, compared to triangles, where Cu was deposited at 15 W.

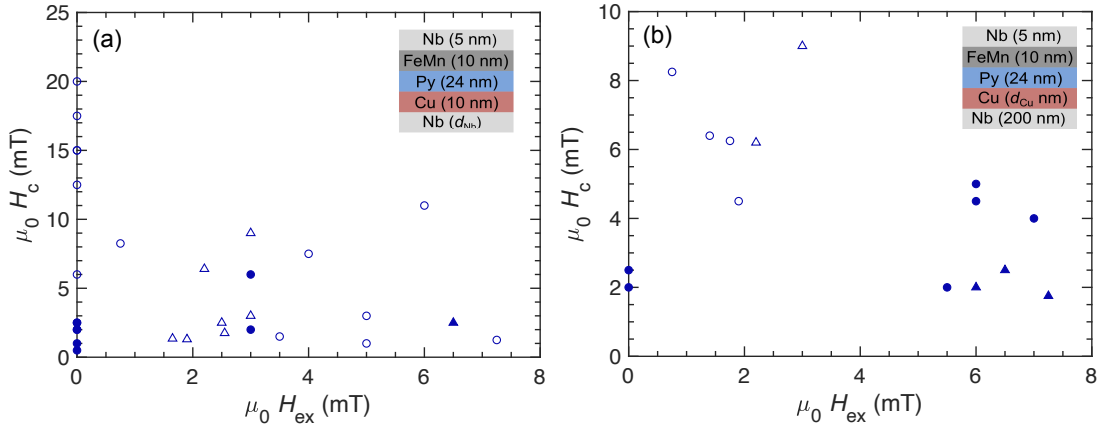


**Figure 4.8:**  $H_c$  vs.  $H_{\text{ex}}$  for the bilayer structures in Fig. 4.7, with those changing Nb layer ( $d_{\text{Nb}}$ ) in (a), and those with changing Cu layer ( $d_{\text{Cu}}$ ) in (b). Filled shapes again correspond to deposition with magnets, and unfilled without. Circles show devices where Cu was deposited at 30 W, compared to triangles, where Cu was deposited at 15 W.

$d_{\text{Cu}} = 30$  nm at 30 W. Overall, Figure 4.7 suggests that the thicker Nb contact layers, which were required for later fabrication procedures, caused the lack of exchange bias. This could be circumvented by using thicker Cu layers, or Cu deposited at lower power.

The reason why thick Nb layers disrupted the exchange bias in these structures is uncertain. As discussed in Section 4.1.1,  $\gamma$ -phase FeMn is the antiferromagnetic phase required for exchange bias, and therefore crystallographic structure and texture of the bilayers may affect  $\mu_0 H_c$ . However, Figure 4.8(a,b) show negative correlation between  $\mu_0 H_c$  and  $\mu_0 H_{\text{ex}}$  for most bilayers, which is as expected for an antiferromagnet [49]. It should be noted that in both Fig. 4.8(a) and (b) the correlation is helped by the reduced  $\mu_0 H_c$  of devices deposited in a magnetic field (filled shapes rather than open) due to the increased induced anisotropy, and those devices in a field with  $\mu_0 H_{\text{ex}} = 0$  mT also have

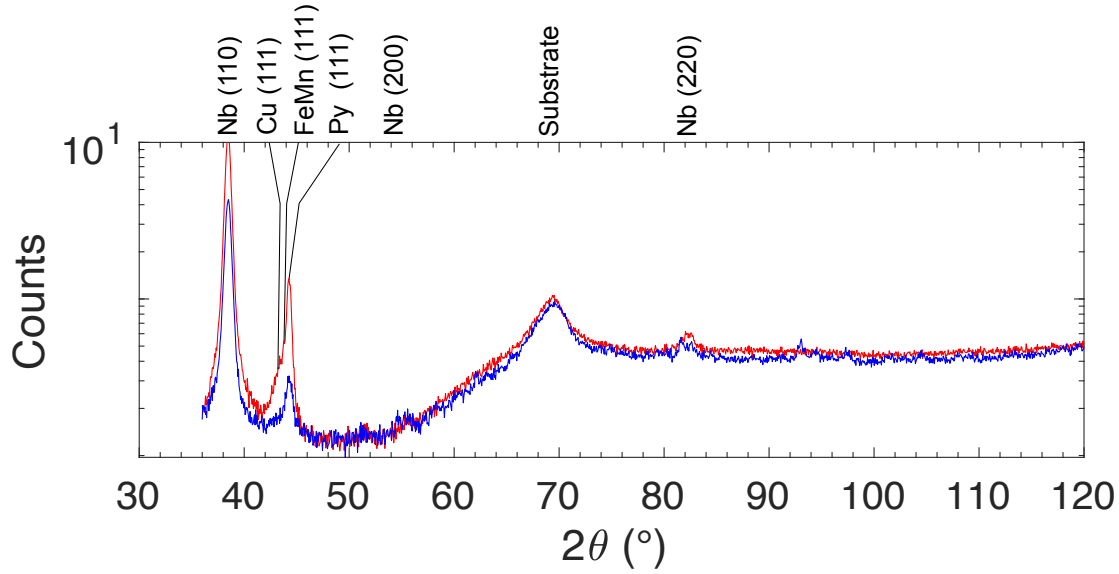


**Figure 4.9:**  $2\theta$  x-ray diffraction scans of two bilayers deposited with the Cu layer at 30 W (blue) and 15 W (red), using Cu  $K\alpha$  radiation and set at an offset of  $-1.5^\circ$ . All layers have the same thickness. The blue bilayer did not show exchange bias, whereas the red bilayer did. The peaks near  $93^\circ$  and  $98^\circ$  may correspond to the (222) planes of Fe and Ni respectively.

small values of  $\mu_0 H_c$ . An attempt was made using X-ray diffraction to determine if the crystallographic structure of FeMn changed from bcc to fcc between bilayers that did not and did demonstrate exchange bias (Figure 4.9). The small thickness of the different layers, combined with the fact Cu, Py, FeMn are all transition metal or transition metal alloys, and all possibly fcc, lead to difficulty distinguishing peaks for the separate layers, particularly in the blue, non-exchange biased bilayer. This is in line with observations made on similar systems [52, 61]. From the successfully biased bilayer (red), it is possible that the increased heights of peaks are a result of increased (111) texture, but there could be other reasons for this peak height, and without other clear peaks from these layers it is difficult to determine. Texture is important because of the different spin faces of FeMn, but the diffraction data collected is insufficient to conclude this is the reason for the trends in exchange bias.

A second potential explanation is interfacial roughness; thicker contact layers are likely to have increased roughness, which has in some cases correlated with decreased exchange bias [55, 61, 64]. Atomic force microscopy was used to measure roughness of different bilayer structures, using the changes discussed above (increased Cu thickness, reduced Cu deposition power, reduced Nb base layer thickness) as shown in Fig. 4.10(a). Extracting roughness values  $R_a$  and  $R_q$ , Fig. 4.10(b) shows that the devices with lowest roughness showed the largest degree of exchange bias. Compared to the base structure, the changes made that helped establish exchange bias are all associated with a lower measured roughness, including the thicker Cu layers, despite expectations that thicker Cu should lead to greater roughness [99]. The structure with lowest roughness used a 50 nm Nb

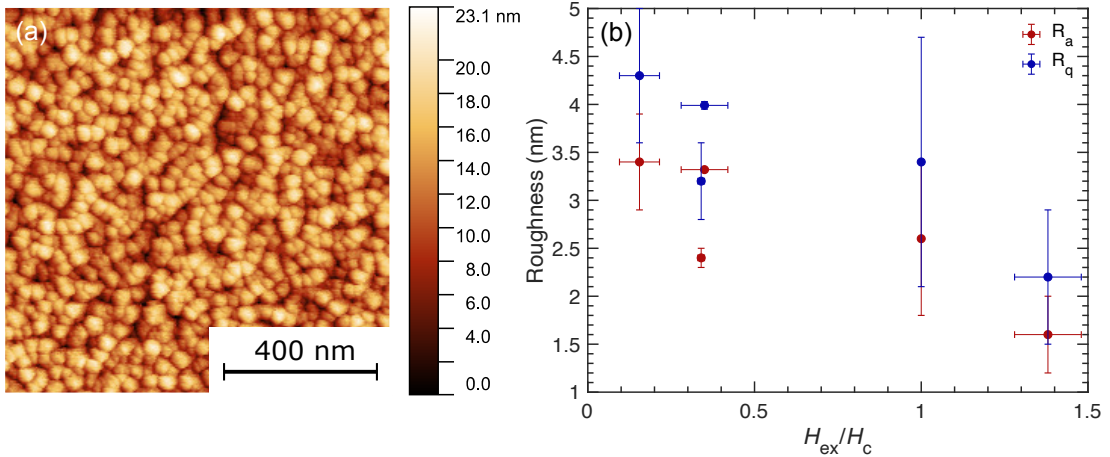


**Figure 4.10:** Example AFM scan ( $1 \times 1 \mu\text{m}$  area) from a bilayer Py/FeMn structure, part of a series which varied the underlying Nb and Cu layers to investigate the effect on exchange bias. (a) ‘Base’ structure, Nb(200)/Cu(10)/Py(24)/FeMn(10)/Nb(5), all layers deposited at 30 W. (b) Roughness quantified by both  $R_a$  and  $R_q$  for a series of bilayers, plotted against degree of exchange bias quantified with  $H_{ex}/H_c$ .  $x$ - and  $y$ -errors are standard deviations from measurements on different substrates with the same structure.

base, and 10 nm Cu deposited at 15 W. However, as shown in Section 4.2.4, increasing number of layers increases the roughness of the structure. Full spin valve structures, which feature more layers, are therefore likely to be rougher below the FeMn layer, yet always demonstrated exchange bias after changes were made to the Cu layer adjacent to the Nb base. It should also be noted that at later stages, when Nb contact layers were swapped for Cu contacts, the bias of the pinned layer increased, from averaging around 5 mT to averaging around 10 mT. However, it cannot be said if this is related to a decrease in overall roughness, or another effect such as more (111) texture propagating through the heterostructure. Therefore, whilst there is a correlation between decreasing roughness and the increased exchange bias, this may be an indirect effect of a different cause.

A simple estimate of exchange interface energy per unit area  $E_{ex} = H_{ex}M_Sd_{Py}$ , where  $M_S$  is the saturation magnetisation of the pinned ferromagnetic layer, can be used to compare different exchange-biased systems. The magnetisation of Py layers in these devices is consistently between  $600\text{--}800 \text{ emu cm}^{-3}$ , which agrees with other values from the literature [57, 100].  $700 \text{ emu cm}^{-3} = 7 \times 10^5 \text{ J T}^{-1} \text{ m}^{-3}$ , such that  $E_{ex} = H_{ex}M_Sd_{Py} = 1.26 \times 10^{-4} \text{ J m}^{-2}$ . Values for FeMn listed in [49] range between  $0.01\text{--}0.47 \text{ erg cm}^{-2}$ , translating as  $1 \times 10^{-3} - 47 \times 10^{-3} \text{ J m}^{-2}$ , at least an order of magnitude greater than those measured here. Comparison with other values from within our group such as in [101] suggests the value of  $H_{ex}$  can be around 90 mT for a Py/Nb/Py/FeMn spin valve, with 5.5 nm FeMn layers (and unknown thickness of Py), an order of magnitude greater than  $H_{ex}$  for the structures deposited here. The inverse relationship between  $H_{ex}$  and  $d_{Py}$  should be accounted for by the estimate however, so the unknown, but likely different  $d_{Py}$

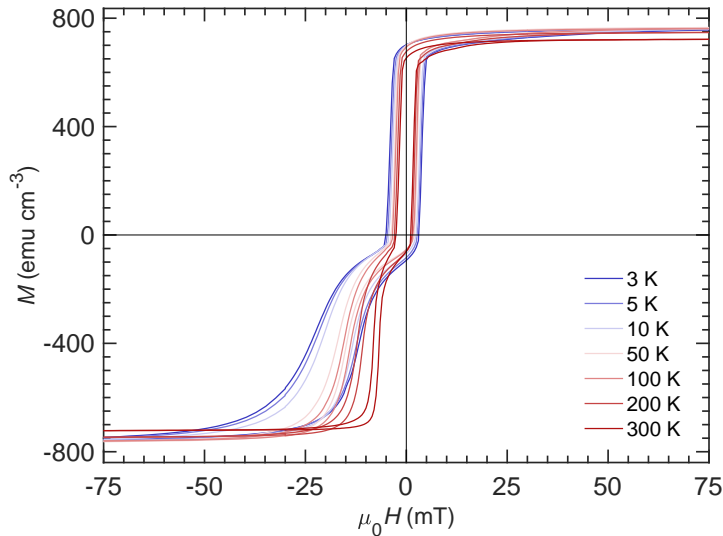


**Figure 4.11:**  $M(H)$  loops measured between 3-300K show an increase of exchange bias at lower temperatures, consistent with [51]. This is a full spin valve heterostructure, Cu(200)/Py(15)/Cu(10)/Nb(25)/Cu(10)/Py(15)/FeMn(10)/Cu(200) (all thicknesses in nm units) as used in the main part of the investigation.

value should not cause the difference in  $H_{\text{ex}}$ . Instead, this may indicate that a large part of the FeMn layer does not contribute to the exchange bias, which links with the difficulties in establishing exchange bias in the beginning. There are indications small ferromagnetic grains may not contribute to exchange bias [65], which could explain this. However, as grain size is a key source of roughness in thin films, the decrease in roughness observed in Fig. 4.10 is probably linked with smaller grains. This would be more in line with the results on polycrystalline films in [64], which suggested smaller antiferromagnetic grains provide greater interfacial coupling, but showed rougher films lead to increased  $H_{\text{ex}}$ . The different dependence in different systems may be a balance between the interfacial coupling and the uniaxial anisotropy in the FeMn, which would indicate that the uniaxial anisotropy in the FeMn in the structures deposited here may be surprisingly low. The negative correlation between  $H_c$  and  $H_{\text{ex}}$ , as expected, is considered to arise from increasing alignments of spins within the antiferromagnet; the low  $H_{\text{ex}}$  indicates the spins in FeMn are not fully aligned, with the variation potentially coming from different domains or interfacial spin clusters, which have previously been observed in some polycrystalline antiferromagnetic films [59].

Separately, the magnitude of  $H_{\text{ex}}$  noticeably increases with decreasing temperature, in agreement with [51]. This is shown for a full spin valve structure with Cu contact layers in Fig. 4.11.

Overall, the thick layers of Nb used as a base for these bilayers prevented exchange bias from appearing in initial structures. This was avoided by using thicker Cu layers, or depositing the Cu at lower power. To ensure the good pinning in complete spin valve structures, the standard ‘lower’ Cu layer used from this point was 20 nm deposited at

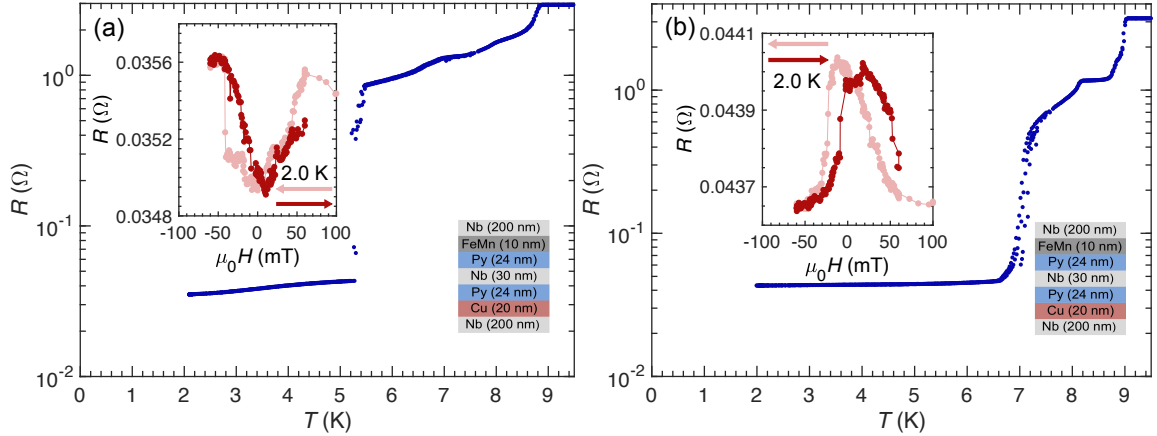


**Figure 4.12:**  $R(T)$  plots, with  $R(H)$  insets (top left), from two adjacent devices on the same substrate with Nb contact layers (heterostructure in bottom right insets). The  $R(T)$  plots demonstrate the uncertainty in identifying the superconducting transition of the central layer given the extended transitions of the contacts. The  $R(H)$  plots demonstrate the inconsistency between different devices. Arrows represent the sweep direction for each colour, starting at high positive fields.

15 W. The exact mechanism by which these Cu changes affected the exchange bias through is uncertain, but increasing exchange bias correlates with reduced roughness in these structures. It appears that even in structures with ‘working’ exchange bias, the value is lower than expected. These issues could be related to some parts of the FeMn not forming the antiferromagnetic  $\gamma$ -phase due to the underlying crystallographic texture, or alternatively interfacial spin clusters having different magnetic orientation.

## 4.2.2 Contact layers

Patterning nanopillars from these structures using FIB milling requires contact layers of a few hundred nanometres [45, 46]. Initially for this investigation, Nb contact layers were used rather than Cu. The Nb contacts were superconducting below their transition temperature, meaning a true four-point measurement could be performed on the pillar, as the ‘wires’ leading to the pillars themselves would have no associated voltage. They were deposited at 90 W, and the bottom contact was followed by a Cu layer below the spin valve, to help set the FeMn exchange bias of the top Py layer (Section 4.2.1), with another Nb contact layer on top of the FeMn.

However, with Nb contacts inconsistencies were observed between devices on the same substrate (insets, Fig. 4.12). Additionally, the Nb contact layers often lead to superconducting transitions drawn out over many degrees, with step-like features, due to the FIB processing of the contact layers (main figures in Fig. 4.12). A decision was made to switch to Cu contact layers, which was expected to allow easier interpretation of the superconducting state of the device (although as discussed in Section 6.2.3.2, this was not the case). With Cu contacts, the resistance of the wires leading to the devices could not be

ignored, becoming quasi-four point measurements instead. This introduced factors complicating the GMR response during measurements (see Sections 5.2.4 and 5.2.5). Finally, because of the variable voltage distribution inside Cu (compared to a superconductor), there exists the possibility of nonuniform current distribution through the device, which has affected magnetoresistance of CPP devices previously [102]. Previous finite element analysis on a nanopillar spin valve with Cu contact layers [46] suggests the voltage distribution is sufficiently uniform to give a reliable vertical current flow through the pillar [Fig. 4.13(a)]. Similar analysis was performed on a nanopillar with Py contacts in [79].

Current bunching, an increase of resistance when a current path is significantly narrowed, is also a potential issue with non-superconducting contacts [28]. An estimate of the current bunching was performed by considering a simple toy model of the resistances that would contribute to a typical measurement, considered as 3 resistances in series, corresponding to the wide wire sections each side of the pillar, the thinned wire sections each side of the pillar, and the pillar itself, such that  $R_{\text{tot}} = R_{\text{pillar}} + R_{\text{wide}} + R_{\text{thinned}}$ , as shown in Fig. 4.13(b). Here,  $R_{\text{wide}} = \frac{\rho_{\text{Cu}}(L-l)}{wd} = 0.1391 \Omega$  where  $L$  and  $l$  are lengths of the wide and thin parts of the wire,  $w$  is the width of the wide part, and  $d$  the thickness of the Cu contacts, 400 nm total, assuming all the current travels in the Cu.  $\rho_{\text{Cu}} = 6.18 \times 10^{-9} \Omega \text{m}$  is the resistivity of Cu measured from a van der Pauw measurement on a 300 nm thick film.  $R_{\text{thinned}}$  contains the contribution from current bunching, following the procedure and calculations from [103] to estimate

$$R_{\text{thinned}} = \frac{\rho_1 h_1}{2ad} + \frac{\rho_2 R_c}{4\pi d} + \frac{\rho_2 h_2}{2bd}. \quad (4.1)$$

Here,  $\rho_1 = \rho_2 = \rho_{\text{Cu}}$ ,  $d$  is the contact layer thickness as before and the ratios  $a/h_1$  and  $h_2/b$  are the aspect ratios of the regions over which the current change takes place. Both are taken as 1 for these devices, as an average estimate, which leads to  $R_c \approx 3.2$  from [103], which will not change more than a factor of 3 (the change of  $R_c$  if  $a/h_1$  were off by an order of magnitude). With these values,  $R_{\text{thinned}} = 2 \times 0.04 \Omega$ , where the factor of two accounts for possible bunching effects either side of the pillar.

The total resistance separate from the pillar therefore is around 0.22  $\Omega$ . Comparison of otherwise identical structures with Cu and superconducting Nb contact layers suggests the difference in resistance is between 0.16 – 0.27  $\Omega$ , where the variation is likely due to the slightly different FIB processing of each device. This agreement suggests this model is a reasonable estimate for current bunching, such that the effect is expected to be confined to the contacts and not affect the current flow in the pillar, as the contribution is from the thinning of the main wire, rather than the change into the pillar. Using standard resistance values from measurements, resistance of the devices alone is therefore in the range  $\approx 0.08$ -0.48  $\Omega$ . Considering the typical measurement current of 50  $\mu\text{A}$ , the voltage across the pillar is therefore  $\approx 4.5 - 24 \mu\text{V}$ .

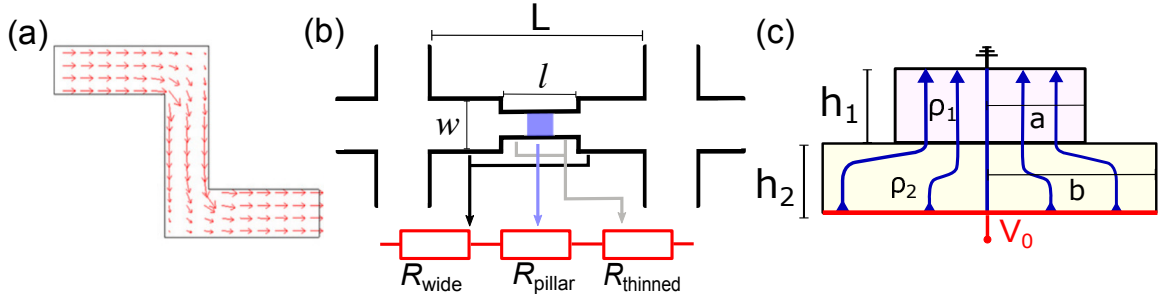


**Figure 4.13:** (a) Finite element analysis of current flow in a nanopillar with Cu contact layers, from [46]. (b) Schematic diagram with labels representing the area under measurement, with wide wires leading to the region thinned by FIB, which contains the pillar. (c) The relevant parameters used in the current bunching estimate. After [103].

### 4.2.3 Cu buffer layers and Py

Initial spin valves did not have central Cu layers between Py and Nb. However, this could lead to magnetic dead layers forming at the interface between Nb and Py [62, 80, 83], which would have detrimental effects on the magnetoresistance and also on the superconducting properties of the spin valve, and so Cu buffer layers were added early in the investigation. These layers were chosen to be 10 nm each for comparison with [14], which added such layers and observed an increase in magnetoresistance. [14] used 10 nm so that for any thickness of Nb between these Cu layers (including  $d_{\text{Nb}} = 0$  nm) the ferromagnetic layers should definitely be decoupled [53, 60].

Figure 4.14(a) shows the impact of changing the thickness of these Cu layers ( $d_{\text{Cu}}$ ) on the magnetoresistance in the normal state for a range of devices. Initially, consider the two different data sets (circles and triangles) separately; each show a lower value for  $d_{\text{Cu}} = 0$  nm, then a peak at 5 nm before a slow decrease with increasing Cu. This is as expected, showing that the significant magnetic dead layers that form for a Py/Nb interface decrease magnetoresistance, and that interface scattering of Py/Cu + Cu/Nb is less than that of Py/Nb. The slow decrease in  $A\Delta R$  as the Cu increases beyond 5 nm is due to the long spin diffusion length in Cu [79, 104, 105]. The large errors (which here are standard deviations from different devices on the same substrate) and comparison between the two data sets demonstrate the significant scatter in results present in these fabricated devices. This is particularly large for the open triangle data points, which were all deposited as part of the same deposition, suggesting the fabrication processes such as milling and FIB milling make a large contribution to the scatter (Section 5.2.6).

Figure 4.14(b) shows  $A\Delta R$  increasing with increasing  $d_{\text{Py}}$ . Similarly to Figure 4.14(a), there is significant scatter in the data, but overall a positive trend is seen, as expected [60]. In this investigation 15 nm of Py is used for the ferromagnetic layers rather than 24 nm, which gives the largest  $A\Delta R$ ; this is because a balance is needed between  $A\Delta R$  and  $T_c$  of the devices, which decreases with increasing  $d_{\text{Py}}$  (Section 6.2.4.1).

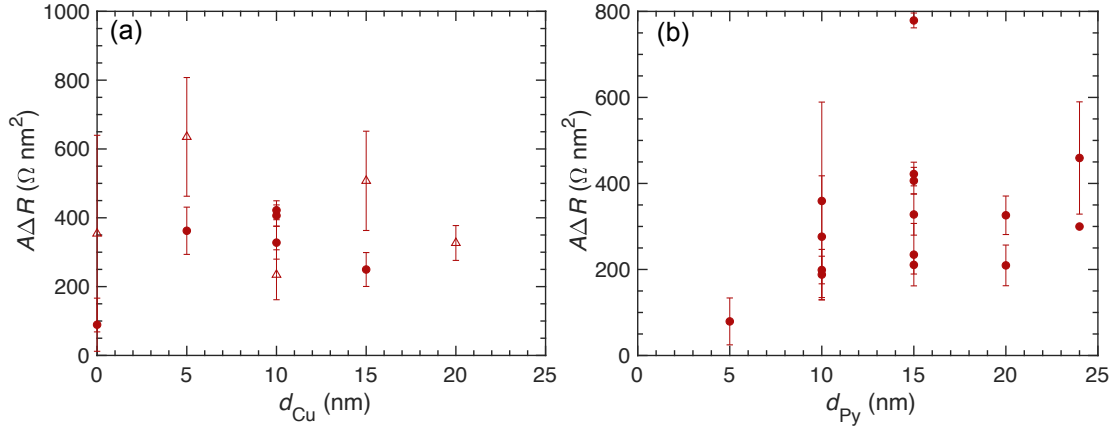


**Figure 4.14:** (a)  $A\Delta R$  vs.  $d_{\text{Cu}}$  of the Cu buffer layers between the Nb spacer and Py layers. Filled circles correspond to sequential depositions when only two structures could be deposited per deposition. Open triangles are data points from a single deposition run, after increasing the number of magnets on the substrate table. (b)  $A\Delta R$  vs.  $d_{\text{Py}}$  showing an increase of magnetoresistance with F layer thickness, as expected after results such as those in [60].

#### 4.2.4 Roughness

The roughness of different layers as the spin valve structures were built up has been characterised; in this case, structures are like Cu contact layer spin valves, but incomplete, such that the structure terminates at a certain layer.

The data show a gradual increase of roughness as the number of layers increases, from  $R_a = 2.5$  nm after the Cu contact layer to  $R_a = 4.0$  nm after the upper Cu buffer layer. No significant difference is observed between the two different Nb spacer thicknesses investigated (20 nm and 30 nm). Comparing with external values, the  $R_q$  value for a 200 nm thick Cu contact in [46] is only 0.5 nm over  $1 \mu\text{m}^2$ , much smaller than the  $R_q = 3.5$  nm value found for the base Cu here. The roughness of these structures is also much greater than for 100 nm Nb contacts in [87] which have  $R_a = 0.79$  nm over  $1 \mu\text{m}^2$ , and structures in [52], although in that case interface roughness was measured with XRR, and these results are therefore not directly comparable. However, it indicates the structures of this investigation may be more rough than those of other investigations, which would have an impact on results.

Beyond the effect on the pinning of the antiferromagnetic layer, it has also been shown that roughness can affect the magnetic properties of Py such as the coercive field [87], further contributing to property variation between substrates. AFM scans performed on a few full spin valve structures over  $500 \times 500$  nm areas have  $R_a = 1.4 \pm 0.3$  nm. This suggests that roughness within single pillars, which usually have areas of this order of magnitude, should be minimal, much less than the thickness of any single layer in the structure, and so not cause significant layer disruption. Roughness is therefore unlikely to be responsible for variation between devices on a single substrate.

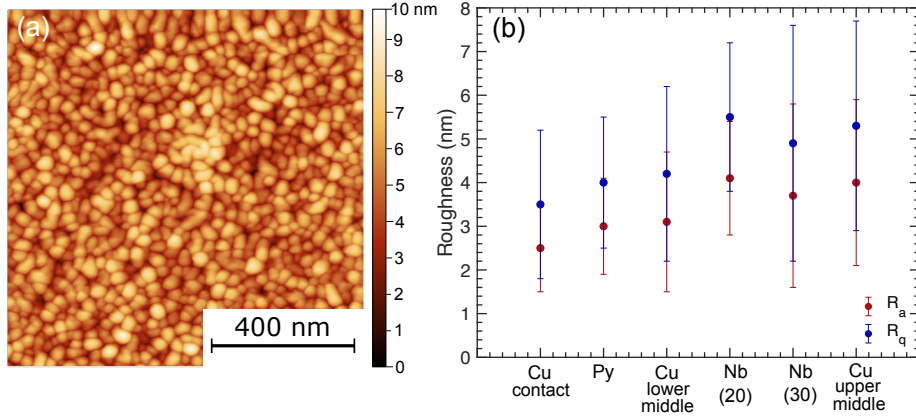


**Figure 4.15:** (a) A  $1 \mu\text{m} \times 1 \mu\text{m}$  tapping AFM scan performed on a ‘built-up’ heterostructure terminating on the lower middle Cu layer, such that the structure is Cu/Py/Cu. (b) Roughness values  $R_a$  and  $R_q$  from this series of ‘built-up’ structures. The  $x$ -label corresponds to the top deposited layer, such that each represents the standard spin valve heterostructure but terminated at different stages of the deposition. The most built up structure features the 10 nm Cu buffer layer on top of a 30 nm Nb layer.

#### 4.2.5 Effect of FIB on $R(H)$

One of the key causes of variation between different devices on the same substrate is likely to be the FIB milling performed to create each nanopillar, as the only fabrication process that differs between devices. Whilst consistency was striven for as much as possible, differences in between pillars was noticed during fabrication, such as some requiring different beam doses, due to different pillar sizes.

One of the most noticeable differences between devices on a substrate could be the variation in switching behaviour, with some devices demonstrating behaviour that seems to indicate coupling between the ferromagnetic layers [62], or very slow domain switching rather than the ‘cleaner’ switching demonstrated by the majority of devices, as shown in Fig. 4.16.

However, no correlation has been found between the FIB parameters used and a deviation in magnetic behaviour, as this behaviour occurs in even on substrates where all devices are designed to be equal. Conflicting results about the effect of FIB milling are reported in the literature (Section 4.1.2.3), and although it is suspected that FIB contributes to the variation in magnetic behaviour here, nothing systematic has been found that can confirm this.

The effect of FIB is visible in the cuts made, and the shape of the material left behind. Some anomalously small results may be linked to the state of the pillars after FIB milling, although other pillars which appear damaged can demonstrate good results. One way that the FIB cuts may affect the magnetic switching is through the stray fields emerging from the Py in the wires. Considering the wires as a line source of field [106],  $B = \mu_0 M_S d_F / 2\pi r$ , where  $M_S$  is the magnetisation of the Py, taken as  $7 \times 10^5 \text{ Am}^{-1}$ ,

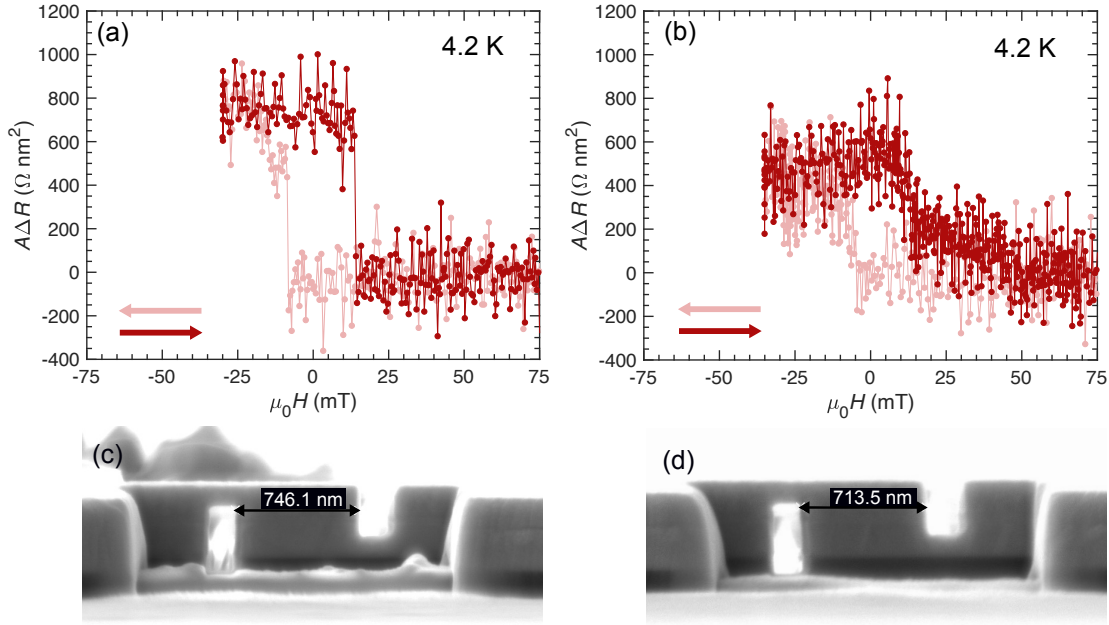


**Figure 4.16:** (a,b) Minor  $R(H)$  loops from devices on the same substrate, with  $d_{\text{Nb}} = 19$  nm, showing a difference in switching characteristics, between extremely sudden switching in (a), and domain or coupling based switching in (b). Arrows represent the sweep direction for each colour, starting at high positive fields. (c,d) SEM images after FIB processing of the devices, showing there is no visual difference between devices with different magnetic characteristics.

$d_F = 15$  nm the thickness of Py, and  $r$  is the width of the cut, the distance between the edge of the wires and the pillar, 150 nm (note however that the pillar length is typically  $> 400$  nm and often around 800 nm, meaning there is a significant difference between the stray field experienced by different parts of the pillar). With these values,  $B = 14$  mT from one Py layer, which indicates that there should be a large effect from FIB cut size on switching, but increasing the cut size to  $r = 300$  nm rather than 150 nm had no effect on magnetic behaviour. The fact that such a large apparent flux density does not appear to have an effect on the switching of the pillar suggests this estimate is not entirely suited to this scenario.

### 4.3 Conclusions

In this chapter, the dependence of exchange bias on the base layers of the heterostructure was investigated, and has successfully ensured reliable switching of complete spin valve devices used for the rest of this investigation. Other aspects of the structure have also been characterised, including the roughness, dependence of magnetoresistance on Cu buffer layer and Py layer thickness, and a toy model of the voltages across the nanopillar devices, including an estimate of the effect of current bunching on the total resistance.

The key results from this chapter used going forward are:

- Cu base layers of 20 nm deposited at 15 W should be used with Nb contacts.
- A switch was made from Nb to Cu contacts to help identify the transition of the central superconducting layer.
- Including Cu buffer layers between the Py and central Nb increases the magnetoresistance of the spin valve. 5 nm would be sufficient for this.
- Magnetoresistance of the spin valve increases with increasing Py. Balancing magnetoresistance with superconducting transition temperature,  $d_{\text{Py}} = 15$  nm has been chosen.
- The roughness in the structure increases layer by layer, but should be insufficient over  $500 \text{ nm} \times 500 \text{ nm}$  areas to cause device variation on a single substrate.



# Chapter 5

## Magnetoresistance in normal state spin valves

In this chapter, the normal state magnetoresistance of the current-perpendicular-to-plane (CPP) Py/Cu/Nb/Cu/Py/FeMn spin valves has been investigated with reference to the theory behind CPP magnetoresistance, and the values of magnetoresistance and spin diffusion length of normal state Nb compared to those reported in the literature. Factors affecting the magnitude of these values are considered.

### 5.1 Background

#### 5.1.1 CIP vs CPP

There are two distinct current transport regimes through a spin valve; current-in-plane (CIP), in which the current travels through the central spacer layer, parallel to the plane of the layers, and current perpendicular-to-plane (CPP) in which the current follows a path perpendicular to the layers, passing through each one. Typically, CPP devices are more complicated to fabricate [107], requiring some structure that forces the current to take the correct path. However, CPP devices have intrinsically higher giant magnetoresistance (GMR) [70] and also provide more direct access to the parameters affecting the magnetoresistance [28, 108].

This comparison between CIP and CPP has been shown experimentally in magnetic multilayers, which feature repeating units of ferromagnetic/normal metal (F/N) layers. In [107, 110], Co/Ag multilayers were experimentally compared in CIP and CPP configurations confirming that the CPP magnetoresistance is greater. Similar results have been reported for Fe/Cr and Co/Cu multilayers [111], and Co/Cu multilayers again in another study (Fig. 5.1) [109], which confirmed that CIP structures were dependent on mean free path, whereas CPP were not. CPP devices are expected to be less dependent on magnetic inhomogeneities than CIP, as mean free path is not fundamental to them,

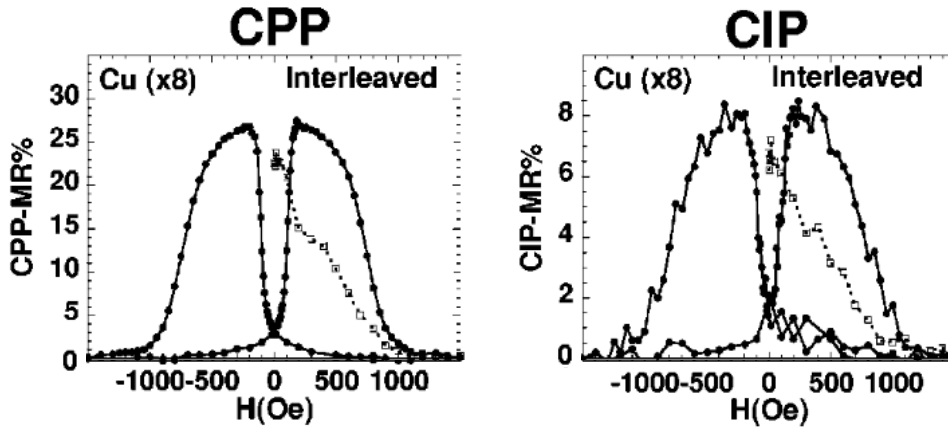


**Figure 5.1:** Comparison between magnetoresistance for CPP and CIP  $[\text{Co}(6)/\text{Cu}(20)/\text{Co}(1)/\text{Cu}(20)]_8$  (all thicknesses in nm units, 8 repeats of the structure) multilayer structures. The CPP structure was measured using superconducting Nb ‘cross-strips’. The CPP device has magnetoresistance around 3.5 times that of the CIP structure. From [109].

but more dependent on structural and patterning changes [70]. Comparisons between CIP and CPP geometries of spin valves rather than multilayers are much more rare: [112] varied spacer layer resistivity and found the absolute resistivity change was the same in CIP and CPP, but did not compare magnetoresistance values. [102] found the difference between parallel and antiparallel states increased with magnetic free layer thickness for both CIP and CPP regimes of the same structure.

### 5.1.2 Modelling CPP magnetoresistance

Two main models exist for describing transport in CPP spin valves; the ‘two current series resistor (2CSR)’ model [113], and the more complete theory developed by Valet and Fert [108], which reduces to 2CSR for particular materials properties.

An early attempt to model giant magnetoresistance, distinguishing between CIP and CPP was made in [113], based upon the fields in the system. Importantly, spin flipping within the spin valve was neglected, which allowed the spin of majority and minority electrons to be considered as two separate non-interacting spin currents. These parallel currents (Fig. 5.2) are scattered in the bulk and interface of every layer, such that the total resistance was effectively a sum of series resistances, each of  $\rho d$  where  $\rho$  is the resistivity and  $d$  thickness of each layer. This ‘two current series resistor’ (2CSR) theory found that unlike GMR in CIP devices, the mean free path  $\lambda$  was not a key parameter in the CPP regime.

Valet-Fert (VF) theory [108], based upon the Boltzmann transport equation, expanded upon 2CSR theory by additionally considering spin flipping, occurring both in the bulk and at (infinitely thin) interfaces, requiring the spin diffusion length  $l_{sf}$  in both normal ( $l_{sf}^N$ ) and ferromagnetic ( $l_{sf}^F$ ) layers. VF theory assumes a single conduction band and

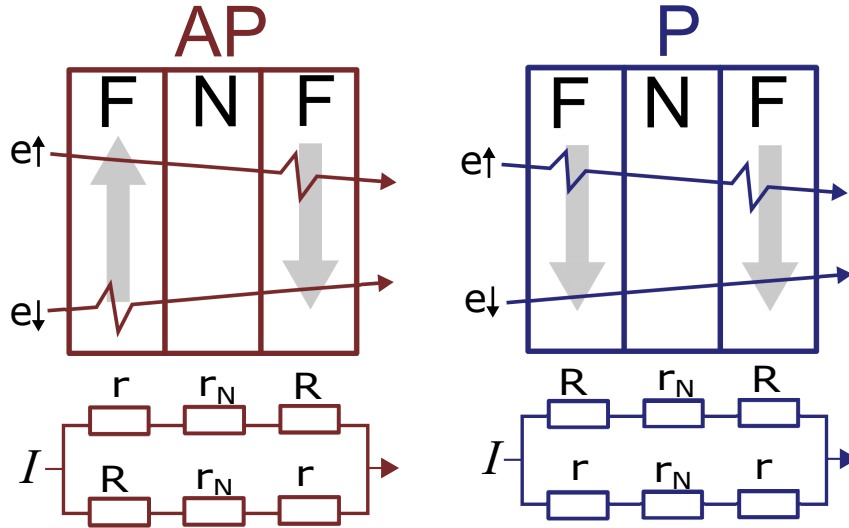


**Figure 5.2:** A schematic diagram of the 2CSR model for a spin valve, as described in [113]. The two spin current directions are considered to flow independently, in parallel with each other. The resistances for each current from every layer of the spin valve are added in series: large resistances,  $R$ , when the spin of the current and ferromagnet are different; smaller resistances,  $r$ , when the spins match; and  $r_N$  for the resistance of the central spacer layer. After [28].

simple Fermi surfaces in both the N and F metals, and shows that when  $l_{sf}^{F,N} \gg \lambda^{F,N}$ , the current densities may be linked to electrochemical potentials in terms of two macroscopic parameters, conductivity  $\sigma^{F,N}$  and  $l_{sf}^{F,N}$ . When the thickness of the layers is much smaller than their spin diffusion lengths - i.e. minimal spin flipping occurs in the layers - VF theory simplifies to 2CSR. GMR results are predicted by considering spin accumulation either side of F/N interfaces in multilayer structures, meaning different structures have different boundary conditions, leading to different equations for GMR.

VF theory equations for Py-based spin valves containing a Cu spacer with central layer inserts [Fig. 5.3(a)] were presented in [53], which suggested that for scattering dominated by the bulk of the inserted N layer of thickness  $d_N$ , the areal magnetoresistance  $A\Delta R$  of the device is:

$$A\Delta R \propto \frac{\exp(-d_N/l_{sf}^N)}{(AR_0 + AR_N)} \quad (5.1)$$

where  $AR_0$  is the areal resistance of the device without the central N layer, and  $AR_N$  is the areal resistance associated with the N layer only. More completely, when interface scattering is considered by the introduction of an interface layer I [with associated thickness  $d_I$ , resistivity  $\rho_I$  and spin diffusion length  $l_{sf}^I$ , see Fig. 5.3(b)]:

$$A\Delta R = 2(\beta\rho_{Py}^*l_{sf}^{Py} + \gamma AR_{Py/Cu}^*)^2 \left( \frac{1}{D_P} - \frac{1}{D_{AP}} \right) \quad (5.2)$$

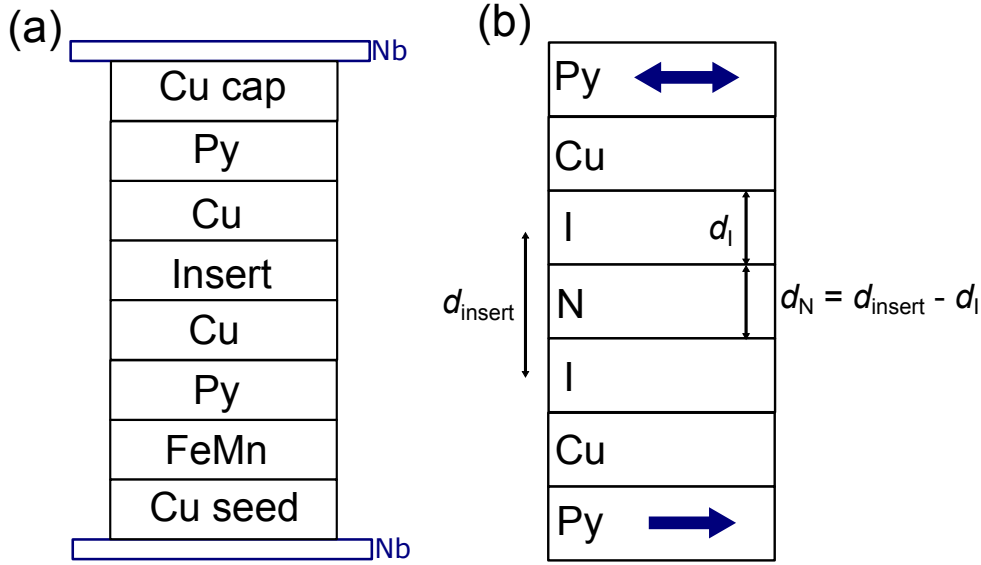


**Figure 5.3:** (a) The structure used in [53], consisting of a basic FeMn/Py/Cu/Py spin valve with an inserted layer, to use the magnetoresistance of the inserted device to test the spin flip length of the insertion, either a single metal or metallic multilayer. The Nb above and below the device are superconducting Nb ‘cross-strip’ contacts. (b) The layers considered in the areal magnetoresistance equations. The interface layers ‘I’ are of a small thickness taken from the thickness of the inserted layer, such that  $d_N = d_{\text{insert}} - d_I$ , and are used to represent the possibility of spin flipping at the interface.

where

$$D_{AP,P} = \rho_{\text{Py}}^* l_{sf}^{\text{Py}} + AR_{\text{Py/Cu}}^* + \rho_{\text{Cu}} d_{\text{Cu}} + \left( \frac{AR_{\text{Cu/N}}}{\delta} \right) \left( \frac{\frac{AR_{\text{Cu/N}}}{\delta} + (\rho_{\text{Nb}} l_{sf}^{\text{Nb}}) \coth(\delta) f_N^{AP,P}}{(\rho_{\text{Cu/N}}/\delta) \coth(\delta) + (\rho_{\text{Nb}} l_{sf}^{\text{Nb}}) f_N^{AP,P}} \right)$$

and

$$f_N^P = \tanh \left( \frac{d_{\text{Nb}}}{2l_{sf}^{\text{Nb}}} \right)$$

$$f_N^{AP} = \cosh \left( \frac{d_{\text{Nb}}}{2l_{sf}^{\text{Nb}}} \right).$$

In these equations,  $\rho_{\text{Py}}^{\uparrow(\downarrow)}$  is the resistivity of electrons with majority (minority) spins in the ferromagnet. Similarly,  $AR_{i/j}$  is the areal resistance between two adjacent layers  $i, j$ , and  $AR_{\text{Py/Cu}}^{\uparrow(\downarrow)}$  are the spin dependent interface resistances. These spin dependent parameters are combined into  $\rho_{\text{Py}}^* = (\rho_{\text{Py}}^{\uparrow} + \rho_{\text{Py}}^{\downarrow})/4$  and  $AR_{\text{Py/Cu}}^* = (AR_{\text{Py/Cu}}^{\uparrow} + AR_{\text{Py/Cu}}^{\downarrow})/4$ , and the anisotropy parameters,  $\beta = [(\rho_{\text{Py}}^{\downarrow} - \rho_{\text{Py}}^{\uparrow})/(\rho_{\text{Py}}^{\downarrow} + \rho_{\text{Py}}^{\uparrow})]$  and  $\gamma = [(AR_{\text{Py/Cu}}^{\downarrow} - AR_{\text{Py/Cu}}^{\uparrow})/(AR_{\text{Py/Cu}}^{\downarrow} + AR_{\text{Py/Cu}}^{\uparrow})]$ , which represent the spin anisotropy within the ferromagnet and at the interface respectively. Finally,  $\delta$  is an interface flipping parameter, representing the probability of spin flip at the interface: probability,  $P = [1 - \exp(-\delta)]$ .

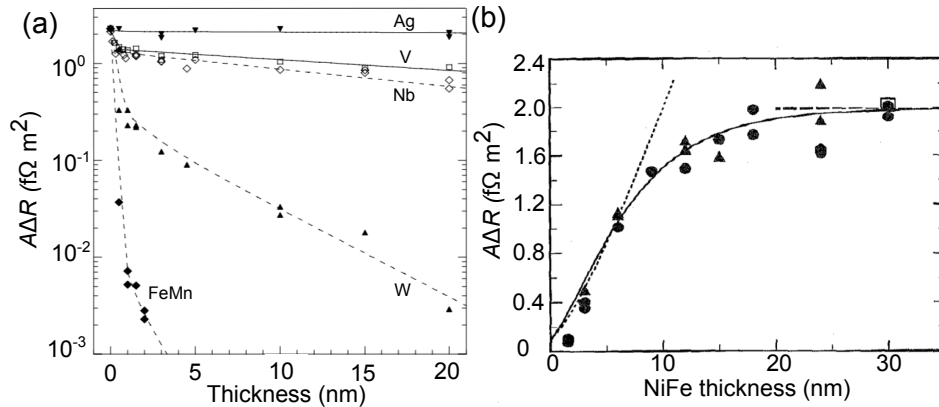


**Figure 5.4:** (a) Spin decay with  $d_N$  for Ag, V, Nb, W and FeMn, measured by inserting these layers into a spin valve between Cu spacers, showing how the different decay lengths of each material have a strong impact on the magnetoresistance of the device. The initial drop for each spacer is associated with the formation of interface layers, followed by a slower decrease representing the spin loss through the bulk. Adapted from [53]. (b)  $A\Delta R$  vs  $d_{Py}$ , showing how the data deviates from an initial linear increase. The dotted line from the origin represents a Py spin flip length of infinity. The horizontal dashed line is for the limit where the thickness of Py is much greater than 5.5 nm, the spin flip length used to fit the solid curve. From [60].

The layers outside the Py ferromagnets do not need to be considered for their contribution to  $A\Delta R$  as  $d_{Py} \gg l_{sf}^{Py} = 5.5$  nm [60]. VF theory is considered to be able to completely describe every example of CPP magnetoresistance [28], although often requires numerical solution, especially when it cannot be simplified in limiting circumstances or through symmetry.

### 5.1.3 Experimental background on factors affecting CPP GMR

#### 5.1.3.1 Spacer Layers

The spin diffusion length  $l_{sf}^N$  of the N spacer layers determines the level of spin decay that occurs between ferromagnetic layers, and hence the size of the spin dependent effects that occur. Increasing the thickness of N,  $d_N$ , or reducing  $l_{sf}^N$  therefore decreases the magnetoresistance - an early example of this was [104], in which spin scattering in the N layers of multilayers was increased by alloying with spin-spin (Mn) or spin-orbit (Pt) scattering materials, and showed a shorter  $l_{sf}^N$  led to reduced GMR. Spin valves were used to demonstrate decreased magnetoresistance as  $d_N$  increases and measure  $l_{sf}^N$  in [53], including a value for  $l_{sf}^{Nb} = 25_{-5}^{+\infty}$  nm<sup>1</sup>, which can be compared to later values found for  $l_{sf}^{Nb}$  such as  $48 \pm 3$  nm [14], which also used a spin valve structure with superconducting contacts, and  $40 \pm 5$  nm from [114], which quantified  $l_{sf}^{Nb}$  as part of a investigation into superconducting spin transport of Nb. [53] and [115] also showed that  $l_{sf}^N$  was shorter in materials with greater spin-orbit coupling, with [53] featuring pure films and Cu/N

<sup>1</sup>The reported bounds here reflect the fact that the maximum Nb thickness in these devices was 20 nm, so a spin diffusion length of 25 nm involves extrapolation, with associated uncertainties.

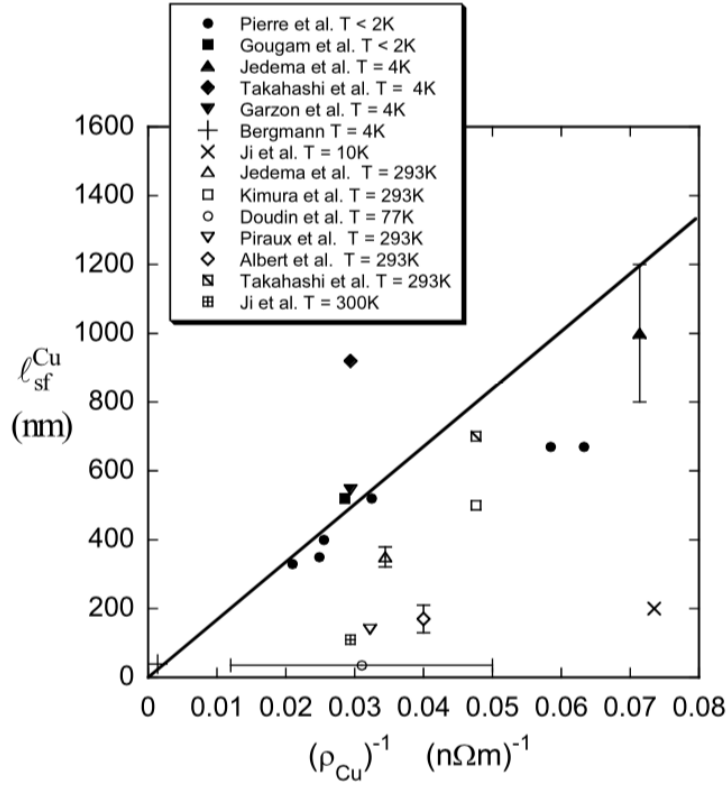


**Figure 5.5:**  $l_{sf}^{Cu}$  vs.  $1/\rho$  from a range of sources, showing how the suitability of the relationship  $l_{sf}^N \propto 1/\rho$  can vary. From [118], Figure 14, and references within.

multilayers of V, Nb and W [Fig. 5.4(a)], while [115] saw a reduced  $l_{sf}^N$  in CuPt compared to Cu. Spin decay with spacer layer thickness was also measured for alloys of Cu and Ag in [116], again demonstrating behaviour agreeing with VF theory predictions, this time in devices with  $d_N$  up to 250 nm thick. This is not the only study using thicker spacer layers; in [79], focused ion-beam (FIB) milled nanopillars of Py/Cu/Py spin valves were used to measure  $l_{sf}^{Cu} = 600 \pm 245$  nm by fitting VF theory to results up to 530 nm thick, and lateral devices featuring contacts with separations of up to  $4\mu\text{m}$  have also been used for Al and Cu N layers [105, 117]. Values from the literature for the spin flip length of all layers in the heterostructure used as part of this investigation are included in Table 5.1.

One simple approximation for comparisons between studies of  $l_{sf}^N$  from different sources is that  $l_{sf}^N \propto 1/\rho$ . The accuracy of this approximation depends upon the main sources of resistance and spin flip scattering within a material, and tends to be more valid when the main source of resistance is an impurity that also flips spins [118]; as shown in Fig. 5.5 it can frequently not be applicable. However, its simplicity can make it a useful tool.

### 5.1.3.2 Ferromagnetic Layers

Some of the first experimental investigations using CPP spin valves [60, 119] investigated the dependence of the magnetoresistance on ferromagnetic layer thickness  $d_{Py}$ , finding that the spin diffusion length in Py was in fact around  $5.5 \pm 1$  nm, rather than the pre-

Layer	$l_{sf}$ (nm)	Reference
Nb	$48.0 \pm 3$	[14]
	$40 \pm 5$	[114]
Cu	$600 \pm 245$	[79]
Ni <sub>80</sub> Fe <sub>20</sub>	$5.5 \pm 1$	[60]
FeMn	$\approx 1.5$	[53]

**Table 5.1:** Spin flip lengths for the metals used in the heterostructure of this investigation. As  $d_{\text{Py}} \gg l_{sf}^{\text{Py}}$ , the layers outside the Py (i.e. the FeMn and Cu contact layers) should not contribute to  $A\Delta R$  [53].

viously assumed  $l_{sf}^{\text{Py}} = \infty$ . This was demonstrated by the plateau of magnetoresistance at higher values of  $d_{\text{Py}}$ , rather than continuing the linear increase seen with lower values of  $d_{\text{Py}}$ , with the departure happening when  $d_{\text{Py}} \approx l_{sf}^{\text{Py}}$  [Fig. 5.4(b)]. Such a dependence of magnetoresistance with  $d_{\text{F}}$  is in agreement with VF theory; similar results have been found in other spin valves [95, 102, 120–122] and multilayers [123] although there is some disagreement: in [121] rather than saturating after the linear increase, the magnetoresistance instead decreased as  $1/d_{\text{F}}$ , and [110] found that in a Co/Ag multilayer magnetoresistance decreased monotonically with increasing  $d_{\text{F}}$ .

The resistivity of the F layers in a spin valve also affects magnetoresistance, as increased resistivity tends to limit the detrimental effects of high resistivity in other parts of the device, shown experimentally with non-magnetic impurities added to CoFeAl F layers [124]. The resistivity of CoFeGe F layers of changing composition was measured in [122], which found the maximum  $A\Delta R$  did not correspond to maximum resistivity, due to additional effects of changing microstructure as the composition varied. Changing CoFe alloy composition also affected magnetoresistance in [123, 125], although the reasoning was different in each case; [123] attributed the change to resistivity changes, but measurement of resistances in [125] suggested that the resistivity did not change in that investigation, and the increase of  $A\Delta R$  was instead attributed to changes in scattering asymmetries, particularly enhanced by addition of Cu interlayers.

### 5.1.3.3 Asymmetric scattering

Scattering asymmetry between spin directions is intrinsic to GMR, and altering the degree of this asymmetry will affect the magnitude of magnetoresistance. Spin asymmetric effects occur within the bulk of the ferromagnets, and at the interface; unlike in magnetic multilayers, for which the interface is far more important than the bulk, in spin valves the lower number of interfaces means bulk effects are significant [126]. This was highlighted in [127], which used combinations of various F layers with different known bulk and inter-

face scattering anisotropies to show that the switching of a spin valve (monitored using current induced magnetisation switching) was dependent on the net scattering anisotropy (both the interface and bulk), rather than just the interface, and also showed that the signs of a spin current and spin accumulation can either be the same, or opposite, leading to potential competition between them. The interface scattering anisotropy of a layer can affect the magnetoresistance even if outside the main spin valve; in [128], a spin valve was designed such that  $A\Delta R = 0 \text{ } \Omega \text{ m}^2$ , and then demonstrated that the magnetoresistance could be made positive or negative by inserting various N layers between the Co F layer and the Nb superconducting contacts. These changes were attributed to the changing of the interfaces, as thicknesses of all layers were much less than their spin diffusion lengths. Notably for the sake of this thesis, Cu/Nb interfaces were shown to be magnetically active if the Nb was in the normal state. This supports earlier measurements of a spin flipping parameter at the Cu/Nb interface in [53], although it should be noted that both of these featured Cu/Nb multilayers rather than single interfaces.

It has also been suggested that scattering asymmetries in ferromagnets may be modified by a large degree of spin accumulation [129]. Nanopillars containing double spin valves (F/N/F/N/F) were constructed, with the outer F layers held antiparallel so that the overall magnetic configuration was the same for either orientation of the central layer, removing standard GMR effects. The magnetoresistance of these devices was shown to be extremely current dependent, whilst the coercive fields were not. As a result, the authors suggested the observed effects were separate from possible spin transfer torque effects and instead proposed that spin accumulation occurring in the central F layer alters the exchange splitting of the density of states. A subsequent investigation [48] used the same structure while changing the thickness of the central F layer, investigating the contributions from interface and bulk, finding that interfacial spin accumulation was larger but could not account for these spin accumulation effects on its own. A change in spin scattering asymmetry has also been invoked to explain roughness dependence [88] (see Section 4.1.2.2) but this is less certain [28].

#### 5.1.3.4 Construction

Beyond the parameters intrinsic to the materials used, physical factors, such as shape and implantation effects from the construction of a CPP device may affect magnetoresistance, as well as the magnetic switching characteristics as discussed previously (Section 4.1.2.3). However, in many cases it can be hard to distinguish between a direct effect on GMR and indirect effect via switching, and the literature considered here will be very similar.

For CPP devices, the areal resistance  $AR$  and magnetoresistance  $A\Delta R$  are the parameters independent of area [75, 95, 115, 123] that should be used to compare between different CPP devices, as shown in Fig. 5.6(a), and areal resistances are considered in VF theory [108]. However, the shapes and aspect ratios achieving such areas can change,

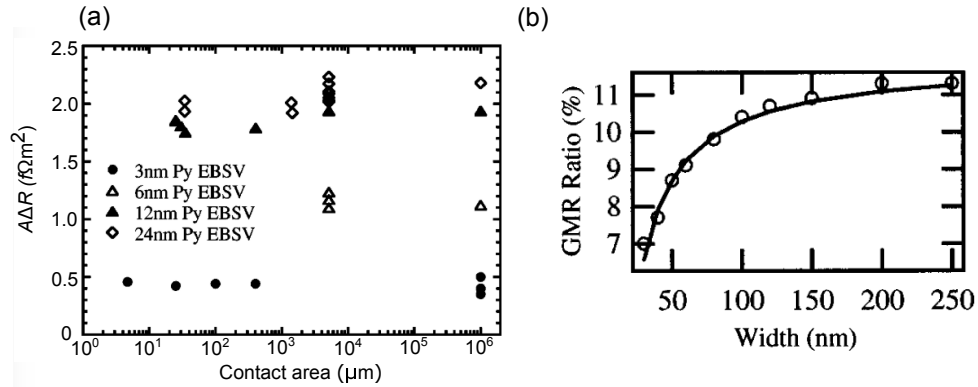


**Figure 5.6:** (a)  $A\Delta R$  is independent of area for CPP multilayers and spin valves, as shown here for Py/Cu/Py spin valves, from [95]. (b) GMR in CoFe/Cu/CoFe CIP spin valves patterned into nanowires using lithography and Ar ion milling decreases with decreasing wire width. The curve corresponds to a model considering parallel paths: an undamaged region and a region damaged by milling, 6 nm thick from each edge, which contributes to total resistance but not magnetoresistance. From [92].

which may affect the GMR. Although there is a distinction between CIP and CPP dependence on these factors, few investigations into the effect of shape on the GMR of nanopillar CPP spin valves have been performed, and so the effects on CIP devices are considered here. [92, 94] saw GMR decrease in thinner CIP nanowires, which may have been the result of either lateral milling or heating from milling affecting these multilayers. Additionally they noted the strong shape anisotropy of their wires suppressed Barkhausen noise (stepwise progression of domain walls jumping from pinning site to pinning site leading to steps in the recorded parameter). [74] similarly saw a CIP GMR decrease for thinner wire, suggesting either an increased importance of scattering at edges or ion-milling affecting transport at the edges as the cause. Exposure to Ga<sup>+</sup> ions from FIB milling decreased the magnitude of GMR in a CIP spin valve in [97], and exacerbated the decrease of GMR in thinner wires in [92], resulting in loss of GMR if devices were too thin [Fig. 5.6(b)]. Although simulation suggested damage should be less than 30 nm from the edge of the wires, the actual results indicate these effects of FIB milling occur over 150-200 nm instead, which may be stress from the implantation causing issues over a larger distance than the expected mean free path of these ions.

[96] noted the impact of dosing with Ga<sup>+</sup> ions as reducing both the anisotropic magnetoresistance (AMR) and GMR demonstrated in their CIP Py/Cu/Py spin valves, although the GMR was affected more, allowing the AMR to become more visible as the GMR decreased. This highlights the coexistence of AMR and GMR in such devices, as shown by [130] in the initial report of a CIP spin valve, and later in [131], which also demonstrates their coexistence and highlights how AMR can be of significant size and yet still hidden by a large GMR effect. [105, 117] note negative dips alongside GMR peaks they attribute to AMR. Similar dips are noted as interesting but unexplained in [132],

whilst [79] notes these small negative peaks and attempts to specifically rule out AMR as a possible explanation.

There is a limited amount of experimental work on ion milled nanopillars - [133] uses CPP nanopillars to estimate the spin diffusion length in Cu at room temperature, obtaining values of  $l_{sf}^{Cu} = 170 \pm 40$  nm and  $140 \pm 30$  nm, which is much shorter than other values from [79, 104, 105], potentially hinting at the damaging effect of ion implantation, although [79] was a FIB milled nanopillar and agrees better with the other results. Nothing could be found on the impact of nanopillar geometry on GMR.

## 5.2 Experimental Results

The results from electrical characterisation of the fabricated CPP spin valves in the normal state are discussed in this section. Comparisons of spin diffusion length and  $A\Delta R$  with other published results are made, and background effects that are visible in the normal state are also considered.

### 5.2.1 GMR

In the normal state, all measurements of interest are  $R(H)$  loops. Examples for devices with low Nb thickness ( $d_{Nb} = 21$  nm) and high Nb thickness ( $d_{Nb} = 63$  nm) are shown in Fig. 5.7(a) and (b), respectively. Although the giant magnetoresistance of devices with low  $d_{Nb}$  is clear, it rapidly decreases in size and is difficult to extract compared to the negative magnetoresistance effects observable in the devices with higher  $d_{Nb}$ . This negative magnetoresistance is hysteretic and, through measurements on the sections of patterned structure without pillars and comparison with literature, is believed to be due to AMR. This is explored more in Section 5.2.4.

One notable aspect of the  $R(H)$  loops is that the values for coercive field of the free layer at least a factor of two greater than those suggested by  $M(H)$  loops, even at low temperature, as shown in Fig. 5.8.  $M(H)$  loops are measured across an entire substrate, and cannot show micromagnetic differences in regions of a structure post-patterning. Therefore, one possible explanation is that the nanopillar devices have a different coercive field from that of the rest of the heterostructure, as they dominate the  $R(H)$  response, yet have a very small magnetic moment that would not cause a noticeable change to the measured  $M(H)$ . The change in coercive field is not exclusive to isolated pillar devices, as measurements on sections of structure with only single FIB cuts rather than the two required for a full pillar (see Section 5.2.5) have the same higher coercive fields - but as noted in the previous chapter (Section 4.1.2.3) ion milling can increase the coercive fields of ferromagnets. A difference between  $R(H)$  and  $M(H)$  loops is not unheard of: [134] noted for CPP Py/Cu/Py devices that  $M(H)$  and  $R(H)$  loops

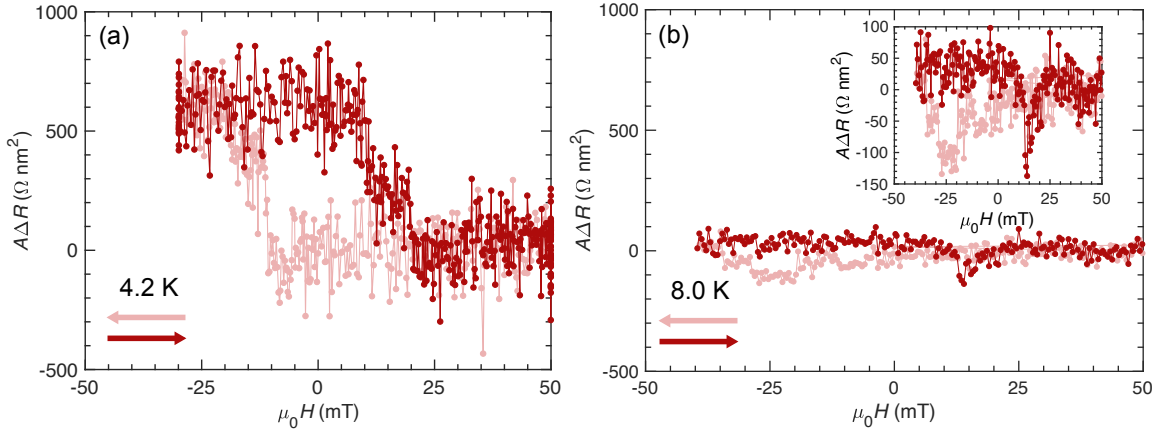


**Figure 5.7:** Minor loops measured on Py/Cu/Nb/Cu/Py/FeMn devices with Cu contact layers. Devices are measured with Nb in the normal state (a)  $d_{\text{Nb}} = 21 \text{ nm}$  ( $T_{\text{device}} = 1.23 \text{ K}$ ) and (b)  $d_{\text{Nb}} = 63 \text{ nm}$  ( $T_{\text{device}} = 6.70 \text{ K}$ ). Inset in (b) is the same data on a smaller  $y$ -scale. The negative magnetoresistance is relatively much more significant at higher values of  $d_{\text{Nb}}$ , which made GMR value extraction more challenging for these loops. In both plots arrows represent the sweep direction for each colour, starting at high positive fields.

tended to have slightly different shapes, with  $M(H)$  loops being more gradual rather than sharp, and this discrepancy increased with Py thickness (comparing 6 nm, 24 nm and 30 nm layers). However, no coercive field difference as shown here was reported. An  $M(H)$  measurement is a volumetric measurement of properties, whereas the CPP  $R(H)$  will depend on the interfaces the current passes through, which may contribute to the discrepancy; alternatively the current itself may affect the coercive field, although in this case a dependence on current direction would be expected, which has not been observed. Finally, the increased shape anisotropy of patterned films compared to unpatterned films may contribute. The exact reason for the difference between  $M(H)$  and  $R(H)$  loops remains uncertain, but may be due to locally increased coercivity near patterned areas.

The magnitude of  $A\Delta R$  from the devices fabricated for this investigation can be compared with selected devices from the literature: one early CPP spin valve study included a Py(15)/Cu(20)/Py(15) structure [60], which gave  $A\Delta R \approx 1.6 \text{ f}\Omega \text{ m}^2$  ( $1600 \text{ } \Omega \text{ nm}^2$ ), and later a FIB milled Py(20)/Cu(10)/Py(40) pseudo-spin valve nanopillar [79] gave  $A\Delta R \approx 1300 \text{ } \Omega \text{ nm}^2$ . With thin Cu central layers, both can be compared to the devices with  $d_{\text{Nb}} = 0 \text{ nm}$ , which average to  $A\Delta R = 1350 \pm 180 \text{ } \Omega \text{ nm}^2$ . This agrees well with the device from [79], and is not far below the value from [60]. Other comparisons can be made with [14], which uses a similar structure to the devices in this investigation, including Nb in the spacer, although with 24 nm Py layers. Devices in [14] with  $d_{\text{Nb}}$  from 20-30 nm, a key range in both investigations (see Chapter 7), give  $A\Delta R$  between 600-700  $\Omega \text{ nm}^2$ . The devices fabricated here exhibit a large degree of scatter and a maximum value of 600  $\Omega \text{ nm}^2$  in that range of  $d_{\text{Nb}}$ . A better comparison over the whole data set can be made by comparing the calculated spin diffusion lengths from each study.

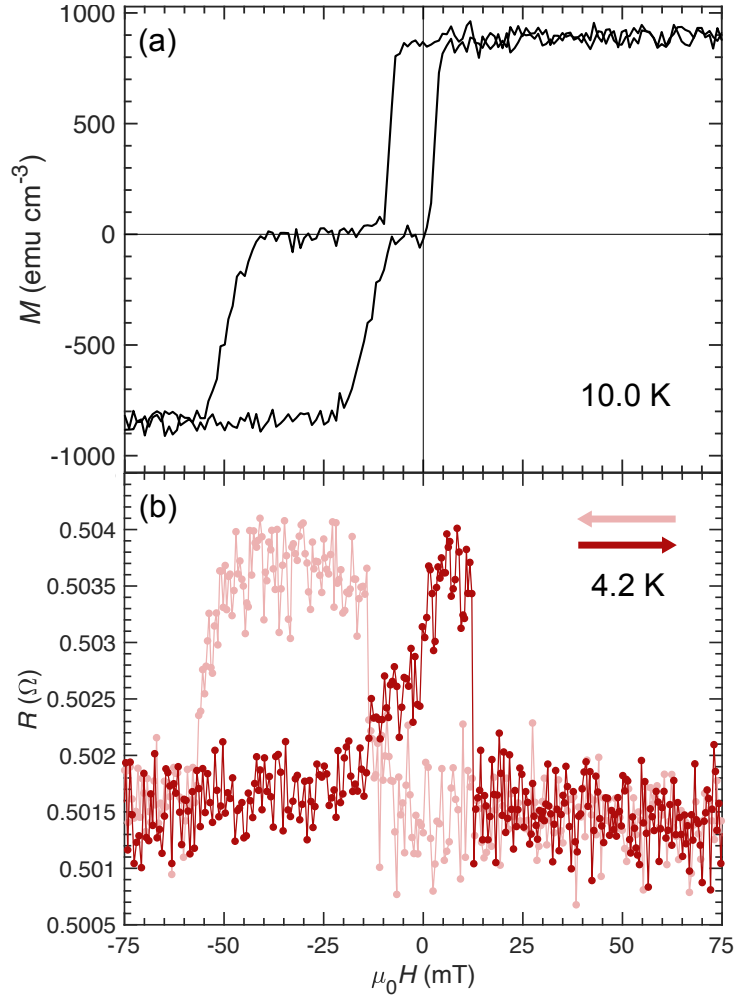


**Figure 5.8:** (a)  $M(H)$  major loop measured at 10 K and (b)  $R(H)$  major loop measured at 4.2 K, which is the normal state for this device ( $T_{\text{device}} < 1.5$  K). Both have the same standard structure with 15 nm of Py. Arrows in (b) represent the sweep direction for each colour, starting at high positive fields. For clarity of the switching, a structure with  $d_{\text{Nb}} = 31$  nm is used [the  $M(H)$  loop in (a) has  $d_{\text{Nb}} = 86$  nm]. Minor loops suggest that thicker Nb would have larger coercive field values.

### 5.2.2 Spacer layer spin diffusion length

A large number of devices with a range of  $d_{\text{Nb}}$  values have been fabricated with an otherwise identical structure. The normal state spin decay length in Nb below 10 K can therefore be calculated, allowing comparison with values measured from other sources, helping to evaluate the fabrication of these CPP FIB-milled nanopillar devices. To calculate  $l_{sf}^N$ , the data have been fit with a series of models, so that comparison between models can indicate important parameters in the data. In this investigation,  $d_{\text{Nb}}$  covers a wide range of values, including beyond previously measured values for  $l_{sf}^{\text{Nb}}$  of 25 nm [53] and 48 nm [14], and  $d_{\text{Py}} = 15 \text{ nm} > l_{sf}^{\text{Py}} = 5.5 \text{ nm}$ , so the 2CSR model is not suitable here. As such, the data has been fit with three models, with  $l_{sf}^{\text{Nb}}$  the free variable in each case: (1) A simple exponential decay,

$$A\Delta R \propto \exp\left(\frac{-d_{\text{Nb}}}{l_{sf}^{\text{Nb}}}\right) \quad (5.3)$$

with the sole aim of capturing the key decay feature in the data, as suggested by equation 5.1. Models (2) and (3) have been fit with equation 5.2 from [53], where in (2) the interface parameter  $\delta$  was set to zero and in (3)  $\delta$  was included as a fitting parameter in addition to  $l_{sf}^{\text{Nb}}$ .  $\rho_{\text{Nb}}$  and  $\rho_{\text{Cu}}$  were measured using a van der Pauw geometry on 300 nm bare films. The values for other parameters in equation 5.2 were taken from Table 8 in [28], which reports the parameters calculated from a fit in [135]. The fits of each model to the data are presented in Fig. 5.9; all three models were fit using orthogonal distance regression (which considers errors in  $x$ -variables as well as  $y$ -variables) to individual device data. For clarity, data is presented as the mean and standard deviation of devices measured across a single substrate rather than each device individually in Fig. 5.9.

The first fit, the simple exponential, suggests  $l_{sf}^{\text{Nb}} = 25 \pm 3 \text{ nm}$ . The second provides  $l_{sf}^{\text{Nb}} = 16.9 \pm 0.3 \text{ nm}$ , and the third leads to  $l_{sf}^{\text{Nb}} = 26.1 \pm 1.7 \text{ nm}$  and  $\delta = 0.24 \pm 0.07$ . There is extremely good agreement between the first and third fits. Given that the simple exponential captures only the decay and is not constrained by any parameters, it can be considered a good estimate for the best fit to the decay aspect of the data. The agreement with the VF theory through equation 5.2 from the third fit therefore suggests VF theory well describes this system, despite the assumption  $d_{\text{Py}} \gg l_{sf}^{\text{Py}} = 5.5 \text{ nm}$  being weaker for this structure (where  $d_{\text{Py}} = 15 \text{ nm}$  rather than 24 nm) than in [53]. Additionally,  $\delta = 0.24 \pm 0.07$  agrees with the value of  $\delta = 0.19 \pm 0.05$  from [53]. The second fit, where  $\delta = 0$ , does not agree with the others, suggesting that allowing  $\delta = 0$  to vary (i.e. including interface scattering) has a large impact on the fit, so interface scattering is important in this system [ $\delta$  is specifically related to the Cu/Nb interface rather than the Py/Cu interface, but this may nevertheless be a magnetically active interface, as noted previously]. The fact that the value for  $l_{sf}^N$  from model (2) also fits the data satisfactorily

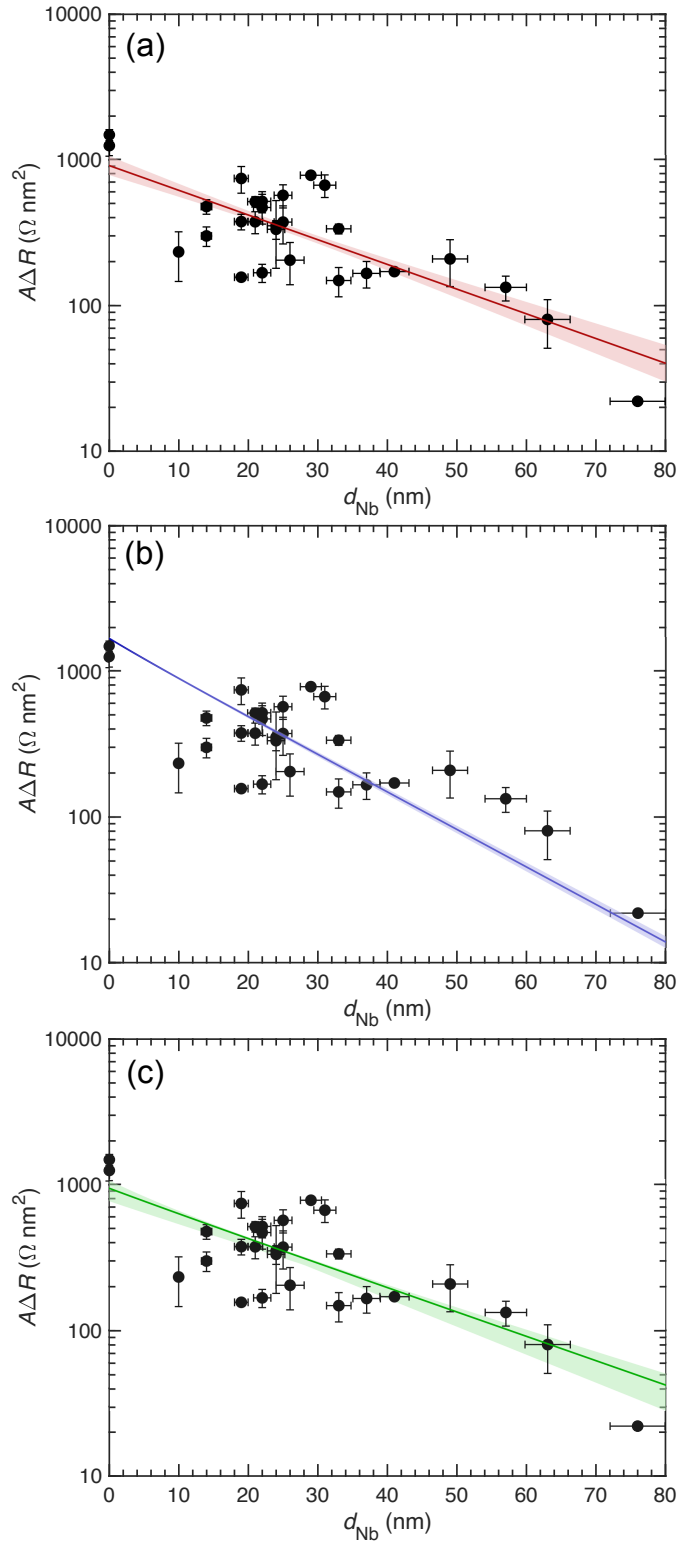


**Figure 5.9:** Black data points and associated  $y$ -errors are the mean and standard deviations from devices across a single substrate. Fits are to the complete data set comprising every device individually. (a) A simple exponential decay fit,  $l_{sf}^{\text{Nb}} = 25 \pm 3$  nm. (b) Equation 5.2 with  $\delta = 0$ , giving  $l_{sf}^{\text{Nb}} = 16.9 \pm 0.3$  nm. (c) Equation 5.2 with  $\delta$  as a fitting parameter,  $l_{sf}^{\text{Nb}} = 26.1 \pm 1.7$  nm,  $\delta = 0.24 \pm 0.07$ . The dark coloured line in each case is the fit, with lighter coloured areas representing the error in each fit. All devices measured in their normal state,  $< 10$  K.

highlights the degree of scatter in the data.

A simple comparison with other measurements of  $l_{sf}^{\text{Nb}}$  can be made using the approximation that  $l_{sf}^N \propto 1/\rho$ . From a van der Pauw measurement on a 300 nm bare Nb film a resistivity of Nb for these devices is measured,  $\rho_{\text{Nb}} = 93 \pm 20 \text{ n}\Omega \text{ m}$ . Comparing to the value of  $l_{sf}^{\text{Nb}} = 48 \pm 3 \text{ nm}$  from [14] (which given its lower error is considered to supersede the value of  $l_{sf}^{\text{Nb}} = 25_{-5}^{+\infty} \text{ nm}$  from the same group in [53]) with an associated  $\rho_{\text{Nb}} = 60 \text{ n}\Omega \text{ m}$  using the inversely proportional relationship suggests the  $l_{sf}^{\text{Nb}}$  value measured in these devices should be 31 nm. Similarly, comparing with the value of between 35-45 nm from [114] ( $\rho_{\text{Nb}} = 70 - 80 \text{ n}\Omega \text{ m}$ ) suggests a value for  $l_{sf}^{\text{Nb}}$  of 32 nm. These values fall outside the error range from the fitting, suggesting either the  $l_{sf}^N \propto 1/\rho$  approximation is not valid in this case, or the resistivity value from the van der Pauw measurement does not well represent these devices. Whilst the approximation is flawed in certain circumstances (see Fig. 5.5), here it is reasonable to consider it as suitable, given the reasonably strong spin orbit scattering in Nb that suggests most impurities would contribute to spin flipping. By contrast, given the extra fabrication steps for the nanopillar devices compared to the bare Nb film, it is likely impurities and defects could have arisen; in particular note that the value from [114] was measured from heterostructures deposited in the same deposition system as used in this investigation, supported by the agreement between  $\rho_{\text{Nb}}$  values, but the measurement of  $l_{sf}^{\text{Nb}}$  came from fitting to ferromagnetic resonance data, without the need for FIB or ion milling. As such, the lower value for  $l_{sf}^{\text{Nb}}$  measured in these CPP nanopillars appears to be a result of scattering sites introduced in the fabrication process of the devices.

### 5.2.3 Device Dimensions

The dimensions of the nanopillar making up the CPP device are expected to have an impact on the measured GMR, either through the effect on the ferromagnetic properties and switching of the device, or a more direct effect on current paths and scattering. Furthermore,  $A\Delta R$  is expected to be constant for a range of areas across a single structure [75, 95, 115, 123]. However, in the devices measured in this investigation, no consistent trend with device dimensions has been observed.

Figure 5.10(a) shows how  $A\Delta R$  varies with area across a large number of substrates and devices. For a given substrate (series of points of same colour/symbol combination)  $A\Delta R$  is not always constant as expected, increasing and decreasing across devices in different cases. Substrates have devices varying by up to  $400 \text{ }\Omega \text{ nm}^2$ , or by as little as  $80 \text{ }\Omega \text{ nm}^2$  for no change in FIB process, suggesting variation based on some unrecorded parameter. Comparison of Fig. 5.10(a) and Fig. 5.10(b), which plots  $A\Delta R$  versus aspect ratio, reveals some substrates have similar trends in both, suggesting non-geometric origins. Thickness gradients, as a result of shadowing in the deposition process, or a systematic change of

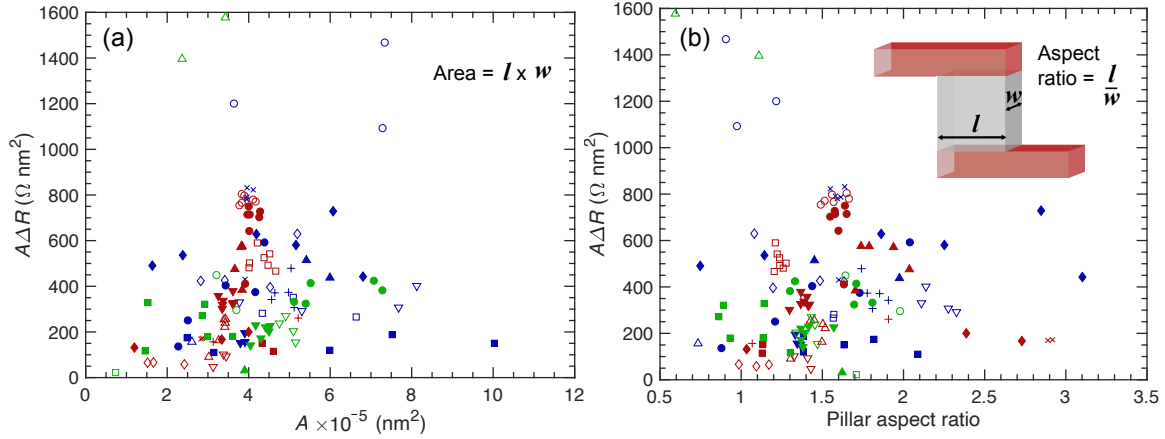


**Figure 5.10:**  $A\Delta R$  versus (a) area and (b) aspect ratio of the nanopillar for a large number of devices across a range of values of  $d_{\text{Nb}}$ . Points with the same symbol/colour combinations represent different devices on the same substrate, and are therefore directly comparable, having identical structure and fabrication processes. Symbols and colours have no meaning beyond differentiating between points. Filled and open shapes count as different symbol shapes (i.e. open triangles are not on same substrate as closed triangles). Devices across some substrates appear to demonstrate a trend, rather than being constant. Furthermore, different substrates demonstrate opposing trends, which hinders identification of a cause.

implantation or damage from the fabrication process as it goes on, could be responsible. However, given both positive and negative trends are observed for various devices, neither suggestion can explain every deviation.

Figure 5.11 plots  $A\Delta R$  against (a) device length, (b) device width. As for the plots in Fig. 5.10, no consistent trends across all substrates and devices appear. This suggests that there is no dependence of  $A\Delta R$  on CPP device geometry over these lengthscales, at least compared to the degree of variation possible from other sources. Comparison with literature such as [74, 92, 94, 96, 97], which all observe trends in GMR devices based upon the effect of ion milling or FIB patterning into devices of various dimensions suggests that if no dependence on device dimensions is being observed then the impact of ion implantation may be less than in those studies, although this is in contrast to the reduced  $l_{sf}^{\text{Nb}}$  as measured in these devices compared to the literature. Device dimensions around critical values (such as 700 nm [73], 200 nm [74] and  $0.45 \mu\text{m}^2$  [75]) may alter domain switching behaviour and therefore magnetoresistance. No sudden change in magnetoresistance exists for the 400-1500 nm length variation or 300-800 nm width variation from these plots, suggesting such a critical value in these devices is below 300 nm.

## 5.2.4 Negative Magnetoresistance

As seen in Fig. 5.7(b), devices with higher values of  $d_{\text{Nb}}$  demonstrate noticeable negative magnetoresistance effects in  $R(H)$  loops. This negative magnetoresistance can occur both gradually and in steps demonstrating a possible link to domains in the ferromagnet, and

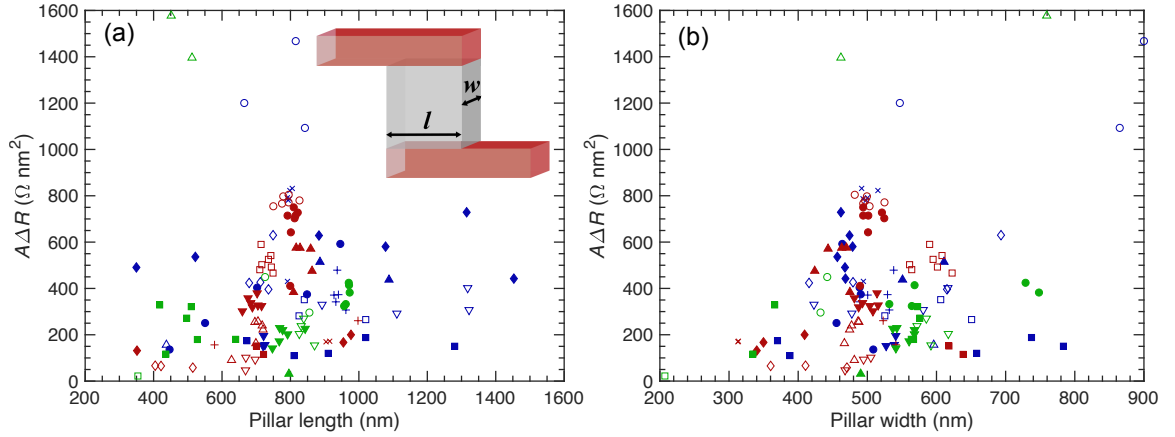


**Figure 5.11:**  $A\Delta R$  vs. (a) pillar length,  $l$ , and (b) pillar width,  $w$ , for a large number of devices across a range of values of  $d_{Nb}$ . As in Fig. 5.10, points with the same symbol/colour combinations represent different devices on the same substrate, and are therefore directly comparable. Symbols and colours have no meaning beyond differentiating between points. Filled and open shapes represent different substrates.

is hysteretic, occurring as the free layer switches in both directions (Fig. 5.12).

The magnitude of this negative effect increases with increasing  $d_{Nb}$ , as shown in Fig. 5.13(a), saturating above  $d_{Nb} = 40$  nm. These data have been normalised using  $R_P$  rather than  $A\Delta R$  as the effect may not be confined to the pillars, as discussed in Section 5.2.5. An increasing effect with increasing spacer layer was also observed in the negative effects seen in [79].  $R(H)$  loops from that paper indicate the effects were associated with the low coercive field layer, when it entered or left the parallel state. Fig. 5.13(b) suggests there is no dependence of the effect on the thickness of the Py layers, although there is a large degree of variation between devices.

One of the most common forms of negative magnetoresistance is anisotropic magnetoresistance (AMR), which for Py is negative when the current flows parallel to the magnetisation within a ferromagnet, and positive when the current flows perpendicular to the magnetisation. In these heterostructures, this could occur in two potential places; firstly, within the pillar, if current did not travel perfectly perpendicular to the planes but instead at an angle, or secondly, in the ‘wires’ - the contact lead part of the heterostructure from which the pillar was milled. As discussed in Section 4.2.2, finite element analyses performed on similar structures previously have suggested the current should be uniform and vertical. Figure 5.14 shows the negative magnetoresistance plotted against pillar length. Examination of devices from the same substrate suggests there is no correlation between device dimensions and these negative effects; if it were a result of such non-perpendicular current, a change with dimensions, particularly length, would be expected. Alternatively, the current may enter the Py in the ‘wires’, with the effect appearing as part of the lead resistance. However, measurements on ‘devices’ without the ‘side cuts’ defining the CPP path do not show such effects, likely due to shunting by the Cu contact layers. These

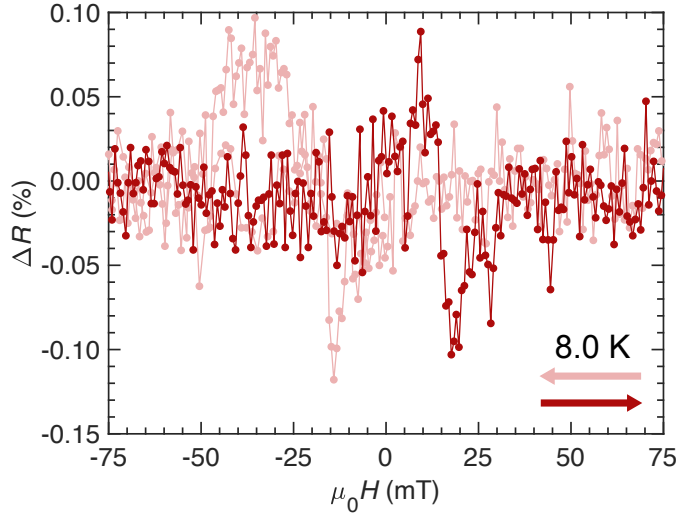


**Figure 5.12:** Major  $R(H)$  loop from a device with 57 nm of Nb, measured in the normal state at a higher current of  $100 \mu\text{A}$  for a better signal:noise ratio to show the negative effects. The negative effects are associated with the free layer entering or leaving the parallel state. Arrows represent the sweep direction for each colour, starting at high positive fields.

results are the same as the findings in [79]. Other parts of the wires, which would not contribute to the voltage measurement across a nanopillar, did demonstrate AMR effects, revealed by a change in sign as the field was applied longitudinally or transverse to the wire. AMR effects do therefore appear in this structure, and cannot be ruled out. The magnitude of the effects is similar to the AMR effects of order  $10^{-4}$  seen in [136]. In that paper, the appearance of only two peaks rather than four for a spin valve was attributed to coupling between the two F layers; here, the distinction that can be made between the switching of each layer rules that out.

The appearance of the effect associated strictly with the free layer suggests the switching characteristics of the free and pinned layers in the structure are different, as suggested in [71], the free layer developing the domain rotation necessary for AMR, whereas the pinned layer does not. The hysteretic nature of the effect, and the definite link between the effect and the switching of layers confirms it is associated with the F layers. The lack of dependence on  $d_{\text{Py}}$  is therefore surprising. There is also variation between devices on a substrate, which suggests different domain formation between different devices, and yet no correlation between the appearance of the effect and device dimensions, which is expected to affect domain behaviour in the F layers. The lack of dependence on dimensions, plus the lack of negative effects in the ‘wires’ compared to the pillars, suggests the cuts isolating the pillars have a role to play in the appearance of this effect.

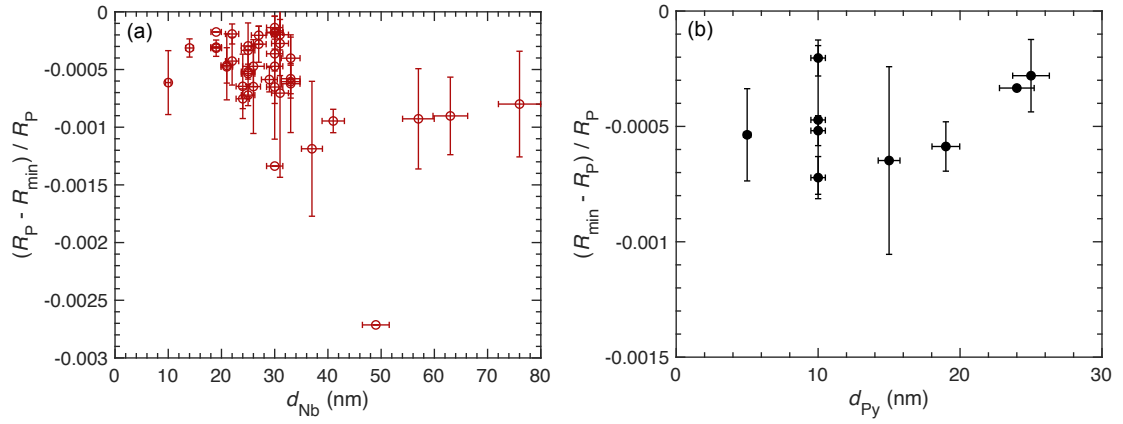


**Figure 5.13:** (a) Negative magnetoresistance plotted against  $d_{\text{Nb}}$ . The negative magnetoresistance is defined as the difference between the lowest resistance in the  $R(H)$  loop  $R_{\min}$ , and the resistance at 100 mT,  $R_P$ , normalised by  $R_P$ . (b) Negative magnetoresistance *versus*  $d_{\text{Py}}$ . The changing thickness of Py does not seem to lead to a change in the magnitude of negative magnetoresistance seen.

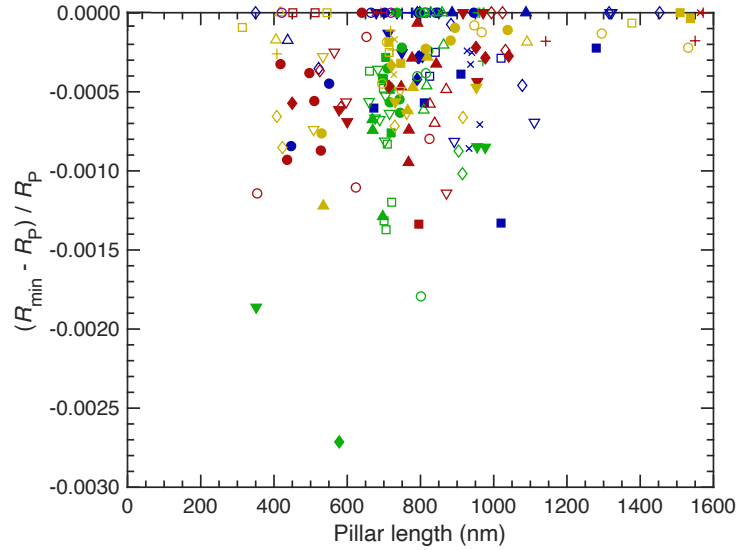


**Figure 5.14:** Negative magnetoresistance as in Fig. 5.13(a) plotted against the length of the device nanopillar. As previously, points with the same shape-colour combinations denote devices from the same substrate. There does not appear to be any dependence on pillar length from devices on the same substrate.

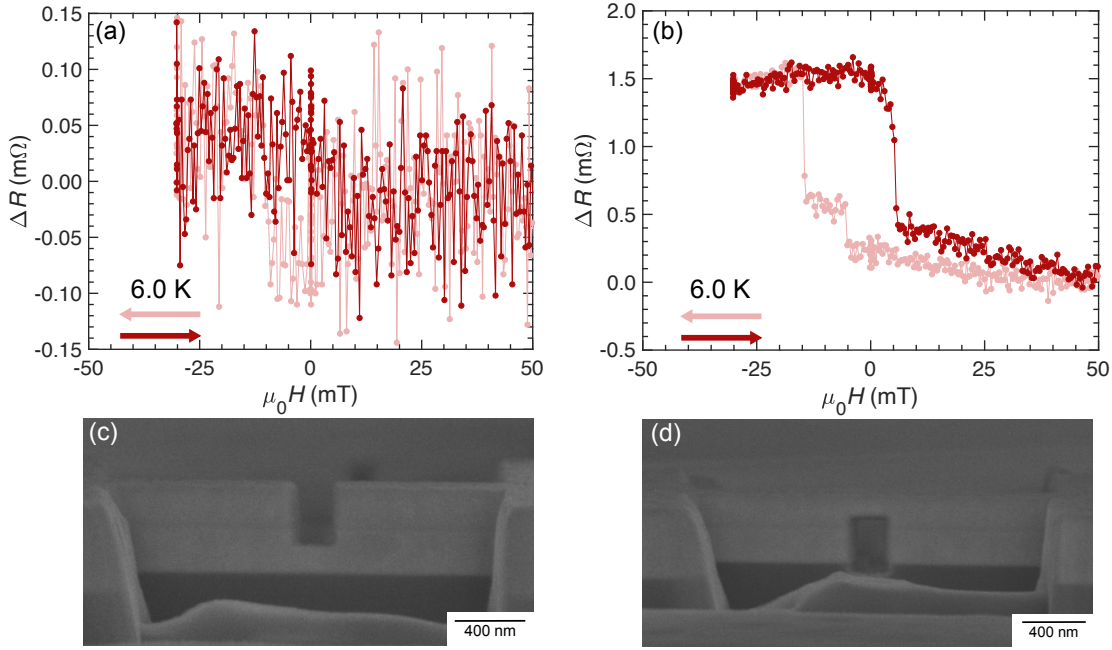


**Figure 5.15:** (a)  $R(H)$  measured on part of the heterostructure with only the ‘top’ pillar isolating cut performed. (b)  $R(H)$  measured on part of the heterostructure with only the ‘bottom’ pillar isolating cut performed, from the same substrate. In both (a) and (b), arrows represent the sweep direction for each colour, starting at high positive fields. (c) SEM image of the device measured in (a). (d) SEM image of the device measured in (b).

### 5.2.5 Single Cuts

Inconsistency in magnetoresistance changes with dimension and temperature led to investigation of the effect of a ‘single cut’ on the magnetoresistance of the heterostructure. Here, instead of the two side cuts made with the FIB to define a vertical pillar - one ‘top cut’ milling the top contact layer and spin valve, and one ‘bottom cut’ milling the bottom contact layer and spin valve - only one or the other was made.  $R(H)$  loops measured for these cuts are displayed in Fig. 5.15(a,b), showing that even without the device fashioned into a distinct pillar, GMR appears in some cases.

The origin of this magnetoresistance is considered to be as follows: left untouched, the current flows in the thick Cu contact layers, top and bottom of the structure. Upon reaching a cut, the current is diverted into the other contact layer, causing the current to travel through the complete spin valve, resulting in GMR. The magnetoresistance for the bottom cut is larger than the top cut, suggesting that more current typically travels in the bottom contact layer - a greater fraction of the total current is therefore susceptible to giant magnetoresistance, leading to a large effect.

GMR from single FIB cuts is extremely interesting, but also has implications for other results in this thesis. Firstly, it may explain the lack of dependence on the pillar dimensions, as discussed in Section 5.2.3, including the variation of  $A\Delta R$ . However, this implies GMR measured from pillars may have contributions from these ‘single cut’ effects.

Comparison of  $\Delta R$  between single cut and two cut devices does not indicate whether such a contribution exists. In the case of devices from one substrate, variation in magnitude of  $\Delta R$  means the value from a single cut -  $\Delta R = 1.3 \text{ m}\Omega$  can be simultaneously half that of one full pillar device ( $\Delta R = 2.2 \text{ m}\Omega$ ) yet also larger than another full pillar device ( $\Delta R = 1.2 \text{ m}\Omega$ ). Devices with large pillar length (e.g.  $> 1000 \text{ nm}$ ) are closest to being two separate ‘one cut’ devices, and yet do not show double the magnitude of one cut, and instead are similar to other pillar devices when their increased area is included as  $A\Delta R$ , as expected for a CPP device. This suggests the observed magnetoresistance is instead simply dominated by the largest resistance difference across the structure. Additionally, if single cut effects were adding to the pillar magnetoresistance, then a dependence on current direction would be expected; as the single cut effect is greater for a bottom cut, if the current runs into the bottom cut first, the resultant total should be larger than in the opposite current direction where the top cut was encountered first. However, such a current direction dependence is not observed.

Overall, magnetoresistance effects have been observed when only a single cut is made to the heterostructure; it is possible this affects the magnitude of GMR measurements of complete devices, but quantitative comparison does not reveal anything. This effect is explored again in Section 6.2.3.3.

### 5.2.6 Consistency

The key challenge with characterising the factors affecting magnetoresistance of these devices is the significant scatter demonstrated, such as in Fig. 5.9. Although scatter is expected for such a large number of devices, and a reasonable trend has been extracted for this  $d_{\text{Nb}}$  dependence, the scatter has hidden the effects of other parameters. The most prominent scatter is between devices from different substrates, so all parts of the fabrication process may contribute. Figure 5.16 plots measured superconducting transition temperature,  $T_c$ , for a number of ‘reference’ films from depositions against residual resistivity ratio (RRR), a measure of the level of impurities in a film, showing the variation possible from various depositions. The linear correlation suggests impurities are the main factor affecting the  $T_c$ . The improvement of the substrate deposition table, with more magnets added, was an attempt to improve consistency across systematic changes of structure by reducing the number of different depositions needed. Deposition power, pressure and initial vacuum do not correlate with the scatter in reference Nb quality. These impurity variations may contribute to some variation in GMR between substrates from different depositions, but cannot account for all variation seen. Furthermore, as shown previously on devices with changing Cu thickness [Fig. 4.14(a)], the scatter between devices on a single substrate, or between substrates from a single deposition could be greater than the variation between substrates from separate depositions. This suggests

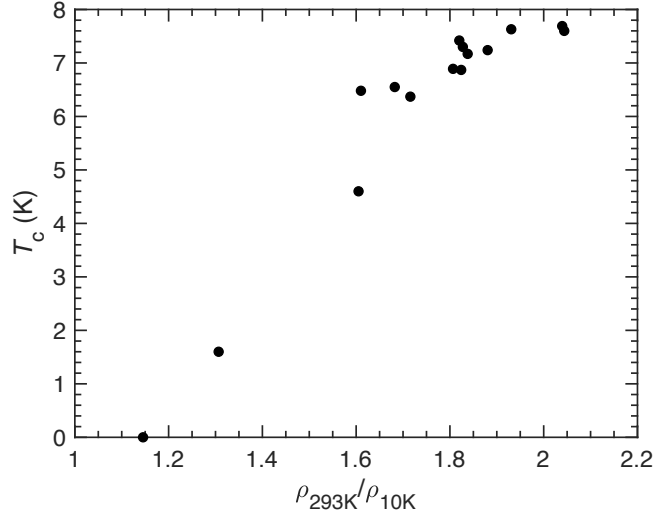


**Figure 5.16:**  $T_c$  of 30 nm ‘reference’ Nb films from various depositions, plotted against the residual resistivity ratio  $\rho_{293K}/\rho_{10K}$  of the references, showing how  $T_c$  variation is affected by impurities from the deposition.

other aspects of the fabrication process were responsible for the variation in results.

Large variation in GMR between devices on a single substrate suggest inconsistency in the FIB process. Variation in the FIB current is a possible cause (with the user setting a target current, which remains consistent, but the actual output current varying between fabrication sessions), as well as implantation from imaging between mills or small variations in the focus of the beam. Given that excellent consistency could be achieved when devices were intended to be identical (same pillar length / width), it is possible variation in attempted pillar geometry resulted in scatter in results due to FIB effects. However, as discussed in Section 5.2.3, no overall trends with device shape were observed, which would be expected if pillar geometry made devices more susceptible to  $\text{Ga}^+$  implantation or damage.

Finally, there can be large differences in results from two adjacent substrates during a deposition, which suggests the ion milling step contributes to this scatter. Discharge and beam details have been recorded from ion beam mills, but do not change enough to account for this variation. Milling rate has appeared to vary between some mills based upon the frequency of use of the equipment, but although differences between devices milled sequentially on the same day have been considered, no trends have been found.

Overall, a number of factors at all stages of the device fabrication process have been considered. However, whilst some parameters correlate with the scatter in the data, none of them do across every device. It appears that in this fabrication process, there are sufficient sources of scatter that identifying trends to determine the root causes is impossible, due to the scatter caused by other effects. Having non-superconducting contacts also impacts this scatter, as there is a greater section of heterostructure - the ‘wires’ - that contributes to the resistance.

## 5.3 Conclusions

In this chapter, current-perpendicular-to-plane devices have been fabricated, and their transport properties measured in the normal state. The devices show clear GMR behaviour and are suitable for spin transport studies over a range of  $d_{\text{Nb}}$ . Comparison of the resulting data such as magnetoresistance and normal state spin diffusion length with values from the literature suggest that aspects of the fabrication process such as FIB milling may lead to implantation reducing the quality of these devices. Background effects such as negative magnetoresistance and a large degree of scatter resulting from the multi-step fabrication process are also observed, which complicate data interpretation.

The key results from this chapter are:

- A spin decay length in normal state Nb of  $l_{sf}^{\text{Nb}} = 26.1 \pm 1.7$  nm was calculated at  $< 10$  K using a fit from Valet-Fert theory.
- This fit is associated with an interface flipping parameter of  $\delta = 0.24 \pm 0.07$  also for  $< 10$  K, which is in agreement with a similar structure from the literature.
- The reduced  $l_{sf}^{\text{Nb}}$  compared to literature values suggests patterning may be influencing the transport within the nanopillar.
- No trend of magnetoresistance with nanopillar area, length or width has been observed.
- Magnetoresistance effects can arise from single cuts to the heterostructure. These effects suggest current travels mainly in the bottom Cu contact layer away from the nanopillar.
- Negative magnetoresistance effects increase and then plateau with increasing Nb thickness.
- The multiple fabrication steps to create these devices and the contribution of structure besides the pillar to total resistance leads to large scatter in magnetoresistance data.



# Chapter 6

## Superconducting spin valves

In this chapter, the superconducting properties of the fabricated spin valves are investigated, with the aim of using these devices to perform spin transport measurements in the superconducting state. The trend of the superconducting critical temperature,  $T_c$ , with the thicknesses of layers within the structure, the response of the devices to magnetic fields, and the difference between the parallel (P) and antiparallel (AP) states are all investigated. Complicating background effects in this state are analysed and discussed. A brief investigation into current-in-plane devices using this structure is also covered.

### 6.1 Background

#### 6.1.1 Current-perpendicular-to-plane spin valves

The study of current-perpendicular-to-plane (CPP) spin valves with superconducting spacer layers is extremely limited, possibly due to the challenges of fabrication of such devices compared with alternative current-in-plane (CIP) or lateral devices. An early investigation of CPP transport through a Py/Nb/Py device was performed by Johnson [137] who found a normal state spin diffusion length of  $l_{sf}^N = 780 \pm 160$  nm, a superconducting spin diffusion length of only 2 nm and that the spin relaxation time is much less than the charge imbalance relaxation time. However, this setup suffered from non-uniform current distribution and non-linear voltage response to increasing current, and later results for the normal state spin diffusion length in Nb were more than an order of magnitude lower [14, 53, 114].

An investigation into the difference in electron transport above and below  $T_c$  of the Nb spacer was performed with a CPP device in [14]. This device featured superconducting Nb leads to ensure homogeneous current density through the spin valve, which consisted of two 24 nm Py layers, one pinned by FeMn, on either side of an Nb spacer layer. Cu buffer layers were also present throughout the structure to improve interface quality. The giant magnetoresistance of the spin valve [inset, Fig. 6.1(a)], which was observed above

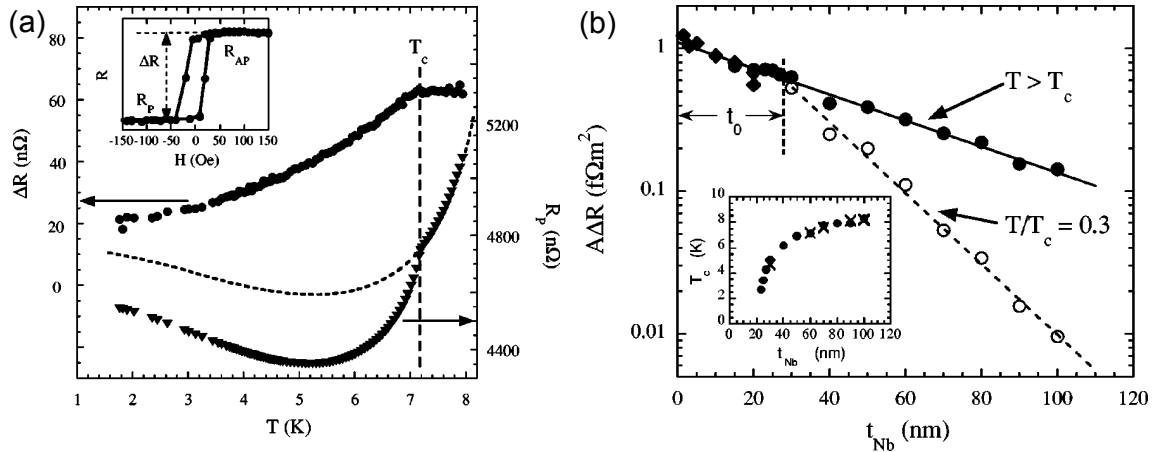


**Figure 6.1:** Spin decay through CPP superconducting spin valves. (a) The change of resistance (triangles) and magnetoresistance (circles) with temperature below  $T_c$ . Inset: A minor  $R(H)$  loop showing magnetoresistance of a device with  $d_{Nb} = 60$  nm. (b) The decreasing magnetoresistance with Nb thickness for devices both above (filled circles) and below (open circles)  $T_c$ . Inset:  $T_c$  vs.  $d_{Nb}$ . From [14].

and below  $T_c$ , was used to quantify the spin decay that occurred across Nb. In the superconducting state magnetoresistance is positive and appears to be GMR, which would be mediated by quasiparticles (QP GMR). This is supported by the decay of magnetoresistance with temperature below  $T_c$  [Fig. 6.1(a)], corresponding to the reduced QP transport at lower temperatures as the superconducting gap increases. The spin decay length in the normal state was  $l_{sf}^N = 48 \pm 3$  nm, and was shorter in the superconducting state,  $l_{sf}^S = 17.5 \pm 0.6$  nm, as shown in Fig. 6.1(b). The shorter length in the superconducting state is attributed to the extra spin decay mechanism of quasiparticles - conversion into Cooper pairs via Andreev reflection. The convergence of the superconducting and normal state magnetoresistance values at a Nb thickness of 28 nm is taken to be the limit below which Andreev reflection of QPs does not occur, which corresponds to roughly twice the calculated Ginzburg-Landau coherence length in Nb; the authors conclude that QP decay via Andreev reflection occurs over a coherence length. Note however, that no spin valves were tested in the superconducting state for Nb thicknesses less than 30 nm.

There are no significant investigations into quasiparticle transport with CPP superconducting spin valves other than these results, and both have issues as discussed. Superconducting Nb nanopillar spin valves have been investigated in [138], but this used the spin valve as a component of a Josephson junction investigating triplet pair transport, and did not consider quasiparticle transport. As a result, a study into the interaction of polarised spin currents and superconductivity over short dimensions is missing from the literature.

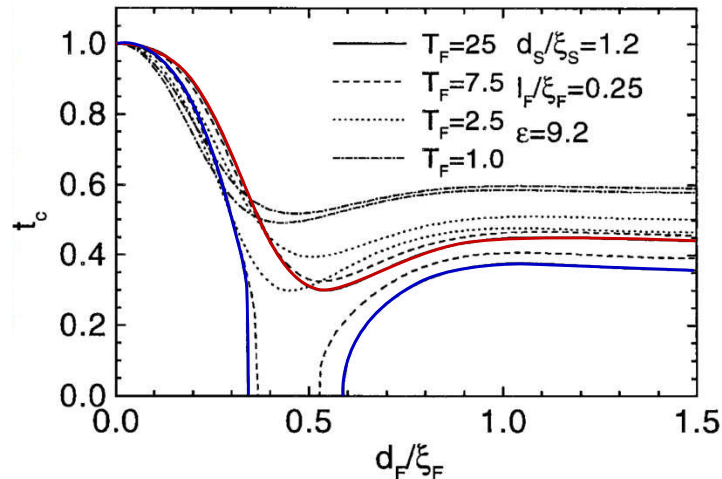


**Figure 6.2:** Dependence of reduced transition temperature,  $t = T_c/T_{c0}$  on  $d_F/\xi_F$ , plotted for different transparencies ( $T_F$ ). The maximum transparency case has been highlighted for clarity. The top line (red) represents the AP-state, and the bottom line (blue) the P-state; the difference in the  $y$ -direction is  $\Delta T_c/T_{c0}$ , where  $T_{c0}$  is the isolated transition temperature. For the highlighted maximum transparency case,  $\Delta T_c/T_{c0} > 0.3$ , so could reasonably be expected to be hundreds of mK or possibly higher given a  $T_{c0}$  of a few Kelvin, suggesting a large theoretical region where infinite magnetoresistance of the spin valve is possible. After [7].

### 6.1.2 Current-in-plane spin valves

A superconducting layer sandwiched by two ferromagnets was first proposed by de Gennes [40], who considered ferromagnetic insulators affecting a central superconductor based upon interfacial interactions, and showed the energy of the superconducting layer was dependent upon the angle between the magnetisations of the ferromagnets. Later, building off the work on normal state spin valves, Oh<sup>1</sup> [41], Tagirov [7], and Buzdin [42] proposed superconducting spin valves in which the superconductivity of the S layer could be switched on and off using relatively small magnetic fields to switch the orientation of the ferromagnets from parallel to antiparallel. These papers predict  $\Delta T_c = T_c^{AP} - T_c^P$  from the superconducting spin valve effect should be of the order of a few Kelvin, influenced by key parameters such as  $d_S/\xi_S$ ,  $d_F/\xi_F$  (where  $d_i$  and  $\xi_i$  are the thickness and coherence length of layer  $i$  respectively) and ferromagnet exchange energy (see Fig. 6.2). Buzdin and Tagirov also consider the transparency of the interfaces as extremely important, and Oh mentions spin orbit scattering as having a significant effect. Unfortunately, experimental realisations of these devices have not been able to match the size of these  $\Delta T_c$  predictions.

The first experimental demonstration [139] of a spin valve used Nb as a spacer with the weak ferromagnet CuNi, with the aim of reducing the exchange energy experienced by the superconductor, and maximising the ratio  $d_F/\xi_F$ , one of the key parameters of the device as suggested by theory, although to define a better AP-state Py layers were

<sup>1</sup>Oh considered an F/F/S heterostructure, rather than the F/S/F of de Gennes, Tagirov and Buzdin, but the physics is similar and the function the same.

added outside each CuNi layer as well. Their measured  $\Delta T_c$  was only 6 mK, much smaller than the superconducting transition width. Other attempts have been made using this structure [140–142] achieving similar  $\Delta T_c$  values, and one study [140] suggested this was in fact the limit of this system, due to the low interface transparency and high  $d_S/\xi_S$  ratio ( $\approx 2$ , where theory suggests a value close to or below 1 is necessary for a strong effect).

The primary issue facing experimental realisation of large  $\Delta T_c$  values is one of finding a way to realistically enter the parameter space required for such values [139]. Investigations of parameters such  $d_S/\xi_S$  and  $d_F/\xi_F$  have indicated trends agreeing with theory, including observation of oscillating  $\Delta T_c$  with changing  $d_F/\xi_F$  [139, 141–144] and an increase of  $\Delta T_c$  with decreasing  $d_S/\xi_S$  [140]. However, achieving the ideal parameter space is challenging; Miao *et al.* [145] used an epitaxial structure with Fe ferromagnetic layers and V as the superconductor, taking care to maximise interface cleanliness but despite multiple papers [140, 141, 143, 144, 146] considering interface transparency one of their key issues, this study still only achieves a maximum  $\Delta T_c = 30$  mK, possibly due to the strong exchange energy of Fe, or the band mismatch between Fe and V. Moraru *et al.* [147] found a significant improvement in  $\Delta T_c$  from a few mK up to 41 mK [Fig. 6.3(a)] for a decrease in Nb spacer layer thickness from 18 nm to 17 nm (or  $d_S/\xi_S$  from  $\approx 3$  to  $\approx 2.8$ ). However, in spin valves with spacer layers less than 17 nm, superconductivity was destroyed completely, preventing  $d_S/\xi_S \approx 1$ . This study uses Ni as strong ferromagnetic layers, as this allows easier access to the clean limit as the superconducting spin valve effect will persist for thicker layers. Studies using weaker ferromagnets may have overly focused on the  $d_F/\xi_F$  ratio, where theory predicts larger  $\Delta T_c$  values are possible for less ideal  $d_F/\xi_F$  as long as transparency and layer cleanliness are good (see Fig. 6.2). There appears to be limited work on the dependence of  $\Delta T_c$  and the superconducting spin valve effect on  $d_S/\xi_S$  beyond acknowledging that smaller values are closer to the theoretical ideal.

The aim for a superconducting spin valve is to maximise the difference in resistance between the two states. A large  $\Delta T_c$  leads to this as it allows a device to be superconducting in the AP-state, and fully normal in the P-state. To achieve this however, it is not the absolute  $\Delta T_c$  that matters, but the ratio of  $\Delta T_c$  to the superconducting transition width,  $\delta T$ . Some studies have instead focused on minimising  $\delta T$  - one F/F/S structure (using Fe for F and In for S) [143, 149] had a maximum  $\Delta T_c = 19$  mK but a  $\delta T \approx 7$  mK, allowing full N to S switching. The small  $\delta T$  value was achieved by applying a magnetic field during measurement, which ensured both F layers were single domain, minimising stray fields that would increase  $\delta T$ . Other studies have also measured  $\Delta T_c$  with a field applied during measurement [139, 148, 150, 151]. The effect of domains on superconducting transition width was also investigated in [152], which concluded Ta was a better growth buffer layer for their IrMn/NiFe/Nb/NiFe spin valves as the spin structure of IrMn encouraged by growth upon Nb lead to increased domains in NiFe, broadening the transition.

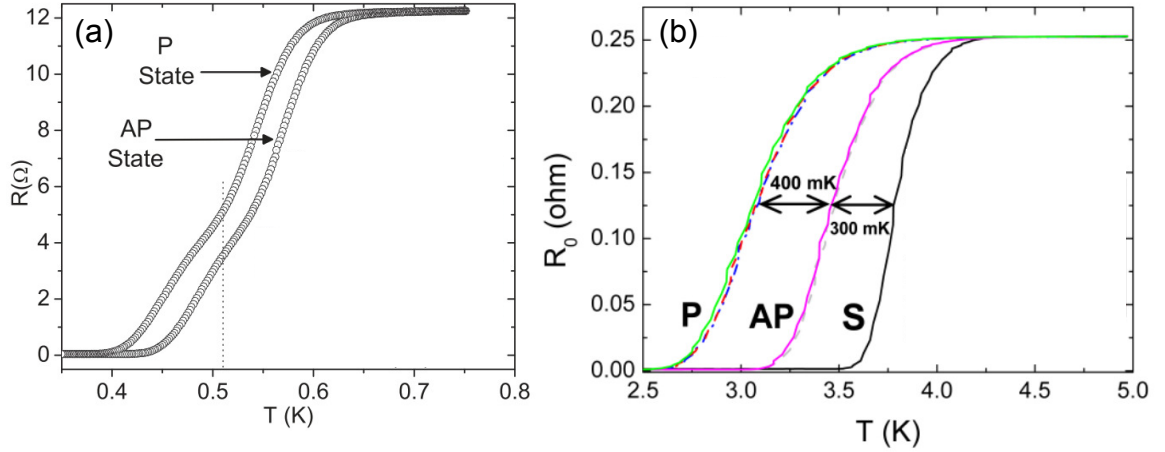


**Figure 6.3:** The spin valve effect,  $\Delta T_c = T_c^{AP} - T_c^P > 0$ , from different spin valves. (a) The largest reported effect for transition metal ferromagnets,  $\Delta T_c = 41$  mK. The transition width is greater than  $\Delta T_c$ . From [147]. (b) Devices with rare-earth metallic ferromagnetic layers have shown values of  $\Delta T_c$  of hundreds of mK. ‘S’ corresponds to Ho in the virgin, spiral magnetic state, which would be of less use than the P-state for a spin valve undergoing constant switching. From [148].

$\Delta T_c$  values of hundreds of mK have been reported in a few instances, for devices with metallic rare earth ferromagnetic layers [Fig. 6.3(b)] such as Ho, Dy and GdN [148, 153] or the ferromagnetic insulator EuS [154]. Smaller  $\Delta T_c$  values were also reported alongside these large values [148, 154], indicating it is not purely materials selection that leads to these increased values; the parameters considered above are still important. Differences between these devices and those with transition metal ferromagnets should be noted; in [148] the exchange energy required by a model fitting the data required an extremely small value of the exchange energy, suggesting some alternative physics was involved. Using ferromagnetic insulators [154] conforms to the original picture proposed by de Gennes, as it does not involve the proximity effect. Other large results based on epitaxial superlattices of Fe/V have also been reported [150, 155] but  $\Delta T_c$  values for these devices were based off of an extrapolation of P-states with field applied, and do not represent a true stable P to AP switch, as a true AP-state appears not to be possible in these devices according to magnetic hysteresis loops.

Negative values of  $\Delta T_c$  have also been reported [136, 156–163]. Some [143, 164] are attributable to the oscillation of  $\Delta T_c$  with  $d_F/\xi_F$  [Fig. 6.4(a)], which occurs due to interference effects of the superconducting wavefunction, which oscillates in ferromagnetic layers. This can occur for both F/F/S [165] and F/S/F structures [166]. For the other results, such as in Fig. 6.4(b), two main explanations have been proposed; the first [156, 160, 162] considered spin accumulation of quasiparticles causing suppression of  $T_c$  in the antiparallel state [167] and the second suggested stray fields from the ferromagnetic layers suppressed the superconductivity [158, 161, 168]. Some groups have conceded stray fields may be the more likely explanation; for example, using similar structures to their previous re-

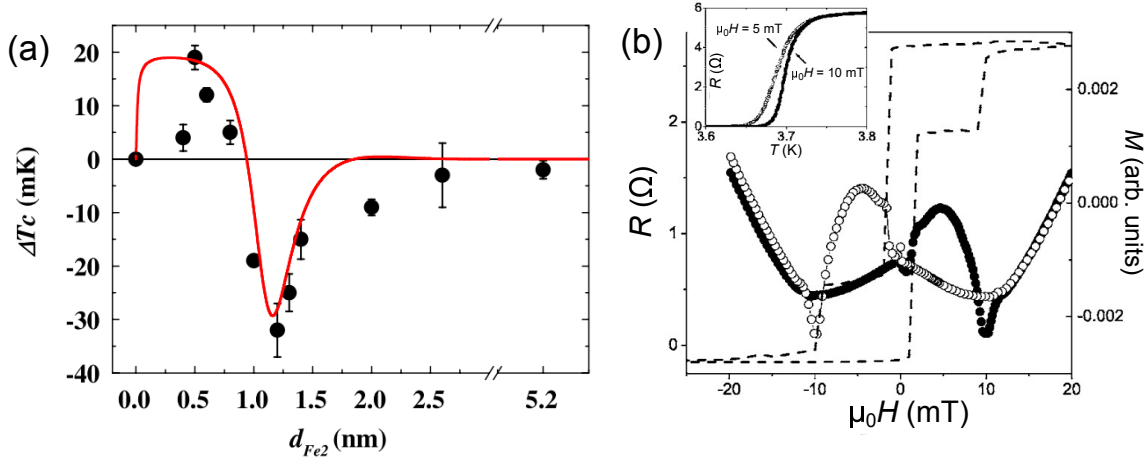


**Figure 6.4:** The inverse spin valve effect,  $\Delta T_c = T_c^{AP} - T_c^P < 0$ . (a) Some negative  $\Delta T_c$  values are associated with an oscillation of  $\Delta T_c$  observed with changing  $d_F$ . From [143]. (b) The inverse spin valve effect is associated with a positive change in resistance upon switching from the parallel to antiparallel state, here claimed to be a result of quasiparticle accumulation. From [156].

sults, the Aarts group demonstrate stray field effects [136] at a later date, contrasting with their earlier work [156]. However, there are still a few discrepancies [157], and other experiments demonstrating negative  $\Delta T_c$  values specifically rule out stray fields as an explanation [159, 160]. There is also limited consideration of the distinction between systems showing stray fields and those not, although it has been noted [163, 166, 169] that typically pseudo-spin valves have given rise to stray field results, whereas spin valves (which pin one ferromagnetic layer via exchange bias) have demonstrated positive  $\Delta T_c$ .

### 6.1.3 Superconducting transport

There are two ways to transport spin in a superconductor: using triplet Cooper pairs (see Section 2.3.4.3) or by using quasiparticles. Studies of the spin behaviour of quasiparticles have typically consisted of attempts to measure the spin diffusion length or the lifetime of quasiparticles in the superconducting state, which is linked to the decay of non-equilibrium (charge and energy) modes in the superconductor as well [170–172]. Spin flip scattering causing spin decay may arise from spin-orbit scattering from non-magnetic impurities [173], electron-phonon scattering [174] (which is reduced in the superconducting state), or as scattering from magnetic impurities [175]. Additionally, decay from Andreev reflection can also contribute, as shown in [14]. Andreev effects are often avoided by using tunnel junctions in a non-local or spin absorption technique (see Fig. 6.5).

The effect of superconductivity on spin transport within a material is still not conclusively shown. Increases in spin polarised quasiparticle lifetimes have been observed [8, 176, 178]. In the double tunnel junction setup used in [8], a bias-dependent tunnelling magnetoresistance was found, with maximum negative (conductance of AP-state

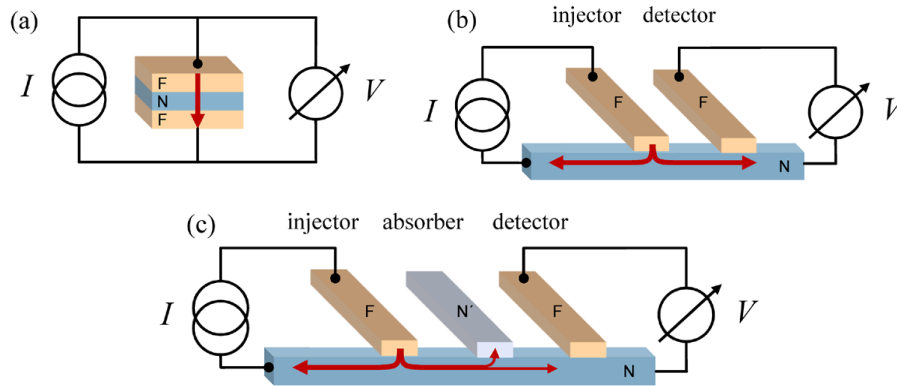


**Figure 6.5:** A selection of different measurement setups used to investigate spin dependent transport behaviours. (a) Local measurement on a spin valve. (b) Non-local measurement: the current takes one path, generating a pure spin current to be detected by the detector electrode. (c) Spin absorption technique: as (b), but with an added material (N') that absorbs some of the pure spin current, allowing quantification of the amount absorbed via comparison with (b). From [170].

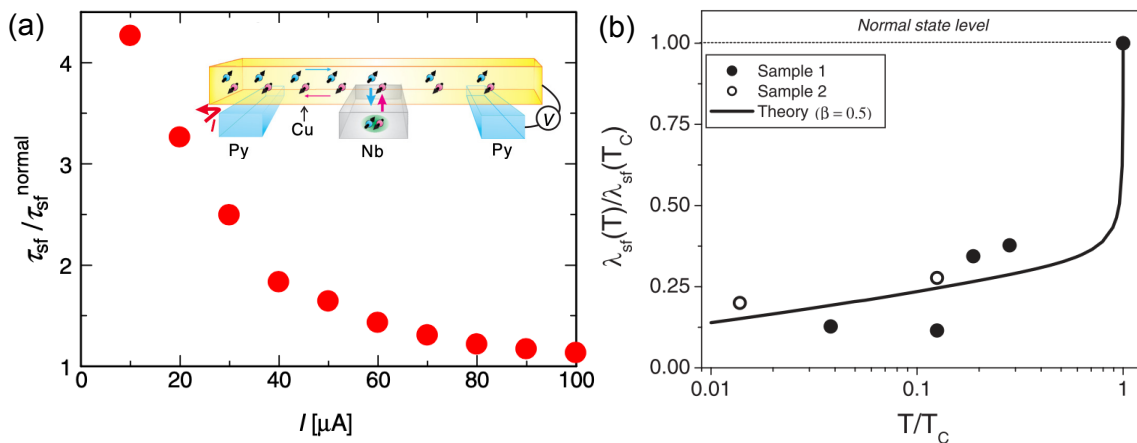


**Figure 6.6:** (a) Spin scattering time in the superconducting state decreasing with increasing bias current, corresponding to a higher temperature. Inset: the spin absorption technique setup used. After [176]. (b) Temperature dependent spin diffusion length in superconducting Al measured using a non-local setup. The reduced spin diffusion length compared to the normal state is attributed to magnetic impurity scattering. From [177].

is greater) magnetoresistance of  $\approx -55\%$  and maximum positive (conductance of P-state greater) magnetoresistance of  $\approx 23\%$ . These differences in conductance led to a spin accumulation in the central superconducting Al that suppressed the gap in the AP-state and was consistent with a  $10^6$  increase in quasiparticle lifetime. A more subdued increase [176] has also been observed [Fig 6.6(a)], possibly due to heating effects broadening the density of states. Decreased lifetimes were measured in [179], although this may have been related to proximity effects at the injector/superconductor interface, in the same way that Gu *et al.* observed a shorter spin diffusion length they attributed to Andreev reflection [14]. This demonstrates how the main decay mechanism determines the exact behaviour; in [177] it is noted that below  $T_c$  the different mechanisms also mean that spin diffusion length should not be given by a single value, but rather a function of energy and temperature, as shown in Fig 6.6(b). In that study, magnetic impurity scattering was found to be significantly more important than spin orbit scattering, and was believed to be the reason for a reduced spin decay length in the superconducting state. A reduced spin decay length in the superconducting state was also measured in [180], with an increase in non-local spin signal attributed to increased spin accumulation.

A series of similar studies reported increased spin diffusion lengths in the superconducting state [181–184]. However, these works featured Zeeman splitting of the superconductor alongside injection of quasiparticles, which introduces non-equilibrium energy imbalance into the superconductor. It has been suggested [171, 185, 186] that the long spin diffusion lengths apparently measured in these experiments are in fact an artifact of quasiparticle excitation due to the heating from the energy imbalance, becoming spin polarised due to the Zeeman splitting of the superconductor.

## 6.2 Experimental Results

This section covers experimental characterisation of the nanopillar spin valves in the superconducting state. Well-characterised superconducting behaviour will allow use of these devices in superconducting spin transport investigations in which the magnetoresistance of the spin valve will be used to quantify the spin decay across different central spacer layer thicknesses, as above  $T_c$ .

### 6.2.1 Superconducting transition

The superconducting transition is a key indication of the superconducting properties of different spin valves. With Cu contact layers, only the Nb spacer layer goes superconducting. However, this did not simplify analysis of the superconducting transition as much as expected (see Section 6.2.3.1 below). The superconducting transition temperature  $T_c$  is defined as  $R(T_c) = 0.5(R_N^{AP} - R_S^{AP})$ , where  $R_N^{AP}$  is the resistance in the antiparallel state

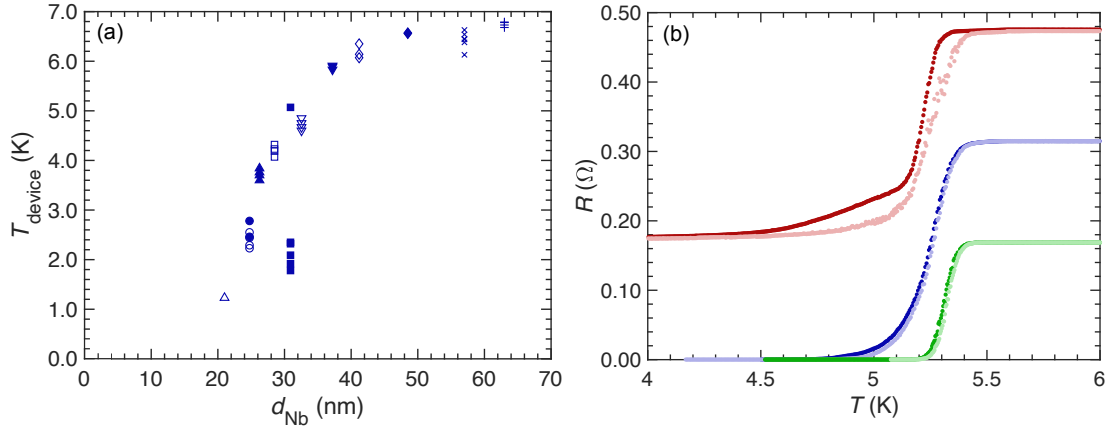


**Figure 6.7:** (a) Trend of the start of the superconducting transition,  $T_{\text{device}}$ , with  $d_{\text{Nb}}$ . Different shapes, including a distinction between filled and open shapes, indicate devices on different substrates. All devices are in the AP-state, measured at  $50 \mu\text{A}$ ,  $0.3 \text{ K s}^{-1}$ . (b) Superconducting transitions for three adjacent devices on the same substrate ( $d_{\text{Nb}} = 30 \text{ nm}$ ), with zero FIB (green), ‘thinning’ to a channel (blue) and shaped into a pillar (red), showing the impact of patterning on  $T_c$ . The red data have been decreased by  $0.4 \Omega$  for the sake of clarity. Dark colours indicate the antiparallel state, light are the parallel state.

at  $T_{\text{device}}$ , the onset of the device transition, and  $R_S^{AP}$  is the resistance in the antiparallel state of the device well below the superconducting transition.  $T_{\text{device}}$  is determined as the temperature at which the gradient changes by 0.03, (an amount consistently greater than background noise) due to the device transition. Figure 6.7(a) shows the dependence of spin valve  $T_c$  on Nb spacer layer thickness for a range of devices, with behaviour as expected, increasing rapidly from a critical thickness at around 20 nm before plateauing at higher Nb thickness, similar to the behaviour in [14] [inset, Fig. 6.1(b)]. Variation in  $T_c$  arises because of factors beyond  $d_{\text{Nb}}$ , including suppression from the proximity effect due to different interface quality, or impurities in Nb, either from the deposition or implanted during the Ar ion milling or FIB processes.

The impact of the processing can be shown through comparison of the  $T_c$  values of films at different processing stages, as in Fig. 6.7(b), which shows  $T_c$  values for untouched wire (green), wire thinned by FIB (blue), and a nanopillar device (red). In each case, the patterning broadens the transition width, and decreases  $T_c$ , from  $T_c^{AP} = 5.30 \text{ K}$ , to  $T_c^{AP} = 5.24 \text{ K}$ , to  $T_c^{AP} = 5.20 \text{ K}$ .

$T_c$  is also affected by the current density passing through the superconductor, as values closer to the critical current of the superconductor  $I_c$  lead to a lower  $T_c$ . In these devices, high currents suppress the superconducting transition, reducing  $T_c$  and broadening the transition so that it occurs over a greater temperature range. Additionally, as explained in Section 6.2.3.1, a number of  $R(T)$  curves of these devices demonstrate a ‘two-step’ behaviour, corresponding to one transition for the pillar and another for the ‘wires’ external to the pillar that are also included in the voltage measurement. Increasing

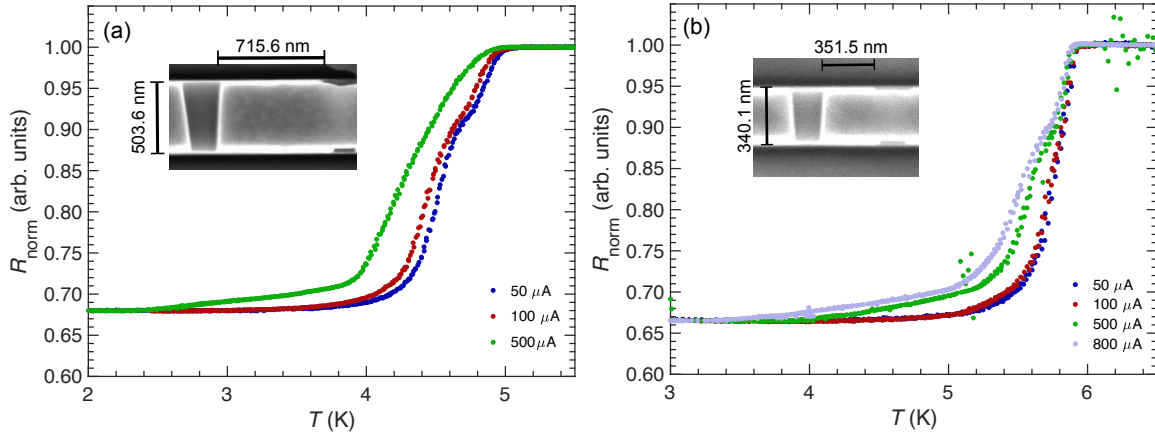


**Figure 6.8:** Normalised  $R(T)$  curves for two different devices in the AP-state for applied currents (labelled) below the superconducting gap. Both devices show a ‘foot’ appearing at the base of the transition for higher currents. (a)  $d_{\text{Nb}} = 32.5$  nm. The ‘two-step’ transition becomes less prominent with increased current. (b)  $d_{\text{Nb}} = 37.2$  nm. The ‘two-step’ transition becomes more prominent with increased current. Insets: SEM images of a plan view of the nanopillars, showing the different sizes.

current can either make this ‘two-step’ behaviour less prominent [Figure 6.8(a)] or more prominent [Fig. 6.8(b)]. This difference is expected to be related to pillar size, the device in Fig. 6.8(b) having an area of  $1.2 \times 10^5$  nm<sup>2</sup>, compared to  $3.6 \times 10^5$  nm<sup>2</sup> in (a), which would lead to a current density three times larger in the smaller device, possibly causing current suppression of  $T_c$ , whereas the broadening observed in other devices could instead be Ohmic heating from the normal state parts of the device. However, measurements of differential resistance vs. current bias, and estimations of current density in these devices (taking 1 mA gives 0.8 MA cm<sup>2</sup>, orders of magnitude less than critical current densities in Nb based nanodevices [187]) suggest these devices are far from the critical current, so further investigation is needed to conclusively show the origin of this different current-dependent behaviour.

These plots also demonstrate other current-dependent aspects of the transition. The devices in both Fig. 6.8(a) and (b) show a significant decrease in gradient towards the base of the transition, giving a ‘foot’ to the transition, suggesting part of the Nb has slightly weaker superconductivity that is more susceptible to increased currents. Observation of this ‘foot’ in a thinned wire with no nanopillar suggests the nanopillar is not the origin of this effect, although the ‘thinned’ wire around the nanopillar compared to the thicker wire untouched by FIB may be responsible. An alternative suggestion is the polycrystalline grain structure of Nb, which gives rise to grain boundaries, which is considered the reason behind similarly shaped  $R(T)$  curves in [163] - the majority of the transition occurs as the grains go superconducting, and then the final resistance decrease occurs as the superconducting coupling across the boundaries increases. This coupling would increase more slowly with decreasing temperature at higher currents. Interestingly, within this foot region it is noted that the AP-state experiences greater current suppression than the P-

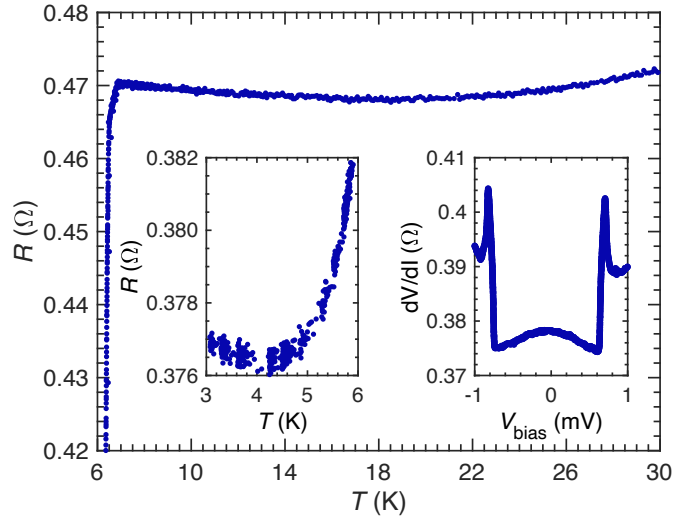


**Figure 6.9:** Main figure:  $R(T)$  from a device with  $d_{\text{Nb}} = 37.2$  nm showing increase of device resistance in the normal state below 20 K. Inset left: the same device below  $T_c$ , showing a resistance increase below 4.2 K. Inset right: differential resistance vs. voltage bias at 1.6 K for the same device, showing the resistance decrease with increasing bias below the gap, which is attributed to the same cause as the increase in resistance below  $T_c$ .

state. It is suspected that the stray fields that exist in the wires AP-state (Section 6.2.3.2) cause increased suppression of  $T_c$  compared to the P-state, which is likely the origin of the lower gap in these wires. With increased current also suppressing  $T_c$ , the AP-state is closer to being fully suppressed than the P-state. As a result, the difference between AP- and P-states is greater at higher current biases than for the standard  $50 \mu\text{A}$  bias.

Another effect visible in  $R(T)$  curves of these devices is the increase of resistivity with decreasing temperature below the superconducting transition, visible in Fig. 6.8(b) and highlighted in the left inset to Fig. 6.9. This increase is particularly observed in devices with  $T_{\text{device}} > 5$  K, and a similar increase is also observed in [14]. This resistance change also shows a voltage dependence below the gap, as shown in Fig. 6.9 (right inset). The curves in Fig. 6.8(b) suggest the minimum of resistivity does not shift in temperature with increasing bias, but rather the resistive foot ‘joins’ the increasing resistance below  $T_c$  at a lower temperature. [188] suggested a competition between excess resistance caused by spin accumulation in F and the increase in interface conductivity due to Andreev reflection could lead to non-monotonic resistance behaviour at F/S interfaces below the superconducting transition. However, the model is calculated for a mesoscopic F/S interface, and not an entire spin valve system. Additionally, for these data, this resistance increase does not appear in every heterostructure, which would indicate that the F/S interface was changing significantly between depositions according to this theory, despite identical deposition layers and conditions. An alternative explanation is the Kondo effect, caused by magnetic impurities in the devices increasing electron scattering at low temperatures. In this case, the dependence on voltage in the right inset to Fig. 6.9 would be explained as

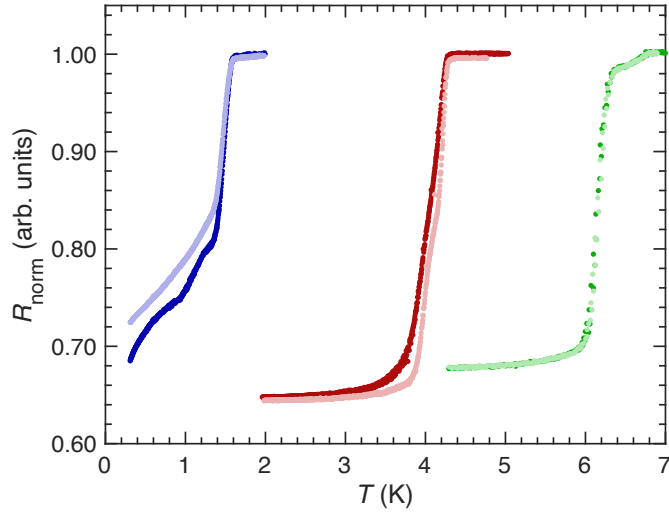


**Figure 6.10:** Normalised  $R(T)$  curves for three devices (21 nm: blue, 28 nm: red, 57 nm: green) in the AP- (dark) and P-states (light) showing the three different levels of relative suppression of  $T_c$  observed for each state -  $\Delta T_c > 0$  for blue,  $\Delta T_c < 0$  for red and  $\Delta T_c = 0$  for green.

local heating of the device, as higher temperatures correspond to lower resistances, given the differential resistance curve was taken at 1.6 K, below the 4.2 K minimum in that device (left inset). Many devices do show an increase in resistance between 20 K and the transition (Fig. 6.9 main plot), and it is possible the increase below  $T_c$  is the continuation of this. Furthermore, some devices with large resistance increases below 20 K do not go superconducting, indicating the presence of magnetic impurities. One likely source of magnetic impurities is resputtered material from the magnets on the substrate table during sputter deposition. However, if this were the source, it might be expected that the Kondo effect would appear for every heterostructure deposited, which is not the case.

### 6.2.1.1 $\Delta T_c$

Comparison of  $R(T)$  curves in the P- and AP-states reveals a temperature difference  $\Delta T_c = T_c^{AP} - T_c^P$  in the devices, such as those shown in Fig. 6.10. Devices show three different behaviours: blue is an example of a device demonstrating positive  $\Delta T_c$ , and red is an example of a device demonstrating negative  $\Delta T_c$ , with the AP-state more suppressed in the device transition. A  $\Delta T_c$  is also observable in the wire transitions, which remains when measurements are made on the wire only. Green data show a device with thick (57 nm) Nb, where no real  $\Delta T_c$  can be seen.

A positive  $\Delta T_c$  is the expected result from a CIP superconducting spin valve, based upon the average exchange energy in the superconductor being dependent on the relative orientation of the adjacent ferromagnetic layers. This is immediately noteworthy as a  $\Delta T_c$  based upon this effect has never been previously observed in an all-metal superconducting CPP spin valve. A negative  $\Delta T_c$  suggests the AP-state has a lower  $T_c$  and

higher resistance. Whilst this could be a result of spin accumulation of the quasiparticles suppressing the superconducting gap in the AP-state as in [8], it is likely the degree of spin accumulation associated with the GMR of the device is too small to cause such a suppression of  $T_c$ , and instead, the reduced  $T_c$  is a result of the positive  $\Delta R$  present in the device, as shown in Fig. 6.11. This link between  $\Delta T_c$  and  $\Delta R$  also explains the non-zero  $\Delta T_c$  of the wires, which have positive values of  $\Delta R$  associated with them (Section 6.2.3.2).

Most spin valves demonstrating positive  $\Delta T_c$  have large separations between the wire and device transitions, and the P-state becomes the higher resistance state at the onset of the lower temperature device transition. The exception to these features is the blue curve in Fig. 6.10, which does not demonstrate a separation between device and wire transition, and shows positive  $\Delta T_c$  behaviour from the start of the wire transition, rather than only the device transition, confirmed by  $R(H)$  measurements on only the wires of that device. By contrast, all other devices have  $\Delta T_c < 0$  in the wires, even where  $\Delta T_c > 0$  in the device. The blue curve in Fig. 6.10 appears notably different to the other  $R(T)$  curves. Partially, this is due to having positive  $\Delta T_c$ , which in all devices is a broader (and hence of shallower gradient) transition than the wire transition. Additionally, the transition does not appear to be fully ‘complete’ for this device, even at 0.3 K, which also affects its appearance. However, the curve is important to include, because it demonstrates  $\Delta T_c > 0$  in the wires. This, and the lack of separation between the two transitions, is attributed to this device having the smallest  $d_{\text{Nb}} = 21$  nm of all devices that could be measured in the superconducting state. This wire behaviour demonstrates that positive  $\Delta T_c$  behaviour is encouraged to appear by the nanopillar; in the wires, a low  $d_{\text{Nb}} = 21$  nm is required, but in the pillars, this effect can appear for higher values of  $d_{\text{Nb}}$ .

The negative  $\Delta T_c$  values do not show any current dependence that can be separated from the increased difference in between AP- and P-states at higher current in the resistive foot, as previously discussed. As this effect is present in thinned wires as well as nanopillar devices, it is not considered to be related to spin accumulation of quasiparticles.

### 6.2.2 $R(H)$ response

The two different behaviours reflected in the  $\Delta T_c$  measurements are confirmed by associated measurements of  $R(H)$ . Figure 6.12 shows minor  $R(H)$  loops recorded at  $T/T_{\text{device}} = 0.3$  (where  $T_{\text{device}}$  is the onset of the superconducting transition), (a) demonstrating a device where the P-state has higher resistance, comparable in shape to  $R(H)$  measurements from CIP investigations in literature [139, 141, 142, 145, 147, 168, 189, 190] and (b) illustrating a minor  $R(H)$  loop with  $R^{AP} > R^P$ . Devices of the type in Fig. 6.12(b) show GMR decreasing with thicker  $d_{\text{Nb}}$  and still show GMR, although now this would be carried by unpaired non-equilibrium quasiparticles - ‘QP GMR’. As in the normal state,  $\Delta R$  values for devices with thick Nb spacers are hard to determine, as the values are very

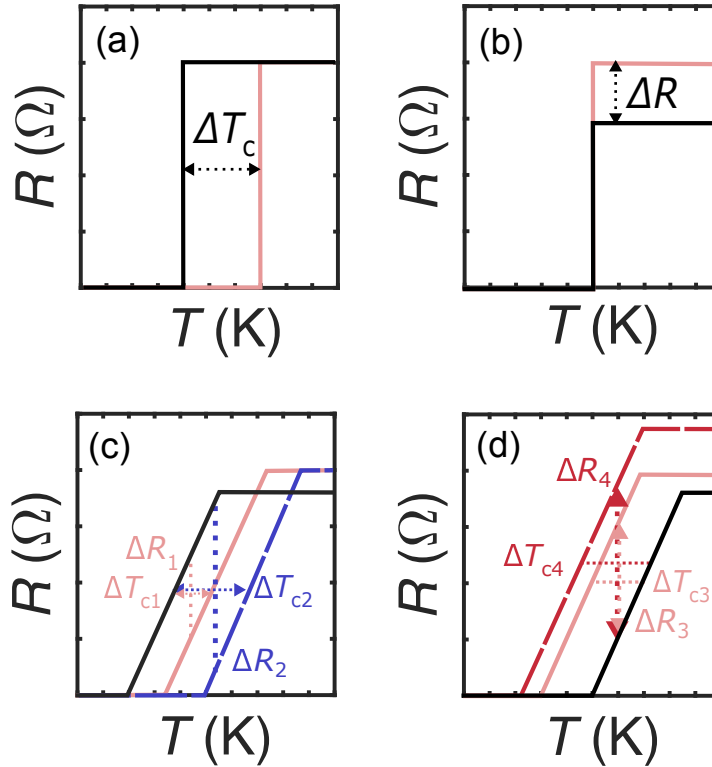


**Figure 6.11:** Schematic illustration demonstrating the link between  $\Delta R$  and  $\Delta T_c$  values, exaggerated for clarity. (a) In an ideal device showing only the superconductor proximity effect, the parallel state (black) has lower  $T_c$  than the antiparallel (pink) state ( $\Delta T_c > 0$ ). (b) In an ideal device showing only GMR, the antiparallel state has a higher resistance above  $T_c$  than the parallel state ( $\Delta R > 0$ ). (c) A finite gradient in the superconducting transition links  $\Delta T_c$  and  $\Delta R$ . Here, for the same normal state  $\Delta R$ ,  $\Delta T_{c2} > \Delta T_{c1}$  ( $\Delta T_{c2}$  is more positive) causing  $\Delta R_2$  in the transition to be more negative than  $\Delta R_1$ . (d) Inversely, a larger  $\Delta R$  in the normal state can lead to a more negative  $\Delta T_c$ : here  $\Delta R_4 > \Delta R_3$ , so  $\Delta T_{c4}$  appears to have a greater (more negative) value than  $\Delta T_{c3}$ .

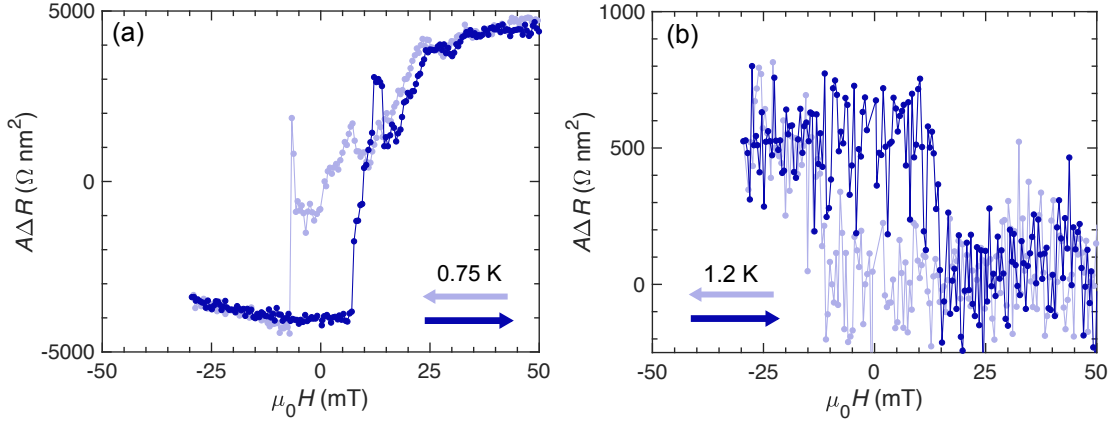


**Figure 6.12:** Minor  $R(H)$  loops for two different devices at  $T/T_{\text{device}} = 0.3$ , demonstrating two distinct behaviours. (a) An example  $R(H)$  for devices with a positive  $\Delta T_c$ , with the P-state higher resistance at  $\mu_0 H = 0$  T. The slight field dependence of resistance away from the central switching region is probably due to the low  $H_{c2}$  value of these devices, which all have lower  $T_{\text{device}}$  values. There are also peaks in the resistance near the coercive field, suggesting stray fields penetrating the superconductor as the magnetisation switches. For this device,  $d_{\text{Nb}} = 31$  nm. (b) An example  $R(H)$  for devices with a negative  $\Delta T_c$ , appearing to show GMR as above  $T_c$  ( $R^{AP} > R^P$ ) although with a reduced magnitude. This GMR must be mediated by quasiparticles, or ‘QP GMR’. For this device,  $d_{\text{Nb}} = 28$  nm. In both plots, arrows represent the sweep direction for each colour, starting at high positive fields.

small and are often overwhelmed by AMR, still observed below  $T_c$ . The two different behaviours observed in  $\Delta T_c$  and  $\Delta R$  are explored in depth in Chapter 7.

### 6.2.3 Complicating factors

The features discussed in this section have been identified as not corresponding to the behaviour of the spin valve within the nanopillar, and therefore not relevant to the main results of the interaction of spin and superconductivity, but important to acknowledge as part of this investigation.

#### 6.2.3.1 Double transition

Some  $R(T)$  traces display a ‘double transition’ behaviour - a step suggesting two distinct superconducting transitions. This only occurs for nanopillar devices, not unpatterned heterostructures or wire sections without ‘side cuts’. This double transition is unrelated to the ferromagnetic layers in the structure, but is a purely geometric effect, as shown in Fig. 6.13(a) where pillars patterned in from Cu/Nb/Cu multilayers showed a double transition (dark blue), compared to the wires (light blue). This also shows that the ‘upper’ transition temperature of the two pillar transitions ( $T_c = 4.60$  K) agrees with the wire transition temperature ( $T_c = 4.39$  K). The agreement is not perfect, but across a substrate the upper  $T_c$  of nanopillars tends to be more constant than the lower  $T_c$ , as noted for a few example substrates in Table 6.1. The origin of the two transitions is

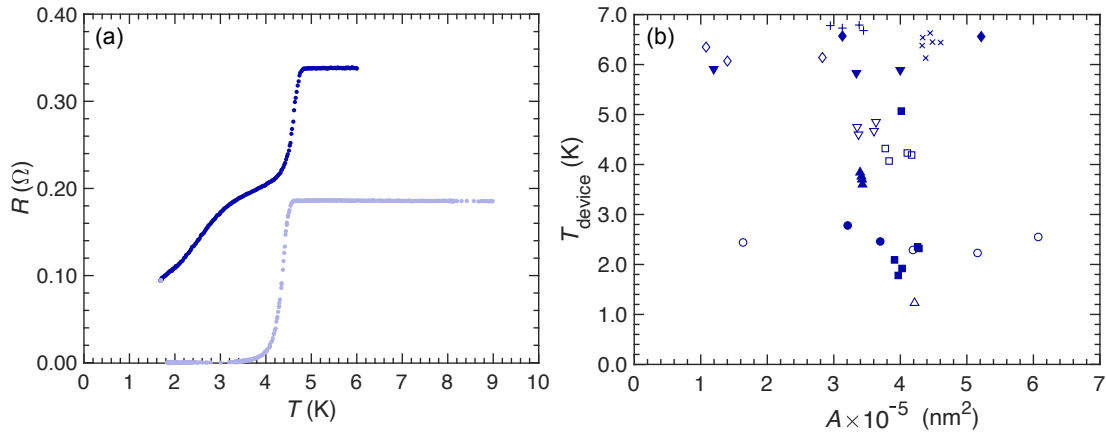


**Figure 6.13:** (a)  $R(T)$  curve measured on a ‘thinned wire’ (light blue) and on a nanopillar device (dark blue) from the same substrate with a Cu(200 nm)/Nb(30 nm)/Cu(200 nm) heterostructure. There is agreement between the ‘wire’ transition and upper part of the device transition. (b)  $T_{\text{device}}$ , the top of the transition, vs. pillar area for a range of devices across multiple substrates. There seems to be no correlation of transition temperature with area, despite the apparent impact of isolating some Nb into the pillar. Shapes correspond to devices on the same substrate.

therefore the separate sections of Nb, in the wires and in the pillar. The variation of the wire  $T_c$  across a substrate is a result of the patterning the heterostructure has undergone (reference Nb transition breadth  $\approx 50$ -100 mK, wire transition breadth  $\approx 500$ -1000 mK), indicating minimal broadening from thickness variation. Patterning also explains the increased transition width of the lower pillar transitions. However, the nanopillar device transition temperature does not depend on the nanopillar area, as shown in Fig. 6.13(b). Similarly, the separation between wire and device transition does not depend on  $d_{\text{Nb}}$  or pillar area and is consistent across devices on a substrate. These observations indicate some unknown effect is causing  $T_c$  suppression.

The fact that some devices still exhibit single transitions, such as 20\_8\_21b J3 and J4 from Table 6.1, is attributed to the two transitions being wide and blending together, such as occurs at higher currents in some devices [Fig. 6.8(a)]. The alternative current-dependent behaviour enhances the double transition appearance, which supports the attribution to the pillar and wires rather than another effect. Equally, one device that demonstrated only a single transition upon first measurement shows a clear double transition when measured again a year later. This supports a pillar vs. wires explanation for the behaviour, as the reduced size of the pillar would make it more susceptible to degradation via oxidation.

Although these structures do have a 10 nm Nb seed layer, this is not the source of one of the superconducting transitions. Both the upper ‘wire’ and lower ‘device’ transitions vary from structure to structure, corresponding to a dependence on the thickness of the Nb central layer, as expected, such as in Fig. 6.7(a). This dependence on  $d_{\text{Nb}}$  strongly

Sample and Device number	$T_{\text{upper}}$ (K)	$T_{\text{lower}}$ (K)
18_8_15c J1	3.90	2.44
18_8_15c J4	3.85	2.29
18_8_15c J5	3.84	2.23
18_8_15c J6	3.90	2.55
20_8_18b J2	5.23	2.32
20_8_18b J3	5.12	1.92
20_8_18b J4	5.10	1.78
20_8_18b J5	5.23	2.09
20_8_18b J7	5.22	2.35
20_8_21b J1	7.01	6.68
20_8_21b J2	7.01	6.73
20_8_21b J3	6.78	6.78
20_8_21b J4	6.79	6.79

**Table 6.1:** Comparison of the temperature at which the upper (higher  $T$ ) and lower (lower  $T$ ) transitions of the double transition occur across different devices showing the effect on three different substrates. The upper transitions are relatively consistent across a substrate, whereas the lower transition temperatures show greater variation. Some substrates, such as 20\_8\_21b, feature devices with a double transition, such as J1 or J2, and some with only a single transition, J3 or J4. There is no visible difference between the nanopillars or correlation with their dimensions to explain this difference.

suggests neither transition is due to the unchanging Nb seed layer. Additionally, in measurements where only the wire was measured, single transitions were observed, at the same temperature as that of the upper transition in the pillars on the same substrate, which were typically consistent for all devices across a substrate.

It is worth noting the Cu/Nb/Cu devices in Fig. 6.13(a) showed a very small resistance increase above  $T_c$ , indicating the Kondo effect is present in low levels. The reduced effect may be because less resputtering of the magnet material occurs for these structures with only three layers. The superconducting transition does not saturate at measured temperatures, likely due to proximitising of the Cu contacts by superconducting Nb. Unfortunately this prevents any identification of a resistance increase below  $T_c$ , which would rule out the possibility of a link to an S/F interface, as discussed in Section 6.2.1.

### 6.2.3.2 Wires

‘Wire effect’ corresponds to any effect outside of the two vertical cuts defining the nanopillar - for example, the higher temperature transition is considered the ‘wire’ transition as opposed to the ‘device’ transition. Measurements have been performed on three types of wire: ‘thinned’ wires (FIB-milled narrowed channels that have not had the vertical cuts that would define a nanopillar), sections without any FIB milling, and also the wires connecting device regions to contact pads to investigate these effects. Above  $T_c$ , these wires show either noise, or magnetoresistance behaviour that inverts when the device is rotated 90°, confirming AMR can be present in these structures. Analogously to CIP results in the literature, in the region of the superconducting transition,  $R(H)$  behaviour can be observed [Fig. 6.14(a)], which is unexpected as positive magnetoresistance corresponding to QP GMR is not likely without the potential difference encouraged by the CPP transport. Additionally, minor  $R(H)$  loops demonstrate that it is possible to apply a field greater than  $-30$  mT, then remove it, and the resistance will remain high. This implies that this effect is not simply associated flux penetration from an applied field, but instead is connected to the domain state of the ferromagnetic layers of the device in the AP-state. This result varies more than in device  $R(H)$  loops. Below  $T_c$ , these wires are completely superconducting for all but the thinnest Nb spacer layer, and only noise is seen in  $R(H)$  measurements [Fig. 6.14(b)].

Positive magnetoresistance has been reported in CIP literature [136, 156–163] and while some have considered spin accumulation of quasiparticles as a potential explanation [156, 160, 162], this is not considered likely here due to the lack of similar GMR above  $T_c$ . Instead, stray fields from the Py layers are considered to be the cause of increased resistance in the AP-state in the transition region, where the  $H_{c2}$  value of the superconductor is low, as in [158, 161, 168]. In pseudo-spin valves, the fields originated from a multi-domain state caused by the two ferromagnetic layers having similar coercivities, and penetrated the spacer layer as the domain states coupled together. Similar results

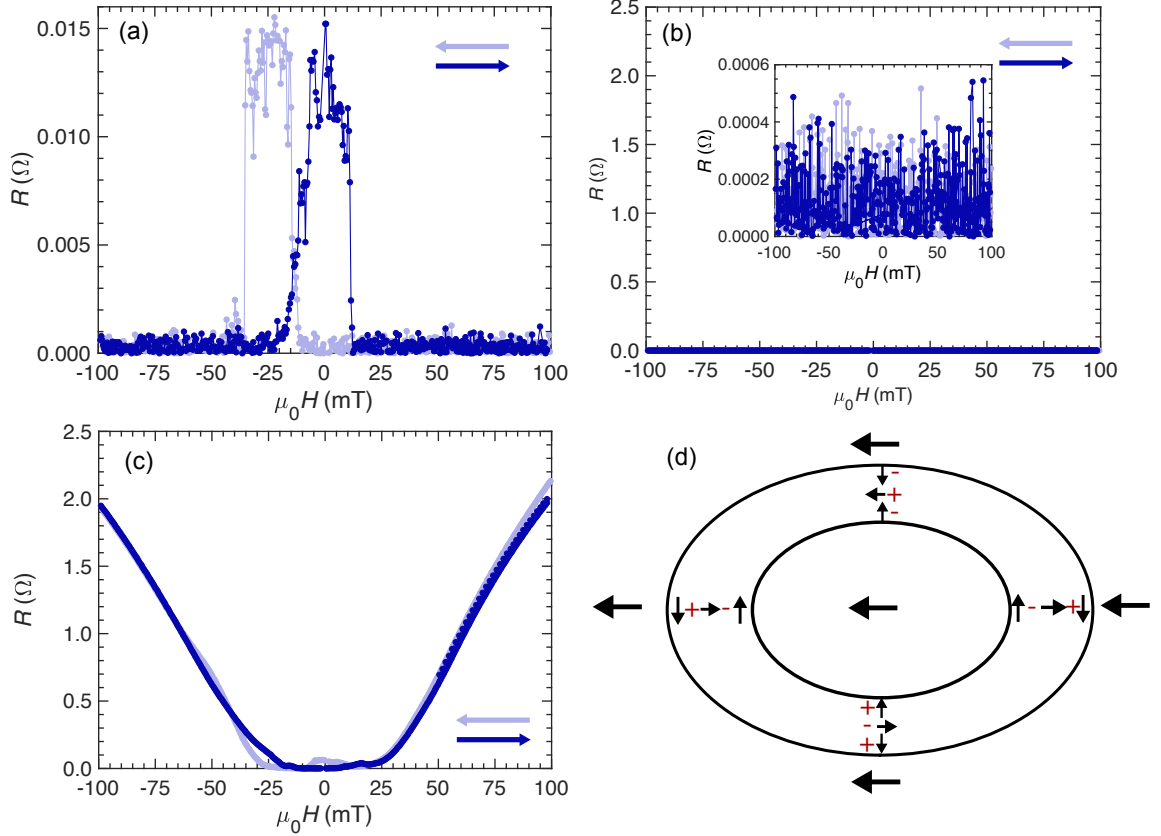


**Figure 6.14:** Major  $R(H)$  loops on various ‘wire’ sections of devices. (a) Mid-transition,  $R(H)$  measurements on the wires show similar responses to the device measurements. This is thought to arise from domain effects causing stray fields. (b) Typically, below the transition the wires show no magnetic response, being fully superconducting with no  $\Delta R$  observed. The inset shows the same data on a smaller scale. (c) For the device with thinnest  $d_{\text{Nb}} = 21$  nm, even at the lowest temperature the wires show a magnetoresistance response, which exclusively for this substrate shows the proximity effect. In all  $R(H)$  plots, arrows represent the sweep direction for each colour, starting at high positive fields. (d)  $360^\circ$  domain structures can remain under an applied field in exchange biased Py layers due to differences in pinning strength across a material. Arrows represent magnetisation direction, + and - represent areas of magnetic charge. After [71].

were found in [136], where pseudo-spin valves demonstrating AMR in the normal state then demonstrated positive magnetoresistance consistent with suppression of superconductivity in the Nb spacer layer, due to the coupled fixed multi-domain structure of the Py layers. The FeMn of the spin valves in this investigation ensure that the layers have different coercivities. However in [71], transmission electron microscopy investigating the switching of Py when adjacent to FeMn or in a spin valve showed that multi-domain states may still arise in an exchange biased spin valve structure. On switching a Py layer adjacent to FeMn,  $360^\circ$  structures of opposing magnetisation could remain beyond field values that would reverse the bulk of the film [Fig. 6.14(d)]. Coupling across the spin valve caused the free layer to switch in a different manner to an isolated Py layer. Although the spacer layers in [71] were thin, [136] indicates that coupling can occur in Py/Nb/Py spin valves in the superconducting transition for Nb spacer layers of 50 nm, with stable vortices in the Nb. Switching of the pinned Py layer was “erratic”, with different areas of the film reversing at different stages, encouraged by pinning to FeMn being stronger in some areas than others. Taken together, these results imply a multi-domain state may be possible in the devices of this thesis, which could lead to stray fields that cause the suppression of the central superconductor. In these devices,  $H_{\text{ex}}$  was also found to be small compared to similar systems (Section 4.2.1), suggesting part of the FeMn was not effectively coupling to the Py, which may also be related to a multi-domain state in these structures. It is worth noting that studies of domain structures in Py wires were also performed in [191], which showed a coercivity increase from “magnetisation buckling” that gave rise to a mixed domain state as a result of patterning. The patterning of the heterostructure could therefore also contribute to the mixed domain state. Overall, the positive magnetoresistance in the wires may be attributable to some mixed domain state that forms in the ferromagnetic layers, with associated stray fields suppressing superconductivity. This domain state may be related to the exchange bias of the FeMn or patterning processes.

An alternative suggestion is crossed Andreev reflection (CAR) occurring in the wires. CAR in this case would occur when the electrons resulting from Cooper pair breakage entered the two separate F layers, which would be increased in the AP-state, leading to a lower  $T_c$  and hence higher resistance. However, CAR would not be expected to lead to the variation upon repeated measurement observed in these wires.

A mixed domain state with penetrating stray fields in the AP-state, as a result of incomplete switching of layers is consistent with the observations made from  $R(H)$  loops, which slightly vary each time, but allow a relatively stable state that is maintained in a minor loop. Patterning also affects domain structure, supported by the discrepancy in coercive fields measured via  $M(H)$  and  $R(H)$  loops. This behaviour does not affect the main findings of these devices, as the wires do not show giant magnetoresistance above  $T_c$ , so those results could not be confused with this. Well below  $T_c$ , the wires are observed to be fully superconducting with no field response, as  $H_{c2}$  is sufficiently large [Fig. 6.14(b)].

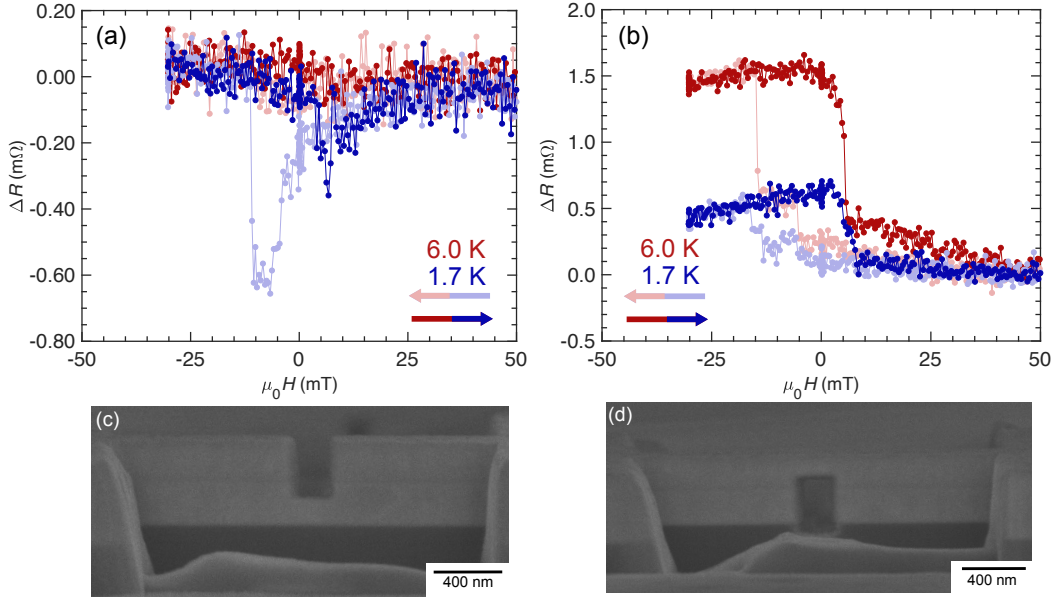


**Figure 6.15:** (a) Minor  $R(H)$  loops from a device with only a single ‘top’ cut in the normal (red) and superconducting (blue) states. For this device, in the superconducting state there is a significant negative magnetoresistance component around the switching of the free layer, and the giant magnetoresistance is similar to the normal state. (b) Normal and superconducting minor  $R(H)$  loops from a device with a single ‘bottom’ cut. For this device, magnetoresistance is clearly greater in the normal state. Arrows in (a) and (b) indicate the field sweep direction of each colour, starting at high positive field. (c) SEM image of the top cut device in (a). (d) SEM image of the bottom cut device in (b).

Devices with a low transition temperature show negative  $\Delta R$  values, which could not be confused with these positive values from the wires. The only results which may be affected by these effects are positive  $\Delta R$  values mid-transition, such as the temperature dependence of the QP GMR (Section 7.2.1.2).

### 6.2.3.3 Single Cuts

As discussed in Section 5.2.5, the effect of a single vertical cut on the electrical response was investigated, and apparent magnetoresistance effects shown to appear. In each of Fig. 6.15(a,b) there is a distinct difference between the magnetoresistance effects in the normal and superconducting states, suggesting different current paths in the superconducting state. The relative sizes of magnetoresistance between the normal and superconducting states for each device suggests the current paths being taken. Given the Nb wires are superconducting, current travels in the Nb (rather than the Cu contacts) until the cut forces the current path to divert away from the Nb layer. In the ‘top cut’ device, magnetoresistance is the same in the superconducting state and normal state ( $\Delta R = 0.05 \text{ m}\Omega$ ). The current passes through the bottom (free) Py layer, through the bottom contact, and through the bottom Py again on the other side of the cut as the current returns to the Nb.  $\Delta R$  arises due to spin decay in the Cu contact over the  $\approx 200 \text{ nm}$  path. This mag-

netoresistance is smaller than most nanopillar devices due to the long current path, but still noticeable because of the long spin flip length of Cu. This is balanced by the fact that in the normal state only a small proportion of current contributes to  $\Delta R$  for the top cut device, so magnetoresistance is about the same. In the ‘bottom cut’ device, magnetoresistance in the superconducting state is smaller than the normal state. The apparent current path is to pass through the Py and then FeMn on top, Cu contact and then FeMn and finally Py on the return. FeMn is known to have an extremely short spin diffusion length [53, 128], and is likely responsible for the reduced  $\Delta R$  in the superconducting state compared to the normal state. However, it is surprising that the FeMn, which is 10 nm thick, does not reduce  $\Delta R$  to zero, and other effects may be involved.

The negative magnetoresistance in the ‘top cut’ in Fig. 6.15(a) is of similar magnitude to that observed in nanopillar devices, further confirming the negative magnetoresistance of those devices is a result of the free layer of Py, and is large compared to the normal state as the current mostly travels in the bottom Cu in the normal state. The magnetoresistances here in the superconducting state are not due to stray fields as the measurement occurred significantly below  $T_c$ , away from the transition.

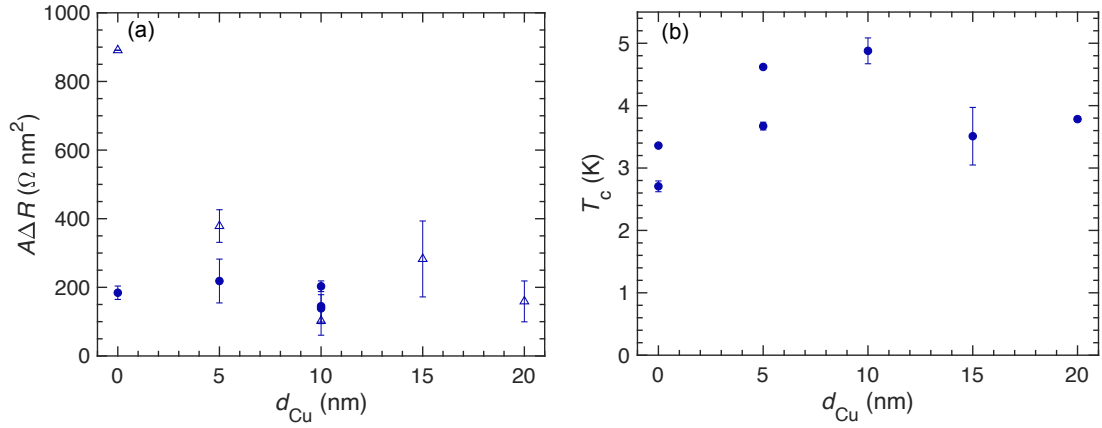
Overall, as discussed previously, the existence of magnetoresistance effects from single cuts is concerning as they indicate that measured effects on complete pillars are not exclusively from the devices. These effects explain an observed change in magnetoresistance below the wire transition temperature but above the pillar transition in devices with a large enough separation for this to be measured. However, note that a decay of magnetoresistance with  $d_{\text{Nb}}$  is still found below  $T_c$  (Fig. 7.3), where these single cut effects should be independent of  $d_{\text{Nb}}$ , and therefore spin transport across the superconductor in the nanopillar spin valves is still being measured.

## 6.2.4 Layer dependence

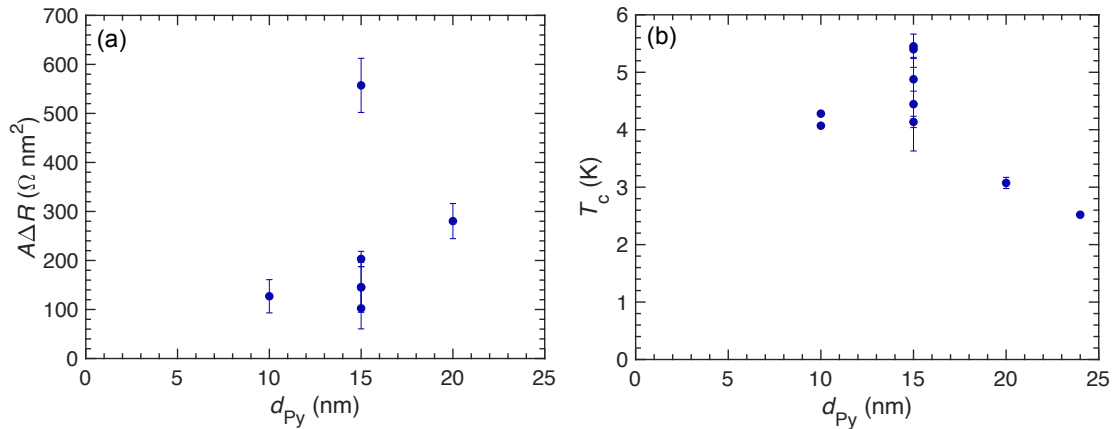
### 6.2.4.1 Cu and Py

Figure 6.16 shows how the superconducting properties of the spin valves change with the thickness of the central Cu buffer layers. In Fig. 6.16(a) the open triangle data, all from a single deposition, suggest a decrease in the superconducting state magnetoresistance with increasing  $d_{\text{Cu}}$ , although other data suggest the Cu does not affect the QP GMR. In Fig. 6.16(b), accounting for the scatter due to fabrication, it appears  $T_c$  follows the same shape as in the normal state;  $T_c$  of Nb is improved when a thin layer of Cu prevents direct contact with the F layers, but increasing  $d_{\text{Cu}}$  then decreases  $T_c$  due to an increasing inverse proximity effect.

Figure 6.17 shows how the same superconducting variables change with the  $d_{\text{Py}}$ , the thickness of the F layers. In line with the behaviour in the normal state, Fig. 6.17(a) shows that magnetoresistance increases with increasing  $d_{\text{Py}}$ , and  $T_c$  decreases with increasing  $d_{\text{Py}}$ ,



**Figure 6.16:** The effect of increasing  $d_{\text{Cu}}$  of the buffer layers on (a)  $A\Delta R$  in the superconducting state from QP GMR devices and (b)  $T_c$  of nanopillar spin valves. As for the normal state, in (a) filled circles correspond to sequential depositions when only two structures were deposited per deposition, and open triangles are structures all from the same deposition.



**Figure 6.17:** The effect of increasing  $d_{\text{Py}}$  on (a)  $A\Delta R$  from QP GMR devices in the superconducting state and (b)  $T_c$ . Apart from an outlier at 15 nm, QP GMR increases with  $d_{\text{Py}}$ , as in the normal state. Increased suppression from more ferromagnetic material leads to a decrease of  $T_c$  with increasing  $d_{\text{Py}}$ . The scatter in devices at  $d_{\text{Py}} = 15$  nm shows that other effects can be greater than the variation due to variation from ferromagnetic layer thickness.

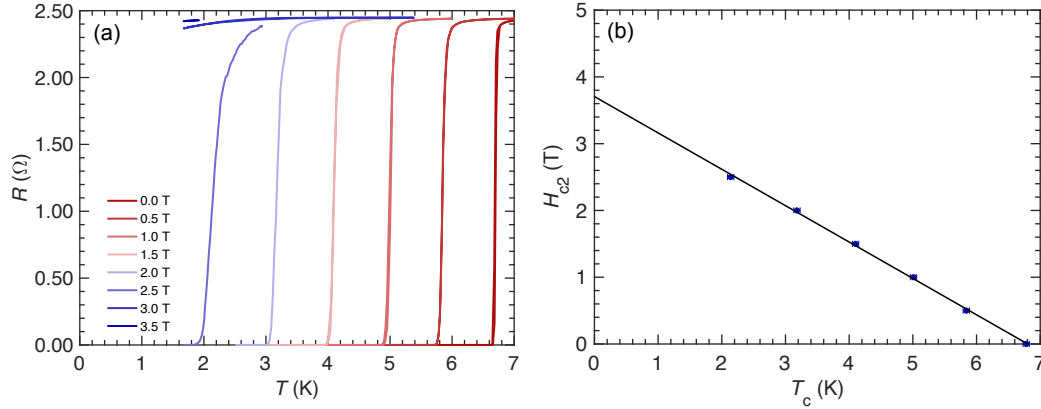


**Figure 6.18:** (a)  $R(T)$  curves from an unpatterned bare Nb film (30 nm) at different applied magnetic fields. (b) The  $T_c$  values extracted from (a), plotted against field, used to estimate a zero temperature  $H_{c2}$  value, with a straight line fit via orthogonal distance regression. Error bars are the same size as the points.

as expected. In both plots the large degree of scatter for devices at 15 nm, of which there were many more created than those of other thicknesses, demonstrates the importance of other effects on magnetoresistance and  $T_c$  as well as  $d_{Py}$ .

### 6.2.5 Coherence length

A coherence length,  $\xi_S = 9.4 \pm 0.3$  nm, was measured via out of plane  $H_{c2}$  measurements on an isolated 30 nm Nb film (Fig. 6.18), using  $H_{c2} = \Phi_0 / (2\pi\xi_S^2)$ , where  $\Phi_0 = 2.07 \times 10^{-15}$  Wb is the flux quantum. This value is not unreasonable compared to other coherence length calculations and measurements in similar spin valve devices [14, 140, 169]. Using  $\xi_S \approx \sqrt{\xi_0\lambda}$ , where  $\xi_0 = 38$  nm [192], this suggests the mean free path in these devices is short at  $2.3 \pm 0.1$  nm. Alternatively, calculating the mean free path using  $\rho_{Nb}\lambda = 0.38$  f $\Omega\text{m}^{-2}$  [193],  $\lambda \approx 4.1 \pm 0.9$  nm. Whilst these values are the same order of magnitude, the discrepancy between them suggests there may be some errors unaccounted for in these measurements: possibly related to the inconsistency of device behaviour as noted in Section 5.2.6.

### 6.2.6 CIP devices

A series of structures were deposited to compare the CIP behaviour of the heterostructure of this investigation to the CPP behaviour that was the main focus. The initial structure used for this was the standard structure without the thick Cu contact layers:

$$\text{substrate/Nb(5)/Py(15)/Cu(10)/Nb}(d_{\text{Nb}}\text{)/Cu(10)/Py(15)/FeMn(10)/Nb(5),$$

for all thicknesses in nm units, and measured without any patterning. The 5 nm Nb layers below the bottom Py and above the FeMn are seed and cap layers respectively. Above the superconducting transition temperature, these devices do not show GMR, but

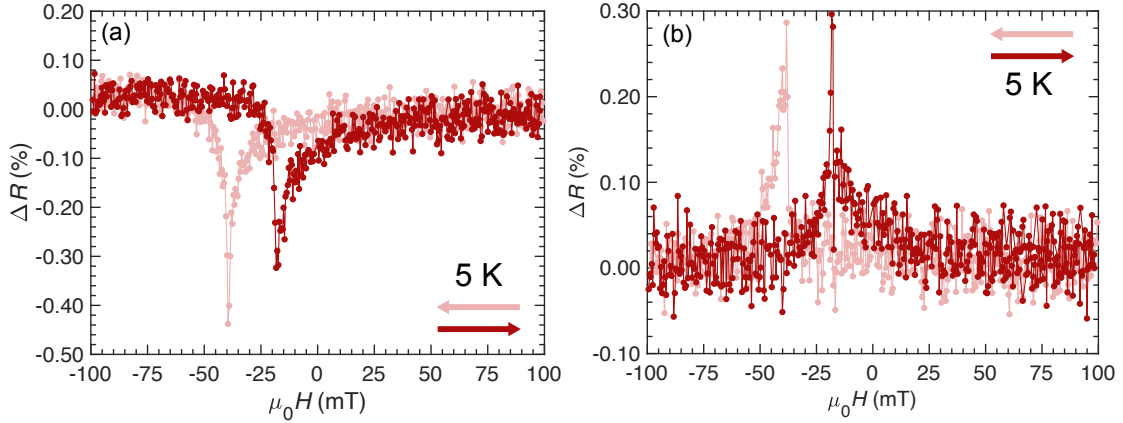


**Figure 6.19:**  $R(H)$  measurements on a CIP structure with  $d_{\text{Nb}} = 30$  nm with current running (a) parallel and (b) orthogonal to the applied field. The inversion of peaks between these two cases is characteristic of AMR behaviour. In both plots, arrows represent the sweep direction for each colour, starting at high positive fields.

are instead dominated by AMR [Fig. 6.19], which was also reported in the literature [136, 163, 168, 194]. This is noteworthy in these structures, given the uncertainty around the origin of negative magnetoresistance in the devices (Section 5.2.4). It is likely the AMR is more visible here as there are no thick Cu contact layers shunting the current away from the F layers. There are only two peaks in AMR, suggesting only a single layer contributes. However, unlike in the patterned devices, the field values of these peaks suggest the AMR is now from the pinned layer rather than the free layer.

Structures with reduced  $d_{\text{Py}} = 5$  nm, and only 5 nm of Cu (with no Nb) as the spacer layer were later deposited, and showed clear GMR behaviour, as seen in Fig. 6.20(a). For this device,  $\text{GMR} = 0.3\%$ , which is an order of magnitude smaller than the devices in [130],  $\text{Py}(15)/\text{Cu}(2.6)/\text{Py}(15)/\text{FeMn}(10)/\text{Ag}(2)$  which shows  $\text{GMR} = 2\%$ , and  $\text{Py}(5)/\text{Cu}(2.6)/\text{Py}(3)/\text{FeMn}(6)/\text{Ag}(2)$  which shows  $\text{GMR} = 3\%$ . This discrepancy may be related to the different Cu thickness, although considering a mean free path of 25.7 nm in Cu [195], this is unlikely. Instead, this suggests the interfaces of the devices deposited here cause increased scattering. Replacing this Cu with 4 nm of Nb resulted in no GMR effect in the normal state. Considering the possibility of magnetic dead layers and the effect of Cu buffer layers in the normal state CPP devices (Section 4.2.3), 10 nm Cu buffer layers were re-added here, but no GMR was seen. Removing the Nb, such that the spacer layer was only 20 nm of Cu, also resulted in no GMR, suggesting the mean free path for these devices may be smaller than 20 nm. Note that in Fig. 6.20(a) the free layer has an incredibly small coercive field, further confirming the increased coercive field causing discrepancy between  $M(H)$  and  $R(H)$  loops in patterned devices (Fig. 5.8) is a result of the fabrication into a nanopillar device. The increased coercivity of the pinned layer is attributed to the fact that it is thinner, which affects the exchange bias from the FeMn layer, as shown in Fig. 6.20(b) and as found in literature (Section 4.1.1).

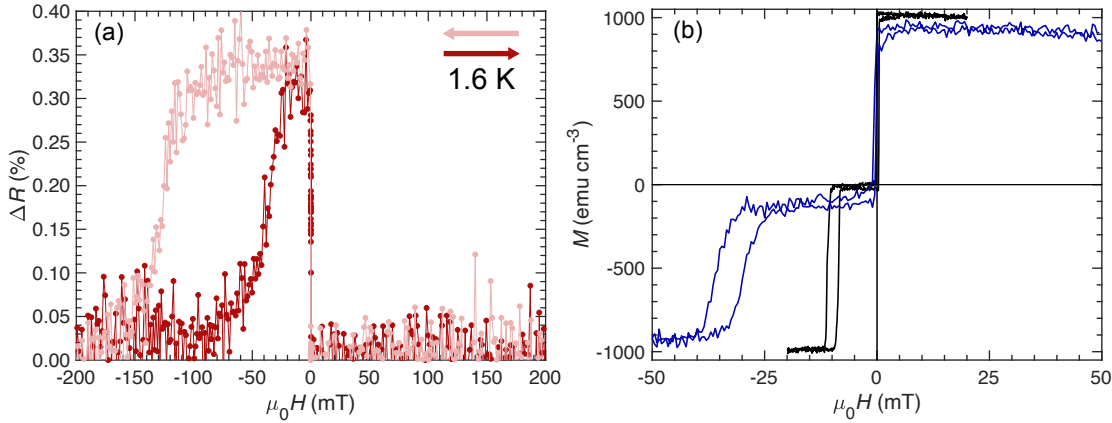


**Figure 6.20:** (a)  $R(H)$  from CIP structure with  $d_{\text{Py}} = 5$  nm and  $d_{\text{Cu}} = 5$  nm as the entire spacer layer. Current is parallel to applied field. Arrows represent the sweep direction for each colour, starting at high positive fields. (b)  $M(H)$  loops at 293 K for a CIP structure with  $d_{\text{Py}} = 15$  nm (black) and  $d_{\text{Py}} = 5$  nm (blue). The higher coercive field and exchange bias demonstrated by the blue curve reflects the values seen in (a).

$d_{\text{Nb}}$  values of 20, 30 and 35 nm were used in these devices to investigate the superconducting properties of the CIP spin valve, covering the thickness range of main experimental interest (see Chapter 7). In the superconducting state, spin valve devices are expected to show a difference between the P- and AP-states within the superconducting transition. However, the devices deposited here do not show a strong difference between  $R(T)$  curves in these states, as shown in Fig. 6.21. Taking  $R(H)$  measurements at temperatures within the transition region suggests it is not the P-state with higher resistance as would be expected, but instead the AP-state. This higher resistance in the AP-state is likely due to stray fields from the Py layers, as discussed in [136, 158, 161, 168], and as considered responsible for the positive magnetoresistance in the transition region of the patterned wires of the CPP structures. The lack of spin valve effect may also result from a dirty interface as suggested by the normal state results.

Further devices, such as a device with 25 nm Nb, a device with 15 nm Py layers with 5 nm Cu spacer for further comparison with [130], a 5 nm Py device with a superconducting central spacer, or the effect of patterning these devices into wires (but not nanopillars) could not be completed within the time constraints of the investigation. There is uncertainty about why structures from some groups show strong stray field dependent behaviour, and some the expected spin valve effect [169]. Further investigation into this using these heterostructures, which have demonstrated the spin valve effect in the CPP regime, would be of interest in the future to address this uncertainty.

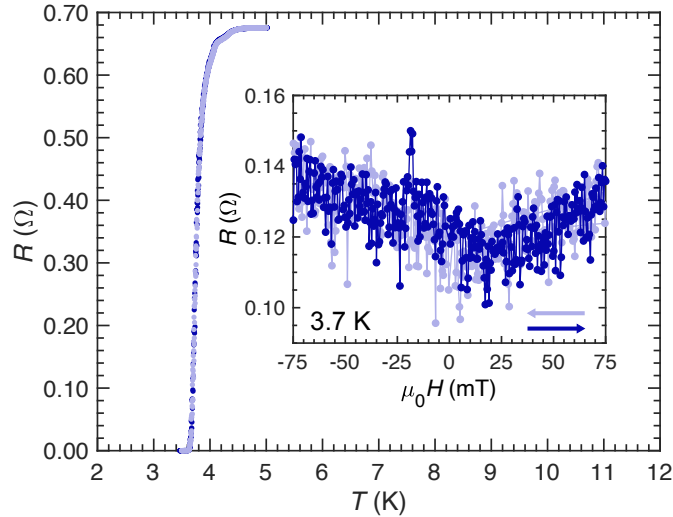


**Figure 6.21:**  $R(T)$  measurements on a CIP structure with  $d_{\text{Nb}} = 30$  nm in the parallel (light blue) and antiparallel (dark blue) states. There is no difference in transition temperature between the two states with no field applied. Inset:  $R(H)$  loop taken near the base of the transition, showing the increased resistance corresponding to the switching into the AP-state, as also found for the wires on patterned CPP substrates. The rise in resistance at higher fields is field suppression of superconductivity. Arrows represent the sweep direction for each colour, starting at high positive fields.

## 6.3 Conclusions

This chapter characterises the spin valves in the superconducting state, and has highlighted a number of complications that need to be considered when using these devices as a part of this structure. These complications are direct results of using the Cu contact layers rather than Nb. With superconducting Nb contact layers, no current would travel in the central layers of the wires, and so the impact of stray fields and the wire transition would be essentially negligible, although the single cut effects above  $T_c$  found may still be relevant. The main issue with Nb contact layers was their superconducting transitions complicating identification of the superconducting state of the spin valve spacer layer. However, Fig. 6.7(a) shows the transition temperature of the nanopillars saturates below 7 K, and with optimisation the contact Nb  $T_c$  can be kept above 8 K. Therefore, in future work of this nature, a return to Nb contacts would be beneficial overall.

This chapter has established that the nanopillar spin valves are superconducting over a range of thicknesses and still demonstrate magnetoresistance under an applied field sweep, rendering them suitable for spin / superconductivity investigations.

The key results from this chapter are:

- Nanopillar spin valves are superconducting above a Nb thickness of 20 nm.
- These spin valves demonstrate two distinct magnetoresistance effects in the superconducting state. These are explored in the next chapter.

- The presence of the Cu buffer layer improves  $T_c$ , but as in the normal state only a few nm thickness is needed.
- The thickness of the Py layer represents a balance between increased magnetoresistance and higher  $T_c$  of these devices. 15 nm is a suitable middle ground.
- Using non-superconducting contacts, especially with a Nb central layer, leads to background effects in measurements of these devices, including magnetoresistance effects from single cuts in the structure.
- These effects have been characterised, but further identification of their exact mechanisms could be of interest.
- Initial attempts at investigating the transition between positive and negative values of  $\Delta T_c$  in CIP devices using this structure have not been successful, but could be further explored.

# Chapter 7

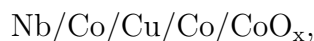
## Transport regimes in superconducting spin valves

Characterisations of the spin valve response in the superconducting state revealed two distinct regimes of behaviour (Section 6.2.2). In this chapter, these two regimes are investigated and a crossover between the two effects is discovered and characterised based upon the properties of the spin valves. A toy model is developed to help explain this crossover.

### 7.1 Background

There are only a few studies that have demonstrated both the spin valve effect, the difference in  $T_c$  in the antiparallel (AP) and parallel (P) states ( $\Delta T_c = T_c^{AP} - T_c^P > 0$ ), and the inverse spin valve effect ( $\Delta T_c < 0$ ) in the same structures. The earliest report was in [168], which used Py/Nb/Py/IrMn spin valves in which the spin valve effect or the inverse spin valve effect could be achieved based upon the sweep direction of the applied magnetic field [Fig. 7.1(a)]. The authors determined the inverse spin valve effect was due to a mixed domain state in the ferromagnetic (F) layers, causing stray fields that penetrated the superconducting layer (S) and gave rise to a resistance via vortex flow, supported by measurements of similar effects in Nb/Py bilayers. In a different study [163] on Py/Nb/Py pseudo-spin valves patterned into bridges, the inverse spin valve effect was seen in all but one device, and again attributed to the multidomain state arising from similar coercive fields of the F layers. In the exceptional device, the spin valve effect was instead seen, possibly due to coincidence of pinning sites in Nb and the flux lines from the domain walls in F.

The final observation of both effects in the same structure used nanowires of



an F/F/S structure [196]. Here,  $\Delta T_c$  is observed to change sign with current bias, from

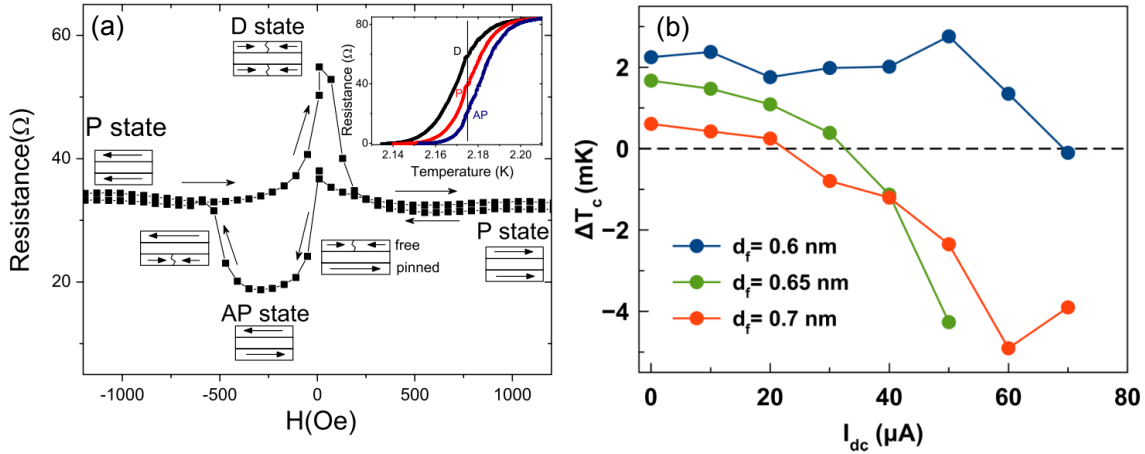


**Figure 7.1:** (a) Major  $R(H)$  loop of a Py/Nb/Py/IrMn spin valve, demonstrating a negative change in resistance, associated with the spin valve effect, for one sweep direction, and a positive change in resistance, corresponding to the inverse spin valve effect, in the other direction. The behaviours are associated with different domain states, as shown by the cartoons. Inset:  $R(T)$  curves for the three different magnetic states: AP (blue), P (red) and mixed domain (black). From [168]. (b) Current bias dependence of  $\Delta T_c$  in a Nb/Co/Cu/Co/CoO<sub>x</sub> nanowire, attributed to a spin Hall effect current perpendicular to the plane of the layers. From [196].

the standard spin valve effect at low biases [ $< 20 - 70 \mu\text{A}$ , depending on ferromagnet thickness, as shown in Fig. 7.1(b)] to the inverse effect at higher biases. This current bias dependence is attributed to the generation of an orthogonal spin current via the spin Hall effect, which suppresses the  $T_c$  of the multilayer differently in the P- and AP-states due to the different conductance of the layers to spin in each state.

These demonstrations of the spin valve and inverse spin valve effects do not cover the situation of the devices measured in this investigation. In [168], the ‘antiparallel’ and ‘domain’ states which give rise to the spin valve and inverse spin valve effect respectively are visible in the major  $R(H)$  loops of the spin valves. For the devices measured here, devices consistently demonstrate one effect or the other, and there is no dependence on sweep direction. The coincidence of pinning sites and domain walls suggested in [163] would not give rise to the systematic dependence of the crossover between the two effects discussed in Section 7.3. Finally, whilst the non-equilibrium state of [196] is similar, the devices in this investigation have current perpendicular-to-plane (CPP) rather than current in plane (CIP), so any orthogonal spin Hall effect current would be flowing in the limited width or length dimension of the nanopillars, parallel to the plane, and therefore would not affect  $\Delta T_c$  in the same way. As a result, the crossover between two behaviours demonstrated by the devices fabricated as part of this thesis is considered to be novel and of great interest.

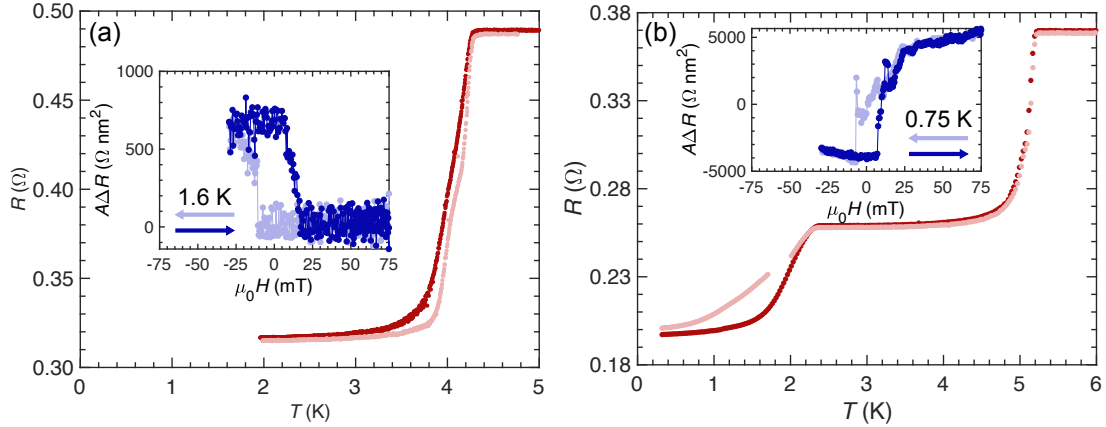


**Figure 7.2:**  $R(T)$  with minor  $R(H)$  loop insets for two devices on separate substrates, demonstrating the two different behaviours seen in this investigation. Dark red in  $R(T)$  is AP-state, and pink the P-state. Light blue in the insets is the sweep from positive to negative (switching from P- to AP-state) and dark blue the return sweep (switching from AP- to P-state), as indicated by the arrows. In (a) the  $T_c$  of the AP-state is more suppressed, which associated with a positive magnetoresistance in  $R(H)$ . In (b),  $T_c^P < T_c^{AP}$ , leading to a positive  $\Delta T_c$  and associated with a negative magnetoresistance. The gap in the pink curve in (b) is explained in the caption to Figure 7.10.

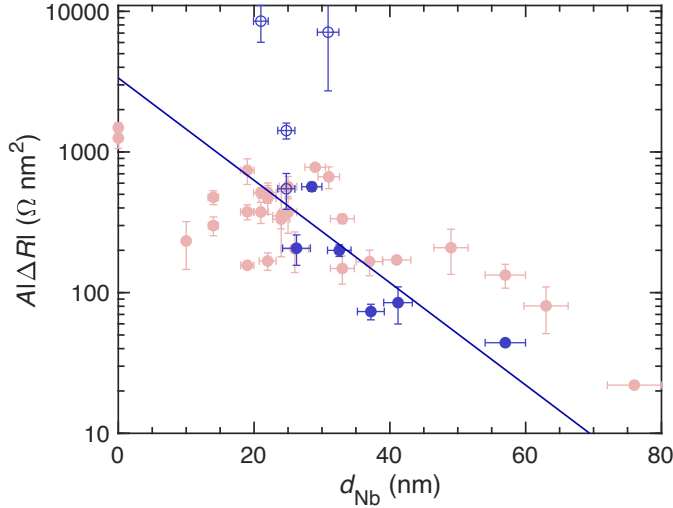
## 7.2 Experimental Results

Figure 7.2 demonstrates the two behaviours exhibited by the spin valve devices in the superconducting state, which suggest two different transport regimes. In Fig. 7.2(a), which is the behaviour shown by the majority of devices, the magnetoresistance is positive, as in the normal state, and  $\Delta T_c$  is negative. The positive magnetoresistance is as expected given results on a similar system [14]. However, other devices demonstrate results such as those in Fig. 7.2(b), which features positive  $\Delta T_c$  and negative magnetoresistance. This behaviour was not observed in [14] and has not been previously reported in CPP superconducting spin valves.

### 7.2.1 Quasiparticle giant magnetoresistance

For the majority of spin valves below the superconducting transition, the  $R(H)$  behaviour is very similar to the behaviour above  $T_c$ , such as in the inset Fig. 7.2(a). In the non-equilibrium spin situation in these devices, the current is injected into S as a flow of spin polarised quasiparticles (QPs). If these QPs do not decay or undergo Andreev reflection through the Nb spacer layer, then they are able to cause giant magnetoresistance (GMR) just as electrons traversing the device in the normal state do. In [14], the positive  $\Delta R$  values were indeed attributed to QP mediated giant magnetoresistance (‘QP GMR’), supported by the reduced decay length compared to the normal state and the dependence of this  $\Delta R$  on temperature below  $T_c$ .

In the devices measured here, the  $\Delta R$  values are reduced compared to the normal



**Figure 7.3:** Absolute  $A|\Delta R|$  values vs  $d_{\text{Nb}}$  for devices in both the normal state (pink) and superconducting state at  $T/T_{\text{device}} = 0.3$  (blue). Points and errors in  $A|\Delta R|$  are mean and standard deviation respectively of devices across a substrate. Open blue circles correspond to superconducting spin valve effect dominated devices, filled circles to QP GMR dominated devices. The blue line is a fit to the QP GMR data using a simple exponential decay, giving  $l_{sf}^S = 12 \pm 4$  nm.

state. Figure 7.3 shows a comparison of  $A|\Delta R|$  values for devices in the normal (pink) and superconducting (blue) states. For consistency between spin valve devices with different transition temperatures, the superconducting data is taken at a temperature of  $T/T_{\text{device}} = 0.3$ , where  $T_{\text{device}}$  is the onset of the device transition in the antiparallel state. In Fig. 7.3, devices exhibiting QP GMR have filled circles, whereas devices with open circles show the spin valve effect (see Section 7.2.2). Fitting an exponential decay to the QP GMR data obtains a spin decay length of  $l_{sf}^S = 12 \pm 4$  nm, which compares to the  $l_{sf}^N = 25 \pm 3$  nm in the normal state using the same simple fit (equation 5.3). Notably, the spin valve effect data do align with this fit to the QP GMR data. Previously [14], this reduced spin decay length has been attributed to Andreev reflection acting as an extra decay mechanism for quasiparticles compared to normal state electrons [39, 170]. Similarly, in these nanopillar spin valves, the QP GMR value approaches the normal state value at lower  $d_{\text{Nb}}$  values as less Andreev reflection occurs.

Positive magnetoresistance in the superconducting state has already been seen in these devices, as discussed in Section 6.2.3.2. However, these stray fields are not the cause of these effects in the nanopillar spin valves below  $T_c$ . Firstly, the stray fields were found to give rise to a  $\Delta R$  only within the superconducting transition region, where  $H_{c2}$  was low enough for the stray fields to have a significant effect. The QP GMR values measured in the devices and presented here were observed far below the transition, where the stray fields in the wires did not cause a  $\Delta R$ . Secondly, stray fields would not be expected to decay exponentially with  $d_{\text{Nb}}$  as the QP GMR does (as in Fig. 7.3), but instead roughly

as  $1/d_{\text{Nb}}$  [197]. Finally, there is current dependent behaviour observed in these devices which is consistent with behaviour expected from  $\Delta R$  dependent on quasiparticles rather than stray fields.

### 7.2.1.1 Current dependence

In these non-equilibrium superconducting devices, the quasiparticle energy is dependent on the current bias applied to the device, and for the typical current used of  $50 \mu\text{A}$ , expected to be below the gap of the Nb in the spin valve. As considered in Section 4.2.2, an estimate of the voltage driving the quasiparticles across the pillar can be made using the total resistance less the contributions from the areas away from the pillar, which suggests a voltage of magnitude  $\approx 24 \mu\text{V}$  for the standard current of  $50 \mu\text{A}$ . The voltage of quasiparticles entering the Nb would be less than this value as some is dropped traversing the FeMn and Py layers and so the quasiparticle voltage is at least two orders of magnitude below the gap of bulk Nb ( $\approx 3 \text{ mV}$  [198]), and likely below the smaller gap of Nb in these devices for low current values, getting closer to the gap edge with increasing current.

The differential resistance  $dV/dI$  curves for these devices illustrates the gap edges of the superconductor as peaks, as there is increased scattering due to the increased density of states around the gap edges. However, beyond this link the  $dV/dI$  does not represent the density of states of the Nb, particularly considering that the wires and non-superconducting layers of the structure are included in the measurement. Figure 7.4(a,b) each show  $dV/dI$  vs.  $I_{\text{bias}}$  for different devices. The AP-state requires less bias before reaching the gap edge, corresponding to the lower  $T_c$  of the devices in the AP-state for these QP GMR devices. Fig. 7.4(c) shows how  $\Delta R$  changes with current as extracted from  $R(T)$  curves, demonstrating a sharp peak followed by a gradual decrease, supported by the minor  $R(H)$  loops in (d), which show an increase in  $\Delta R$  from essentially 0% below the gap edge to  $\Delta R = 0.9\%$  above the corresponding gap edge indicated in (b). The origin of this dramatic increase is considered to be the quasiparticle energy increasing past the AP-state gap edge. Above the gap, the QPs do not decay into the condensate, allowing spin transport across the whole of S, increasing the magnetoresistance of the device. The exact peak location is at a higher bias than the AP-state gap edge because the P-state still features QPs below the gap, decaying into Cooper pairs, so increasing current corresponds to increasing available quasiparticle states in the AP-state compared to the P-state, increasing  $\Delta R$ . The rate of increase slows, then reverses, as quasiparticle states above the gap become available in the P-state, until the  $\Delta R$  levels off as the rate of energy levels opening is roughly equal for both states. In this scenario, most quasiparticles in both the AP- and P-states are contributing to giant magnetoresistance. It must be noted however, that the  $\Delta R$  at this point tends to a value larger than the normal state  $\Delta R$ . This is because at these increased currents the device and wires are halfway through superconducting transition, where the increased gradient of the  $R(T)$  curves lead

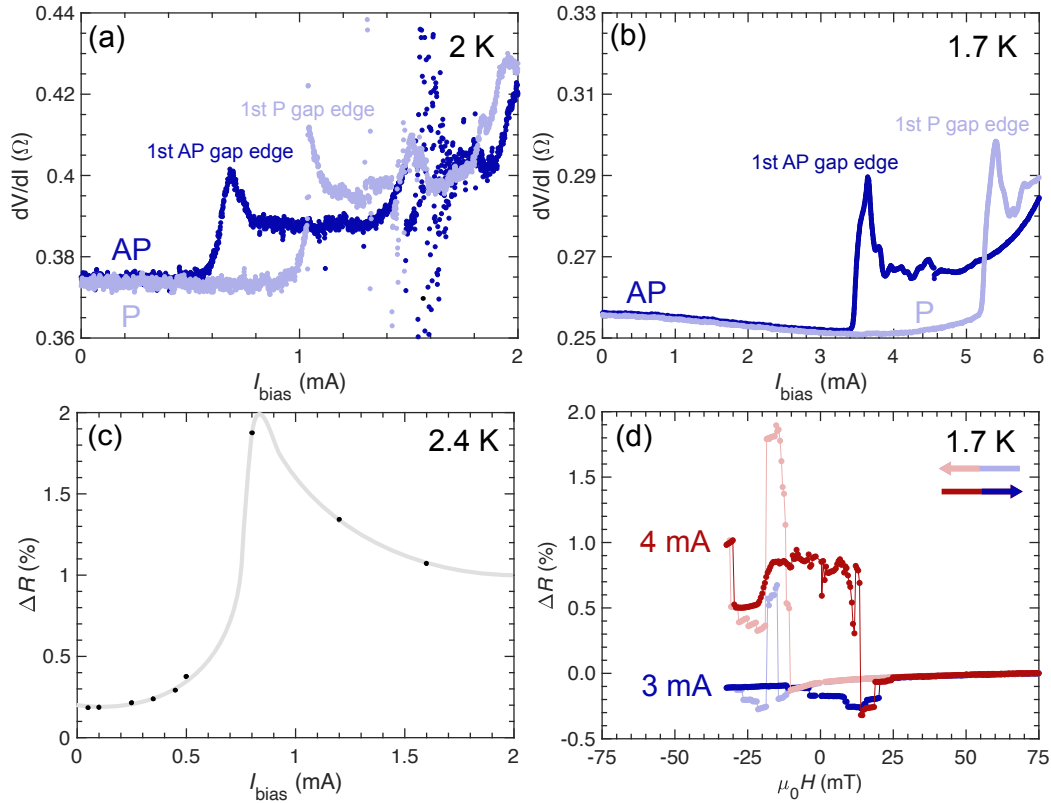


**Figure 7.4:** Current bias dependence of  $\Delta R$ .  $dV/dI$  vs  $I_{\text{bias}}$  for devices with (a)  $d_{\text{Nb}} = 25$  nm, and (b)  $d_{\text{Nb}} = 53.5$  nm. Dark blue corresponds to AP-state, light blue to P-state. (c)  $A\Delta R$  from comparisons of  $R(T)$  in the AP- and P-states vs.  $I_{\text{bias}}$  for the device in (a), showing the large increase in  $A\Delta R$  as the bias is increased past the gap, confirming spin is carried by quasiparticles in these devices. (d) Minor  $R(H)$  loops measured at 3 mA (below gap edge, blue) and 4 mA (above gap edge, red) for the device in (b), showing the change as the gap edge is passed. Light colour is initial sweep from positive field to negative field, dark is the return sweep from negative to positive, as indicated by the arrows.

to a greater difference between P- and AP-states than far from the transition (Fig. 6.11).  $R(T)$  curves suggest the superconducting transition still occurs even at these high current values. This suggests partial spin-charge separation is occurring in the spin valves, with quasiparticles transporting spin thereby enabling GMR, and the charge transport performed by the Cooper pairs in S.

Alternative sources of this peak in  $\Delta R$  with  $I_{\text{bias}}$  include the devices rising through the superconducting transition with increasing current bias, giving rise to peaks in  $\Delta R$  as they pass  $T_c$ , due to the maximum gradient of the  $R(T)$  curve. Suppression of  $T_c$  via current bias, or Ohmic heating could cause such an effect. However, the data in (c) was extracted at a consistent temperature of 2.4 K that was below  $T_c$  for every current value, and so below the peak corresponding to the transition. Furthermore, as can be seen in Fig. 7.4(a) multiple steps in the  $dV/dI$  occur for these devices, and it is reasonable to suspect that a peak in  $\Delta R$  is associated with each one. The  $T_c$  suppression explanation could not give rise to multiple such peaks. As a result, this is considered as an indication of quasiparticle based behaviour within these devices, supporting the QP GMR picture.

### 7.2.1.2 Temperature dependence

Quasiparticle transport is related to the magnitude of the superconducting gap: as the gap increases, more quasiparticles have energies below the gap, leading to increased decay into the condensate, and reduced  $\Delta R$ . In a previous investigation into CPP superconducting spin valves [14], this temperature dependence was used as evidence for quasiparticle mediated spin transport.

Here, the temperature dependence of  $\Delta R$  differs significantly. In the transition (of both the wires and the devices), there is a peak in  $\Delta R$  at  $T_c$ , which arises due to the large  $dR/dT$  in the transition, leading to a large  $\Delta R$  given the difference in  $T_c$  between the AP- and P-states. It is difficult to distinguish any changes in  $\Delta R$  with temperature that are not related to this peak, although three devices which may show such  $\Delta R(T)$  dependence as in [14] are presented in Fig. 7.5, which features  $R(T)$  and  $\Delta R(T)$  curves from each device. Figure 7.6 then shows  $\Delta R$  data from  $R(H)$  measurements of these devices (colours consistent with Fig. 7.5), showing an increase with temperature below  $T/T_c = 0.8$ , which are separate from the peak in  $\Delta R$  associated with the transition, as the  $\Delta R(T)$  curves suggest this effect does not go below  $T/T_c = 0.7$ . Therefore, there may be some temperature dependent behaviour in these devices.

The temperature dependence in these devices is reduced compared to the dependence in [14]. One explanation for this is that a large proportion of quasiparticles are near the gap edge in the devices in [14], leading to a heavy dependence on temperature, whereas the quasiparticles in these devices could all be significantly below the gap edge. Alternatively, the difference may result from interface quality; the temperature dependence of the resistance of an F/S interface is dependent on transparency [188], and this is also

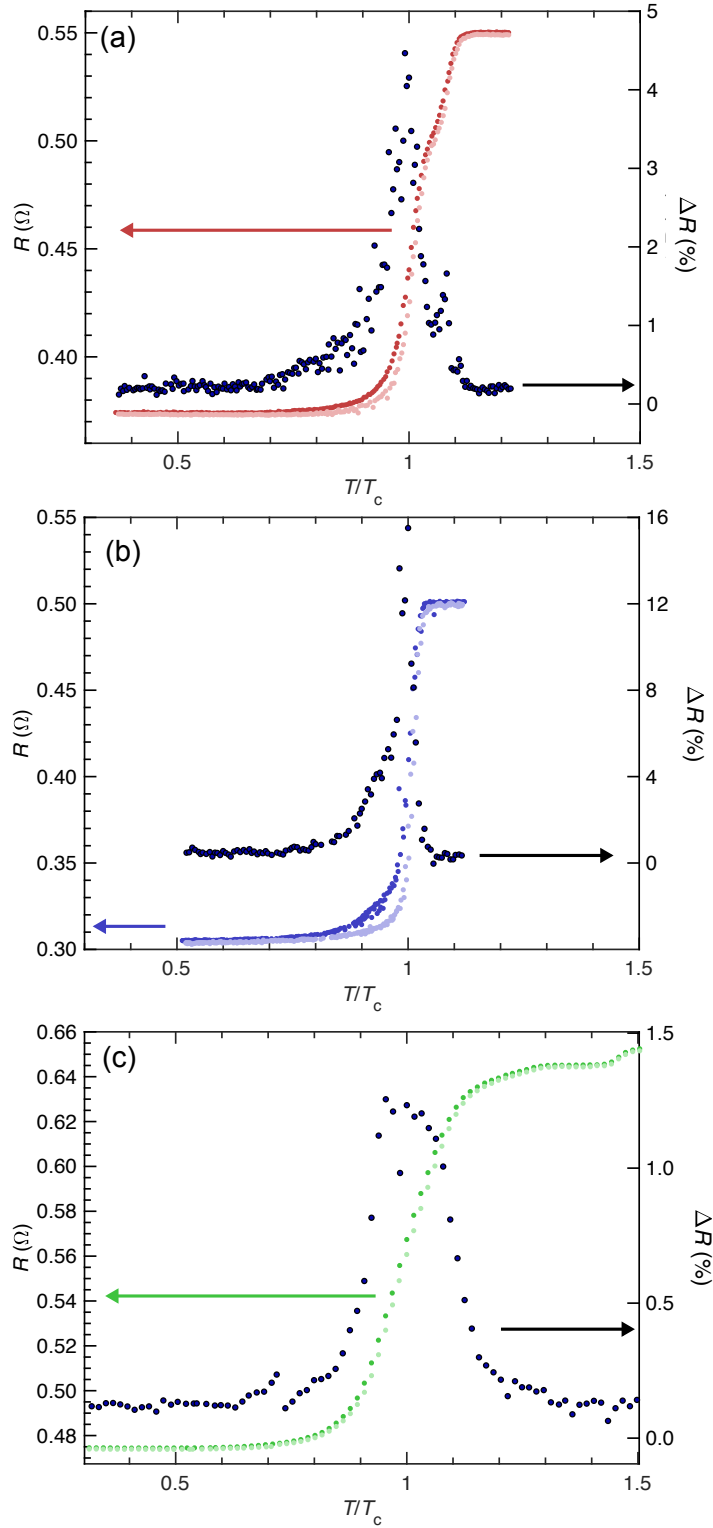


**Figure 7.5:**  $R(T/T_c)$  plots for three devices (coloured, left axes), for both P (light) and AP (dark) states, plotted with  $\Delta R(T)$  (black, right axes) extracted from these curves. (a)  $d_{Nb} = 25$  nm, red. (b)  $d_{Nb} = 28.5$  nm, blue. (c)  $d_{Nb} = 34$  nm, green. The peak in  $\Delta R(T)$  corresponds to the midpoint of the transition, and is an artefact of the steep gradients in the transition.

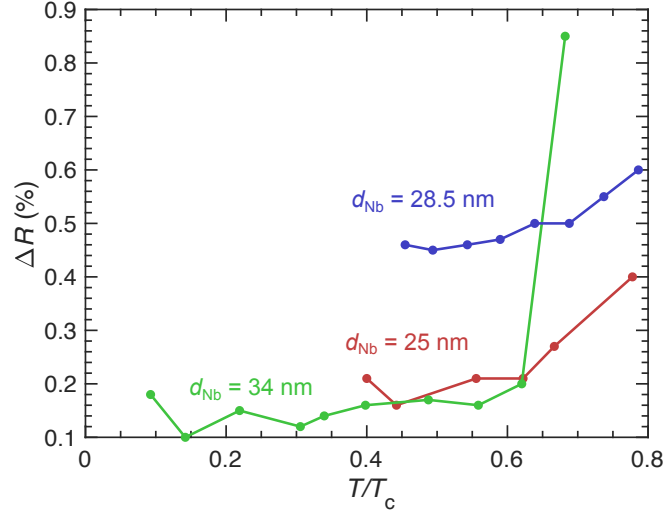


**Figure 7.6:** The magnetoresistance change with relative temperature for the three devices in Fig. 7.5. Colours are as for that plot. All devices show an increase with temperature, which may be separate from the transition based peak in  $\Delta R(T)$ . This feature occurs above  $T/T_c = 0.7$ , whereas the increase in magnetoresistance with temperature here occurs below  $T/T_c = 0.8$ . This indicates changing quasiparticle penetration of the superconductor with changing gap size.

likely to affect the temperature dependence of magnetoresistance. Consider two devices, shown in Fig. 7.7. The top has a perfectly opaque interface, and so the transition from F to S involves a sudden step in the superconducting gap (pink line). In this case, a temperature change (changing the size of the gap, i.e. the height of the pink line) makes minimal difference to the penetration of quasiparticles, unless they are right at the gap edge. By contrast, for a transparent interface where the superconducting gap changes gradually from the interface, a change in temperature will have a much greater effect on penetration of quasiparticles below the gap edge, and hence  $\Delta R$ .

Finally in [14] the  $T$ -dependence of the QP GMR appears to be significant only for devices with  $d_{Nb} > 50$  nm. In the devices of this investigation, the QP GMR is so small for devices of comparable thickness it is difficult to extract the GMR from the noise and negative magnetoresistance. It is therefore possible this temperature dependence is present here, but hidden by the other effects.

### 7.2.2 Proximity effect

The second transport regime in these devices features higher resistance in the P-state compared to the AP-state. In CIP spin valves showing the superconducting spin valve effect, the P-state has higher resistance because of the increased average exchange field in the spacer layer, suppressing  $T_c^P$ . The higher resistance P-state in these nanopillar spin valves has the same origin. To help distinguish from GMR, which in normal state spintronics can also be known as the spin valve effect, this effect is referred to henceforth as proximity effect dominated behaviour. This effect is demonstrated by the positive  $\Delta T_c$

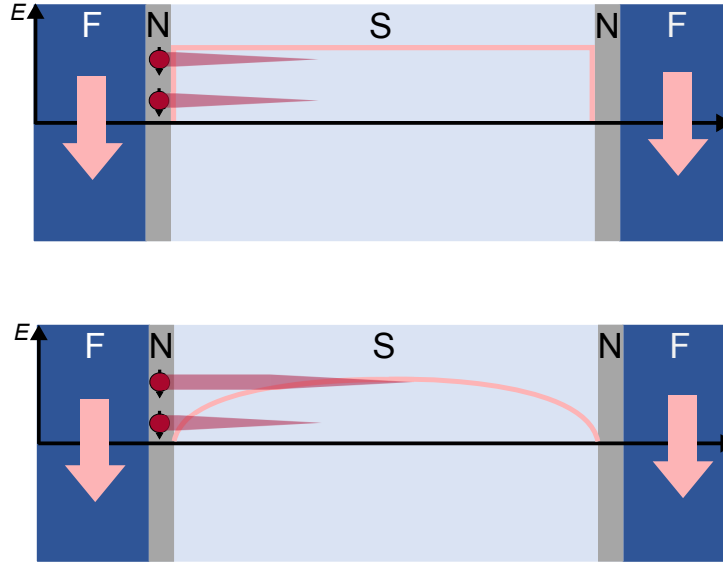


**Figure 7.7:** Cartoon showing how the effect of different levels of interface transparency could have an effect on the temperature dependence of quasiparticle penetration. Pink line is the superconducting gap, and quasiparticles are in red. On the black axes, vertical position of gap and quasiparticles represents relative energies, and horizontal position represents penetration into the superconductor (shown by red triangles). The more gradual change of gap size in the transparent case means a change in temperature will affect penetration of a greater range of quasiparticle energies; in the opaque case, only quasiparticles with energies near the gap edge would be affected. Top: opaque interface, Bottom: transparent interface.

values from  $R(T)$  measurements, and negative magnetoresistance in minor  $R(H)$  loops, which appear similar to those reported in the literature for CIP devices [139, 142, 145, 147, 168, 189].

Observation of this proximity effect dominated behaviour in a CPP spin valve has not been reported in the literature, partially because of the limited investigation into superconducting CPP spin valves. Negative magnetoresistance effects do exist, including anisotropic magnetoresistance (AMR), which has been observed in heterostructures. This occurs (in the negative sense) around  $H_c$  for devices where the current through a ferromagnet flows parallel to the magnetisation of the ferromagnet. However, the effect under discussion here is only visible within the lower superconducting transition of certain devices, and AMR is not linked to the appearance of superconductivity. Furthermore, this behaviour is dependent on parameters such as superconducting transition temperature and Nb thickness. AMR is therefore not responsible for this transport regime.

Another effect that gives rise to a similar resistance change in ferromagnet / superconductor devices is crossed Andreev reflection (CAR) [199]. CAR can occur when two contacts are separated by a superconductor of size less than the coherence length, and involves an incoming electron injected into the superconductor from one contact correlating with a hole of opposite spin entering the other contact from the superconductor. Where these contacts are ferromagnetic, the AP-state is of reduced resistance because

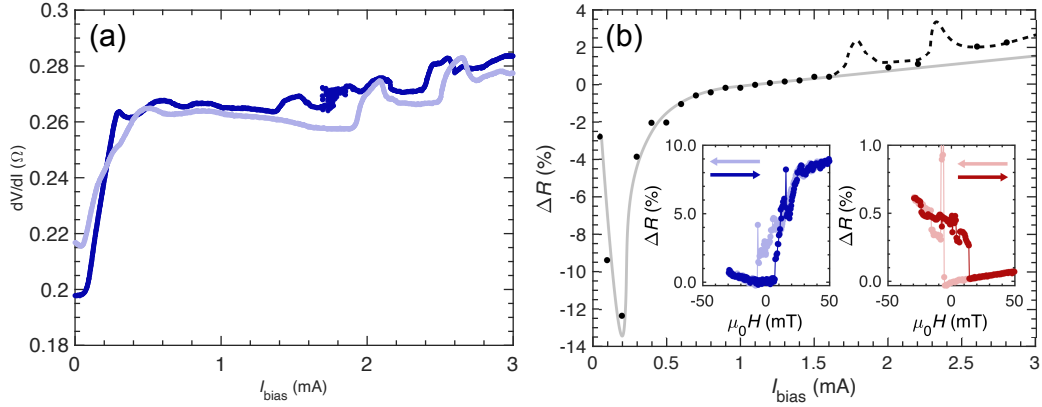


**Figure 7.8:** (a)  $dV/dI$  vs  $I_{\text{bias}}$  for a device showing proximity effect dominated behaviour at 0.3 K. The proximity effect is associated with the valley observable at lower currents, below 300  $\mu\text{A}$ . At higher currents, peaks similar to Fig. 7.4 are observed. (b) Normalised magnetoresistance for the same device at different current biases, extracted from minor  $R(H)$  loops. These suggest the transition from proximity effect dominated behaviour to GMR behaviour occurs at 1.1 mA. The grey line is a guide to the eye, and the dashed black line is an alternative guide, showing peaks assuming QP GMR behaviour. Insets: normalised minor  $R(H)$  loops at 0.3 K for 50  $\mu\text{A}$  (blue) and 1.6 mA (red).

the asymmetric density of states for each spin direction increases the probability of CAR in this alignment (each contact contributing opposing spins). Crossed Andreev reflection has been reported multiple times in the literature [200–203] and has been considered as an option for a magnetoresistance mechanism in CIP devices [204] but is generally considered a non-local effect, where the second contact is separate from the current path. One potential report of a local measurement of CAR exists [205] but the origin of this magnetoresistance was uncertain and the authors do not consider it conclusive that the cause was CAR rather than a spin valve effect. There is no literature on how CAR would interact or compete with the superconducting spin valve effect in a local measurement. As mentioned in Section 6.2.3.2, CAR could also be considered to give rise to the opposite effect, in situations where pair breaking instead of generation is encouraged by the effect, giving a reduced  $T_c$  in the AP-state.

### 7.2.2.1 Current dependence

Current dependence of the proximity effect dominated behaviour has been difficult to measure. This is primarily due to the Ohmic heating seen within the devices with increased currents. For instance, in the  $R(H)$  loops measured for Fig. 7.8, the measurement temperature was set to 0.3 K, but noted as increasing for the different currents, up to 0.565 K for the 2.8 mA measurement, and the local temperature in the device is likely to be higher than that measured value. As the proximity effect devices are still mid-transition even at 0.3 K, this temperature change has a large impact on the results, and is at least partially responsible for the disagreement between the  $dV/dI$  vs  $I_{\text{bias}}$  curves

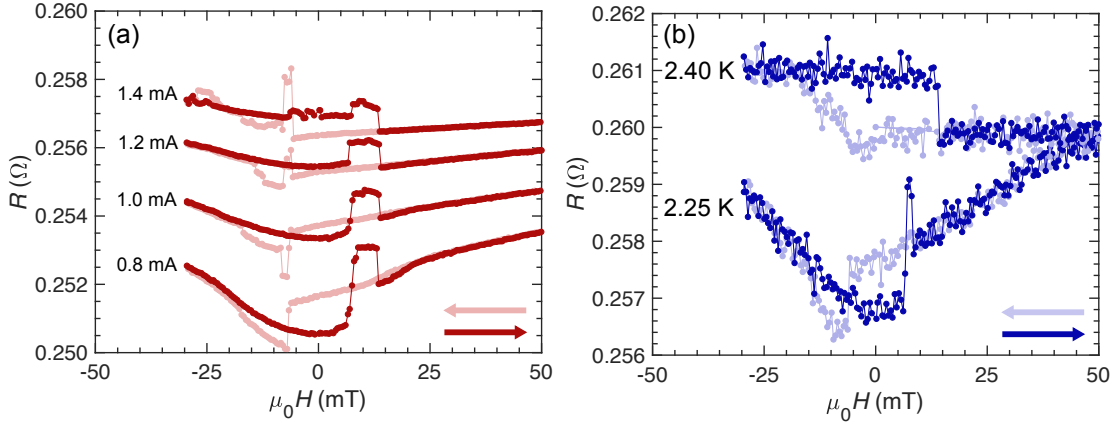


**Figure 7.9:** (a)  $R(H)$  curves for a series of currents showing how the proximity effect behaviour gives way to GMR. The transition is a gradual change rather than a sudden switch. (b)  $R(H)$  curves for two temperatures, above and below the start of the device transition temperature  $T_{\text{device}} = 2.35$  K, where the P-state  $R(T)$  curve decreases below the AP-state curve, showing similar behaviour to (a). Arrows in (a) and (b) show field sweep directions, starting at positive fields.

in Fig. 7.8(a) which suggest switching between the proximity effect dominated behaviour occurs at  $200 \mu\text{A}$  and the curve in (b), which suggests that crossover occurs at  $1.2 \text{ mA}$ . This is an extremely large disagreement, and it is suspected that the  $dV/dI$  may not accurately represent the difference between P and AP states at higher current values.

Figure 7.8(a) shows an initial superconducting gap at low current biases. Through measurements of  $dV/dI$  at different temperature, it was determined that this gap corresponds to the proximity effect dominated behaviour and the device superconducting transition. The initial dip observed at  $0.2 \text{ mA}$  in Fig. 7.8(b) does not appear to correspond to features from the  $dV/dI$  curve, and may be due to device heating through the transition, corresponding to the associated peak (inset, Fig. 7.10). The grey and dashed black lines in (b) are guides to the eye, with the dotted one being a suggestion for peaks associated with the gap edges in (a), akin to those in 7.4(b). These would fit the increase in  $\Delta R$  at higher currents that do not fit the gradual linear increase suggested by the solid line from the values below  $1.5 \text{ mA}$ . The shape of the gap associated with the proximity effect behaviour is more rounded than those in associated with the QP GMR behaviour. This is consistent with the device being mid-transition, as  $dV/dI$  measurements when the wires are mid-transition also give rise to more rounded gaps.

$R(H)$  loops from the current values surrounding the change from proximity effect dominated behaviour to GMR behaviour are shown in Fig. 7.9(a). These suggest a gradual shift between the two effects rather than a sudden switch, as the negative effects shrink to zero followed by the increase of positive effects from zero.

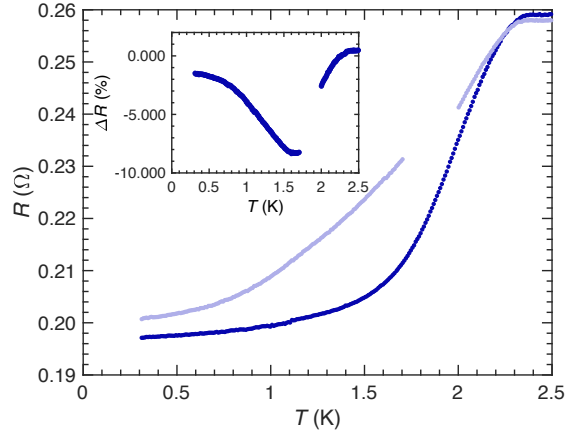


**Figure 7.10:**  $R(T)$  curve for the device transition only, showing proximity effect dominated behaviour. The inset shows  $\Delta R(T)$ , showing the usual peak around the centre of the transition, but now inverted because of the proximity effect. The region of missing data in the parallel state curve is because the data here is from separate measurements, using the He-3 insert probe from 0.3-1.7 K, and a standard probe for above 1.7 K in the pulse tube measurement system. The system did not reach its lowest possible temperature during this measurement.

### 7.2.2.2 Temperature dependence

Figure 7.10 shows a device transition demonstrating proximity effect dominated behaviour. The difference between P- and AP-states is significant, leading to large values of  $\Delta T_c$  and  $\Delta R$ . The inset shows the temperature dependence of  $\Delta R$ , extracted from the  $R(T)$  curve, which again shows a peak (although negative for this proximity effect device) associated with the centre of the transition where the gradient is greatest. Measurements of  $R(H)$  also show this dependence on temperature.

All devices demonstrating the proximity effect dominated behaviour have low temperature device transitions, such that even at the lowest temperature of 0.3 K it appears that the transition may not be complete. As a result,  $\Delta R$  values from these data are inflated by being mid-transition, and  $\Delta T_c$  is more uncertain as the exact value of  $T_c$  is unknown. The lack of complete transition raises an interesting question about what would happen below the transition. In the literature, devices showing this behaviour are all CIP, and hence below the superconducting transition are fully superconducting. It is possible that this is a transition dependent behaviour, focused around  $T_c$  because the effect is reliant on the relative suppression of  $T_c$  in the P- and AP-states. However, considering the inset to Fig. 7.10, the  $\Delta R$  appears to be levelling off to a constant value below zero at low temperatures, suggesting the effect may continue in CPP devices.

## 7.3 Crossover between behaviours

After observing previously unreported behaviour in CPP spin valves, efforts were made identify the factors causing such behaviour to appear. Within the spin valves deposited as

part of this work, there is a systematic crossover between QP GMR behaviour and proximity effect dominated behaviour. Understanding the parameters affecting this crossover can help identify what makes this proximity effect dominate.

### 7.3.1 Layer dependence

#### 7.3.1.1 Nb thickness

The crossover between QP GMR and proximity effect dominated behaviour can be shown clearly as a function of the spacer layer thickness, as shown in Fig. 7.11. Both  $A\Delta R$  data in (a) and  $\Delta T_c$  data in (b) show the crossover occurring at the same thickness, corresponding to around  $d_{\text{Nb}} = 26$  nm. Using  $d_{\text{Nb}}$  as the independent parameter has the advantage that it is easy to relate the crossover and other trends to controllable physical values. Starting from the thickest  $d_{\text{Nb}}$ , the devices demonstrate essentially no spin transport ( $\Delta R = 0$ ), as the central spacer is too thick. As the central spacer thickness is reduced, the QP GMR increases exponentially as expected, and shown earlier in Fig. 7.3, reaching a peak value at around 28 nm, and then decreases before crossover into negative values of  $A\Delta R$  at  $d_{\text{Nb}} = 26$  nm. The  $\Delta T_c$  data shows the same trend, although this will at least partially be because of the link between  $\Delta R$  and  $\Delta T_c$ . The appearance of the peak followed by a decrease into the proximity effect behaviour is interesting, as it suggests the crossover is not a sudden switch in behaviours but instead two competing effects, the QP GMR and proximity effect. The proximity effect seems to have no effect on spin valves with too large a spacer layer, but has a strong effect on devices with thicknesses below a certain value. The black curves in both plots correspond to the toy model fit to the data (Section 7.3.3).

The  $\Delta T_c$  values reported are very large compared to other transition metal based spin valves reported in the literature [136, 139, 140, 142, 144, 145, 147, 149, 156–163, 168, 169, 196], the largest of which is 41 mK [147]. The possibility that the CPP regime lends itself to greater values of  $\Delta T_c$  than CIP can be considered: one suggestion, inspired by the increased magnitude of  $\Delta R$  in CPP spin valves compared to CIP, is that the direction of current flow forces the Cooper pairs to interact strongly with both ferromagnetic layers, whereas in the CIP case, Cooper pair transport is limited to the centre of the superconducting layer, allowing the pairs to find the minimum point of interaction with the average exchange field [206]. The associated  $\Delta R$  values are an order of magnitude larger than the values from QP GMR, as a result of the  $dR/dT$  link mid-transition combined with the broad transition, which can be up to 2 K wide, as shown in Fig. 7.10. These large results are therefore unlikely to be technologically useful, as infinite magnetoresistance, the goal of superconducting spin valves, requires a  $\Delta T_c$  smaller than the transition width.

Simple comparisons with previous CPP superconducting spin valves [14] can be made using the QP GMR data. The maximum value in Fig. 7.11(a) is  $615 \Omega \text{ nm}^2$ , or  $0.615 f\Omega \text{ m}^2$ , which compares well to the value in [14] at around 27 nm which appears to be in the region

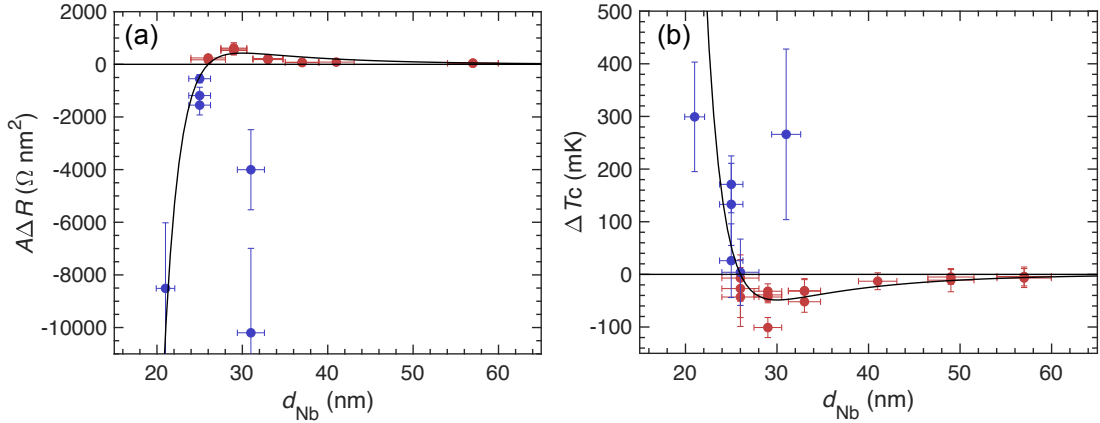


**Figure 7.11:** (a)  $A\Delta R$ , measured at  $T/T_{\text{device}} = 0.3$ , and (b)  $\Delta T_c$  vs.  $d_{\text{Nb}}$ . Red points are devices demonstrating QP GMR, blue are devices demonstrating the proximity effect. The black lines are fits according to the model (Section 7.3.3), excluding the points at  $d_{\text{Nb}} = 31$  nm.

of  $0.65 f\Omega \text{ m}^2$ . However, the decay length of this data is shorter than the  $17.5 \pm 0.6$  nm in [14], at  $l_{sf}^S = 12 \pm 4$  nm, although the relative difference between the two values is less than in the normal state. Whilst comparing the proximity effect  $A\Delta R$  with literature values is not useful due to the inflated values from the effect of the low transition, note that the largest three proximity effect values are in fact greater than values predicted using the measured resistivity of Nb and assuming it goes completely superconducting. This non-physical result implies there are additional effects contributing to  $\Delta R$ .  $R(H)$  measurements on the wires indicate a contribution from them for the device with  $d_{\text{Nb}} = 21$  nm, the only structure to demonstrate the proximity effect behaviour in the wires. This is of particular note as for this structure with thinnest Nb, the stray field effects in the wires would be strongest; instead, this proximity effect behaviour dominates. Other possible contributions include the proximitising of the central Cu buffer layers and part of the Py layers. The impact of single cuts on proximity effect devices has not been investigated.

One additional point should be noted: the normal state data demonstrate a large degree of scatter, as discussed previously. This has an impact on the magnitude of  $\Delta R$  below  $T_c$  as well, and comparing the relative normal state GMR values of the devices at 26 nm with other QP GMR devices suggests that that substrate has devices with a smaller  $\Delta R$  due to impurities rather than the appearance of the proximity effect. However, even ignoring this particular set of devices, the interpretation of Fig. 7.11(a) remains the same. Additionally, that substrate well fits the trend in  $\Delta T_c$  in (b), although this may be as a result of the link between  $\Delta R$  and  $\Delta T_c$ .

### 7.3.1.2 Cu and Py

Attempts to investigate the effect of changing thickness of the central Cu buffer layers suggested there was minimal impact on  $T_c$  beyond a few nm (Section 6.2.4.1). Similarly, no

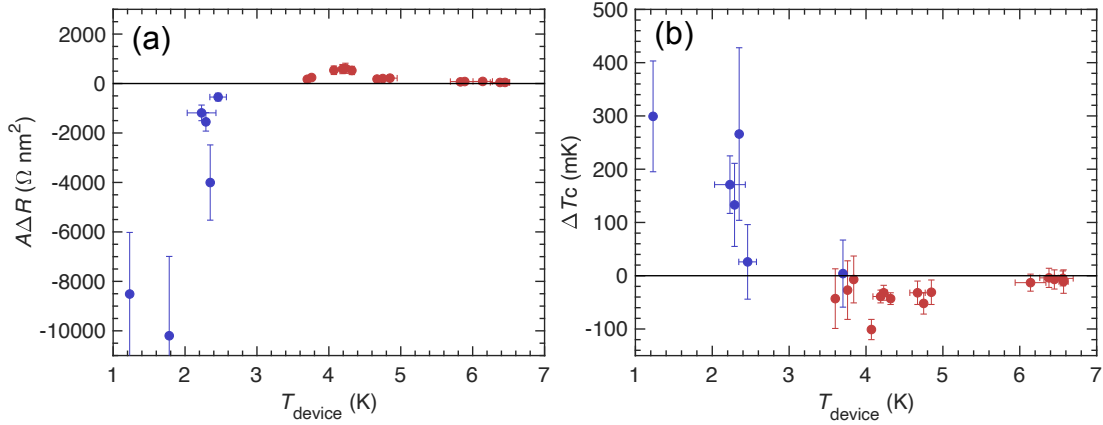


**Figure 7.12:** (a)  $A\Delta R$ , measured at  $T/T_{\text{device}} = 0.3$ , and (b)  $\Delta T_c$ , as in Fig. 7.11 now plotted vs.  $T_{\text{device}}$ . Red points are devices demonstrating QP GMR, blue are devices demonstrating the proximity effect.

systematic effect on the appearance of the proximity effect has been seen. The proximity effect has been observed in structures with Cu buffer layer thicknesses of 5 nm, 10 nm, 15 nm, and also 0 nm (i.e. no Cu). Unfortunately, inconsistency in the devices has meant systematic dependence on this Cu layer cannot be determined. However, these structures had  $d_{\text{Nb}}$  around 30 nm, and the appearance of the effect in a structure with Py separation greater than the crossover thickness of 26 nm, additionally with greater Cu thickness, suggests it is not absolute Py separation but rather the separation in terms of the superconducting order parameter that is relevant here.

The proximity effect dominated behaviour has only appeared across a limited number of substrates. As a result, no inferences can be made upon the impact of changing Py layer thickness on the appearance of the effect, although as the strength of the exchange fields and superconductivity influence the superconducting spin valve effect, this would be of interest in future work.

### 7.3.2 Dependence on superconducting order

The limited effect of changing Cu thickness and the outliers at 31 nm in Fig. 7.11 suggest there is more to the crossover dependence than just the thickness of the central spacer layer. This is further highlighted by comparison of the substrate of the two outlier devices with the substrate deposited adjacent, in the same slot in the same deposition. A comparison between the two was shown in Fig. 7.2, where the substrate in (a) shows QP GMR, and the substrate in (b) shows the proximity effect. Fig. 7.2(a) is expected to have a  $d_{\text{Nb}} = 28$  nm, and (b)  $d_{\text{Nb}} = 31$  nm, with the difference arising due to suspected different deposition rates based upon radial location on the substrate table. Despite (a) having the lower  $d_{\text{Nb}}$ , (b) shows the proximity effect. The obvious difference between the two devices is the large suppression of the device transition temperature in (b). This, plus the varia-

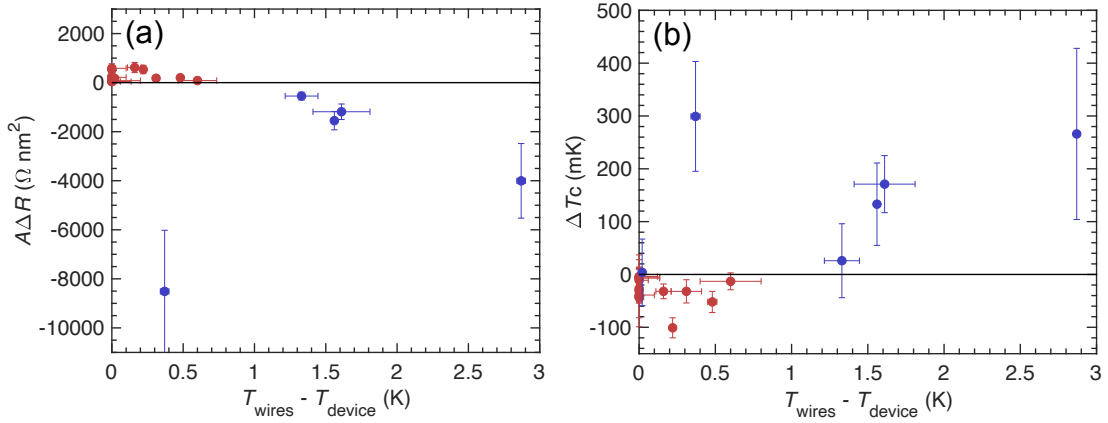


**Figure 7.13:** (a)  $A\Delta R$ , measured at  $T/T_{\text{device}} = 0.3$ , and (b)  $\Delta T_c$  vs. temperature difference between the wire and device transitions for each device.

tion between different devices on the same substrate suggests Ar-ion milling and focused ion beam (FIB) milling in the fabrication process may be affecting the appearance of the proximity effect, although the proximity effect could also be the cause of the suppressed transition. The lower  $T_c$  of the device would be associated with a smaller superconducting gap, and longer coherence length of the central Nb layer. However, note that the substrate with  $d_{\text{Nb}} = 31$  nm does not fit the trend of  $T_{\text{device}}$  vs.  $d_{\text{Nb}}$  in Fig. 6.7, whereas other proximity effect devices do, suggesting it is possible this substrate has  $d_{\text{Nb}}$  less than expected for some unknown reason. Considering the impact of patterning on the appearance of the proximity effect is still of interest however, as the spin valve with thinnest  $d_{\text{Nb}} = 21$  nm is the only one that demonstrates the proximity effect dominated behaviour in the wires. Thicker devices show stray field dominated behaviour in the wires, but the proximity effect dominated behaviour in the pillars, suggesting patterning increases the likelihood of this spin valve effect, either because of the increased implantation from FIB milling, or because of the controlled current paths vertically through the device.

Figure 7.12 shows (a)  $A\Delta R$ , measured at  $T/T_{\text{device}} = 0.3$ , and (b)  $\Delta T_c$ , as in Fig. 7.11, but plotted against  $T_{\text{device}}$ , the start of the superconducting transition of the device, as a representation of the size of the gap in the superconductor. It can be seen that the previous outliers now agree more closely with the other proximity effect data, suggesting the strength of superconductivity does have an effect on the appearance of the proximity effect dominated behaviour. The trend is mostly similar to that in Fig. 7.11, as the  $T_{\text{device}}$  will be higher for devices with large  $d_{\text{Nb}}$  on average. The crossover between QP GMR and proximity effect dominated behaviour appears to be between 3 – 3.5 K, and the maximum QP GMR effect at around 4.1 K.

Rather than the absolute value of  $T_{\text{device}}$ , an alternative way to measure the impact of the FIB process specifically is to take the difference between the transitions of the wires,  $T_{\text{contacts}}$  and the device,  $T_{\text{device}}$  (both taken at the start of the relevant transition).  $A\Delta R$

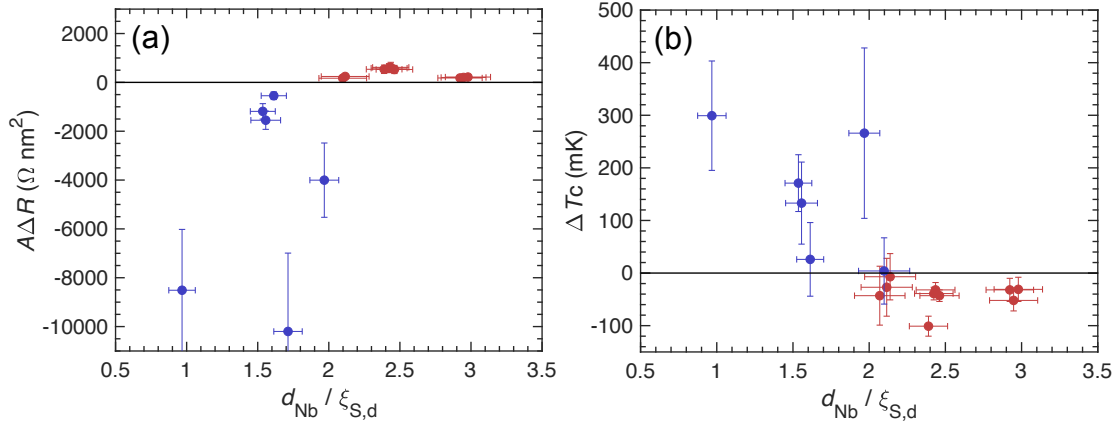


**Figure 7.14:** (a)  $A\Delta R$ , measured at  $T/T_{\text{device}} = 0.3$ , and (b)  $\Delta T_c$  vs.  $d_{\text{Nb}}/\xi_{S,d}$ , where  $\xi_{S,d}$  is the dirty limit coherence length.

at  $T/T_{\text{device}} = 0.3$  and  $\Delta T_c$  are plotted against this difference in Fig. 7.13. Both (a) and (b) do seem to show an overall trend when plotted in this way, although notably devices with larger  $d_{\text{Nb}}$  do not fit with this trend, nor does the device with  $d_{\text{Nb}} = 21$  nm. Outside of these however, there is a fairly consistent trend in each of (a) and (b) which roughly corresponds to half of the pattern seen in the previous figures. However, (b) is particularly notable as the trend appears linear, rather than the exponential assumption made earlier. It is possible this represents how the degree of patterning influences the appearance of the proximity effect, with outliers (at a separation of 0 K and particularly the one at 0.32 K) representing devices with  $d_{\text{Nb}}$  outside a range that can be affected by the patterning.

In an attempt to represent this effect using more direct physical parameters, Fig. 7.14 shows the same data again, this time plotted against  $d_{\text{Nb}}/\xi_{S,d}$ , where  $\xi_{S,d}$  is the dirty limit coherence length, calculated as

$$\xi_{S,d} = \sqrt{\frac{\hbar D}{1.764 k_B T_{\text{device}}}}$$

where  $k_B$  is the Boltzmann constant and  $D = 1.4 \times 10^{-4} \text{ m}^2\text{s}^{-1}$  is the electron diffusivity, calculated using the measured coherence length (Section 6.2.5) and associated  $T_c$ . In this case, the outlier points agree less well than when  $T_{\text{device}}$  is used as the independent parameter on its own. However, these plots suggest that the crossover between behaviours occurs when  $d_{\text{Nb}}/\xi_{S,d} = 2$ . As the coherence length is the scale over which interfacial effects are significant, allowing the exchange effects from each interface to interact, this is an extremely notable result that provides a link to imagining a physical picture to describe the crossover between the two effects.

### 7.3.3 Modelling

A phenomenological model has been developed and fit to the data vs  $d_{\text{Nb}}$  in an attempt to stimulate further understanding of the competing effects discussed above. A simple model was proposed in [14] to explain the QP GMR dependence on temperature and  $d_{\text{Nb}}$ , considering an exponential decay, as with the spin decay above  $T_c$ :

$$\Delta R_{E<\Delta} = A \exp \left[ \frac{-(d_{\text{Nb}} - d_0)}{l_S} \right] \quad (7.1)$$

where the prefactor  $A = 1 - 2f(\Delta)$  includes the temperature dependence by representing the quasiparticles below the energy gap ( $f$  is the Fermi-Dirac distribution function),  $d_0$  is the value at which the QP GMR value equals the normal state GMR, and  $(l_S)^{-1} = \sqrt{(l_N)^{-2} + (\xi_0)^{-2}} - (l_N)^{-1}$  is the QP GMR decay length, consisting of the spin decay length due to scattering  $l_N$  (assumed equal to the value above  $T_c$ ) and the penetration of the quasiparticles into the superconductor,  $\xi_0$ , such that when  $l_N \gg \xi_0$ ,  $l_S \approx \xi_0$ . Considering our superconducting  $\Delta R$  at a fixed temperature ( $0.3T/T_c$ ), this model works well for our QP GMR data. However, it cannot account for the proximity effect data or the crossover between the two. Note that [14] did not investigate superconducting devices with  $d_{\text{Nb}} < 30$  nm, assuming that the QP GMR reaching the same value as the normal state GMR at  $d_0 = 28$  nm was indication that Andreev reflection ceased at this thickness, and decay for devices with smaller  $d_{\text{Nb}}$  would therefore match the normal state. They find agreement between this  $d_0$  and twice their calculated coherence length  $\xi_{GL}$ , concluding that Andreev reflection therefore occurs over a lengthscale of the coherence length, and when  $d_{\text{Nb}} < 2\xi_{GL}$  the quasiparticles can therefore travel across the superconductor below the energy gap without decaying into a pair state. However, the results reported above indicate that instead the superconducting spin valve effect starts to dominate in this regime.

To describe these data a model requires two parts; one to describe the QP GMR regime for higher values of  $d_{\text{Nb}}$ , based on the [14] model, and one to describe the superconducting spin valve effect regime.  $d_{\text{Nb}}$  is used as the parameter, to provide physical basis to the model and to allow comparison with [14].

A model of this type<sup>1</sup>:

$$\Delta R = A \exp \left[ \frac{-(d_{\text{Nb}} - d_0)}{l_S} \right] - B \exp \left[ \frac{-(d_{\text{Nb}} - d_0)}{\Lambda_S} \right], \quad (7.2)$$

where the first exponential models QP GMR ( $\Delta R > 0$ ) and the second the proximity effect ( $\Delta R < 0$ ) was fit to the data in Fig. 7.11. To achieve the key peak then fall trend with decreasing  $d_{\text{Nb}}$  in the data, the superconducting spin valve effect has also been

<sup>1</sup>Dr X. Montiel reviewed this model and provided input to ensure it was physical.

described with an exponential; here  $\Delta R$  depends on the difference in gap size in the P- and AP-states,  $\Delta^{AP} - \Delta^P$ , which this model therefore assumes has an exponential dependence on  $d_{\text{Nb}}$ . This part of the model is phenomenological, based upon achieving the best fit to the data.

The parameters in the model have a very high degree of correlation, leading to a variety of possible parameter sets that can be obtained from fitting. It was found that some of the best fits arose when  $d_0$  was set to be 26 nm, the crossover thickness between the two effects (causing  $A = B$  by consequence). Next, the value of  $l_S$  can be set to  $12 \pm 4$  nm, the value of  $l_{sf}^S$  found in Fig. 7.3, which also used a simple exponential. With these constraints in place, the fitting was performed to both  $A\Delta R$  and  $\Delta T_c$  data, which gave different values for  $\Lambda_S$ . These different fits are inspected visually, and both found to reasonably represent potential values, so the mean of the two is taken:  $\Lambda_S = 2.16 \pm 0.71$  nm.

The proximity effect dominated behaviour may be expected to decay over a coherence length. However, there are issues with this expectation, as the QP GMR is also considered to decay over a coherence length [14], and the results presented here show that these effects have different decay lengths. Additionally, if  $\Lambda_S$  were considered the superconducting coherence length, it would imply the superconductor is in the clean limit (mean free path is either  $\lambda = 4.1$  nm or  $\lambda = 2.3$  nm depending on method as mentioned in Section 6.2.5), which is extremely unlikely for sputter deposited Nb in a metallic heterostructure patterned with Ar ion and FIB milling. Although the similarity of  $\Lambda_S = 2.16 \pm 0.71$  nm and  $\lambda = 2.3$  nm is noted, this would appear to be coincidental, as the mean free path should not be a limiting parameter to a superconducting proximity effect based behaviour. The assumption of exponential behaviour in the model for the superconducting state could instead be at fault. However, given the exponential describing the QP GMR data, an exponential is needed for the proximity effect dominated data to match the ‘peak then fall’ shape. Alternatively, the decay of  $\Lambda_S$  may not represent the superconducting coherence length, and instead  $l_S = 12 \pm 4$  nm is the coherence length - equivalent to  $d_0/2$  within error. Notably, the measured coherence length of a bare Nb film  $\xi_S = 9.4 \pm 0.3$  nm also falls within the expected error. This conforms with the physical interpretation of the results based on that in [14], including the match to  $d_0/2$ . This interpretation is used as a basis for the picture described below.

For  $d_{\text{Nb}} > d_0$ , the superconducting gap is a barrier to quasiparticle transport, causing Andreev reflection into a pair state. This barrier is of height  $\Delta_{\text{QP}} = \Delta^{\text{AP}} = \Delta^{\text{P}}$  and width  $d_{\text{Nb}} - d_0$ , and within the barrier exponential decay of the quasiparticles occurs with decay length  $l_S$ , which is much shorter than the normal state length and hence the only lengthscale that matters. When  $d_{\text{Nb}} < d_0$ , the quasiparticles are able to penetrate all the way across the superconductor and this form of decay is negligible. The width of the barrier is set at  $d_{\text{Nb}} - d_0$  because at each interface, the lengthscale for Andreev reflection occurring is  $l_S = d_0/2$ , which may be the superconducting coherence length.

When the interfaces are within two coherence lengths of each other, Andreev reflection no longer occurs. This is the picture described by [14]. Consider an extension to this picture as follows: when the interfaces are within two coherence lengths, as suggested by Fig. 7.14, in addition to Andreev reflection not occurring, the crossover to the proximity effect behaviour occurs, as the ferromagnets are now close enough to interact and have an cooperative effect on the size of  $\Delta$ , leading to a difference in the superconducting gap between the parallel and antiparallel states,  $\Delta^{\text{AP}} - \Delta^{\text{P}}$ , which leads to a difference in  $R$  between the two states, causing the  $\Delta R$  for these thicknesses that is related to Cooper pairs, not spin transport. Spin transport still occurs via QP GMR but the device resistance is dominated by the Cooper pair based effect. The decay length for the dependence of this gap difference on  $d_{\text{Nb}}$  is short, and not represented by the superconducting coherence length. As the size of the gap and the superconducting coherence length are related, this physical picture includes the implications of Fig. 7.12, that the size of the gap is related to the appearance of the superconducting spin valve effect, as the smaller  $T_{\text{device}}$  values correspond to a smaller gap, and hence a longer coherence length: allowing them to overlap and cause the spin valve effect more easily, even in a device with larger  $d_{\text{Nb}}$ .

There are still unanswered questions even with this interpretation however: the increased magnitude of  $\Delta T_c$  compared to other values in the literature,  $A\Delta R$  values exceeding the expected physical maximum for devices with  $d_{\text{Nb}} = 21$  nm and 31 nm and the incredibly small decay length of the spin valve effect. It is worth noting this small decay length does bear parallels with some reported CIP data, such as in [147], which reported a decay from  $\Delta T_c = 41$  mK to “only a few mK” for an increase of  $d_{\text{Nb}}$  from 17 to 18 nm. Further work into this dependence of the spin valve effect on  $d_{\text{Nb}}$  would therefore be of value. Interestingly, the issues discussed here appear to cancel; if the  $A\Delta R$  and  $\Delta T_c$  values were smaller (closer to zero) for the same values of  $d_{\text{Nb}}$ , then the spin decay length would be longer, and perhaps more relatable to a physical value.

## 7.4 Conclusions

Positive magnetoresistance corresponding to GMR carried by quasiparticles (‘QP GMR’) has been observed in these devices, along with the superconducting spin valve effect. This effect is previously unreported in the literature for CPP devices. Furthermore, a crossover between these two regimes with a systematic dependence on  $d_{\text{Nb}}$  has been observed, linked to the strength of superconductivity in the Nb. A physical interpretation of these results considers QP GMR dominating when the two ferromagnetic layers do not interact within the superconductor, with spin decay occurring via Andreev reflection over a superconducting coherence length. When  $d_{\text{Nb}}$  is less than twice the coherence length, the entirety of the superconductor is influenced by the ferromagnets, causing the superconducting spin valve effect to dominate. The decay of this effect appears to be

shorter than the superconducting coherence length. These results are novel for CPP spin valves, and suggest further physics is yet to be discovered in these devices. They have relevance to the future production of superconducting spintronics circuits, which will use CPP devices, and designers will need to take these two effects into account.

The key results from this chapter are:

- For  $d_{\text{Nb}} > 26$  nm, quasiparticle transport occurs across the device, with a spin decay length of  $12 \pm 4$  nm, in CPP superconducting spin valves at temperatures of  $T/T_{\text{device}} = 0.3$ .
- This agrees with previous results suggesting that Andreev reflection occurs over the superconducting coherence length.
- Extending beyond those results, for  $d_{\text{Nb}} < 26$  nm, the parallel state has higher resistance and lower  $T_c$ , showing that the superconducting spin valve effect exists in CPP spin valves.
- These effects compete within the superconductor, the crossover between the two occurring at  $d_{\text{Nb}} = 2\xi_{S,d}$ .

# Chapter 8

## Conclusions and future work

### 8.1 Summary of conclusions

In this investigation, current perpendicular-to-plane (CPP) nanopillar superconducting spin valves have been fabricated, characterised in the normal and superconducting states, and used to investigate spin transport through a superconductor. In particular, a novel observation of the superconducting spin valve effect in CPP devices has been made for devices with  $d_{\text{Nb}} < 2\xi$ .

Overall, the main results of this thesis include

- The normal state spin decay length of Nb below 10 K was calculated using a fit from Valet-Fert theory,  $l_{sf}^{\text{Nb}} = 26.1 \pm 1.7$  nm, which is associated with a Cu/Nb interface flipping parameter of  $\delta = 0.24 \pm 0.07$ .
- This value of  $l_{sf}^{\text{Nb}}$  is low compared to other results from the literature. This is attributed to increased resistivity of the devices, due to the FIB patterning process.
- The interface flipping parameter  $\delta$  agrees with previous results from the literature.
- In the superconducting state, transport through the spin valves exhibits a systematic dependence on  $d_{\text{Nb}}$ , due to two competing effects.
- The devices exhibit quasiparticle-mediated giant magnetoresistance when  $d_{\text{Nb}} > 2\xi_{S,d}$ . This can be used to investigate spin transport through a superconductor.
- The quasiparticles have a spin decay length in the superconducting state, of  $l_{sf}^{\text{Nb}} = 12 \pm 4$  nm, which corresponds to the superconducting coherence length.
- For the first time, the superconducting spin valve effect has been observed in a CPP device, occurring when  $d_{\text{Nb}} < 2\xi_{S,d}$ .
- This effect appears more readily in a CPP nanopillar than in CIP wires or large area devices.

- The use of normal state contacts in these nanopillar devices can give rise to background effects which detract from the main results under consideration. Of particular note is the discovery that significant effects can result from the impact of single cuts through a heterostructure. This will have to be accounted for by future users of devices of this type.

## 8.2 Future Work

### 8.2.1 Device construction

This thesis has covered the development of CPP superconducting spin valve nanopillars, and a number of lessons have been learnt for the construction of these devices going forward. The primary finding associated with the nanopillar fabrication is the importance of using superconducting contact layers if the central devices feature superconductors, to avoid the background effects that occur in the wires, including possible stray field effects and single cut magnetoresistance, by ensuring the central nanopillar is measured by a true four-point measurement. If non-superconducting effects are being measured in the nanopillar, use of normal state contacts is more reasonable, such as used in [46, 48, 79]. However, in these cases, care should still be taken over the impact of single cut magnetoresistance, and the resistance of the wires will result in obtained  $\Delta R$  values from spin valve devices having lower or incomparable magnetoresistances to other devices from literature. If a true four-point measurement with Cu contacts is necessary, a four-wire structure may be fabricated using a more complex focused-ion beam (FIB) procedure [207]. However, given the impact of the FIB process to the results in this investigation, increased FIB milling may be undesirable. Although no systematic changes with device dimensions were seen, varying pillar sizes may have caused differences between devices. Good consistency with the FIB is possible when all devices across a substrate are made the same. As a result, in future works, all devices should be made with the same dimensions.

The structure used in this investigation could also be optimised. It should be noted that if Nb contacts are used, a Cu layer above the bottom Nb contact deposited at lower power (such as 15 W) or made thicker ( $\geq 20$  nm) may be necessary to ensure successful exchange bias. Cu buffer layers between the Py and central Nb improve results and should be included, but can be of reduced thickness to those used here - less than 5 nm may be ideal. The choice of 15 nm Py layers seems to be a reasonable balance between achieving larger magnetoresistance and higher  $T_c$  values, but could be changed depending on the needs of the investigation. Finally, developing this structure into a non-local setup would allow comparison between spin decay results with and without associated charge flow. This would also be of use in spin-orbit coupling investigations, as described below.

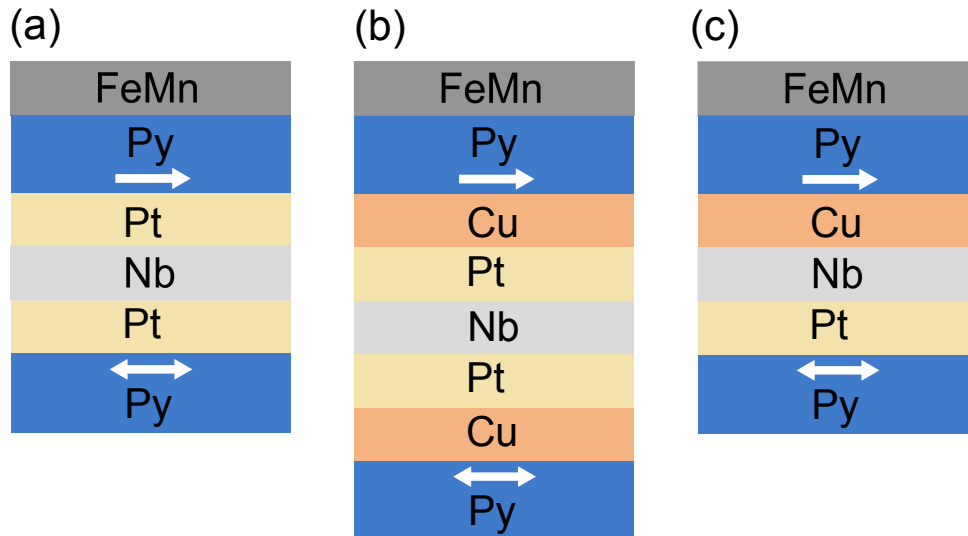


**Figure 8.1:** Three variations on the structure used in these experiments, now including Pt contact layers for the investigation into the effect of spin-orbit coupling on spin transport in a superconductor. All structures would additionally have seed and contact layers (not shown) and would be fabricated into nanopillars and tested in the CPP regime. (a) A symmetric structure, for investigation into triplet pair generation. (b) Varying thickness of Cu layers will investigate the impact of changing exchange field within the Pt. (c) An asymmetric structure will help test the impact of Pt with regards to current transport direction through the structure.

## 8.2.2 Spin-orbit coupling

These devices have been shown to effectively measure spin transport through a superconductor. Modification of the devices will therefore allow investigation into the effect of various materials on spin transport through a superconductor, via layer addition or substitution. One possibility is to swap one or both of the Cu buffer layers with Pt, to investigate the effect of spin-orbit coupling on the spin transport. Spin orbit coupling in the presence of an exchange field has been proposed as a source of triplet Cooper pairs [208]. Similarly, devices using ferromagnetic resonance of Py to investigate the spin transport through superconducting Nb have been found to change from quasiparticle transport to triplet Cooper pair transport upon the addition of a Pt ‘spin-sink’ adjacent to the Nb [114]. The similarity of that structure with that used here makes the devices fabricated here ideally suited to further investigate that effect in a system with static ferromagnets and transport current, which would be more technologically useful than the ferromagnetic resonance setup.

In [114], the exchange splitting of the Pt, combined with its spin-orbit coupling, is thought to give rise to the triplet generation. Schematic diagrams of proposed structures to test this effect are shown in Figure 8.1. In a symmetrical structure such as Fig. 8.1(a), Py/Pt/Nb/Pt/Py/FeMn, the impact of Pt in the system and ideally the generation of triplet pairs could be demonstrated. This could be developed by keeping Cu between the Py and Nb, in a Py/Cu/Pt/Nb/Pt/Cu/Py/FeMn structure [Fig. 8.1(b)], where the

Cu could be made of various thicknesses to investigate if the strength of exchange field in Pt has an effect on the degree of triplet generation. Use of an asymmetric structure, Py/Cu/Nb/Pt/Py/FeMn [Fig. 8.1(c)] will also be important, to investigate whether Pt on both sides of the Nb is necessary, or possibly is detrimental to spin transport when on the current path due to its large spin-orbit coupling. Investigating this asymmetric structure with the Pt replacing the bottom Cu buffer layer instead of the top would also be of interest. In [114], the change of transport with temperature for different Nb thicknesses was used as proof of triplet transport; here, this would require Nb thicknesses between 30-40 nm, as the Nb would need to be thick enough to avoid the superconducting spin valve effect, but thin enough for strong magnetoresistance effects to still be seen. Alternatively, a change in behaviour from the superconducting spin valve effect as shown here may signify the presence of triplets, which do not experience pair breaking effects from exchange fields due to their aligned spins. At any point, Pt could also be substituted for a number of other spin mixers, suitable for testing alternative triplet generation mechanisms.

### 8.2.3 Superconducting spin valve effect

A primary result of this thesis is the novel observation of the superconducting spin valve effect in CPP spin valves, where  $d_{\text{Nb}} < 2\xi_S$ . This suggests further understanding of the physics behind this effect is possible, and these structures could be optimised to investigate this without the complications found in these results.

Firstly, further investigation into the superconducting spin valve in these devices would be useful. The impact of changing Py layer thickness (thereby changing the strength of exchange fields in the system) could be of interest. Using larger pillar areas to minimise device heating could allow investigation of the effect at higher currents, and optimising superconductivity of the devices so that the base of the device transition can be reached should provide interesting insight into the effect.

The structure in general could also be used to answer why some devices in literature are dominated by stray field effects, whereas others demonstrate the spin valve effect. Using this structure in CIP devices, measured at every stage of fabrication would be of interest - studying why effect appears in the nanopillars, but not the wires, for devices between  $21 \text{ nm} < d_{\text{Nb}} < 26 \text{ nm}$  may reveal interesting insights into the physics of superconducting spin valves, particularly at non-equilibrium currents. For instance, it may be found that the current passing perpendicularly through the layers encourages the effect, or alternatively it may be found that the reduced area of the nanopillars is key to its appearance, as stray fields might be less significant or not appear in such small devices.

# References

- [1] J. Shalf, *Philos. Trans. R. Soc.* **378**, 1 (2020).
- [2] A. Andrae and T. Edler, *Challenges* **6**, 117 (2015).
- [3] I. I. Soloviev, N. V. Klenov, S. V. Bakurskiy, M. Y. Kupriyanov, A. L. Gudkov, and A. S. Sidorenko, *Beilstein J. Nanotechnol.* **8**, 2689 (2017).
- [4] J. Linder and J. W. A. Robinson, *Nat. Phys.* **11**, 307 (2015).
- [5] M. Eschrig, *Reports Prog. Phys.* **78**, 104501 (2015).
- [6] I. Žutić, J. Fabian, and S. Das Sarma, *Rev. Mod. Phys.* **76**, 323 (2004).
- [7] L. R. Tagirov, *Phys. Rev. Lett.* **83**, 2058 (1999).
- [8] H. Yang, S.-H. Yang, S. Takahashi, S. Maekawa, and S. S. P. Parkin, *Nat. Mater.* **9**, 586 (2010).
- [9] L. N. Bulaevskii, V. V. Kuzii, and A. A. Sobyenin, *JETP Lett.* **25**, 290 (1977).
- [10] A. I. Buzdin, *Rev. Mod. Phys.* **77**, 935 (2005).
- [11] R. S. Keizer, S. T. B. Goennenwein, T. M. Klapwijk, G. Miao, G. Xiao, and A. Gupta, *Nature* **439**, 825 (2006).
- [12] T. S. Khaire, M. A. Khasawneh, W. P. Pratt, and N. O. Birge, *Phys. Rev. Lett.* **104**, 137002 (2010).
- [13] J. W. A. Robinson, J. D. S. Witt, and M. G. Blamire, *Science* **329**, 59 (2010).
- [14] J. Y. Gu, J. A. Caballero, R. D. Slater, R. Loloee, and W. P. Pratt, *Phys. Rev. B* **66**, 140507 (2002).
- [15] J. M. D. Coey, *Magnetism and Magnetic Materials*, (Cambridge University Press 2010).
- [16] S. Chikazumi, *Physics of Ferromagnetism*, (Oxford Science Publications 1997) 2nd edn.
- [17] J. Stohr and H. C. Siegmann, *Magnetism: From Fundamentals to Nanoscale Dynamics*, (Springer 2006).
- [18] R. Jungblut, R. Coehoorn, M. T. Johnson, J. aan de Stegge, and A. Reinders, *J. Appl. Phys.* **75**, 6659 (1994).
- [19] G. M. Stocks, W. A. Shelton, T. C. Schulthess, B. Újfalussy, W. H. Butler, and A. Canning, *J. Appl. Phys.* **91**, 7355 (2002).
- [20] T. C. Schulthess, W. H. Butler, G. M. Stocks, S. Maat, and G. J. Mankey, *J. Appl. Phys.* **85**, 4842 (1999).

- [21] C. Kittel, *Introduction to Solid State Physics*, (John Wiley & Sons 2004) 8th edn.
- [22] R. E. Hummel, *Electronic Properties of Materials*, (Springer-Verlag, New York 2011) 4th edn.
- [23] M. Ziese and M. J. Thornton (eds.) *Spin Electronics* vol. 569 of *Lecture Notes in Physics*, (Springer, Berlin, Heidelberg 2001).
- [24] P. M. Tedrow and R. Meservey, *Phys. Rev. B* **7**, 318 (1973).
- [25] M. Johnson and R. H. Silsbee, *Phys. Rev. Lett.* **55**, 1790 (1985).
- [26] M. Johnson and R. H. Silsbee, *Phys. Rev. B* **37**, 5326 (1988).
- [27] M. Johnson and R. H. Silsbee, *Phys. Rev. B* **37**, 5312 (1988).
- [28] J. Bass, *J. Magn. Magn. Mater.* **408**, 244 (2016).
- [29] S. S. P. Parkin (ed.) *Ultrathin Magnetic Structures II* vol. 156 of *Lecture Notes in Physics*, (Springer-Verlag, Berlin, Heidelberg 1994).
- [30] M. N. Baibich, J. M. Broto, A. Fert, F. N. Van Dau, F. Petroff, P. Eitenne, G. Creuzet, A. Friederich, and J. Chazelas, *Phys. Rev. Lett.* **61**, 2472 (1988).
- [31] G. Binasch, P. Grünberg, F. Saurenbach, and W. Zinn, *Phys. Rev. B* **39**, 4828 (1989).
- [32] J. Bardeen, L. N. Cooper, and J. R. Schrieffer, *Phys. Rev.* **108**, 1175 (1957).
- [33] M. Tinkham, *Introduction to Superconductivity: Second Edition*, (Dover Publications 2004).
- [34] L. P. Gor'kov, *Phys. Rev.* **36**, 1364 (1959).
- [35] M. G. Flokstra, Ph.d. thesis Leiden University (2010).
- [36] F. S. Bergeret, A. F. Volkov, and K. B. Efetov, *Phys. Rev. B* **69**, 1 (2004).
- [37] M. Eschrig and T. Löfwander, *Nat. Phys.* **4**, 138 (2008).
- [38] J. Clarke, *Phys. Rev. Lett.* **28**, 1363 (1972).
- [39] J. P. Morten, A. Brataas, G. E. W. Bauer, W. Belzig, and Y. Tserkovnyak, (2008).
- [40] P. De Gennes, *Phys. Lett.* **23**, 10 (1966).
- [41] S. Oh, D. Youm, and M. R. Beasley, *Appl. Phys. Lett.* **71**, 2376 (1997).
- [42] A. I. Buzdin and A. Vedyayev, *Europhys. Lett.* **48**, 686 (1999).
- [43] M. Ohring, *The Materials Science of Thin Films*, (Academic Press 2001).
- [44] J. A. Thornton, *J Vac Sci Technol* **11**, 666 (1974).
- [45] C. Bell, G. Burnell, D.-J. Kang, R. H. Hadfield, M. J. Kappers, and M. G. Blamire, *Nanotechnology* **14**, 630 (2003).
- [46] M. C. Wu, A. Aziz, J. D. Witt, M. C. Hickey, M. Ali, C. H. Marrows, B. J. Hickey, and M. G. Blamire, *Nanotechnology* **19**, 3 (2008).
- [47] C. Bell, G. Burnell, D. J. Kang, R. H. Hadfield, M. J. Kappers, and M. G. Blamire, *Nanotechnology* **14**, 630 (2003).
- [48] N. Banerjee, A. Aziz, M. Ali, J. W. A. Robinson, B. J. Hickey, and M. G. Blamire, *Phys. Rev. B* **82**, 1 (2010).
- [49] J. Nogués and I. K. Schuller, *J. Magn. Magn. Mater.* **192**, 203 (1999).

- 
- [50] C. Tsang, N. Heiman, and K. Lee, *J. Appl. Phys.* **52**, 2471 (1981).
- [51] C. Tsang and K. Lee, *J. Appl. Phys.* **53**, 2605 (1982).
- [52] K. Y. Kim, H. C. Choi, S. Y. Jo, and C. Y. You, *J. Appl. Phys.* **114**, 1 (2013).
- [53] W. Park, D. V. Baxter, S. Steenwyk, I. Moraru, W. P. Pratt, and J. Bass, *Phys. Rev. B* **62**, 1178 (2000).
- [54] W. Kuch, L. I. Chelaru, and J. Kirschner, *Surf. Sci.* **566-568**, 221 (2004).
- [55] C. M. Park, K. I. Min, and K. H. Shin, *J. Appl. Phys.* **79**, 6228 (1996).
- [56] J. H. Greiner, *J. Appl. Phys.* **37**, 1474 (1966).
- [57] D. Mauri, E. Kay, D. Scholl, and J. K. Howard, *J. Appl. Phys.* **62**, 2929 (1987).
- [58] H. Sang, Y. W. Du, and C. L. Chien, *J. Appl. Phys.* **85**, 4931 (1999).
- [59] K. O'Grady, L. E. Fernandez-Outon, and G. Vallejo-Fernandez, *J. Magn. Magn. Mater.* **322**, 883 (2010).
- [60] W. P. Pratt, S. Steenwyk, S. Hsu, W.-C. Chiang, A. Schaefer, R. Loloee, and J. Bass, *IEEE Trans. Magn.* **33**, 3505 (1997).
- [61] K. T. Kung, L. K. Louie, and G. L. Gorman, *J. Appl. Phys.* **69**, 5634 (1991).
- [62] J. C. Kools, *J. Appl. Phys.* **77**, 2993 (1995).
- [63] J. A. Caballero, A. C. Reilly, Y. Hao, J. Bass, W. P. Pratt, F. Petro, and J. R. Childress, **199**, 198 (1999).
- [64] C. Liu, C. Yu, H. Jiang, L. Shen, C. Alexander, and G. J. Mankey, *J. Appl. Phys.* **87**, 6644 (2000).
- [65] L. Alonso, T. R. F. Peixoto, and D. R. Cornejo, *J. Phys. D. Appl. Phys.* **43** (2010).
- [66] M. J. Johnson, P. J. H. Bloemen, F. J. A. den Broeder, and J. J. de Vries, *Reports Prog. Phys.* **59**, 1409 (1996).
- [67] Y. K. Kim and T. J. Silva, *Appl. Phys. Lett.* **68**, 2885 (1995).
- [68] S. F. Cheng, P. Lubitz, Y. Zheng, and A. S. Edelstein, *J. Magn. Magn. Mater.* **282**, 109 (2004).
- [69] M. S. Blois, *J. Appl. Phys.* **26**, 975 (1955).
- [70] J. I. Martín, J. Nogués, K. Liu, J. L. Vicent, and I. K. Schuller, *J. Magn. Magn. Mater.* **256**, 449 (2003).
- [71] M. F. Gillies, J. N. Chapman, and J. C. S. Kools, *J. Appl. Phys.* **78**, 5554 (1995).
- [72] A. Y. Rusanov, M. Hesselberth, J. Aarts, and A. I. Buzdin, *Phys. Rev. Lett.* **93**, 1 (2004).
- [73] K. Nordquist, *J. Vac. Sci. Technol. B Microelectron. Nanom. Struct.* **15**, 2274 (1997).
- [74] L. Kong, Q. Pan, B. Cui, M. Li, and S. Y. Chou, *J. Appl. Phys.* **85**, 5492 (1999).
- [75] C. Bell, G. Burnell, C. W. Leung, E. J. Tarte, D. J. Kang, and M. G. Blamire, **84**, 1153 (2003).
- [76] J. Fluitman, *Thin Solid Films* **16**, 269 (1973).

- [77] I. V. Roshchin, J. Yu, A. D. Kent, G. W. Stupian, and M. S. Leung, *IEEE Trans. Magn.* **37**, 2101 (2001).
- [78] A. O. Adeyeye, J. A. Bland, C. Daboo, J. Lee, U. Ebels, and H. Ahmed, *J. Appl. Phys.* **79**, 6120 (1996).
- [79] C. W. Leung, C. Bell, G. Burnell, and M. G. Blamire, *Phys. Rev. B* **72**, 1 (2005).
- [80] J. W. A. Robinson, S. Piano, G. Burnell, C. Bell, and M. G. Blamire, *Phys. Rev. B* **76**, 1 (2007).
- [81] F. Wilhelm, U. Bovensiepen, A. Scherz, P. Pouloupoulos, A. Ney, H. Wende, G. Ceбалlos, and K. Baberschke, *J. Magn. Magn. Mater.* **222**, 163 (2000).
- [82] A. Ernst, M. Lueders, W. M. Temmerman, Z. Szotek, and G. Van Der Laan, *J. Phys. Condens. Matter* **12**, 5599 (2000).
- [83] C. Bell, R. Loloee, G. Burnell, and M. G. Blamire, *Phys. Rev. B* **71**, 2 (2005).
- [84] S. Hirayama, S. Kasai, and S. Mitani, *Jpn. J. Appl. Phys.* **57**, 2 (2018).
- [85] Y. Jiang, S. Yao, and W. Zhang, *Thin Solid Films* **516**, 3210 (2008).
- [86] W. C. Chiang, W. Pratt, M. Herrold, and D. V. Baxter, *Phys. Rev. B* **58**, 5602 (1998).
- [87] R. K. Singh, N. D. Rizzo, M. Bertram, K. Zheng, and N. Newman, *IEEE Magn. Lett.* **9**, 8 (2017).
- [88] M. C. Cyrille, S. Kim, M. E. Gomez, J. Santamaria, C. Leighton, K. M. Krishnan, and I. K. Schuller, *Phys. Rev. B* **62**, 15079 (2000).
- [89] A. Zambano, K. Eid, R. Loloee, W. P. Pratt, and J. Bass, *J. Magn. Magn. Mater.* **253**, 51 (2002).
- [90] J. L. Leal and M. H. Kryder, *IEEE Trans. Magn.* **32**, 4642 (1996).
- [91] R. W. Moseley, W. E. Booij, E. J. Tarte, and M. G. Blamire, *Appl. Phys. Lett.* **75**, 262 (1999).
- [92] J. A. Katine, M. K. Ho, Y. S. Ju, and C. T. Rettner, *Appl. Phys. Lett.* **83**, 401 (2003).
- [93] D. Ozkaya L, R. M. Langford, W. L. Chan, and A. K. Petford-Long, *J. Appl. Phys.* **91**, 9937 (2002).
- [94] J. A. Katine, A. Palanisami, and R. A. Buhrman, *Appl. Phys. Lett.* **74**, 1883 (1999).
- [95] R. D. Slater, J. A. Caballero, R. Loloee, and W. P. Pratt, *J. Appl. Phys.* **90**, 5242 (2001).
- [96] W. M. Kaminsky, G. A. Jones, N. K. Patel, W. E. Booij, M. G. Blamire, S. M. Gardiner, Y. B. Xu, and J. A. Bland, *Appl. Phys. Lett.* **78**, 1589 (2001).
- [97] E. Kerr, S. Van Dijken, R. M. Langford, and J. M. Coey, *J. Magn. Magn. Mater.* **290**, 124 (2005).
- [98] G. Xiong, D. A. Allwood, M. D. Cooke, and R. P. Cowburn, *Appl. Phys. Lett.* **79**, 3461 (2001).
- [99] M. T. Le, Y. U. Sohn, J. W. Lim, and G. S. Choi, *Mater. Trans.* **51**, 116 (2010).

- 
- [100] G. Nahrwold, J. M. Scholtyssek, S. Motl-Ziegler, O. Albrecht, U. Merkt, and G. Meier, *J. Appl. Phys.* **108** (2010).
- [101] C. Bell, Ph.d. thesis University of Cambridge (2005).
- [102] M. Hosomi, E. Makino, I. Konishiike, N. Sugawara, and S. Ohkawara, *J. Appl. Phys.* **91**, 8099 (2002).
- [103] P. Zhang and Y. Y. Lau, *IEEE J. Electron Devices Soc.* **1**, 83 (2013).
- [104] Q. Yang, P. Holody, S. F. Lee, L. L. Henry, R. Loloee, P. A. Schroeder, W. P. Pratt, and J. Bass, *Phys. Rev. Lett.* **72**, 3274 (1994).
- [105] F. J. Jedema, M. S. Nijboer, A. T. Filip, and B. J. van Wees, **15** (2001).
- [106] T. W. Clinton and M. Johnson, *J. Appl. Phys.* **85**, 1637 (1999).
- [107] W. P. Pratt, S. F. Lee, J. M. Slaughter, R. Loloee, P. A. Schroeder, and J. Bass, *Phys. Rev. Lett.* **66**, 3060 (1991).
- [108] T. Valet and A. Fert, *J. Magn. Magn. Mater.* **121**, 378 (1993).
- [109] K. Eid, D. Portner, J. A. Borchers, R. Loloee, M. Al-Haj Darwish, M. Tsoi, R. D. Slater, K. V. O'Donovan, H. Kurt, W. P. Pratt, and J. Bass, *Phys. Rev. B* **65**, 544241 (2002).
- [110] S. F. Lee, Q. Yang, P. Holody, R. Loloee, J. H. Hetherington, S. Mahmood, B. Ikegami, K. Vigen, L. L. Henry, P. A. Schroeder, W. P. Pratt, and J. Bass, *Phys. Rev. B* **52**, 15426 (1995).
- [111] M. A. Gijs, S. K. Lenczowski, J. B. Giesbers, R. J. van de Veerdonk, M. T. Johnson, and J. B. aan de Stegge, *Mater. Sci. Eng. B* **31**, 85 (1995).
- [112] J. C. Read, T. M. Nakatani, N. Smith, Y. S. Choi, B. R. York, E. Brinkman, and J. R. Childress, *J. Appl. Phys.* **118** (2015).
- [113] S. Zhang and P. M. Levy, *J. Appl. Phys.* **69**, 4786 (1991).
- [114] K.-R. Jeon, C. Ciccarelli, A. J. Ferguson, H. Kurebayashi, L. F. Cohen, X. Montiel, M. Eschrig, J. W. A. Robinson, and M. G. Blamire, *Nat. Mater.* **17**, 499 (2018).
- [115] S. Urazhdin, N. O. Birge, W. P. Pratt, and J. Bass, *Appl. Phys. Lett.* **84**, 1516 (2004).
- [116] Q. Fowler, B. Richard, A. Sharma, N. Theodoropoulou, R. Loloee, W. P. Pratt, and J. Bass, *J. Magn. Magn. Mater.* **321**, 99 (2009).
- [117] F. J. Jedema, M. S. Nijboer, A. T. Filip, and B. J. van Wees, *Phys. Rev. B* **67**, 1 (2003).
- [118] J. Bass and W. P. Pratt, *J. Phys. Condens. Matter* **19**, 183201 (2007).
- [119] S. D. Steenwyk, S. Y. Hsu, R. Loloee, J. Bass, and W. P. Pratt, *J. Magn. Magn. Mater.* **170**, 1 (1997).
- [120] A. C. Reilly, W. Park, Y. Hsu, R. Loloee, W. P. Pratt, E. Lansing, and G. Rapids, **34**, 939 (1998).
- [121] S. Dubois, L. Piraux, J. M. George, K. Ounadjela, J. L. Duvail, and A. Fert, *Phys. Rev. B* **60**, 477 (1999).

- [122] S. Maat, M. J. Carey, and J. R. Childress, *Appl. Phys. Lett.* **93**, 1 (2008).
- [123] H. Yuasa, M. Yoshikawa, Y. Kamiguchi, K. Koi, H. Iwasaki, M. Takagishi, and M. Sahashi, *J. Appl. Phys.* **92**, 2646 (2002).
- [124] A. Jogo, K. Nagasaka, T. Ibusuki, Y. Shimizu, A. Tanaka, and H. Oshima, *J. Magn. Magn. Mater.* **309**, 80 (2007).
- [125] S. Isogami, M. Tsunoda, K. Noguchi, T. Nakamura, H. Osawa, and M. Takahashi, *Phys. Status Solidi Appl. Mater. Sci.* **204**, 4033 (2007).
- [126] H. Yuasa, H. Fukuzawa, H. Iwasaki, M. Yoshikawa, M. Takagishi, and M. Sahashi, *J. Appl. Phys.* **93**, 7915 (2003).
- [127] M. AlHajDarwish, H. Kurt, S. Urazhdin, A. Fert, R. Loloee, W. P. Pratt, and J. Bass, *Phys. Rev. Lett.* **93**, 8 (2004).
- [128] K. Eid, H. Kurt, W. P. Pratt, and J. Bass, *Phys. Rev. B* **70**, 1 (2004).
- [129] A. Aziz, O. P. Wessely, M. Ali, D. M. Edwards, C. H. Marrows, B. J. Hickey, and M. G. Blamire, *Phys. Rev. Lett.* **103**, 4 (2009).
- [130] B. Dieny, V. S. Speriosu, S. S. Parkin, B. A. Gurney, D. R. Wilhoit, and D. Mauri, *Phys. Rev. B* **43**, 1297 (1991).
- [131] Y. Uehara, K. Yamada, and H. Kanai, *IEEE Trans. Magn.* **32**, 3431 (1996).
- [132] J. A. Caballero, C. E. Moreau, W. P. Pratt, and N. O. Birge, *IEEE Trans. Magn.* **37**, 2111 (2001).
- [133] F. J. Albert, N. C. Emley, E. B. Myers, D. C. Ralph, and R. A. Buhrman, *Phys. Rev. Lett.* **89**, 1 (2002).
- [134] S. D. Steenwyk, S. Y. Hsu, R. Loloee, J. Bass, and W. P. Pratt, *J. Appl. Phys.* **81**, 4011 (1997).
- [135] L. Vila, W. Park, J. A. Caballero, D. Bozec, R. Loloee, W. P. Pratt, and J. Bass, *J. Appl. Phys.* **87**, 8610 (2000).
- [136] M. Flokstra, J. M. Van Der Knaap, and J. Aarts, *Phys. Rev. B* **82**, 1 (2010).
- [137] M. Johnson, *Appl. Phys. Lett.* **65**, 1460 (1994).
- [138] S. Komori, J. M. Devine-Stoneman, K. Ohnishi, G. Yang, Z. Devizorova, S. Mironov, X. Montiel, L. A. Olthof, L. F. Cohen, H. Kurebayashi, M. G. Blamire, A. I. Buzdin, and J. W. Robinson, *Sci. Adv.* **7**, 1 (2021).
- [139] J. Y. Gu, C.-Y. You, J. S. Jiang, J. Pearson, Y. B. Bazaliy, and S. D. Bader, *Phys. Rev. Lett.* **89**, 267001 (2002).
- [140] A. Potenza and C. H. Marrows, *Phys. Rev. B* **71**, 180503 (2005).
- [141] P. Cadden-Zimansky, Y. B. Bazaliy, L. M. Litvak, J. S. Jiang, J. Pearson, J. Y. Gu, C. Y. You, M. R. Beasley, and S. D. Bader, *Phys. Rev. B* **77** (2008).
- [142] J. Zhu, I. N. Krivorotov, K. Halterman, and O. T. Valls, *Phys. Rev. Lett.* **105**, 1 (2010).
- [143] P. V. Leksin, N. N. Garif'yanov, I. A. Garifullin, J. Schumann, V. Kataev, O. G. Schmidt, and B. Büchner, *Phys. Rev. Lett.* **106**, 067005 (2011).

- 
- [144] P. V. Leksin, N. N. Garif'yanov, A. A. Kamashev, Y. V. Fominov, J. Schumann, C. Hess, V. Kataev, B. Büchner, and I. A. Garifullin, *Phys. Rev. B* **91**, 214508 (2015).
- [145] G.-X. Miao, A. V. Ramos, and J. S. Moodera, *Phys. Rev. Lett.* **101**, 137001 (2008).
- [146] Y. Luo and K. Samwer, *Epl* **91**, 2 (2010).
- [147] I. C. Moraru, W. P. Pratt, and N. O. Birge, *Phys. Rev. Lett.* **96**, 037004 (2006).
- [148] Y. Gu, G. Halász, J. W. A. Robinson, and M. G. Blamire, *Phys. Rev. Lett.* **115** (2015).
- [149] P. V. Leksin, N. N. Garif'yanov, I. A. Garifullin, J. Schumann, H. Vinzelberg, V. Kataev, R. Klingeler, O. G. Schmidt, and B. Büchner, *Appl. Phys. Lett.* **97**, 102505 (2010).
- [150] G. Nowak, H. Zabel, K. Westerholt, I. A. Garifullin, M. Marcellini, A. Liebig, and B. Hjörvarsson, *Phys. Rev. B* **78**, 1 (2008).
- [151] G. Nowak, K. Westerholt, and H. Zabel, *Supercond. Sci. Technol.* **26**, 025004 (2013).
- [152] U. D. Chacón Hernandez, M. A. Sousa, F. J. Litterst, V. P. Nascimento, and E. Baggio-Saitovitch, *J. Magn. Magn. Mater.* **390**, 114 (2015).
- [153] Y. Zhu, A. Pal, M. G. Blamire, and Z. H. Barber, *Nat. Mater.* **1**, 1 (2016).
- [154] B. Li, N. Roschewsky, B. A. Assaf, M. Eich, M. Epstein-Martin, D. Heiman, M. Münzenberg, and J. S. Moodera, *Phys. Rev. Lett.* **110**, 1 (2013).
- [155] K. Westerholt, D. Sprungmann, H. Zabel, R. Brucas, B. Hjörvarsson, D. A. Tikhonov, and I. A. Garifullin, *Phys. Rev. Lett.* **95**, 1 (2005).
- [156] A. Y. Rusanov, S. Habraken, and J. Aarts, *Phys. Rev. B* **73**, 060505 (2006).
- [157] J. Aarts and A. Y. Rusanov, *Comptes Rendus Phys.* **7**, 99 (2006).
- [158] R. Steiner and P. Ziemann, *Phys. Rev. B* **74**, 1 (2006).
- [159] A. Singh, C. Sürgers, and H. V. Löhneysen, *Phys. Rev. B* **75**, 1 (2007).
- [160] A. Singh, C. Sürgers, R. Hoffmann, H. V. Löhneysen, T. V. Ashworth, N. Pilet, and H. J. Hug, *Appl. Phys. Lett.* **91**, 71 (2007).
- [161] D. Stamopoulos, E. Manios, and M. Pissas, *Phys. Rev. B* **75**, 1 (2007).
- [162] P. V. Leksin, R. I. Salikhov, I. A. Garifullin, H. Vinzelberg, V. Kataev, R. Klingeler, L. R. Tagirov, and B. Büchner, *JETP Lett.* **90**, 59 (2009).
- [163] T. J. Hwang, D. H. Kim, and S. Oh, *IEEE Trans. Magn.* **46**, 235 (2010).
- [164] P. V. Leksin, N. N. Garif'yanov, I. A. Garifullin, Y. V. Fominov, J. Schumann, Y. Krupskaya, V. Kataev, O. G. Schmidt, and B. Büchner, *Phys. Rev. Lett.* **109**, 1 (2012).
- [165] Y. V. Fominov, A. A. Golubov, T. Y. Karminskaya, M. Y. Kupriyanov, R. G. Deminov, and L. R. Tagirov, *JETP Lett.* **91**, 308 (2010).
- [166] S. V. Mironov and A. Buzdin, *Phys. Rev. B* **89**, 1 (2014).
- [167] S. Takahashi, H. Imamura, and S. Maekawa, *Phys. Rev. Lett.* **82**, 3911 (1999).

- [168] J. Zhu, X. Cheng, C. Boone, and I. N. Krivorotov, *Phys. Rev. Lett.* **103**, 1 (2009).
- [169] I. C. Moraru, W. P. Pratt, and N. O. Birge, *Phys. Rev. B* **74** (2006).
- [170] D. Beckmann, *J. Phys. Condens. Matter* **28**, 163001 (2016).
- [171] F. S. Bergeret, M. Silaev, P. Virtanen, and T. T. Heikkilä, *Rev. Mod. Phys.* **90**, 1 (2018).
- [172] C. H. L. Quay and M. Aprili, *Philos. Trans. R. Soc. A Math. Phys. Eng. Sci.* **376** (2018).
- [173] T. Yamashita, S. Takahashi, H. Imamura, and S. Maekawa, *Phys. Rev. B* **65**, 172509 (2002).
- [174] Y. Yafet, *Phys. Lett.* **98A**, 287 (1983).
- [175] J. P. Morten, A. Brataas, and W. Belzig, *Phys. Rev. B* **72**, 014510 (2005).
- [176] T. Wakamura, N. Hasegawa, K. Ohnishi, Y. Niimi, and Y. Otani, *Phys. Rev. Lett.* **112**, 036602 (2014).
- [177] N. Poli, J. P. Morten, M. Urech, A. Brataas, D. B. Haviland, and V. Korenivski, *Phys. Rev. Lett.* **100**, 136601 (2008).
- [178] B. Leridon, J. Lesueur, and M. Aprili, *Phys. Rev. B* **72**, 1 (2005).
- [179] Y.-S. Shin, H.-J. Lee, and H.-W. Lee, *Phys. Rev. B* **71**, 144513 (2005).
- [180] M. Urech, J. Johansson, N. Poli, V. Korenivski, and D. B. Haviland, *J. Appl. Phys.* **99**, 2004 (2006).
- [181] F. Hübler, M. J. Wolf, D. Beckmann, and H. v. Löhneysen, *Phys. Rev. Lett.* **109**, 207001 (2012).
- [182] M. J. Wolf, F. Hübler, S. Kolenda, H. v. Löhneysen, and D. Beckmann, *Phys. Rev. B* **87**, 024517 (2013).
- [183] C. H. L. Quay, D. Chevallier, C. Bena, and M. Aprili, *Nat. Phys.* **9**, 84 (2013).
- [184] M. J. Wolf, C. Sürgers, G. Fischer, and D. Beckmann, *Phys. Rev. B* **90**, 144509 (2014).
- [185] M. Silaev, P. Virtanen, F. S. Bergeret, and T. T. Heikkilä, *Phys. Rev. Lett.* **114**, 167002 (2015).
- [186] I. V. Bobkova and A. M. Bobkov, *Phys. Rev. B* **93**, 024513 (2016).
- [187] A. I. Gubin, K. S. Il'in, S. A. Vitusevich, M. Siegel, and N. Klein, *Phys. Rev. B* **72**, 064503 (2005).
- [188] W. Belzig, A. Brataas, Y. V. Nazarov, and G. E. Bauer, *Phys. Rev. B* **62**, 9726 (2000).
- [189] D. Stamopoulos, E. Manios, and M. Pissas, *Phys. Rev. B* **75**, 014501 (2007).
- [190] N. Banerjee, C. B. Smiet, R. G. J. Smits, A. Ozaeta, F. S. Bergeret, M. G. Blamire, and J. W. A. Robinson, *Nat. Commun.* **5**, 3048 (2014).
- [191] M. H. Kryder, K. Y. Ahn, N. J. Mazzeo, S. Schwarzl, and S. M. Kane, *IEEE Trans. Magn.* **16**, 99 (1980).
- [192] W. Buckel, *Supraleitung*, (Physik-Verlag, Weinheim 1984) 3rd edn.

- 
- [193] H. W. Weber, E. Seidl, C. Laa, E. Schachinger, M. Prohammer, A. Junod, and D. Eckert, *Phys. Rev. B* **44**, 7585 (1991).
- [194] D. H. Kim and T. J. Hwang, *Physica C: Superconductivity and its Applications* **455**, 58 (2007).
- [195] S. Garzon, I. Žutić, and R. A. Webb, *Phys. Rev. Lett.* **94**, 1 (2005).
- [196] A. A. Jara, E. Moen, O. T. Valls, and I. N. Krivorotov, *Phys. Rev. B* **100**, 1 (2019).
- [197] R. E. Matlack, *J. Appl. Phys.* **35**, 3331 (1964).
- [198] V. Novotny and P. P. Meincke, *J. Low Temp. Phys.* **18**, 147 (1975).
- [199] G. Deutscher and D. Feinberg, *Appl. Phys. Lett.* **76**, 487 (2000).
- [200] D. Beckmann, E. B. Weber, and H. V. Löhneysen, *Phys. Rev. Lett.* **93**, 1 (2004).
- [201] D. Beckmann and H. V. Löhneysen, *Appl. Phys. A Mater. Sci. Process.* **89**, 603 (2007).
- [202] A. Kleine, A. Baumgartner, J. Trbovic, and C. Schönenberger, *Europhys. Lett.* **87** (2009).
- [203] J. L. Webb, B. J. Hickey, and G. Burnell, *Phys. Rev. B* **86**, 1 (2012).
- [204] F. Giazotto, F. Taddei, F. Beltram, and R. Fazio, *Phys. Rev. Lett.* **97**, 1 (2006).
- [205] P. Cadden-Zimansky, Z. Jiang, and V. Chandrasekhar, *New J. Phys.* **9** (2007).
- [206] M. G. Blamire, *Private discussion*, 2021.
- [207] C. W. Leung, C. Bell, G. Burnell, and M. G. Blamire, *Nanotechnology* **15**, 786 (2004).
- [208] F. S. Bergeret and I. V. Tokatly, *Phys. Rev. B* **89**, 134517 (2014).